INVESTIGATING THE THERMAL AND THERMO-MECHANICAL PERFORMANCES OF GEOTHERMAL HEAT EXCHANGER WITH SPIRAL-TUBES

WANG DEQI

Ph.D

The Hong Kong Polytechnic University

2016

The Hong Kong Polytechnic University

Department of Building Services Engineering

Investigating the Thermal and Thermo-mechanical Performances of Geothermal Heat Exchanger with Spiral-tubes

WANG Deqi

A thesis submitted in partial fulfilment of the requirements

for the degree of Doctor of Philosophy

June 2016

CERTIFICATE OF ORIGINALITY

I hereby declare that this thesis is my own work and that, to the best of my knowledge and belief, it reproduces no material previously published or written, nor material that has been accepted for the award of any other degree or diploma, except where due acknowledgement has been made in the text.

____________________ (Signed)

WANG Deqi (Name of student)

Department of Building Services Engineering

The Hong Kong Polytechnic University

Hong Kong SAR, China

June 2016

ABSTRACT

Abstract of thesis entitled: Investigating the Thermal and Thermo-mechanical Performances of Geothermal Heat Exchanger with Spiral-tubes

Submitted by: WANG Deqi

For the degree of: Doctor of Philosophy

At The Hong Kong Polytechnics University in June, 2016

Ground-coupled heat pump (GCHP), one of renewable energy technologies, is a heat transfer device with high energy efficiency and little impact on the environment, which can transfer the heat from a cool space to a warm space or enhance the natural flow of heat from a warm place to a cool one. As a central heating and cooling system, GCHP utilises the ground as a heat source or sink to extract (in the winter) or store (in the summer) the heat energy. Without thermal disturbance, the temperature beneath approximate 6 meters of the ground surface varies within a small range, generally maintaining between 10 and 16 ℃. Due to this characteristic of little thermal disturbance, GCHP has better efficiency performance and lower operational costs compared to the conventional heating and cooling systems.

The geothermal heat exchanger (GHE) is the key connecting component between the heat pump unit and ground sources. Its heat transfer performance is regarded as the most important parameter of a GCHP system in either design or construction stage. The

system efficiency can be influenced directly by the GHE installation configuration, e.g. horizontal GHEs and vertical GHEs. Although the heat transfer mechanics of GHEs have been studied for many years, the current efforts have been focused on the linear type GHEs (U-tubes and W-tubes) and less on the modelling of GHE with spiral-tubes.

The spiral GHEs are initially used in horizontal GCHP systems. Compared with the traditional linear GHEs, spiral-tubes can greatly improve the heat transfer efficiency, and consequently, can reduce initial costs and the required installation area. Therefore, it is essential to establish a reliable analytical solution for the horizontal GHE with spiral-tubes. Additionally, with the increasing application of GCHP system in the urban area, presently the spiral-tubes can also be applied in vertical GHEs, especially for pile geothermal heat exchangers (PGHEs), also called energy pile. PGHE is a combination of a concrete pile foundation and GHE pipes. This special combination makes the classic vertical analytical models, e.g. cylindrical source model, fail to estimate the heat transfer performance of PGHE with spiral-tubes. Therefore, a new analytical model is needed to better describe the heat transfer process of PGHE with spiral-tubes. Furthermore, the study of the thermo-mechanical performance of PGHE is limited. The traditional design methods for foundation pile may fail due to the varying thermo-mechanical behaviours (such as the stress in the piles, and the reduction of ultimate bearing capacity) corresponding to the large underground temperature variations (up to 20ºC) during cooling or heating operation of GCHP. Therefore, it's important to systemically examine the thermo-mechanical behaviour for PGHE with spiral-tubes.

Accordingly, a research work on modelling the heat transfer performance of GHE with spiral-tubes and investigating the thermal-mechanical behaviour of PGHE with spiral-tubes has been carried out in this thesis.

This thesis begins with establishing a new analytical model for horizontal GHEs with spiral-tubes. In this new model, the spiral heat exchanger is simplified into a series of ring coils that inject/extract heat in/from a semi-infinite medium. A single ring model in an infinite medium is first introduced. Then, based on the method of images and superposition, the multiple ring-coils analytical solution is given. As the temperature variation at the ground surface has a significant influence on the heat transfer performance of horizontal GHEs, a sinusoidal temperature boundary condition is taken into consideration in the modelling process. To validate this new model, the results of temperature response from an on-site experiment and the proposed analytical model are compared. In addition, a numerical simulation model has also been used to verify the long-term operation of the proposed model. Good agreements were shown in these two validation processes. The temperature responses under different surface conditions were calculated by means of the valid analytical model and were further discussed.

Secondly, a novel composite analytical model for Pile GHE with spiral-tubes is presented. This new model successfully considered both the special geometrical shape of spiral-tubes and the difference of thermal properties between the pile and ground soil. Based on the Green's function theory, instantaneous heat source solutions are firstly derived by the Laplace method, and then a transient solution is obtained by integrating the instantaneous solution over time. This new analytical model was validated by a 3-D finite-element simulation model, and well agreement between the two models was observed. This newly developed analytical model can better describe the heat transfer process of the PGHE with spiral-tubes, especially the pile foundation temperature responses. As shown in the calculation results, the difference of thermal properties has a great influence on the heat transfer performance of PGHE with spiral-tubes. When the thermal conductivity of pile is twice as the one of soil, the dimensionless temperature at the middle of the pile is 0.3832 which is almost twice as the temperature response in the homogeneous case. Thus, it can be believed that this new model provides a more accurate tool for the design of PGHE system, and accurate performance estimation.

Thirdly, a semi-analytical solution for PGHE with spiral tubes under groundwater advection is presented. Applying the finite-element methods, a 3-D simulation model is established to investigate the effect of groundwater flow on PGHE with spiral-tubes in short-term operation. The numerical model is validated by the ring-coils source model in which no groundwater flow is considered. Based on the simulation results, a corrected parameter, effective groundwater flow velocity (L_{eff}), has been proposed to modify the moving source analytical solution. Without this corrected parameter, the relative errors of the original analytical model can attain to more than 300% in short-term operation. By introducing the effective groundwater flow velocity, the relative errors can be controlled within 10% in the area of concrete pile.

Finally, to investigate the thermo-mechanical behaviour under different thermal loads, an interface behaviour experiment is reported firstly. Then, based on the experiment results, a numerical model is presented to investigate the thermo-mechanical behaviour of PGHE with spiral-tubes in full size. A new direct shear apparatus which could control and monitor the test temperature was introduced, including the design concept and implement method. Based on this new apparatus, two groups of interface tests, sand-concrete and clay-concrete, were conducted. Based on the experimental data of friction angle and adhesion strength, a finite-element numerical model is established. The heat exchange process of GHE has a great effect on the skin friction behaviour of the pile. A 34.4% increase of bearing capacity is observed in the case of heating simulation and a 15.37% capacity decrease has been found in the case of cooling simulation.

In summary, in this thesis, the thermal and thermo-mechanical issues related to GHE with spiral-tubes are systematically studied. The academic contributions of this thesis can be summarized into four aspects: 1) a new analytical model, considering the sinusoidal temperature boundary condition, is established to examine the thermal performance of horizontal GHE with spiral-tubes; 2) a new composite analytical model, considering both the special geometrical shape of spiral-tubes and the difference of thermal properties between the pile and ground soil, is established to study the thermal performance of pile GHE with spiral-tubes; 3) for the situation of groundwater advection, a semi-analytical model is established for pile GHE with spiral-tubes to study the effect of groundwater advection on the pile thermal performance and 4) the thermo-mechanical performance of pile GHE with spiral-tubes were investigated by a new direct shear apparatus and a finite-element simulation model.

PUBLICATIONS DURING PHD STUDY

Journal papers arising from the thesis:

Wang, D., Lu, L., Cui, P. (2016). Experimental investigation of soil-concrete interface behaviour under thermal loads. Geomechanics for Energy and the Environment. (To be submitted).

Wang, D., Lu, L., Cui, P. (2016). Numerical study of the thermo-mechanical behaviour for energy pile under thermal loads. Applied Energy (To be submitted).

Wang, D., Lu, L., Cui, P. (2016). A novel composite-medium solution for pile geothermal heat exchangers with spiral coils. International Journal of Heat and Mass Transfer, 93, 760-769.

Wang, D., Lu, L., Cui, P. (2016). A new analytical solution for horizontal geothermal heat exchangers with vertical spiral coils. International Journal of Heat and Mass Transfer, 100, 111-120.

Wang, D., Lu, L., Zhang, W., Cui, P. (2015). Numerical and analytical analysis of groundwater influence on the pile geothermal heat exchanger with cast-in spiral coils. Applied Energy, 160, 705-714.

Wang, D., Lu, L., Zhang, W., Cui, P. (2014). Numerical and analytical analysis of groundwater influence on the pile ground heat exchanger with cast-in spiral coils. Energy Procedia, 61, 1784-1788.

Conference papers:

Wang, D., Lu, L., Cui, P. (2016). Numerical simulation of heat exchanger foundation pile considering its thermo-mechanical behaviour. Paper presented at the Internation ground source heat pump association, Dever.

Wang, D., Lu, L., Cui, P., Jiang, Y. (2015). CFD simulation of wind environment around a high-rise building at pedestrian level in Hong Kong. Paper presented at the 14th International Conference on Sustainable Energy Technologies, Nottingham.

Wang, D., Lu, L., Cui, P. (2015). A new analytical solution of pile geothermal heat exchangers with spiral coils in a composite body. Paper presented at the Second International Conference on Sustainable Urbanization, Hong Kong.

Wang, D., Cui, P., Yang, H. (2013). Numerical thermal investigation on the pile ground exchangers with groundwater seepage. Paper presented at the 12th International Conference on Sustainable Energy technologies, Hong Kong, Paper ID: 109.

Cui, P., Wang, D., Yang, j., Diao, N. (2013). Numerical simulation and experimental verification of horizontal ground heat exchangers. Paper presented at the 12th International Conference on Sustainable Energy technologies, Hong Kong, Paper ID: 417.

Monograph:

Wang, D. Application and Design Examples of Hybrid Solar-Wind Power Generation Technologies, Chapter 8 in book of Application of Hybrid Solar-Wind Power Generation Technologies. Beijing: China Architecture & Building Press. 2014. ISBN: 978-7-112-17328-0.

ACKNOWLEDGEMENTS

This thesis is my three-year hard work, and I believe that it is hard to finish without the help and supports of many people. I would like to acknowledge with my deep gratitude to all of them for their great help during my study period.

First and foremost, I would like to express my sincerest gratitude for my chief supervisor, Dr. Lu Lin. During my three-year Ph.D. study, Dr. Lu gave me a lot of advice and helped me conquer many difficulties in both my study and my life. I offer my sincere appreciation to her great encouragement, relentless advocacy, professional guidance and edits of my manuscripts. Without her consistent and illuminating instruction, this thesis could not have reached its present form.

I also would like to appreciate my co-supervisor, Dr. Cui Ping, for her insightful views and great help on my study and life. She provides me informative suggestions for my papers and thesis.

Furthermore, I would like to express my thanks to Prof. Yin Jianhua from CEE for his generosity to share his lab resources for my research project, and the members from the Laboratory of Soil Mechanics in the Hong Kong Polytechnic University, in particular, Mr. Chen Wenbo.

I would also appreciate my heartfelt gratitude to all the members of the Renewable Energy Research Group (RERG) for their help during my Ph.D. study period, especially for Dr. Zhang Wenke, Mr. Jiang Yu, and Mr. Shen Zhicheng, who give much support

for my experiment setting.

Finally, I would like to give my heartfelt appreciation to my wife, Ms. Fu Tong and to my parents for their full supports and encouragement for my work and life. Thank you for encouraging me to be a brave, independent and optimistic man, and I am so happy to being with you.

TABLE OF CONTENTS

LIST OF FIGURES

LIST OF TABLES

NOMENCLATURE

Abbreviations

AR	Analytical Results
CFD	Computational Fluid Dynamics
COP	Coefficient of Performance
DAVI	Diffused Air Volume Indicator
DSA-T	Direct Shearing Apparatus with Temperature Control
DSA-S	Direct Shear Apparatus with Suction Control
EMSD	Electrical and Mechanical Services Department
FLS	Finite Line Source
GCHP	Ground Coupled Heat Pump
GF	Green’s Function
GFSE	Green’s Function Solution Equation
GHE	Ground Heat Exchanger
GSHP	Ground Source Heat Pimp
GWHP	Ground Water Heat Pump
HAEPD	High Air Entry Porous Disk
HVAC	Heating Ventilation Air Conditioning
IAM	Improved Analytical Model
ILS	Infinite Line Source
LVDT	Linear Voltage Displacement Transformers

OAM	Original Analytical Model
PDE	Partial Differential Equation
PGHE	Pile Geothermal Heat Exchanger
PGHE-SC	Pile Geothermal Heat Exchanger with Spiral Coils
SR	Simulation Results
SWHP	Surface Water Heat Pump

Ordinary Symbols

A_α	dimensionless thermal diffusivity ratio	
b	pitch of the coil or spiral heat source	(m)
B	dimensionless coil pitch	
C_2	inertial resistance factor	
c_p	specific heat capacity value	(J kg^{-1} K^{-1})
E_f	total fluid energy	(J/kg^{-1})
E_s	total solid medium energy	(J/kg^{-1})
Fo	Fourier number	
h	length of finite ring coil source or spiral source	(m)
H	dimensionless depth	
h_1, h_2	depth	(m)
k	ground thermal conductivity	(W m^{-1} K^{-1})
k_f	fluid phase thermal conductivity	(W m^{-1} K^{-1})
k_s	solid medium thermal conductivity	(W m^{-1} K^{-1})

K	dimensionless thermal conductivity ratio	
l_r	radius of pile	(m)
l_z	depth of pile	(m)
N	number of spiral coils	
q_{ring}^{i}	instantaneous heat release rate per ring coil	(Wm)
q_{ring}	heat release rate per ring coil	(W)
r_0	radial circle	(m)
R	dimensionless radius	
T_0	initial temperature	
v	water flow velocity inside pipe	(m s^{-1})
x, y, z	Cartesian coordinates	(m)
X, Y, Z	dimensionless Cartesian coordinate	

Greek symbols

α	thermal diffusivity	(m^2 s^{-1})
α_p	permeability	(m/s)
ε	void fraction	
Θ	dimensionless excess temperature	
θ	excess temperature	
τ	time	(s)
φ	angular coordinate	(rad)
μ	viscosity	(Pa s)

ρ	density	(kg m^{-3})
ρ_f	fluid density	(kg m^{-3})

Superscript

$'$	integration parameter

Subscripts

$ring$	ring-coil heat source
i	infinite model
f	finite model

CHAPTER 1

INTRODUCTION

With the social and economic development, a thermal comfort working or living space becomes the basic requirements for modern people. With the increase of these requirements, the energy use in commercial and residential buildings has become a significant part of social energy consumption. According to the data from Building Energy Conservation Research Centre (Tsinghua University), the total energy consumption in Chia is 36.2 billion tons of standard coal in 2014, in which the building energy consumption accounts for 22.3% (Jiang & Wu, 2014). For the residential building, especially buildings in northern areas, more than 65% energy is consumed by heating and air conditioning, and nearly 15% energy is used for domestic hot water (Jun, 2007). For the commercial building, the energy used for ventilation and air-conditioning accounts for more than 60% in the total building energy consumption (Xue, 2005). Clearly, the air-conditioning system always plays an important role in the building energy consumption. In addition, with the higher and higher comfort requirements, this energy consumption keeps growing in recent years, and the growing energy has now become a great challenge to the society. To solve this problem, on the one hand, studies and measures have been conducted on improving the thermal insulation performance of building structure, and on the other hand, more efforts is focused on developing clean renewable energy technologies.

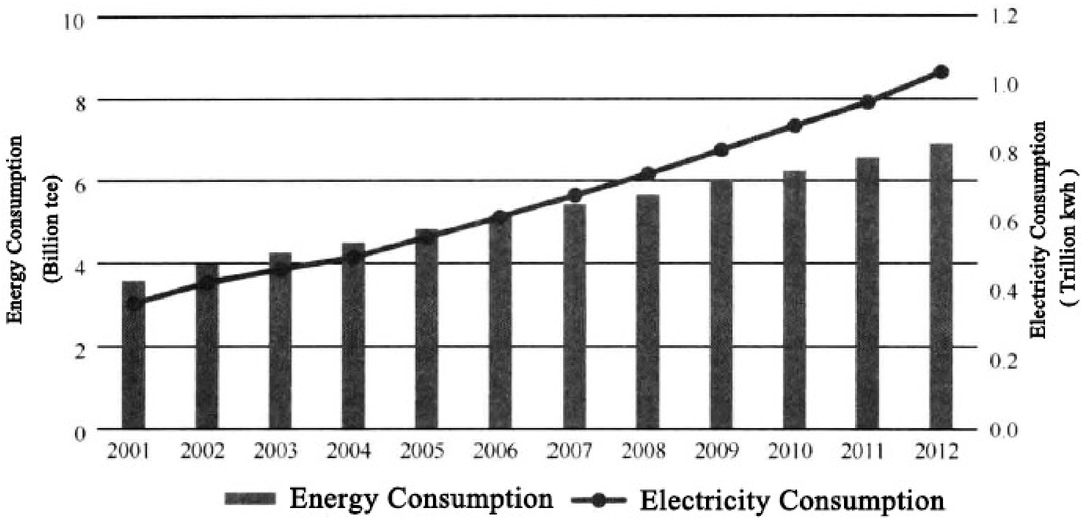

Figure 1-1 Building energy and electricity consumption (Jiang & Wu, 2014)

1.1 Background of Ground Source Heat Pump System (GSHP)

As one of renewable energy technology, ground source heat pump system (GSHP), one of renewable energy technologies, is a heat transfer device with high efficiency and environment-friendly, which can transfer the heat from a cool space to a warm space or enhance the natural flow of heat from a warm place to a cool one. GSHP is a central heating and cooling system which utilizes the ground as a heat source or sink to extract (in the winter) or store (in the summer) the heat energy. This system is quite different from the traditional geothermal power system which is using a high-temperature heat resource at deep ground to generate electricity. GSHP does not directly absorb the heat from the centre of the Earth, but utilizes the surface energy from solar. Without the disturbance of GSHP, the temperature beneath about 6 meters of the ground surface usually maintains between 10 and 16 ℃ (Barbier, 2002). The shallow layer ground temperature varies within a small range. Due to this characteristic, GSHP has a better efficiency and lower operational costs compared to conventional heating and cooling systems. Generally, the coefficient of performance (COP) of GSHP is higher than 3.5, which is almost twice than that of the conventional air-source heat pump systems. For either commercial or residential buildings, GSHP could be convinced as the most energy efficient technologies for providing heating, ventilation, and air-conditioning (HVAC).

A typical GSHP system mainly includes a geothermal heat exchanger (GHE) system, heat pump unit and heat distribution terminal system. GHE is the key connecting device between the heat pump unit and ground sources. It is regarded as the most important component of a GSHP system in either design or construction stage. The system efficiency can be influenced indirectly by pipe installation type of GSHP and there is various GSHP systems, such as open loops surface water heat exchangers, closed loops horizontal heat exchangers and so on. These systems could be basically grouped into three categories (ASHRAE, 2011): (1) ground coupled heat pump (GCHP) systems, (2) ground-water heat pump (GWHP) systems, and (3) surface water heat pump (SWHP) systems, as shown in Figure 1-2.

The GWHP is an open-loop system using underground water source as the heat source and sink. Groundwater is extracted directly to the heat pump unit and injected into other well or river after the heat exchange process. The GWHP has many advantages, such as high efficiency, lower initial cost and easy installation. But several factors are the bottleneck constraining its applications. Compared with the closed-loop systems, the open-loop system is more easily polluted by mineral deposits or corrosion.

Additionally, the discharge water may impact the surrounding environment, which limits the utilization of areas adjacent to lakes or rivers.

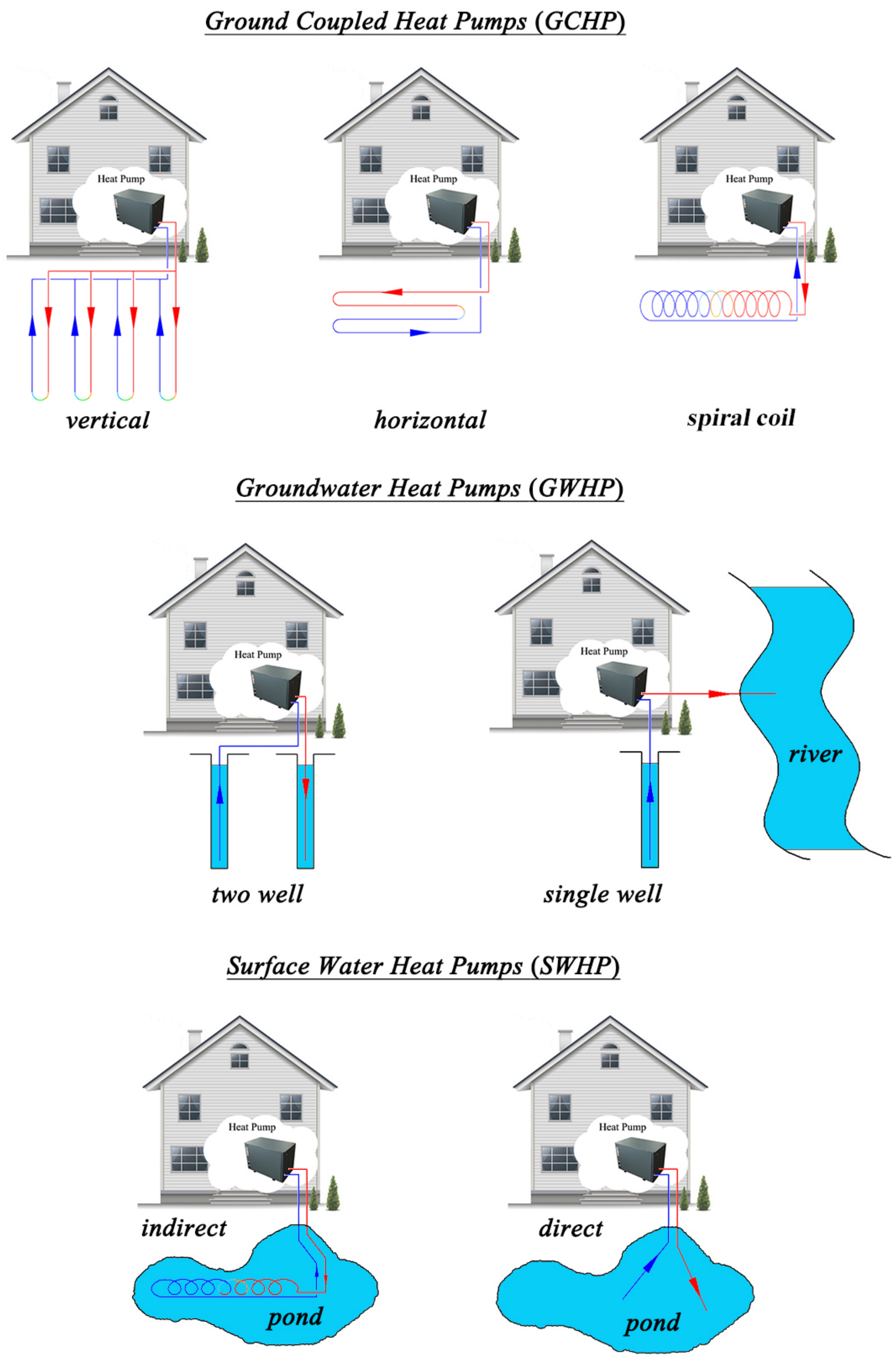

Figure 1-2 Schematics of different ground source heat pumps

The SWHP system can be either open-loops or closed-loops. Closed-loops are a group of pipes in which the cycle fluid indirectly contacts the surface water when heat rejection/extraction happens. The natural convection around group pipes is the primary heat transfer process in SWHP system. Because of this characteristic, the water temperature always influences the system operation, especially in winter, which could be its biggest disadvantage. For the SWHP system with open-loops, its features are the one of the GWHP system.

The GCHP, the most widely used GSHP in China, is usually a closed-loop system. The heat is captured from or dissipated to the ground via the closed loop through which pure water or an antifreeze solution circulates. According to the extension direction of heat exchange pipes, the GCHP can be further subdivided into horizontal GCHP systems and vertical GCHP systems. In a horizontal GCHP system, the GHEs lays beneath the ground surface at least 1.2 m deep. The major advantages of this system are the short construction period and lower initial cost, but requires a large amount of installation area. It is an ideal air-conditioning solution for big farms, golf courses, private villas and spas. However, like the SWHP system, the ground temperature may fluctuates with the weather, the season and the buried depth. Due to this character, the system COP is not stable during annual operations.

Vertical GCHP systems are widely applied in residential and commercial buildings in an impacted area. In a traditional vertical GCHP system, one or two U-tubes are buried in boreholes. The tubes are typically 20 to 40 mm in diameter. Depending on the local geological conditions, the depth of boreholes normally ranges from 15m to 180m with a diameter ranging from 100mm to 150mm. To enhance the heat transfer of boreholes and to prevent the damage of groundwater, some special materials, e.g. grout, will be poured into boreholes. Compared with the horizontal GCHP system, the vertical system has the advantages of small installation area and high efficiency. It can be installed at any ground only if the area can be drilled or trenched. However, the obvious drawback of this type of GCHP system is the very high installation cost. The depth of borehole is more than 100 m, which requires spiral drilling equipment and experienced contractors to conduct such works. The drilling cost usually accounts for more than 45% in the total investment of a GCHP system. This cost is even higher when granite or marble exists in the installation area. As a consequence, the high installation cost restricts its wide application in GCHP system. To solve this problem, engineers combine the GHE with foundation piles and invent a new type of vertical GHE, called pile geothermal heat exchanger (PGHE).

1.2 Background of Pile Geothermal Heat Exchanger (PGHE)

PGHEs system is a novel vertical GCHP system applied in recent years, which is also called energy pile. For a single PGHE, one or several high strength polyethylene pipes were buried in the concrete pile foundation to serve as GHEs, which means that these piles cannot only provide support for building structures but also act as heat exchangers for GCHP. A schematic diagram of a GCHP system with PGHE is illustrated in Figure 1-3.

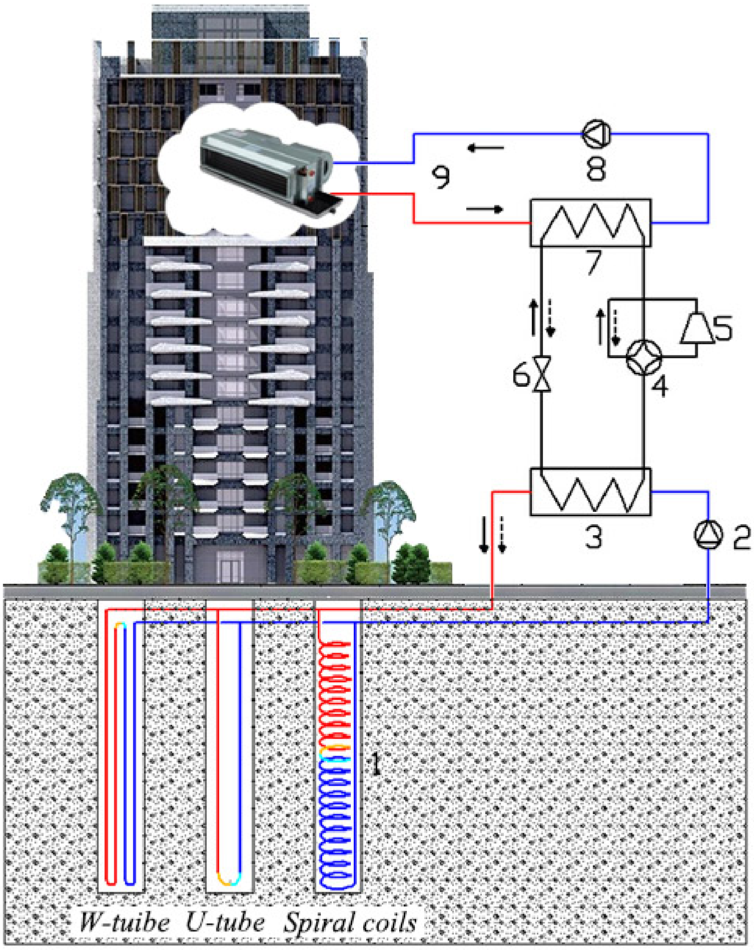

Figure 1-3 Schematic diagram of a GCHP system with PGHEs
(1. PGHE; 2, 8 circulation pump; 3, 7 condenser and evaporator; 4 reversing valve; 5 compressor; 6 expansion valve; 9 terminal device)

However, with the application of PGHE system, some concerns have been raised. The heat transfer characteristic of PGHE are quite different with those of the borehole GHEs. Typically, for borehole GHEs, the length of borehole is tens of meters, which is far larger than its radius. Thus, in GCHP system design or simulation, the borehole usually be simplified as a line heat source. However, this simplification is invalid for PGHE, because the pile radius is much larger and its length is shorter than the borehole GHE. Furthermore, the geometrical shape of heat exchange tubes buried in PGHE is more complicated than borehole heat exchangers. A vertical borehole can accommodate only one or two closed loops, and the heat exchange tube is only allowed to arrange in a straight line stretching from the ground surface to the borehole bottom. But for PGHE system, more than 5 U-tubes can be attached on the reinforcement cage's surface in a large pile foundation. The heat exchange pipes can be pre-intertwined as U type, W type and even spiral type. Therefore, the classic analytical model used in vertical GHE is no longer suitable for PGHE. In addition, the PGHE has a short application history and its security of this system is still questioned. The traditional design methods for foundation pile may fail due to the varying thermo-mechanical behaviours (such as the stress in the piles, and the reduction of ultimate bearing capacity) corresponding to the large underground temperature variations (up to 20ºC) during the long-term cooling or heating GHP operation. Therefore, it's important to systemically investigate its thermo-mechanical performance under different thermal and mechanical load.

1.3 Aims and Objectives

As mentioned, the initial cost and the required installation area are the main concern for any type of GCHP system. It has been found that the GHE with spiral-tubes can efficiently improve the heat transfer performance of GCHP system for either horizontal or vertical GCHP system. However, due to the complex structure of spiral-tubes, the studies on its heat transfer performance are insufficient.

For horizontal GCHP, previous studies are mainly focused on single or multiple linear GHEs, but few for GHE spiral-tubes. Among the different types of GHEs, the spiral-tubes always has the best heat transfer performance (Congedo et al., 2012). The tubes can be laid flat at the bottom of a wide trench (slinky-loops) or placed vertically in a narrow trench (spiral-loops). Because of the complex configuration of the spiral tubes, the classic analytical models, e.g. line source model, fail to describe the heat transfer process of GHE with spiral tubes. Li et.al. (2012b) proposed an analytical solution for slinky-loops, which shows a good accuracy for short time prediction. But for spiral-loops, it remains to be established. Additionally, as stated above, the temperature variation on the ground surface has great influence on the temperature response of horizontal GCHP. In the Li's model, the ground surface is simplified as a uniform wall with constant temperature. As a consequence, that model can only be used for short time prediction. Therefore, for horizontal GCHP, two existing problems should be solved. One is that there is no reliable analytical model for horizontal GHE with spiral-tubes and the other one is that there is no analytical solution taking the temperature fluctuations of the ground surface into consideration during the modelling process.

For vertical GHEs, the most widely used heat exchangers in GCHP system, many studies have reported either by experimental or theoretical methods. However, previous researches are mainly focused on the heat transfer model development of borehole GHEs including the heat conduction model and heat transfer model under groundwater advection. But for the novel vertical GHEs, pile geothermal heat exchanger, limited research results are available. For borehole GHEs, its length is much bigger than its radius, thus, the backfilled material of boreholes can normally be ingored and the GHEs is usually simplified as a line heat source or sink for system design and simulation purposes. However, the length of pile is quite small only about one-tenth of that of traditional boreholes, but the pile has a bigger section radius. Due to these special characteristics, the heat transfer mechanism of borehole GHE is quite different with the traditional GHEs and the classic analytical used in vertical boreholes is no longer suitable for PGHEs. Cui et. al. (2011) established an analytical model for PGHE with spiral coils, without considering the thermal difference between concrete and soil. In practice the heat exchangers buried in the concrete pile has the same dimension with pile, and the homogenous simplification cannot be accepted.

More importantly, the heat transfer process of GHEs can induce the temperature changes in the pile and the soil ground, which will cause additional stress or stain of the pile and further affect its security. This thermo-mechanical behaviour of PGHE should be fully investigated to avoid the pile failure and to protect the entire buildings. Although several in-suit tests have been reported to examine the thermo-mechanical behaviour of PGHE with U-tubes, the understanding is still limited, especially for spiral-tubes. For the thermo-mechanical behaviour, the interface behaviour between concrete and soil under the thermal loading in the key issue. The temperature changes of PGHE can cause the mechanical changes of ground soil which may increase or decrease the shear force between soil and pile. As the shear force has a direct relationship with the ultimate bearing capacity of pile, the pile performance is fully affected and even the whole building could suffer the risk of collapse. Therefore, the traditional civil design method failed to examine the building with PGHEs. The thermo-mechanical behaviour of PGHE need to be carefully investigated.

In summary, the studies of GHE with spiral-tubes is limited, and the issues both for its thermal performance and thermo-mechanical behaviour need to be studied and solved urgently.

Based on the discussion above, the objectives of this thesis are summarized as follows:

a) To investigate the heat transfer process of horizontal GHE with spiral-tubes and establish a transit analytical model for long-term operation. To investigate the influence of surface temperature changes on horizontal GHE with spiral-tubes and to develop a solution which can predict the temperature response under different boundary condition.

b) To develop an analytical solution in composite medium for PGHE with spiral-tubes which can distinguish the thermal difference between soil and concrete, and to investigate the influence of the thermal difference on its heat transfer performance

c) To establish a simulation model and to investigate the influence of seepage on PGHE with spiral-tubes. To establish a semi-analytical model based on the simulation results.

d) To investigate the interface behaviour between soil and concrete using the modified direct shearing equipment and to qualitatively and quantitatively analyse the influence of thermal load on the shear strength. To develop a numerical model to investigate the thermo-mechanical behaviour of PGHE in full-size.

1.4 Organization of This Thesis

In Chapter 1, the basic concept and a brief background of GSHP are introduced, especially for the GCHP. Different conventional GHEs are subsequently discussed with the main focus on the GHEs with spiral-tubes. Then, a novel vertical GHE, PGHE, together with its application background is introduced and discussed. The main aims and objectives are also presented in this chapter.

Chapter 2 presents the comprehensive and critical literature review concerning the study of this thesis. Different analytical and numerical models of GHEs with spiral-tubes, both for the horizontal GHEs and the PGHEs, are presented and discussed. Additionally, the study on the thermo-mechanical behaviour of PGHE is also reviewed. The flowchart of the research method is also provided.

Chapter 3 presents a new analytical heat transfer solution for horizontal GHE with spiral-tubes in order to accurately model its thermal performance. The solution is validated by comparing the temperature response with the results from an on-site experiment. In addition, a simulation model is established to validate the new analytical solution in the long-term system estimation.

In Chapter 4, the heat transfer characteristics of PGHE with spiral-tubes are analytically investigated. Comprehensively considering the difference of thermal properties between concrete and soil and the special geometry of spiral-tubes, a novel analytical model is established. Based on the analytical model, the importance of the difference of thermal properties are analysed and discussed in this chapter.

Chapter 5 presents a semi-analytical solution for PGHE with spiral-tube when groundwater advection exists. The limitation of the moving source model is firstly presented, and then a modified numerical method is proposed to improve the accuracy of the analytical model. Finally, the influence of groundwater advection on PGHE with spiral-tubes is discussed.

In Chapter 6, an interface behaviour test is introduced for analysing the element behaviour of concrete-soil under different thermal loads. A detailed experiment design concept and experiment progress is presented. All the experiment results are given and discussed this chapter.

In Chapter 7, based on the experimental results, a numerical simulation model is established to systematically analyse the thermo-mechanical performance of PGHE with spiral-tubes. Heating and cooling conditions are both simulated in this chapter.

Finally, Chapter 8 summarizes the main conclusions together with the recommendations for future works. It is believed that the outcomes from this thesis can effectively promote the application of GCHP technology.

CHAPTER 2

LITERATURE REVIEW AND METHODOLOGIES

2.1 Introduction

The GSHP technology can be can be traced back to the beginning of last century (Ball et al., 1983), the first system was successfully established in American (Bloomquist, 1999) until 1948. Before the development of polyethylene pipe, the open-loops GSHP mastered the market until 1979. After the first oil crisis in the 1970s, GSHP technology had entered a rapid period of vigorous development (Lund et al., 2004). Various types of GSHP systems have been developed both for residential and commercial buildings. As of 2007, there are more than 550,000 units installed worldwide and this number keeps growing at an average annual increase rate of 10% (Zhai et al., 2011). GCHP system is the main type of GSHP, because of its higher efficiency and lower environmental impact. With the growing application of GCHP, more research attention has been paid on improving the system efficiency and reducing the cost, especially in the field of the geothermal heat exchanger (GHE).

GHE is a key component to transfer heat energy between the heat pump units and the ground through circulating a heat carrier medium. Based on the buried direction, GHEs can be divided into two categories: (1) horizontal and (2) vertical. The horizontal GHEs are widely used when there is a sufficient installation area, and can be easily to constructed. But, the traditional horizontal GHEs have lower heat transfer efficiency with typical heat exchanging rate ranging from 15 to 30 W per meter trench (Lund et al., 2004), compared with the vertical ones. Vertical GHEs are commonly used in high-density city where the landscape is rare and expensive. It generally requires higher installation costs, but less installation areas.

For either vertical or horizontal GHEs, there are several configurations applied in practical engineering. But, among the different types of GHEs, the GHE with spiral-tubes has the best heat transfer performance and attracted the greatest interest (Sarbu & Sebarchievici, 2014). In this chapter, a detailed literature review concerning various analytical and simulation models of spiral GHEs are presented for both horizontal and vertical GHEs.

2.2 Studies on Horizontal Geothermal Heat Exchanger (HGHE)

Based on the configuration of the heat exchangers, the HGHE can be classified into three types: single-pipe, multiple-pipe, and spiral-type systems (ASHRAE, 2011). The spiral-type system can be further divided into slinky loops and spiral loops exchangers. Different models, either numerical or analytical, have been built up to analyse the heat transfer performance of HGHEs.

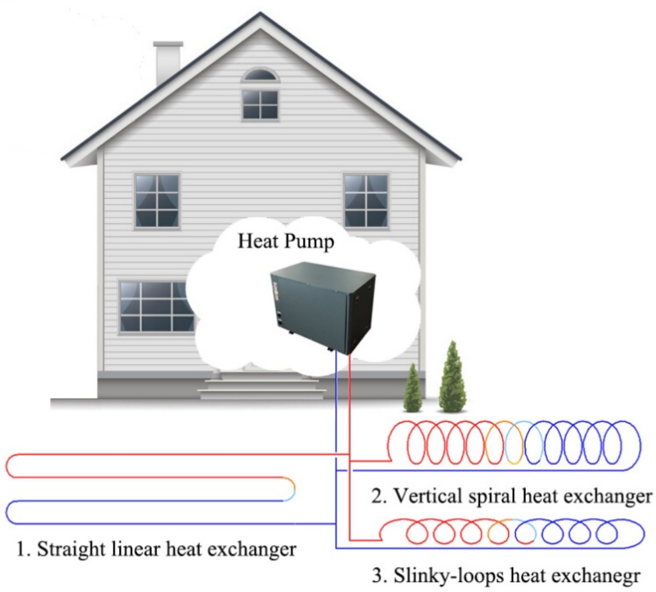

Figure 2-1 Schematics of different horizontal geothermal heat exchangers

For straight line GHEs (single-pipe and multiple-pipe), generally, there are two kinds of analytical models (Ingersioll et al., 1954). The first one is the Kelvin line source theory (Ingersoll & Plass, 1948), which is a one-dimensional solution in an infinite medium:

$$T(r,\tau)-T_0=\frac{q_l}{4\pi k}\int_{\frac{r^2}{4\alpha\tau}}^{\infty}\frac{e^{-u}}{u}du \tag{2.1}$$

where, r is the distance from the line source, T_0 is the initial temperature of the ground; and q_l is the heating rate per length of the line source.

This approach is simple and requires less computation time. However, because of the simplification of the infinite ground medium, it can only be used for small pipes and within a limited time (Eskilson, 1987; Fang et al., 2002).

The cylindrical infinite source model is the other wide application model used in the past decades. It is first developed by Carslaw and Jaeger (1962) and refined by

Ingersoll (1954). Then, this model has been applied in many research studies (Kavanaugh, 1985; Deerman, 1990; Bernier, 2001). In the cylindrical source model, the heat exchanger is assumed as an infinite cylinder surface surrounded by the homogeneous medium with constant properties, i.e. the ground. It also assumes that the heat transfer between the borehole and soil with a perfect contact is pure heat conduction:

$$T - T_0 = \frac{q_l}{\pi^2 k r_0}\left[\int_0^{\infty}\left(\mathrm{e}^{-au^2\tau} - 1\right)\frac{J_0(ur)Y_1(ur_0) - Y_0(ur)J_1(ur_0)}{u^2\left[J_1^2(ur_0) + Y_1^2(ur_0)\right]}du\right] \tag{2.2}$$

In the cylindrical source model the domain $r_0 < r < \infty$ is considered, and the heating flux is directly exposed to the cylinder surface, or the borehole wall. That means the heat capacity of the "hot rod" is totally ignored. Thus, it is also called as "hollow" cylindrical infinite source model. Due to the complex expression of this model, several approximate solutions have been proposed (Kavanaugh, 1985; Hellström, 1991).

Both the Kelvin's infinite model and the cylindrical source model neglect the heat transfer through the ground surface, so they are inadequate for the long-term operation of HGHE systems. A modified analytical model was proposed by Mei (1991), who took the effect of temperature variation of the ground surface into consideration.

Except for the analytical models, researchers also used numerical techniques to model the heat transfer process of straight line GHEs (Negiz et al., 1995; Chung et al., 1999; Bøhm, 2000; Mihalakakou, 2002; Ling & Zhang, 2004). Esen et al. (2007) proposed a 2-D simulation model for line GHE taking the temperature distributions of the ground into consideration. This simulation model is based on the finite difference method, and has been compared with Esen's lab test. An acceptable tolerance was shown within the operation time of 8 hours, but the tolerance becomes larger with the time going on. This simulation model is modified by considering the effect of the soil moisture, but, being restricted with the 2-D model itself, the model causes some error on the results especially for long-time simulation. Aiming to find the temperature response in three dimensions, Demir et al. (2009) established a virtual 3-D simulation model including the effect of weather conditions. Neglecting the temperature gradient along the pipe axis, dynamical boundary conditions were applied to a two-dimensional geometry. The temperature distribution within the pipe was calculated by linking the two-dimensional solution domains. The simulation results were also compared with in-suit experiment, and a good performance has been found within the test time of 30 days. This model neglected the effect of backfill material, and as a consequence, the simulation results are always higher than the experiment results. But, for the prediction of short time operation, it is still a reliable model. So far, there are lots of research works, both numerical and analytical, have been conducted for linear geothermal heat exchangers, but studies on spiral heat exchangers are limited, especially for spiral-tubes (Bose & Smith, 1992; Doherty et al., 2004; Wu et al., 2010).

H. Li et al. (2012b) proposed an analytical solution for slinky-loops heat exchangers. In this solution, the slinky-loops were simplified as a series of separated ring coils source releasing/absorbing heat into a semi-infinite medium with zero surface temperature. The solution was given as follow:

$$\begin{cases} \theta_{slinky,c}\left(r,z,t\right)=\dfrac{q_r r_0}{4k\pi}\displaystyle\sum_{n=0}^{N-1}\int_0^{2\pi}\dfrac{1}{r_{n+}}erfc\left(\dfrac{r_{n+}}{\sqrt{4\alpha t}}\right)-\dfrac{1}{r_{n-}}erfc\left(\dfrac{r_{n-}}{\sqrt{4\alpha t}}\right)d\sigma \\ r_{n+}=\sqrt{\left(nb+r_0\cos\sigma-r\cos\varphi\right)^2+\left(r_0\sin\sigma-r\sin\varphi\right)^2+\left(z+z'\right)^2} \\ r_{n-}=\sqrt{\left(nb+r_0\cos\sigma-r\cos\varphi\right)^2+\left(r_0\sin\sigma-r\sin\varphi\right)^2+\left(z-z'\right)^2} \end{cases} \tag{2.3}$$

where b is the space between two neighbouring ring-coil and N is the number of total ring-coils.

The analytical solution agrees well with the lab experiment within a short time operation. But, as the surface condition is neglected, a large error can be detected in long-term estimation. Based on this solution together with the moving source method, the author also proposed an analytical solution for slinky-loops under groundwater advection (H. Li et al., 2012a). Besides, a simplified 3-D numerical model was developed to investigate the heat transfer efficiency of HGHEs in different configurations by Congedo et al. It was found that the HGHE with spiral-tubes enabled a better heat transfer performance than those of the linear and slinky HGHEs (Congedo et al., 2012). This finding was further confirmed by field tests (P. Cui et al., 2013). To the best of my knowledge, no reliable analytical model is available to describe the heat transfer behaviour of HGHEs with vertical spiral-tubes.

Compared with straight linear and slinky-loop HGHEs, HGHEs with spiral-tubes have a short application history. However, due to the higher heat transfer efficiency and less land area requirements, this spiral heat exchangers have been attracting increasing interests recently (Congedo et al., 2012). But, due to the complex configuration of the vertical spiral pipes, the previous analytical models of HGHE failed to describe its heat transfer process. Hence, a need for a new analytical model has been expected for the design/simulation of HGHEs with vertical spiral-tubes. Additionally, it is well noted that the temperature of the soil surrounding the HGHEs is sensitively affected by the temperature of the ground surface, and the soil temperature also has the ability to quickly retrieve its original temperature once cooling or heating operations have ceased (Self et al., 2013). Thus, it is important to take the temperature fluctuations of the ground surface into consideration during the heat transfer modelling process (Xiong & Lee, 2013). Accordingly, the boundary solution for vertical spiral HGHEs should also be derived.

2.3 Thermal Studies on Pile Geothermal Heat Exchanger (PGHE)

With the aims of further reducing the land requirement and installation cost, the foundation pile integrated with the geothermal heat exchangers, usually called “energy pile”, is one of the options for ground-coupled heat pump system. For a typical energy pile, one or several polyethylene pipes are fixed on the reinforcement cage and covered by concrete. The pipes can be buried as different configurations, e.g. U-tubes, W-tubes or spiral-tubes. A good tightness between the buried pipe and concrete can efficiently reduce the thermal contact resistance and improve the heat transfer efficiency. Compared with the traditional borehole GHE, the energy pile has different dimension sizes and filling materials, so the classic analytical models, e.g. Kelvin’s line source model (Ingersoll & Plass, 1948; Ingersoll et al., 1950) and ‘‘hollow” cylindrical source model (H. Carslaw et al., 1962), fail to describe the heat transfer process of PGHE.

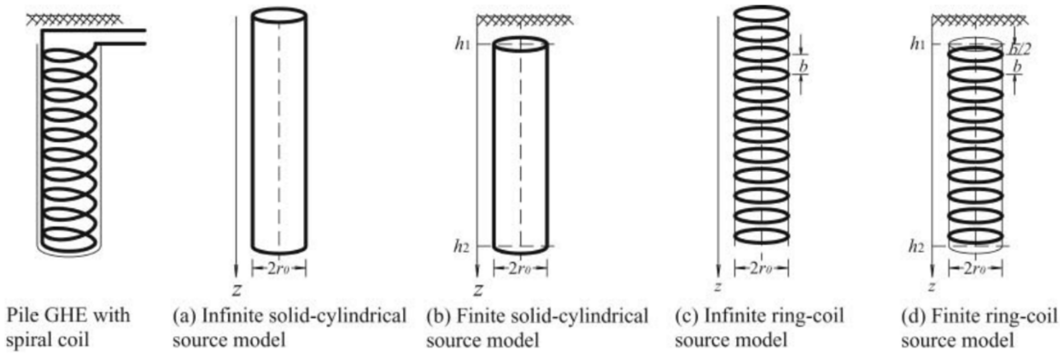

Figure 2-2 Schematics of different pile geothermal heat exchangers models

2.3.1 Solid cylindrical heat source model

Man et al. (2010) presented a “solid” cylindrical heat source model, taking the special characteristics of PGHE into proper consideration. Based on the line source or the ‘‘hollow” cylindrical model, the “solid” model supposed that the cylinder is no longer a cavity, but filled with the medium identical to that out of the cylinder, so that the whole infinite domain is composed of a homogeneous medium. This analytical solution of this problem was obtained directly by the Green’s function method:

$$T_{cyl,c}\left(r,z,\tau\right)=\frac{q_l}{\rho c}\int_0^{\tau}\int_0^{h}\frac{1}{8\left[\sqrt{\pi\alpha\left(\tau-\tau'\right)}\right]^3}I_0\left[\frac{rr_0}{2\alpha\left(\tau-\tau'\right)}\right]$$
$$\left\{\exp\left[-\frac{r^2+r_0^{\,2}+\left(z'-z\right)^2}{4\alpha\left(\tau-\tau'\right)}\right]-\exp\left[-\frac{r^2+r_0^{\,2}+\left(z'+z\right)^2}{4\alpha\left(\tau-\tau'\right)}\right]\right\}dz'd\tau' \tag{2.4}$$

This 2-D model, presented here, considered the influences of the finite length of the cylindrical heat source and the boundary. The assumption of a single homogeneous medium outside and inside the heat source is still valid to make the problem clear and analytical solution feasible. By introducing the following dimensionless variables: $\Theta = \dfrac{kTr_0}{q_l}$, $Fo = \dfrac{\alpha\tau}{r_0^2}$, $Fo' = \dfrac{\alpha\tau'}{r_0^2}$, $R = \dfrac{r}{r_0}$, $Z = \dfrac{z}{r_0}$, $Z' = \dfrac{z'}{r_0}$ and $H = \dfrac{h}{r_0}$, the dimensionless temperature excess at (R, Z) can be expressed as a function of the following dimensionless variables:

$$\Theta_{c,f}\left(R,Z,Fo\right) = \frac{1}{8\pi}\int_0^{Fo}\frac{1}{Fo-Fo'}\cdot\exp\left[-\frac{R^2+1}{4\left(Fo-Fo'\right)}\right]\cdot I_0\left[\frac{R}{2\left(Fo-Fo'\right)}\right]$$
$$\cdot\left[erf\left(\frac{H-Z}{2\sqrt{Fo-Fo'}}\right)+2erf\left(\frac{Z}{2\sqrt{Fo-Fo'}}\right)-erf\left(\frac{H+Z}{2\sqrt{Fo-Fo'}}\right)\right]dFo' \tag{2.5}$$

This model is designed for PGHE with spiral coils, but it also can be used for PGHE with U-tubes when the heat exchange pipes are arranged evenly and tightly on the steel reinforcement. Although the ‘‘solid’’ cylindrical source model has made marked progress from the classical line source or ‘‘hollow’’ cylindrical source models, it fails to distinguish the effect of the spiral pitches because the coil is simplified as a continuous cylindrical surface. In practice, the temperature distribution fluctuates significantly along the axial direction in the vicinity of the cylindrical surface due to the non-integrity of the heat source. This feature is of great importance in analysing the temperature rise of the buried pipe.

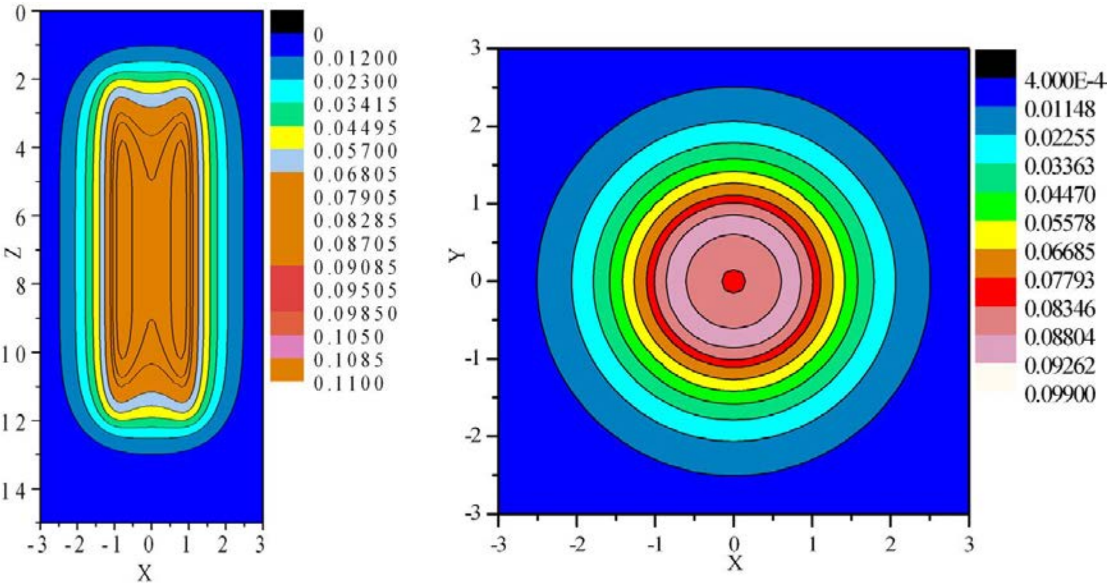

Figure 2-3 The isothermals on pure conduction model of solid cylindrical heat source.

Based on this analytical model, Zhang (2013) derived an analytical solution under advection. Assuming the groundwater flow along the *x*-axis direction, with the velocity of u, the temperature response in a semi-infinite homogeneous medium can be expressed as follow:

$$T_{cyl,gw}(x,y,z,\tau)=\frac{q_l}{16\pi^2 k}\int_0^{2\pi}d\varphi'\int_0^{\tau}\frac{1}{(\tau-\tau')}\exp\left\{-\frac{\left[x-r_0\cos\varphi'-U(\tau-\tau')\right]^2+(y-r_0\sin\varphi')^2}{4\alpha(\tau-\tau')}\right\}$$
$$\times\left\{\begin{array}{l} erfc\left[\dfrac{z-h_1}{2\sqrt{\alpha(\tau-\tau')}}\right]-erfc\left[\dfrac{z-h_2}{2\sqrt{\alpha(\tau-\tau')}}\right]-erfc\left[\dfrac{z+h_1}{2\sqrt{\alpha(\tau-\tau')}}\right] \\ +erfc\left[\dfrac{z+h_2}{2\sqrt{\alpha(\tau-\tau')}}\right]\end{array}\right\}d\tau' \tag{2.6}$$

where $U=u\rho c/\rho_w c_w$ is equivalent speed, ρc is volume specific heat capacity of soil, $\rho_w c_w$ is volume specific heat capacity of water, and u is the velocity of groundwater. It can also be expressed as non-dimensional parameters by introducing the corresponding factors： $\Theta = \frac{kTr_0}{q_l}$, $Fo = \frac{\alpha\tau}{r_0^2}$, $Fo' = \frac{\alpha\tau'}{r_0^2}$, $R = \frac{r}{r_0}$, $Z = \frac{z}{r_0}$, $Z' = \frac{z'}{r_0}$ and $H = \frac{h}{r_0}$.

$$\Theta_{cyl,gw}\left(x, y, z, \tau\right) = \frac{1}{16\pi^2}\int_0^{2\pi} d\varphi' \int_0^{\tau} \frac{1}{\left(Fo - Fo'\right)} \exp\left\{-\frac{\left[X - \cos\varphi' - S\left(Fo - Fo'\right)\right]^2 + \left(Y - \sin\varphi'\right)^2}{4\left(Fo - Fo'\right)}\right\}$$
$$\times\left\{\begin{array}{l} erfc\left[\frac{Z - H_1}{2\sqrt{Fo - Fo'}}\right] - erfc\left[\frac{Z - H_2}{2\sqrt{Fo - Fo'}}\right] - erfc\left[\frac{Z + H_1}{2\sqrt{Fo - Fo'}}\right] \\ + erfc\left[\frac{Z + H_2}{2\sqrt{Fo - Fo'}}\right] \end{array}\right\} dFo' \tag{2.7}$$

However, the limitation of this model is obvious. In the moving source method, the groundwater velocity is assumed to be absolutely uniform within the whole calculation domain, which means the groundwater could pass through the pile foundation and take away the heat energy. The heat conduction process within pile foundation is assumed to be a convection process. This assumption results in a large error for short-term estimation of PGHE.

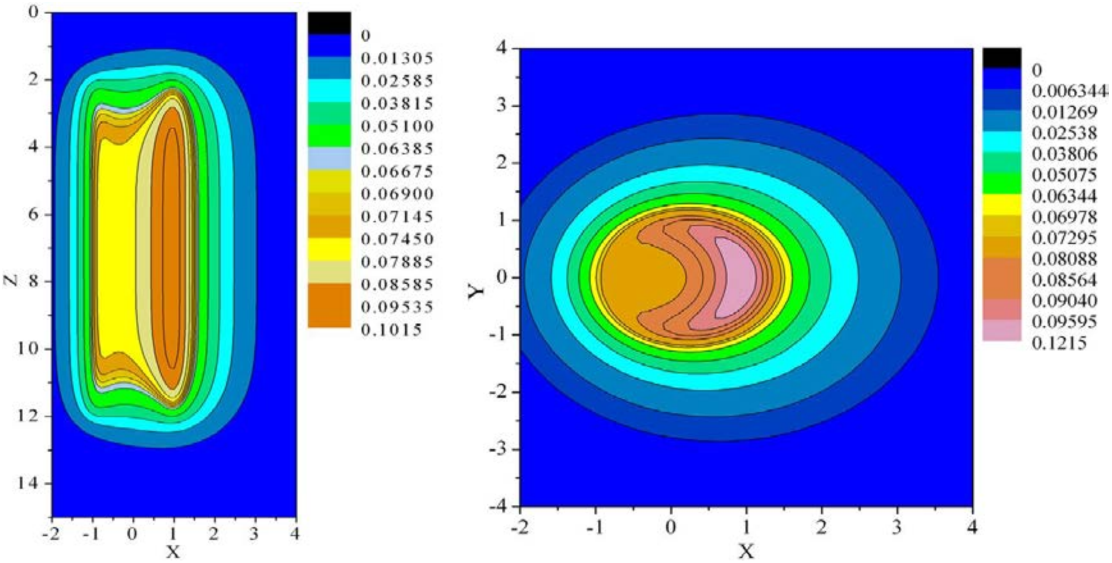

Figure 2-4 The isothermals on solid cylindrical heat source model with groundwater flow.

2.3.2 Ring-coil heat source model

To better describe the heat transfer process of the PGHE with spiral coils, ring-coil source mode (P. Cui et al., 2011) has been established. In this model, the spiral coils buried in the pile are simplified as a number of separated rings on the cylindrical surface. Based on the governing equation of the transient heat conduction along the given boundary with initial conditions, the two-dimensional heat conduction problem in the infinite medium can be formulated in the cylindrical coordinate:

$$
\begin{aligned}
&\frac{\partial T}{\partial \tau} = a\left(\frac{\partial^2 T}{\partial r^2} + \frac{1}{r}\frac{\partial T}{\partial r} + \frac{\partial^2 T}{\partial z^2}\right) + \frac{q\delta}{2\pi r_0 \rho c}, && \text{for } 0 < \mathrm{r} < \infty, -\infty < \mathrm{z} < \infty, \tau > \tau' \\
&\frac{\partial T}{\partial r} = 0, && \text{for } \mathrm{r} = 0, -\infty < \mathrm{z} < \infty, \tau > \tau' \\
&T = 0, && \text{for } 0 < \mathrm{r} < \infty, -\infty < \mathrm{z} < \infty, \tau = \tau' \\
&T \to 0, && \text{for } \mathrm{r} \to \infty, -\infty < \mathrm{z} < \infty, \tau > \tau' \\
&T \to 0, && \text{for } \mathrm{z} \to \pm\infty
\end{aligned} \tag{2.8}
$$

The temperature response at the location (r, z) in the humongous medium to a series of ring sources can be obtained according to the Green's function theory:

$$T_{ring,c}=\frac{q_l b}{8\rho c}\int_0^{\tau}\frac{1}{\left[\sqrt{\pi\alpha\left(\tau-\tau'\right)}\right]^3}\cdot I_0\left[\frac{rr_0}{2\alpha\left(\tau-\tau'\right)}\right]\cdot\exp\left[-\frac{r^2+r_0^2}{4\alpha\left(\tau-\tau'\right)}\right]$$
$$\cdot\sum_{n=0}^{m-1}\left\{\exp\left[-\frac{\left(z-h_1-nb-0.5b\right)^2}{4\alpha\left(\tau-\tau'\right)}\right]-\exp\left[-\frac{\left(z+h_1+nb+0.5b\right)^2}{4\alpha\left(\tau-\tau'\right)}\right]\right\}d\tau' \tag{2.9}$$

The coil is then approximated as m pieces of rings, $m=\mathrm{int}\left[\left(h_2-h_1\right)/b\right]$. By defining $H_1=\frac{h_1}{r_0}$, then the Eq.(2.9) can be rewritten as the dimensionless form:

$$\Theta_{ring,c}=\frac{B}{8}\int_0^{Fo}\frac{1}{\left[\sqrt{\pi\left(Fo-Fo'\right)}\right]^3}\cdot I_0\left[\frac{R}{2\left(Fo-Fo'\right)}\right]\cdot\exp\left[-\frac{R^2+1}{4\left(Fo-Fo'\right)}\right]$$
$$\cdot\sum_{n=0}^{m-1}\left\{\exp\left[-\frac{\left(Z-H_1-nB-0.5B\right)^2}{4\left(Fo-Fo'\right)}\right]-\exp\left[-\frac{\left(Z+H_1+nB+0.5B\right)^2}{4\left(Fo-Fo'\right)}\right]\right\}dFo' \tag{2.10}$$

Its advection model was also established by Zhang et al. (2014):

$$T_{ring,gw}=\frac{q_l b}{16\pi^{5/2}k}\sum_{n=0}^{m-1}\int_0^{2\pi}d\varphi'\int_0^{\tau}\frac{1}{\sqrt{\alpha}\left(\tau-\tau'\right)^{3/2}}\exp\left\{-\frac{\left[x-r_0\cos\varphi'-U\left(\tau-\tau'\right)\right]^2+\left(y-r_0\sin\varphi'\right)^2}{4\alpha\left(\tau-\tau'\right)}\right\}$$
$$\times\left\{\exp\left[-\frac{\left(z-h_1-nb-0.5b\right)^2}{4\alpha\left(\tau-\tau'\right)}\right]-\exp\left[-\frac{\left(z+h_1+nb+0.5b\right)^2}{4\alpha\left(\tau-\tau'\right)}\right]\right\}d\tau' \tag{2.11}$$

In this ring-coil source model, the discontinuity of the heat source is considered, and the impact of the coil pitch is investigated by introducing more appropriate approximations of the real coil. In both the solid cylindrical-source and the ring-coil-source models, proposed for pile GHEs with spiral coils, it is assumed that heat is released from the coil pipe wall and the difference between the thermal properties of soil and foundation piles is ignored. The ring-coil-source model treats the spiral coil as a series of separated rings releasing heat in an infinite or semi-infinite homogeneous medium. The solid cylindrical-source model describes spiral coil as a cylindrical surface releasing heat into the ground. Similarly, the traditional line-source theory has also been used to evaluate the performance of energy piles, which also ignores the difference between thermal properties of piles and soil.

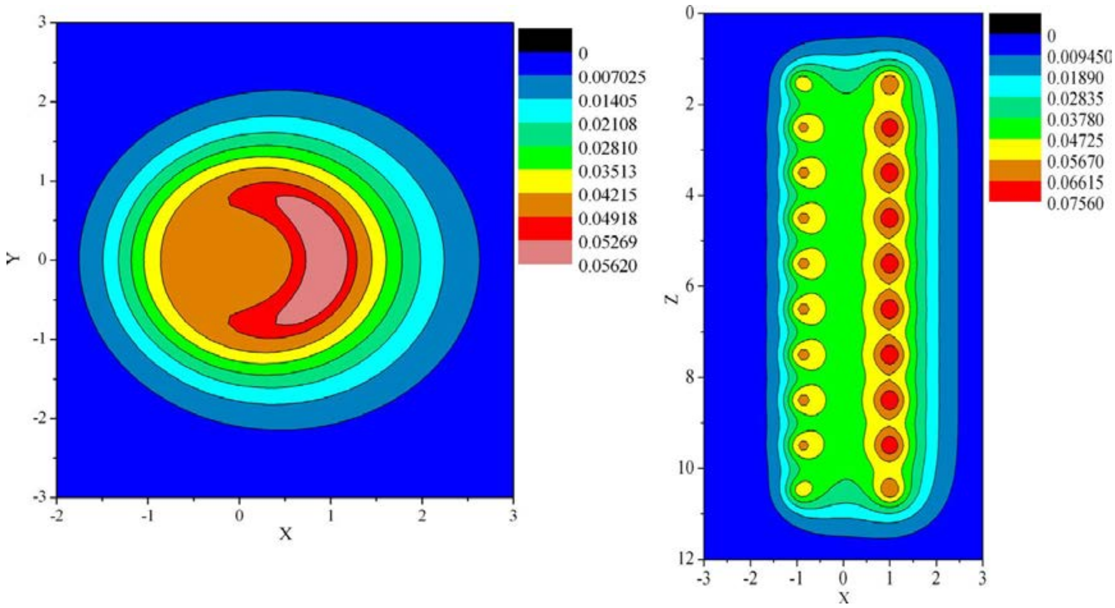

Figure 2-5 The isothermals of ring-coils source model under groundwater advection

Similar to the cylindrical source model under groundwater advection, this advection model also neglects the physical shape of pile foundation, and thus the temperature rise is always lower than the real situation, especially in the concrete pile.

2.3.3 Spiral heat source model

Y. Man et al. (2011) further improved the spiral shape of the analytical model and proposed a finite spiral source model. The spiral model does not distinguish the thermal properties between pile and concrete. The whole calculation domain is assumed to be uniform and homogeneous:

$$T_{spiral,c} = \frac{q_l b}{16\pi\rho c}\int_0^{\tau}\frac{d\tau'}{\left[\pi\alpha\left(\tau-\tau'\right)\right]^{3/2}}\exp\left[-\frac{r^2+r_0^2}{4\alpha\left(\tau-\tau'\right)}\right]\cdot\int_{2\pi h_1/b}^{2\pi h_2/b}\exp\left[\frac{2rr_0\cos\left(\varphi-\varphi'\right)}{4\alpha\left(\tau-\tau'\right)}\right]$$
$$\times\left\{\exp\left[-\frac{\left(z-b\varphi'/2\pi\right)^2}{4\alpha\left(\tau-\tau'\right)}\right]-\exp\left[-\frac{\left(z+b\varphi'/2\pi\right)^2}{4\alpha\left(\tau-\tau'\right)}\right]\right\}d\varphi' \tag{2.12}$$

It can be expressed by dimensionless temperature expression as below:

$$\Theta_{spiral,c} = \frac{B}{16\pi^{5/2}}\int_0^{\tau}\left(\frac{1}{Fo-Fo'}\right)^{3/2}\exp\left[-\frac{R^2+1}{4\left(Fo-Fo'\right)}\right]\cdot\int_{2\pi H_1/\mathrm{B}}^{2\pi H_2/\mathrm{B}}\exp\left[\frac{2R\cos\left(\varphi-\varphi'\right)}{4\left(Fo-Fo'\right)}\right]$$
$$\times\left\{\exp\left[-\frac{\left(Z-B\varphi'/2\pi\right)^2}{4\left(Fo-Fo'\right)}\right]-\exp\left[-\frac{\left(Z+B\varphi'/2\pi\right)^2}{4\left(Fo-Fo'\right)}\right]\right\}d\varphi'\,dFo \tag{2.13}$$

In addition, one composite analytical model has been established by Li (2012), based on the Jaeger's solution (1944) for an instantaneous line-source in composite solids. Similar to the "solid" cylindrical model, the composite cylindrical model considers the heat exchange pipes as a continuous cylindrical surface:

$$T_{cc,in}(r,t) = \frac{q_l}{2\pi k_1}\int_0^{+\infty}\left[1-\exp\left(-\alpha_1 u^2 t\right)\right]\cdot\frac{J_0(ur)J_0(ur')\left[R_{\phi,0}R_{g,0}-R_{\psi,0}R_{f,0}\right]}{\left(R_{\phi,0}{}^2+R_{\psi,0}{}^2\right)u}du \qquad \text{for } 0\le r<l_r,\ 0\le r'<l_r,\ 0<t \tag{2.14}$$

$$T_{cc,out}(r,t) = \frac{q_l}{\pi^2 r_b}\int_0^{+\infty}\left[1-\exp\left(-\alpha_1 u^2 t\right)\right] \cdot \frac{J_0(ur^{'})\left[R_{\psi,0}J_0(aur)-R_{\phi,0}J_0(aur)\right]}{\left(R_{\phi,0}{}^2+R_{\psi,0}{}^2\right)u^2}du \quad \text{for } l_r < r < \infty,\ 0 \le r^{'} < l_r,\ 0<t \tag{2.15}$$

where:

$$R_{\phi,0} = aKJ_0(l_r u)J_0^{'}(al_r u) - J_0^{'}(l_r u)J_0(al_r u); \quad R_{\psi,0} = aKJ_0(l_r u)Y_0^{'}(\kappa l_r u) - J_0^{'}(l_r u)Y_0(al_r u)$$

$$R_{f,0} = aKY_0(l_r u)J_0^{'}(al_r u) - Y_0^{'}(l_r u)J_0(al_r u); \quad R_{g,0} = aKY_0(l_r u)Y_0^{'}(al_r u) - Y_0^{'}(l_r u)Y_0(al_r u)$$

$$a = \sqrt{\alpha_1/\alpha_2}\ ;\ K = k_2/k_1$$

This continuous cylindrical-surface solution in composite media successfully took the effect of thermal properties difference on the heat transfer performance of PGHE into consideration, but it is a one-dimension model ignoring the heat transfer along the depth direction. Obviously, as this model ignore the finite characteristic of energy pile, it cannot be used to estimate the temperature response of pile top and toe.

Up to now, different analytical models have been developed, but there is no analytical model both considering the difference of thermal properties between the concrete pile and soil and the finiteness of PGHE geometry. Therefore, a new analytical model considering these two characteristics simultaneously should be established for better evaluating the thermal performance.

2.4 Thermo-mechanical Studies on Pile Geothermal Heat Exchanger (PGHE)

Piles including PGHE are primarily transferring building load to the earth from the building structure. Thus its geotechnical role is important for building safety. The traditional geotechnical design method may not be suitable for PGHE, because its internal stress and interface behaviour are greatly influenced by the heat exchanging process. In this section, the main aspects related to geotechnical design of traditional deep foundation and the existing thermo-mechanical studies of PGHE are reviewed. The main purpose is to identify the aspects which need to be further studied related to the PGHE. Only axial piles are considered in this thesis.

2.4.1 Existing design method for traditional piles

Piles foundations are used to control the building settlement and to avoid excessive settlement which may cause collapse of the upper structure. Thus, the design of PGHE must be satisfy the requirements of the Ultimate Limit State (U. L. S.) and the Serviceability Limit State (S. L. S.), which are the limits to guarantee both structure and settlement safe (Batini et al., 2015).

The bearing capacity of pile ($Q_{bearing,c}$) should be the sum of the tip resistance (Q_b) and the shaft resistances (Q_s) minus the weight of pile self (W_p), shown as the following equation.

$$Q_{bearing,c} = Q_s + Q_b - W_p \tag{2.16}$$

The tip and shaft resistances may not be mobilise at the same time, but they can be different with the soil medium.

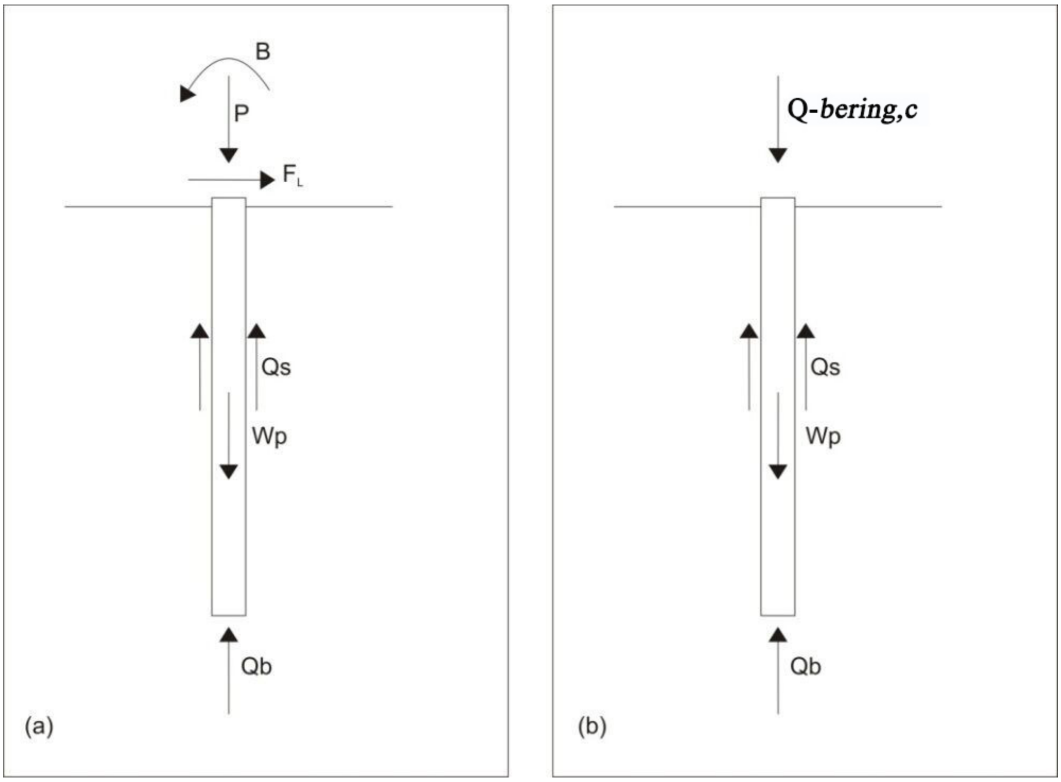

Figure 2-6 Equilibrium of an axially loaded pile

As shown in Figure 2-7, the shaft force is mobilized fully while a vertical settlement of 1% of the diameter of the pile for both clayey soil and sandy soil. The tip resistance reaches its limits when a settlement of 2% is observed in case of clayey soil, but more than 10% in case of sandy soil.

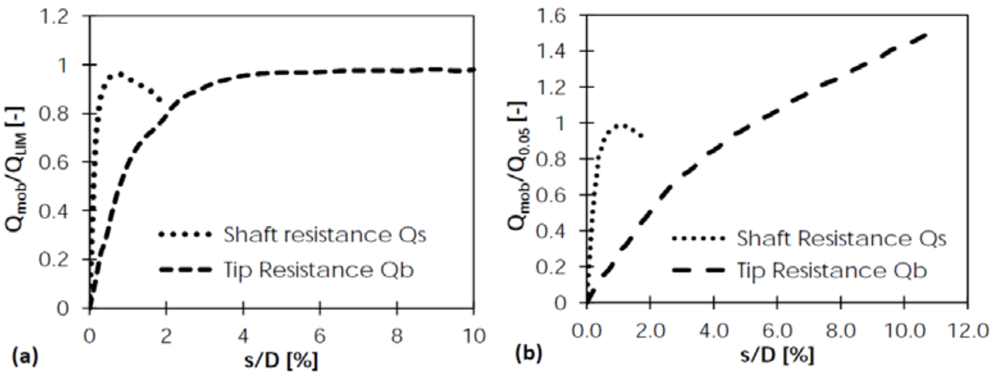

Figure 2-7 Mobilised resistance normalised with respect to bearing capacity for bored piles in: (a) clayey soils, and (b) sandy soil (Reese & O'Neill, 1989)

The pile capacity, which is defined as (1) the load at that settlement continues to increase without further added load or (2) the load causing a settlement of 10% of the pile diameter, has a strict link to the allowable settlement. In-situ measured load-settlement curves were first proposed in the 1970s (Fellenius, 1980; Fleming et al., 2008). These curves can be obtain directly by in-suit load tests (Davisson, 1993). However, the in-suit load tests are difficult and time-consuming, so, alternative design methods are essential and important when the in-situ tests are not available. Thus, various calculation equations were proposed by meant researchers for tip and shaft resistance, based on their experiment and experience (Meyerhof, 1983; Chen & McCarron, 1991).

For drained conditions:

$$Q_b = q_b A_b = \left(c' N_c + \sigma'_{vb} N_q\right) A_b \tag{2.17}$$

$$Q_s = q_s A_s = \overline{\sigma'_{v0}} A_s \overline{\beta} = \overline{\sigma'_{v0}} A_s \overline{K} \tan\delta \tag{2.18}$$

For undrained conditions:

$$Q_b = q_b A_b = \left(s_u N_c + \sigma_{vb}\right) A_b \tag{2.19}$$

$$Q_s = q_s A_s = \overline{\alpha} S_u A_s \tag{2.20}$$

where q_b is the tip bearing capacity per unit area, q_s is the lateral bearing capacity per unit area, A_b is the area of foundation basis, A_s is the area of lateral surface, c' is the soil cohesion, σ'_{vb} is the effective vertical stress, σ_{vb} is the total vertical stress, s_u is the undrained shear resistance, $\overline{\sigma'_{v0}}$ is the averaged vertical effective stress along the pile lateral surface, $\overline{K}$ is the earth pressure coefficient and δ is the friction angle at the interface between the pile and the soil.

In the traditional design, the friction angle can be determined from correlations between pile and soil (Stas & Kulhawy, 1984; Reese & O'Neill, 1989). In PGHE, the friction angle may be influenced by the thermal load, which, consequently, affects the shaft resistance of the pile. It needs to be further investigated.

2.4.2 Thermal strain of PGHE

The investigation of PGHE thermo-mechanical behaviour for structural safety has been attracting great concerns in the recent years. The thermal deformation and induced thermal stress in the pile/soil due to the thermal processes will affect the pile’s mechanical behaviour. Some in-situ experiments proved that the thermal stress in the pile is considerable depending on the surrounding soil and the fixity conditions at the toe and head of the pile. The combined thermodynamic and geotechnical performance of a heat exchanger pile was firstly examined by Laloui et al. (2006). In this instance, an instrumented test pile was installed as part of a new structure at the Swiss Federal Institute of Technology in Lausanne, and the thermal testing were carried out at intervals during the construction of the building. The heating and recovery cycles were applied with the increasing head load increments resulting from construction of each floor level. The axial response of the test pile was measured using optical fibre sensors, extensometers and a load cell in the base of the pile. The observed response at the final stage of loading, with a head load of about 1300kN, is shown in Figure 2-8. The results imply that the axial load in the pile was approximately doubled with respect to the head load during the applied thermal cycle, in which a temperature increase of about 15℃ was applied. In terms of this axial loading the thermal effect is most apparent at the toe of the pile.

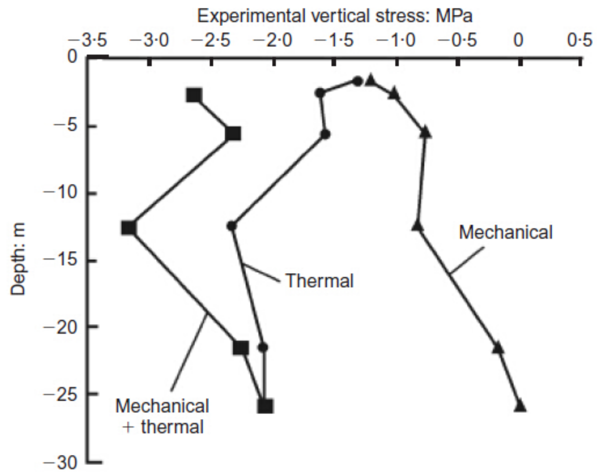

Figure 2-8 Load distribution in Lausanne test pile (Laloui et al., 2006)

Another on-site test results (P. J. Bourne-Webb et al., 2009) involving an instrumented heat exchanger pile are shown in Figure 2-9. From the test data, the authors concluded that, in the specific test situation, the pile was floating in the ground with little constraint on its movement at both ends, contrary to the situation that occurred in Laloui‘s. As a consequence, the load increase in the pile was much less uniform. On this basis, Bourne-Webb proposed a simplified scheme to assess the response of the pile to thermal loading with uniform lateral friction along the pile shaft. It was assumed that the degree of freedom was maximal (equal to unity) at the extremities of the pile and minimal in the middle of the pile at the null point where no thermal induced displacement is observed.

A geotechnical numerical analysis method (Knellwolf et al., 2011) has been proposed based on the load-transfer approach to assess the main effects of temperature changes on the pile behaviours. The method is validated by on-site measurements of the loads and deformations experienced by heat exchanger test piles. This numerical method is based on the load-transfer method (Coyle & Reese, 1900; Seed & Reese, 1900), and considers the shear resistance of the surrounding soil and the tip resistance of the soil at the bottom of the pile. The pile–soil interaction system is represented by an elastic-plastic model, by utilizing the load-transfer curves that link the mobilized bearing forces to pile displacements (Randolph & Wroth, 1978; Armaleh & Desai, 1987; Frank et al., 1991). An iterative procedure allows the thermal strains and the associated additional efforts, but the pile is subjected to both axial mechanical loading and temperature changes. Therefore, the heating of the pile induces the additional compression in the pile and increases the mobilized shear stress. The cooling can induce a release of mobilized shear stress, possibly leading to the reversal of shear stress signs and the development of tensile stress in the pile.

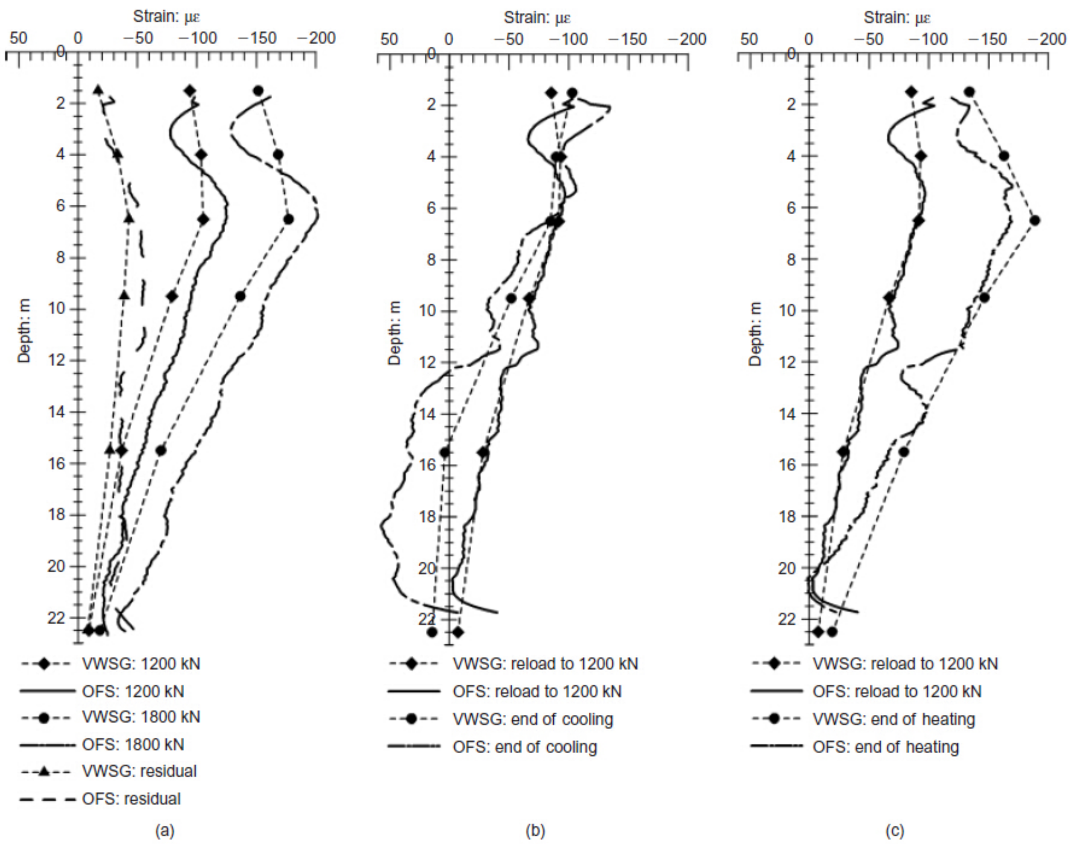

Figure 2-9 Comparison of strain profiles from VWSG and OFS systems: (a) during initial loading test; (b) thermal test at end of cooling; (c) thermal test at end of heating

Knellwolf et al. (2011) proposed a simple geotechnical analysis theory to explain the thermo-mechanical behaviour in the on-site experiment mentioned before. This method was established based on the load-transform method (Seed & Reese, 1957; Coyle & Reese, 1966). The pile is subdivided into a series of rigid elements. Each element is connected by springs with the neighbour elements, and has an elastoplastic interaction with the surrounding soil, as shown in Figure 2-10 (a). The shaft friction has the functional relationship with the pile displacement, which could be expressed as load-transform functions. Considering the shrink ability of PGHE while absorbing heat energy from the soil, the authors imaged the classic load-transfer curve (Frank, 1982) from the second to the fourth quadrant, shown in Figure 2-11. It should be pointed out that this method is based on the assumption that the interface properties of soil and pile are known, and the interface behaviours of each element do not change with temperature.

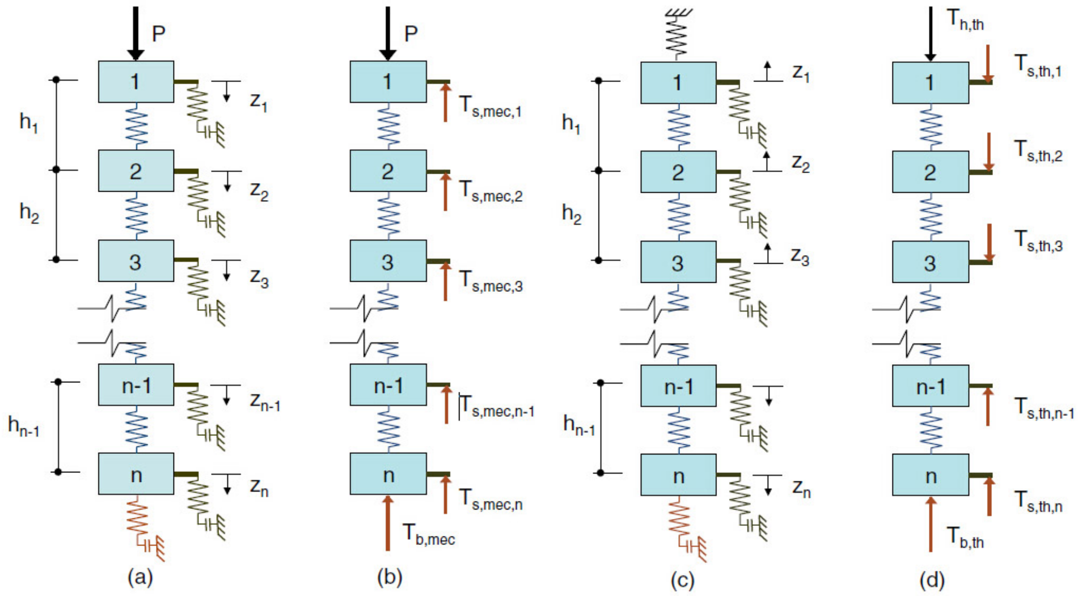

Figure 2-10 Finite-difference model for heat exchanger pile load and displacement computation: (a) model for mechanical load (z_i: displacement of pile segment i); (b) external forces $T_{s;mec;i}$ and $T_{b;mec}$ mobilized by mechanical loading; (c) model for thermal loading (z_i: displacement of pile segment i); (d) external forces $T_{h,th}$, $T_{s,th,i}$, and $T_{b,th}$ mobilized by thermal loading. (Knellwolf et al., 2011)

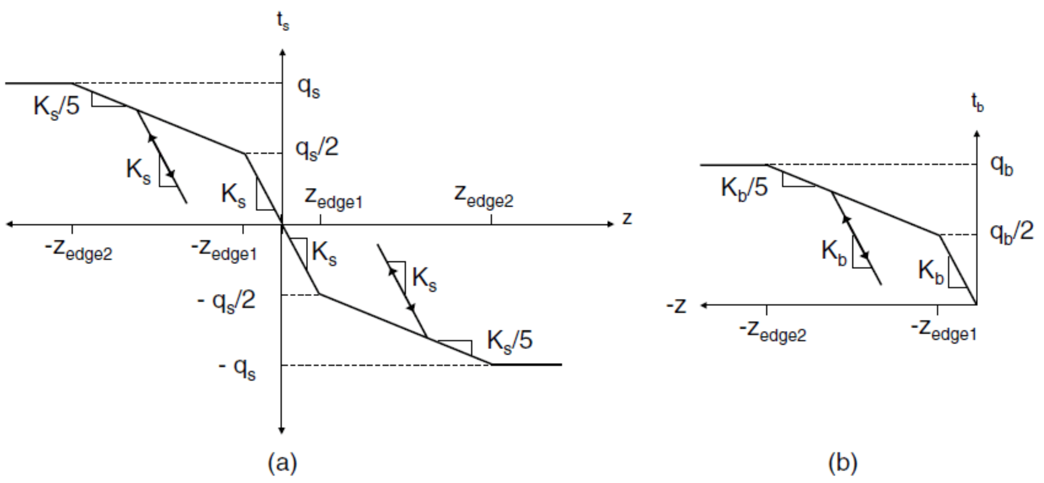

Figure 2-11 Load-transfer curves proposed by Frank and Zhao; (a) evolution of the mobilized shaft friction t_s with respect to pile displacements; (b) evolution of the mobilized reaction on the base of the pile t_b with respect to pile displacements

In this method, it first selects a null point and assumes there is no displacement at this null point. The pile is assumed to be expanded and shrank around the null point. Setting all the elements free to move, the initial strain is calculated by the product of pile thermal expansion coefficient and the pile increasing/decreasing temperature. Then, by using the load-transfer curve, an initially mobilized reaction stress of each element can be obtained directly. This stress corresponds to a blocking force, $\varepsilon=\sigma/\mathrm{E}$, and a new force value can be calculated by subtracting this blocking force from the initial stain. Repeat these steps until the blocking force equals to the calculated one.

The strains of pile under different thermal loads were compared to the proposed model and compared with those from an in-suit experiment conducted in Swiss Federal Institute of Technology Lausanne (EPFL). It shows a good agreement between the results from the experiment and the proposed model when the temperature changes are within 17.4 ℃, but a relatively large error when the temperature change is up to 21.8 ℃. But, the author gives no further explanation about this error. This error may be related to the changing of interface properties under a large thermal load.

2.4.3 Interface behaviour between the pile and the soil

An interface formed between a structural material and an unsaturated soil is important in pile foundation design. The ultimate shear strength at the interface is a critical parameter for the design and safety assessment of the structures in the soils and a key factor in the design and analysis of the ultimate bearing capacity of the pile foundation. Matric suction has a predominant effect on the shear strength and volume change behaviour of the soil and soil-concrete interfaces, so proper characterization of interface behaviour is important for its accurate performance predictions. The thermal load of PGHE can force the soil water to be redistributed. Thus, the interface behaviour between a structural material and an unsaturated soil may be affected by the changing of the matric suction.

The term of "soil suction" was firstly be used by Schofield (1935) to represent the "pressure deficiency" in the pore water of any soil in saturated and unsaturated states. Soil suction plays a key role in unsaturated soil mechanics (Sivakumar, 1993; Oloo & Fredlund, 1996) and is frequently referred as the free energy state of soil water, which can be measured in terms of its partial vapour pressure. From the thermodynamic perspective, the total suction in soil can be described using Kelvin's equation:

$$\psi = -\frac{RT}{v_{w0}\omega_v} In\left(\frac{u_v}{u_{v0}}\right) \tag{2.21}$$

where ψ is total suction (kPa); R is the universal gas constant [J/(mol • K)]; v_{w0} is the specific volume of water or the inverse of the density of water (m3/kg); u_v is the partial pressure of pore-water vapour (kPa); ω_v is the molecular mass of water vapour (g/mol); T is the absolute temperature (K); u_{v0} is the saturation pressure of water vapour over a flat surface of pure water at the same temperature (kPa), and $\left(u_v / u_{v0}\right)$ represents the relative humidity, RH (%).

The surface tension of the pore fluid in menisci causes the capillary effects. The value of matric suctions is a function of surface tension (T_s) and the radius of curvature of the menisci characterized by radii R_1 and R_2 (refer to Figure 2-12) and is defined by Kelvin's law as follows:

$$s = u_a - u_w = T_s = \left(\frac{1}{R_1} + \frac{1}{R_2} \right) \tag{2.22}$$

where u_a and u_w are the gas and fluid pressures, respectively, acting on both sides of the fluid surface.

As the water content reduces, the menisci withdraws into smaller pore spaces and the menisci radius of curvature also reduces, and hence matric suction increases. Clayey soil possesses smaller pore sizes. As a result, higher matric suctions can be developed in it compared to coarse granular soils. Any variation of relative humidity in the soil normally results in a change of total suction. Relative humidity in soil can be reduced due to the occurrence of a curved water surface as a result of capillary phenomenon, that is, contractile skin (Fredlund & Rahardjo, 1993). The change in the radius of curvature of the curved water surface is dependent on the air pressure (u_a) and water pressure (u_w) in the soil fabric. The radius of curvature is noted to be inversely proportional to the difference between u_a and u_w diagonally to the surface, i.e., $u_a - u_w$, and is termed as matric suction. Variation in relative humidity due to the presence of dissolved salts in pore water is referred to osmotic suction. The concentration of dissolved salts in the pore fluid of the soil directly influences the osmotic suction, and it is measured in terms of pressure.

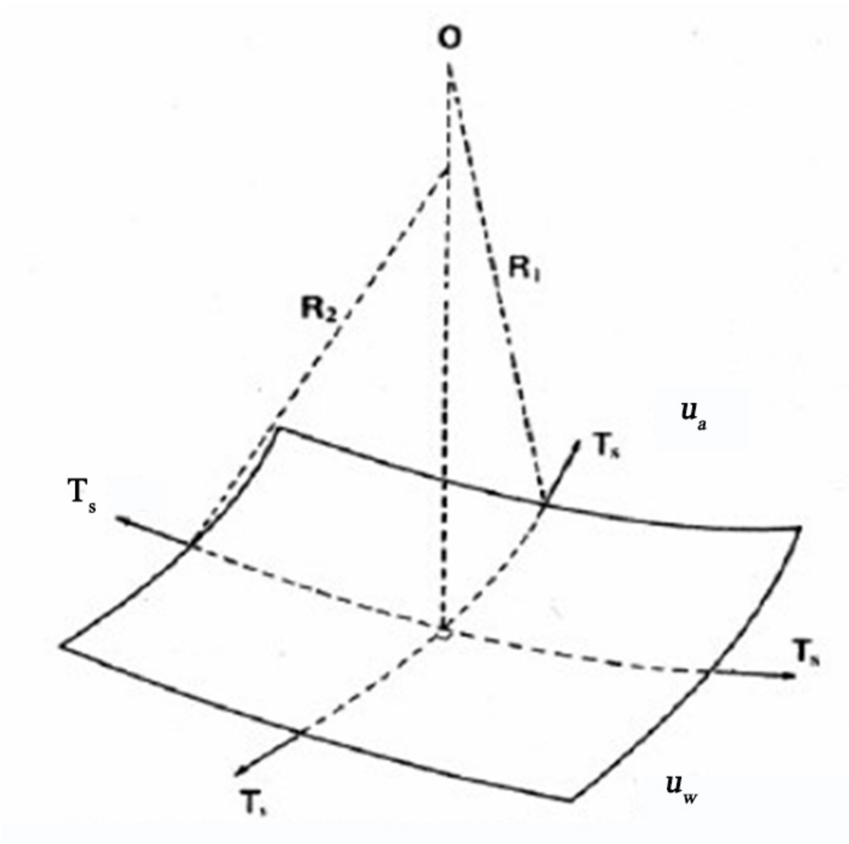

Figure 2-12 Surface tension on a warped membrane (Fredlund & Rahardjo, 1993)

Matric suction significantly influences the flow of water and mechanical behaviour of unsaturated soils. Nevertheless, it is difficult to identify the effect of osmotic suction on the mechanical behaviour of unsaturated soil (Hossain, 2010) , which has been controversial (Alonso et al., 1987). Soil characteristics including mechanical and hydraulics behaviour are significantly influenced by the suction (Fredlund & Rahardjo, 1993). Many researchers have studied the effects of suction on yielding and compressibility. The increase of suction stiffens the unsaturated soil against the external loading which results in an increase of apparent pre-consolidation pressure (yielding stress). The yielding surfaces are enlarged with the increased suction, resulting in a gradual suction-hardening effect. By contrast, the compressibility of unsaturated soil increases with a reduction in suction value (Alonso et al., 1990). However, Wheeler and Sivakumar (1995) and Chiu and Ng (2003) have conducted extensive experimentation and have demonstrated that the compressibility under saturated conditions is smaller than that under unsaturated conditions. The compressibility of silty soil does not change monotonically with suction. The degree of specimen compaction plays an important role in influencing the compressibility at a given suction. The compressibility in an unsaturated soil is dependent on suction, compaction conditions and wetting-induced change of the fabric. The volumetric response of unsaturated soils is highly dependent on the stress path due to the irreversibility.

The shear strength in unsaturated soil increases with an increase in suction, which may sometimes result in an increase in apparent cohesion while maintaining constant friction angle (Hossain & Yin, 2010). Nevertheless, the gain in shear strength with respect to increasing in suction cannot persist for an indefinite period. The experimental findings (Ng & Menzies, 2007) showed that the suction increases the elastic shear modulus. Furthermore, the suction increases the dilatancy and brittleness of an unsaturated soil (Y. Cui & Delage, 1996; Ng & Zhou, 2005; Hossain & Yin, 2009; Borana et al., 2013).

Bishop (1960) proposed a relationship in Eq. (2.6) for determining the unsaturated shear strength of the soil:

$$\tau_f = c' + \left[\sigma_n - u_a + \chi\left(u_a - u_w\right)\right]\tan\phi' \tag{2.23}$$

where τ_f is the shear strength, c' is effective cohesion, ϕ' is the effective friction angle, σ_n is total stress, χ is a coefficient (ranging from 0 to 1), u_a is pore air pressure and u_w is the pore-water pressure. But Bishop's equation fails to explain the collapse potential of some soil on wetting and it also has difficulties in predicting values of χ.

Lamborn proposed a modified equation by extending a micromechanics model and is as follows (1986):

$$\tau_f = c' + \left(\sigma - u_a\right)\tan\phi' + \left(u_a - u_w\right)\theta_w \tan\phi' \tag{2.24}$$

where, θ_w is the volumetric water content and defined as the ratio of the volume of water to the total volume of the soil. The volumetric water content decreases as the matric suction increases, and it is a nonlinear function of matric suction. However, it must be noted that unless the volumetric water content is equal to 1, the friction angle associated with matric suction does not become equal to ϕ'.

A simple and practical model based on the soil water characteristic curve (SWCC) to determine the shear strength of the soil was proposed by Vanapalli (1996) as shown below:

$$\tau_f = c' + \left(\sigma_n - u_a\right)\tan\phi' + \left(u_a - u_w\right)_f \Theta^k \tan\phi^b \tag{2.25}$$

where, Θ^k is the normalized water content obtained from SWCC, and *k* is the soil parameter. Zhan and Ng have modified the equation (2.25) by incorporating the volume change behaviour into the shear strength, and the equation is rewritten as:

$$\tau_f = c' + \left(\sigma_{nf} - u_{af}\right)\tan\left(\phi' + \psi\right) + \left(u_a - u_w\right)_f \tan\phi^b \tag{2.26}$$

where, ψ is the dilation angle. Hossain and Yin (2010) have further modified the unsaturated shear strength model, proposed by Vanapalli et al. by considering the matric suction induced soil dilatancy, as follows:

$$\tau_f = c' + \left(\sigma_n - u_a\right)\tan\left(\phi' + \psi\right) + \left(u_a - u_w\right)_f \Theta^k \tan\left(\phi' + \psi\right) \tag{2.27}$$

2.4.4 Moisture movement under thermal gradient

The heating and cooling cycle of PGHE may have a possibility to change the properties of the soil moisture contents. Therefore, the thermo-hydro behaviours of unsaturated soil is essential for the thermal-mechanic analysis of PGHE. For common soil or rock, various models of the mechanistic approach have been proposed (Philip & De Vries, 1957; Sophocleous, 1979; Ewen & Thomas, 1989). The moisture transfer equations are cast in terms of the matric potential (ψ-based equations) because this approach can handle saturation conditions. The main simplifying assumptions made in the derivations are that the soil is assumed to be homogenous and isotropic within each defined unit of soil.

For the liquid transfer, the Darcy's law can be extended to the unsaturated soil by using the gradient of the total potential, $\Phi = \psi + z$, and defining the hydraulic conductivity, K (m/s), as a function of the soil water matric potential.

$$u_{\ell} = -K(\psi)\nabla\Phi = -K\nabla\psi - K\hat{k} \tag{2.28}$$

By applying the continuity equation to the liquid moisture content of a control volume of soil, the conservation of liquid can be written as:

$$\frac{\partial \theta_{\ell}}{\partial t} = -\nabla \cdot u_{\ell} - E \tag{2.29}$$

The liquid content is a function of the matric potential and temperature. Therefore, the time derivative of the liquid content can be expanded by the chain rule as given below:

$$C_{\psi\ell}\frac{\partial \psi}{\partial t} + C_{T\ell}\frac{\partial T}{\partial t} = \nabla \cdot \left[K\nabla\psi\right] + \frac{\partial K}{\partial z} - E \tag{2.30}$$

For the vapour transfer, the vapour diffusion in a gas-filled pore can be approximated by modifying the Fick's law of diffusion by assuming a uniform and constant total pressure, P (Nakano & Miyazaki, 1979; Hermansson et al., 2009):

$$\dot{m}_v = -D_a\left[\nabla\rho_v + \frac{\rho_v}{T}\left(\nabla T\right)_p\right] \tag{2.31}$$

The molecular diffusivity of water vapour in air, D_a, is given by Eq.(2.32) and $\left(\nabla T\right)_p$ is the temperature gradient across a single gas-filled pore:

$$D_a = c\left(\frac{P_o}{P}\right)\left(\frac{T}{T_0}\right)^n \tag{2.32}$$

The reference pressure is $P_0 = 101325Pa$, the reference temperature is $T_o = 273.15K$, $c = 2.17\times10^{-5}\ m^2/s$, and $n = 1.88$. The vapour density of the pores can be expressed as the product of the relative humidity, φ, and the saturated vapour density, ρ_{vs}.

$$\rho_v = \rho_{vs}\varphi \tag{2.33}$$

Assuming that the soil liquid and vapour are in thermodynamic equilibrium, and in the absence of solutes, the relative humidity in the soil pores may be written as (Edlefsen & Anderson, 1943):

$$\varphi = \exp\left(\frac{\psi g}{R_v T}\right) \tag{2.34}$$

Rewrite the vapour diffusion equation by introducing the Eq.(2.33) and (2.34):

$$\dot{m}_v = -D_a\varphi\rho_{vs}\left[\frac{g}{R_v T}\nabla\psi + \left(\frac{1}{\rho_{vs}}\frac{\partial\rho_{vs}}{\partial T} + \frac{1}{T} - \frac{\psi g}{R_v T^2} + \frac{g}{R_v T}\left.\frac{\partial\psi}{\partial T}\right|_{\theta}\right)\left(\nabla T\right)_p\right] \tag{2.35}$$

Only the first of the four temperature gradient coefficient terms is significant for most situations. The last two terms are important for $\psi < -10^4$ m. When applying the vapour mass flux given by Eq.(2.35) to a porous soil system, the effects of the reduced cross section for diffusion, the tortuosity, and the interactions between the vapour and liquid phases must be addressed. A vapour diffusion correction factor, $f\left(\theta_\ell\right)$, is added to account for these effects (De Vries, 1958).

$$\begin{aligned} f\left(\theta_\ell\right) &= \eta && \text{for } \theta_\ell \le \theta_k \\ f\left(\theta_\ell\right) &= \theta_a + \theta_a\theta_\ell / \left(\eta - \theta_k\right) && \text{for } \theta_\ell > \theta_k \end{aligned} \tag{2.36}$$

The vapour mass flux in Eq.(2.35), divided by the liquid density for consistency with the liquid-transfer equation, can be written for the soil system as:

$$\frac{\dot{m}_v}{\rho_\ell} = -D_{\psi v} \nabla \psi - D_{Tv} \nabla T \tag{2.37}$$

where the matric and thermal vapour diffusivities are:

$$D_{\psi v} = f(\theta_\ell) D_a \frac{\rho_{vs}}{\rho_\ell} \frac{\varphi g}{R_v T} \tag{2.38}$$

$$D_{Tv} = f(\theta_\ell) D_a \varphi \frac{\rho_{vs}}{\rho_\ell} \left(\frac{1}{\rho_{vs}} \frac{\partial \rho_{vs}}{\partial T} + \frac{1}{T} - \frac{\psi g}{R_v T^2} + \frac{g}{R_v T} \frac{\partial \psi}{\partial T}\bigg|_\theta \right) \frac{(\nabla T)_p}{(\nabla T)} \tag{2.39}$$

The temperature gradients across the gas-filled pores are higher than the gradient across the system because of the lower thermal conductivity of the gas-filled pores. The vapour content is expressed as an equivalent liquid content. With assumed thermodynamic equilibrium between the liquid and vapour, we can write:

$$\theta_v = \frac{(\eta - \theta_\ell)\rho_v}{\rho_\ell} \tag{2.40}$$

Expanding $(\partial \theta_v / \partial t)$, and using the chain rule to include the dependence on moisture and temperature yields:

$$\frac{\partial \theta_v}{\partial t} = C_{\psi v} \frac{\partial \psi}{\partial t} + C_{Tv} \frac{\partial T}{\partial t} \tag{2.41}$$

where the matric and thermal vapour capacitances are:

$$C_{\psi v} = \frac{\rho_{vs} \varphi}{\rho_\ell} \left[\frac{(\eta - \theta_\ell) g}{R_v T} - \left(\frac{\partial \theta_\ell}{\partial \psi} \right)_T \right] \tag{2.42}$$

$$C_{Tv} = \frac{\rho_{vs} \varphi}{\rho_\ell} \left[\frac{(\eta - \theta_\ell)}{\rho_{vs}} \left(\frac{\partial \rho_{vs}}{\partial T} \right) - \left(\frac{\partial \theta_\ell}{\partial T} \right)_\psi \right] \tag{2.43}$$

The conservation of vapour content can be written as:

$$\frac{\partial \theta_v}{\partial t} = -\nabla \cdot \left(\dot{m}_v / \rho_\ell \right) + E \tag{2.44}$$

The governing equation for vapour transfer can now be derived by substituting of Eqs. (2.37) and (2.41) into (2.44).

$$C_{\psi v} \frac{\partial \psi}{\partial t} + C_{Tv} \frac{\partial T}{\partial t} = \nabla \left[D_{\psi v} \nabla \psi \right] + \nabla \left[D_{Tv} \nabla T \right] + E \tag{2.45}$$

For the total moisture transfer, the moisture transfer equation is then derived by combining the equations for liquid and vapour transport together：

$$C_{\psi m} \frac{\partial \psi}{\partial t} + C_{Tm} \frac{\partial T}{\partial t} = \nabla \left[D_{\psi \mathrm{m}} \nabla \psi \right] + \nabla \left[D_{T\mathrm{m}} \nabla T \right] + \frac{\partial \mathrm{K}}{\partial \mathrm{z}} \tag{2.46}$$

Applying the numerical method, the moisture movement under a temperature gradient can be simulated, and an obvious moisture movement can be observed, as shown in Figure 2-13 (Kanno et al., 1996).

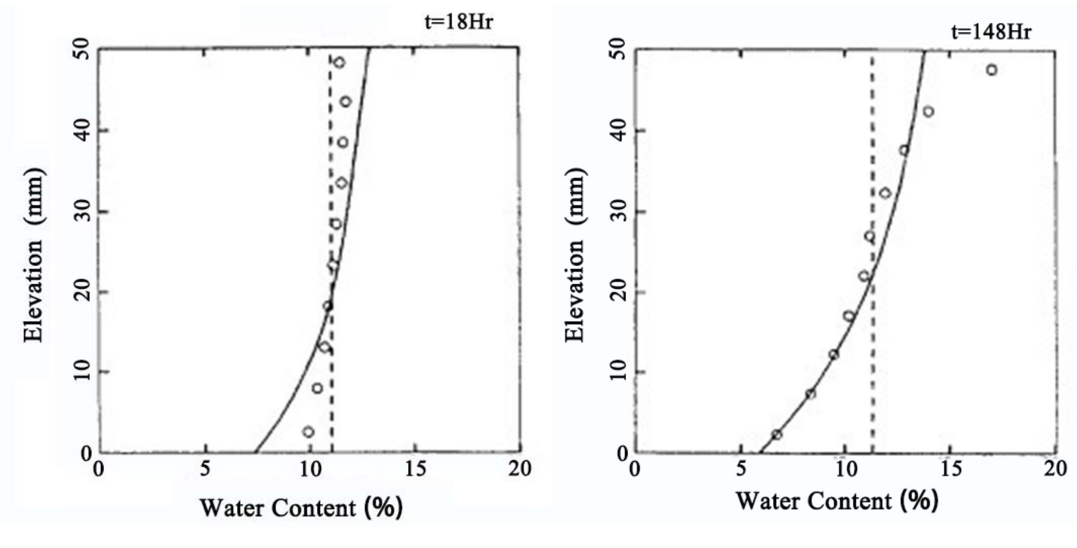

Figure 2-13 Experimental and calculated results of water content distributions

2.5 Limitation of the past studies

This chapter presents a comprehensive literature review on the heat transfer mechanism of GHE with spiral-tubes, especially for the PGHE systems. The thermo-mechanical studys of PGHE are also summarized. The previous heat transfer models and design method for spiral heat exchangers have their application limitations, and they fail to predict the thermal performance of spiral heat exchangers accurately. In addition, with the increasing application of PGHE with spiral-tubes, the thermo-mechanical behaviour of this novel type pile requires to be studied and resolved urgently for its safety perspective. In summary, we have the following observations:

a) The existing analytical models (e.g. slinky source model and Kelvin line source model) cannot describe the heat transfer process of HGHE with spiral-tubes. Furthermore, all the existing analytical models assume the surface boundary condition is temperature constant or heat isolation, and fail to consider the temperature changes of the soil surface with the time.

b) Most of the existing analytical models of PGHE assume the soil and pile have the same thermal properties, which cause a large deviation between experimental and analytical results during long-term operation estimation. No analytical model for PGHE with spiral-tubes both considered the difference of thermal properties between pile and soil, and the finiteness of PGHE geometry.

c) The existing advection models of PGHE fails to take the blocking effect of the concrete pile, and consequently, they are hard to describe the temperature profile of PGHE in short-term operation, especially the temperature profile within the concrete pile.

d) The research on the thermo-mechanical behaviour of PGHE is a limited, especially in the interface behaviour of pile and soil. No numerical or experimental studies considering the temperature effect on the soil-concrete interface.

2.6 Methodology

As proposed in the literature review section, the spiral-tubes are mainly applied as 1) Horizontal GHEs and 2) Pile GHEs, The study of heat transfer mechanism for these geothermal heat exchangers is the critical part of this thesis, which is fully investigated in Chapter 3, Chapter 4 and Chapter 5. Based on the Green’s function theory, a ring-coil source model has been established for HGHE with spiral-tubes. Details of this model can be found in Chapter 3 together with an in-suit experiment validation. For the PGHE with spiral-tubes, a heat conduction model is present in Chapter 4, which can fully represent the difference of thermal properties between concrete and soil. By building and simulating the heat transfer process of PGHE under groundwater advection, a new semi-analytical model has been established, as given in Chapter 5.

The interface behaviour between the soil and pile is a key factor affecting the geotechnical design for the traditional pile. Thus, a modified direct shear test rig has been established to investigate the thermal load on the interface behaviour of concrete and soil and further to discover the thermal-mechanic performance of PGHE with spiral-tubes. Details of the experimental method can be found in Chapter 6. Based on the experiments results from Chapter 6, a numerical simulation model is established in Chapter 7 to model the thermo-mechanical performance of PGHE with spiral-tubes. The methodology is summarized as a flow chart, as shown in Figure 2-14.

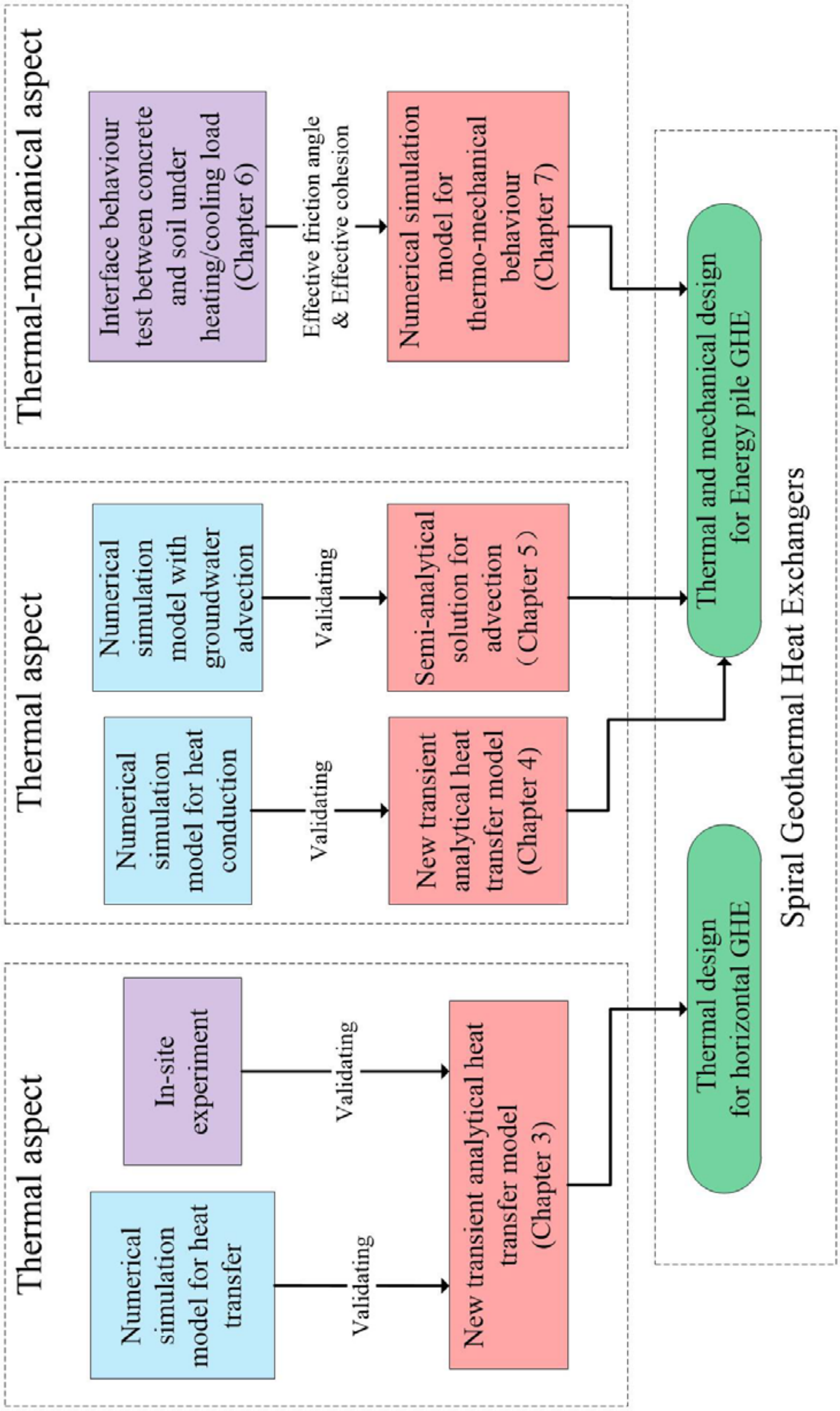

Figure 2-14 A flow chart of the methodology for experimental, analytical and numerical studies

CHAPTER 3

HEAT TRANSFER MODEL DEVELOPMENT FOR HORIZONTAL GEOTHERMAL HEAT EXCHANGER

3.1 Introduction

As discussed in chapter 2, the spiral heat exchanger has the best heat transfer performance among the various types of geothermal heat exchangers (Congedo et al., 2012). However, the previous investigations on the HGHE with spiral-tubes were mainly conducted by experimental or numerical methods, and the analytical investigation is limited. As no reliable analytical model can accurately describe the heat transfer performance of HGHE with spiral-tubes is available, it is necessary to investigate its heat transfer mechanism and to establish a new analytical solution to accurately model its heat transfer process. In this study, the new analytical model for HGHE with spiral-tubes is based on the Green's function theory which is widely applied in the analytical modelling for GHE heat transfer (Yi Man et al., 2010; P. Cui et al., 2011; H. Li et al., 2012b). Furthermore, referring to the literature review, in these previous GHE models, the ground surface temperature is assumed to be constant or the ground surface is considered as an adiabatic boundary. But, for horizontal GHEs, the surface temperature is always changing during the whole year and has a non-negligible effect on its heat transfer performance. To address these gaps, the main works conducted in this chapter are summarized as follows:

1) Based on the Green's function theory, a new ring-coils source model has been

established for HGHE with spiral coils, in which the spiral tube is simplified as a number of separated ring-coils. The new analytical model is validated by an in-suit experiment for short-term operation and a numerical simulation model for long-term operation.

2) The ground surface temperature is fully considered in the new analytical model. A sinusoidal changed boundary solution is proposed to model the temperature variation during a whole year, which can be not only applied for modelling HGHE with spiral-tubes but also used for other types of HGHE, e.g. liner GHEs or slinky GHEs.

3.2 Ring-coil Heat Source Solution for HGHE with spiral-tubes

Taking the geometrical features of vertical spiral HGHEs and the impact of surface temperature into account, a new model, i.e. the ring source model, is established. This new model was represented by a series of separated rings with a radius $\boldsymbol{r_0}$ and pitch $\boldsymbol{b}$ being coincident with the y-axis. In line with the assumptions in previous analytical models of geothermal heat exchangers (P. Cui et al., 2011; H. Li et al., 2012b), the ground is assumed to be a homogeneous medium with thermal properties remaining constant in the face of temperature change. The initial temperature of the ground soil is assumed to be uniform and constant. In this new model, the assumptions are summarized as follow:

1) The medium has a uniform initial temperature, T_0;

2) The ground is considered to be a semi-infinite medium and the temperature of the ground surface is assumed to be unchanged with a fixed value of T_0 ;

3) No groundwater advection exists around the pile foundation;

4) The ring-coils heat source with its radius of r_0 releases heat energy since the initial time, $t=0$.

Based on the transient heat conduction equation, and with the given assumptions and initial conditions, this heat conduction problem can be expressed as follows:

$$
\begin{aligned}
&\frac{\partial^2\theta}{\partial x^2}+\frac{\partial^2\theta}{\partial y^2}+\frac{\partial^2\theta}{\partial z^2}+\frac{1}{k}g\left(x,y,z,t\right)=\frac{1}{\alpha}\frac{\partial\theta}{\partial t}, && \text{in} \quad -\infty<x<+\infty,\ -\infty<y<+\infty,\\
& && \qquad 0\le z<+\infty,\ t>0\\
&\theta=A\cdot\sin(\omega t+\varepsilon), && \text{at} \quad z=0,\ t>0\\
&\theta=0, && \text{for} \quad t=0,\ \text{in the region}
\end{aligned}
\tag{3.1}
$$

According to the Green's function theory (Cole et al., 2010), the temperature response can be obtained by dividing the equation into energy generation, $\theta_g(x,y,z,t)$ and the boundary , $\theta_{b,c}(x,y,z,t)$, as shown in Eq.(3.2).

$$
\begin{aligned}
&\theta\left(x,y,z,t\right)=\theta_g(x,y,z,t)+\theta_{b,c}(x,y,z,t)\\
&\theta_g(x,y,z,t)=\int_{\tau=0}^{t}\int_R\frac{\alpha}{k}G\left(x,y,z,t\middle|x',y',z',\tau\right)g\left(x',y',z',\tau\right)dv'd\tau\\
&\theta_{b,c}(x,y,z,t)=-\alpha\int_{\tau=0}^{t}\sum_{j=1}^{s}\int_{S_j}f_j\left(\mathbf{r}_j',\tau\right)\frac{\partial G}{\partial n_j'}\bigg|_{r'=r_j'}ds_j'd\tau
\end{aligned}
\tag{3.2}
$$

Before developing the ring-coil model, a simple model, i.e. the single ring-coil heat source model with zero surface temperature, is first introduced as the basic function of the horizontal ring-coil model.

3.2.1 Single ring-coil heat source in a semi-infinite medium

The temperature response at points (*x*, *y*, *z*) for an impulse heat source located at (*x'*, *y'*, *z'*) in an infinite solid with zero initial temperature at an initial temperature of τ can be expressed as:

$$\theta_p\left(x,y,z,t\right)=\frac{1}{8\left[\pi\alpha\left(t-\tau\right)\right]^{3/2}}\exp\left[-\frac{\left(x-x'\right)^2+\left(y-y'\right)^2+\left(z-z'\right)^2}{4\alpha\left(t-\tau\right)}\right] \quad (3.3)$$

Thus, the temperature increase due to a single ring source can be obtained by integrating the point source along a ring circle:

$$\theta_{rsi,c}\left(x,y,z,t\right)=\int_{\tau=0}^{t}\int_{l}\frac{\alpha}{k}G_{in}\left(x,y,z,t\middle|x',y',z',\tau\right)g\left(x',y',z',\tau\right)ds'd\tau$$
$$G_{in}\left(x,y,z,t\middle|x',y',z',\tau\right)=\frac{1}{8\left[\pi\alpha\left(t-\tau\right)\right]^{3/2}}\exp\left[-\frac{\left(x-x'\right)^2+\left(y-y'\right)^2+\left(z-z'\right)^2}{4\alpha\left(t-\tau\right)}\right]$$

(3.4)

Assuming the ring source releases heat with a strength of q_r with a centre point (0, 0, v_c) and a radius of r_0 on the surface of $y=0$, as shown in Figure 3-1, the temperature at points (*x*, *y*, *z*) at time *t* can be expressed as:

$$\theta_{rsi,c}\left(x,y,z,t\right)=q_r\frac{\alpha}{k}\int_0^t\int_0^{2\pi}\frac{r_0}{8\left[\pi\alpha\left(t-\tau\right)\right]^{3/2}}$$
$$\times\exp\left[-\frac{\left(x-r_0\sin\sigma\right)^2+y^2+\left(z-r_0\cos\sigma-v_c\right)^2}{4\alpha\left(t-\tau\right)}\right]d\sigma d\tau$$
$$=\frac{q_r r_0}{4\pi k}\int_0^{2\pi}\frac{1}{r_*}ercf\left(\frac{r_*}{\sqrt{4\alpha t}}\right)d\sigma$$

(3.5)

where $ercf(u) = 2/\pi \int_u^{\infty} \exp(-\beta^2)\, d\beta$ is the error function and r_* is the distance between the observation point and heat source, which can be written as $r_* = \sqrt{\left(x - r_0 \sin\sigma\right)^2 + y^2 + \left(z - r_0 \cos\sigma - v_c\right)^2}$.

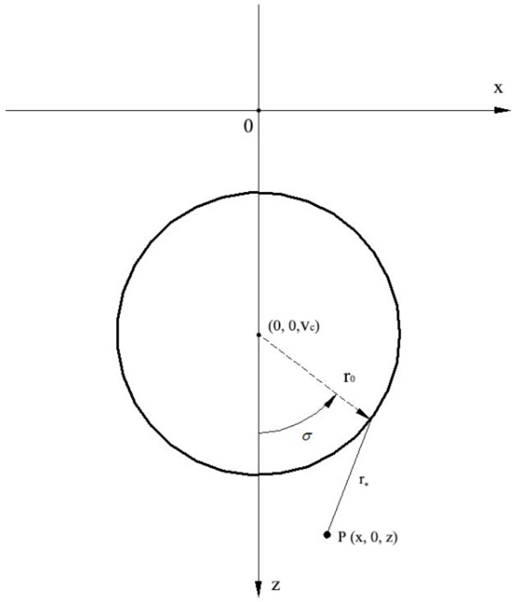

Figure 3-1 Schematic representation of signal ring-coil in an infinite medium

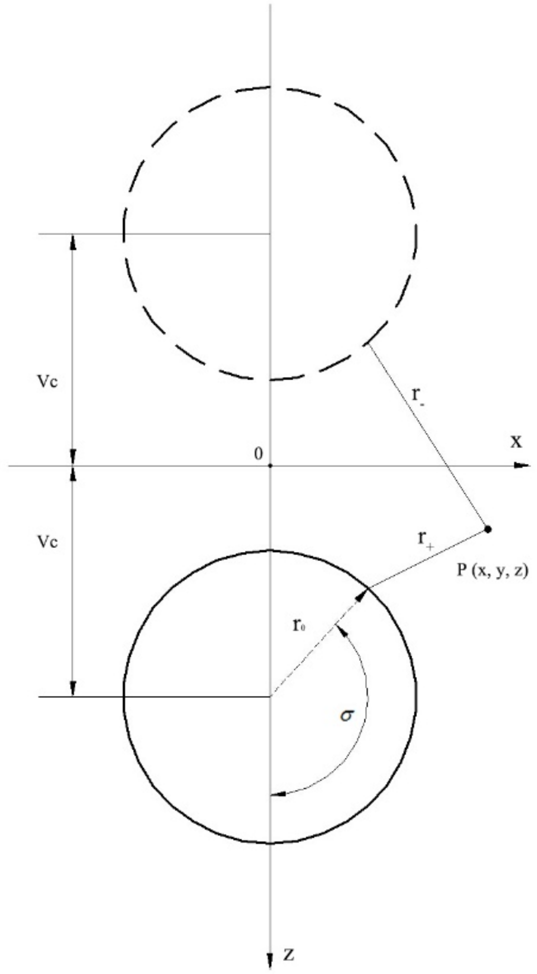

Figure 3-2 Schematic representation of signal ring-coil in a semi-infinite medium

The imaging method is applied to find the single ring source in a semi-infinite medium. As shown in Figure 3-2, a virtual ring source with the same geometry is applied symmetrically over the boundary surface. The heat discharging rate of the virtual ring source is considered to be the opposite of the original one.

By applying this virtual ring source, the temperature at the ground surface is always maintained at zero. Therefore, the temperature rise of the single ring source in a semi-infinite medium can be obtained directly by superposing the solution of a virtual ring source into Eq.(3.5). The temperature at points (*x, y, z*) at time *t* can then be expressed as:

$$\theta_{rss,c}\left(x,y,z,t\right)=\int_{\tau=0}^{t}\int_{l}\frac{\alpha}{k}G_{sin}\left(x,y,z,t\middle|x',y',z',\tau\right)g\left(x',y',z',\tau\right)ds'd\tau \tag{3.6}$$

$$\begin{aligned}G_{sin}\left(x,y,z,t\middle|x',y',z',\tau\right)=&\frac{1}{8\left[\pi\alpha\left(t-\tau\right)\right]^{3/2}}\exp\left[-\frac{\left(x-x'\right)^2+\left(y-y'\right)^2}{4\alpha\left(t-\tau\right)}\right]\\&\times\left\{\exp\left[-\frac{\left(z-z'\right)^2}{4\alpha\left(t-\tau\right)}\right]-\exp\left[-\frac{\left(z+z'\right)^2}{4\alpha\left(t-\tau\right)}\right]\right\}\end{aligned} \tag{3.7}$$

By using the error function to simplify these equations, the temperature can then, be written as:

$$\begin{cases}\theta_{rs,c}\left(x,y,z,t\right)=\dfrac{q_r r_0}{4k\pi}\displaystyle\int_0^{2\pi}\dfrac{1}{r_+}erfc\left(\dfrac{r_+}{\sqrt{4\alpha t}}\right)-\dfrac{1}{r_-}erfc\left(\dfrac{r_-}{\sqrt{4\alpha t}}\right)\,d\sigma\\ r_+=\sqrt{\left(x-r_0\sin\sigma\right)^2+y^2+\left(z-r_0\cos\sigma-v_c\right)^2}\\ r_-=\sqrt{\left(x-r_0\sin\sigma\right)^2+y^2+\left(z+r_0\cos\sigma+v_c\right)^2}\end{cases} \tag{3.8}$$

By introducing the following dimensionless variables: $Fo=\alpha t/r_0^2$, $\Theta=k\theta r_0/q$, $V=v_c/r_0$, $X=x/r_0$, $Y=y/r_0$, $Y'=y_0/r_0$, $Z=z/r_0$, the dimensionless temperature can be rewritten as a function of the following:

$$\begin{cases}\Theta_{rs,c}=\dfrac{1}{4\pi}\displaystyle\int_0^{2\pi}\dfrac{1}{R_+}erfc\left(\dfrac{R_+}{\sqrt{4Fo}}\right)-\dfrac{1}{R_-}erfc\left(\dfrac{R_-}{\sqrt{4Fo}}\right)\,d\sigma\\ r_+=\sqrt{\left(X-\sin\sigma\right)^2+Y^2+\left(Z-\cos\sigma-V\right)^2}\\ r_-=\sqrt{\left(X-\sin\sigma\right)^2+Y^2+\left(Z+\cos\sigma+V\right)^2}\end{cases} \tag{3.9}$$

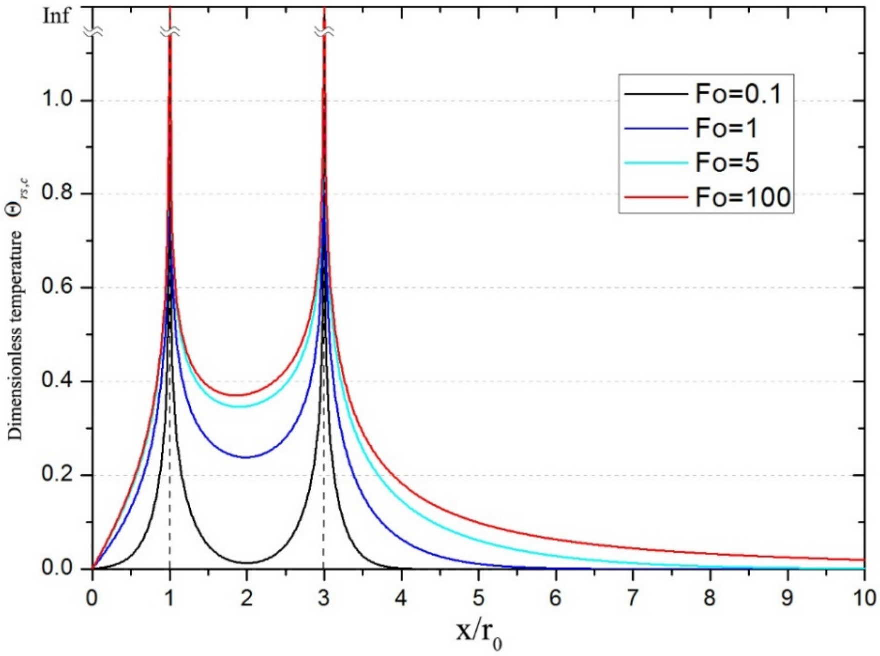

Figure 3-3 Dimensionless temperature response with different *Fo*

3.2.2 Multiple ring-coils source model

The superposition method is used to obtain the analytical solution of the multiple ring-coil source model. In the multiple ring-coil model, the spiral HGHEs are assumed to be a series of ring-coil sources buried in a semi-infinite medium. The distance between two neighboring ring coils is assumed to be the same with the spiral pitch of the spiral heat exchanger. The number of ring-coils (N) is equal to the ratio of the trench length to the spiral pitch of the spiral heat exchanger.

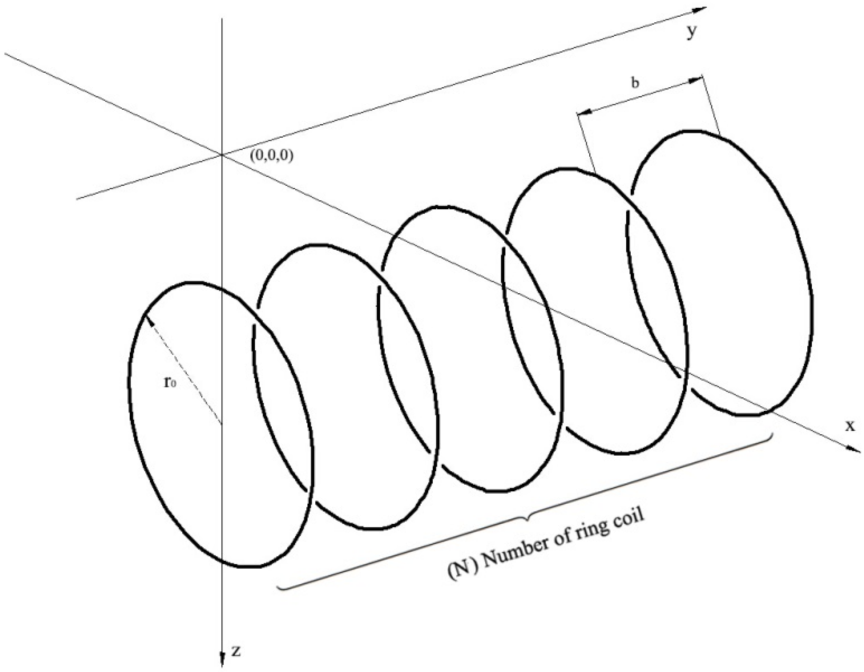

Figure 3-4 Schematic representation of horizontal ring-coil source model

The multiple ring-coils source model with a zero surface temperature solution can be regarded as the superposition of a single sing-coil source model with finite times:

$$\theta_{mrs,c}\left(x,y,z,t\right)=q_r\frac{\alpha}{k}\sum_{n=0}^{N-1}\int_0^t\int_0^{2\pi}\frac{r_0}{8\left[\pi\alpha\left(t-\tau\right)\right]^{3/2}} \times\exp\left[-\frac{\left(x-r_0\sin\sigma\right)^2+(y-nb)^2+\left(z-r_0\cos\sigma-v_c\right)^2}{4\alpha\left(t-\tau\right)}\right]d\sigma d\tau \tag{3.10}$$

$$\begin{cases}\theta_{mrs,c}\left(x,y,z,t\right)=\dfrac{q_r r_0}{4k\pi}\displaystyle\sum_{n=0}^{N-1}\int_0^{2\pi}\dfrac{1}{r_{n+}}erfc(\dfrac{r_{n+}}{\sqrt{4\alpha t}})-\dfrac{1}{r_{n-}}erfc(\dfrac{r_{n-}}{\sqrt{4\alpha t}})\ d\sigma \\ r_+=\sqrt{\left(x-r_0\sin\sigma\right)^2+\left(y-nb\right)^2+\left(z-r_0\cos\sigma-v_c\right)^2} \\ r_-=\sqrt{\left(x-r_0\sin\sigma\right)^2+\left(y-nb\right)^2+\left(z+r_0\cos\sigma+v_c\right)^2}\end{cases} \tag{3.11}$$

By defining $B=b/r_0$, Eq. (3.11) can be rewritten as follow:

$$\begin{cases} \Theta_{mr,c} = \dfrac{1}{4\pi}\sum_{n=0}^{N-1}\int_0^{2\pi} \dfrac{1}{R_+} erfc(\dfrac{R_{n+}}{\sqrt{4Fo}}) - \dfrac{1}{R_-} erfc(\dfrac{R_{n-}}{\sqrt{4Fo}})\ d\sigma \\ R_{n+} = \sqrt{\left(X - \sin\sigma\right)^2 + \left(Y - nB\right)^2 + \left(Z - \cos\sigma - V\right)^2} \\ R_{n-} = \sqrt{\left(X - \sin\sigma\right)^2 + \left(Y - nB\right)^2 + \left(Z + \cos\sigma + V\right)^2} \end{cases} \tag{3.12}$$

3.2.3 Solution of surface boundary

It is well known that the temperature of the ground surface changes periodically during the whole year and this temperature change has a great impact on the operation of the horizontal heat exchangers (Sanaye & Niroomand, 2010). Therefore, it is essential to take the boundary influence into consideration when estimating the heat transfer performance. Based on the Green's function theory, the solution of the surface boundary can be obtained from the derivative of the Eq. (3.7):

$$\frac{\partial G_{sin}}{\partial z'}\Big|_{z'=0} = \frac{z}{8\left(\pi\right)^{3/2}\left[\alpha\left(t-\tau\right)\right]^{5/2}} \exp\left[-\frac{\left(x-x'\right)^2 + \left(y-y'\right)^2 + z^2}{4\alpha\left(t-\tau\right)}\right] \tag{3.13}$$

The temperature solution of the boundary condition will then, be obtained by computing the integral of the ground surface:

$$\begin{aligned} \theta_{b,c}(x,y,z,t) &= -\alpha\int_{\tau=0}^{t}\sum_{j=1}^{s}\int_{S_j} f_j\left(\mathbf{r}_j^{'},\tau\right)\frac{\partial G}{\partial n_j^{'}}\Big|_{r'=r_j^{'}} ds_j^{'} d\tau \\ &= \alpha\int_{\tau=0}^{t}\int_{-\infty}^{\infty}\int_{-\infty}^{\infty} f\left(\tau\right)\frac{z}{8\left(\pi\right)^{3/2}\left[\alpha\left(t-\tau\right)\right]^{5/2}}\exp\left[-\frac{z^2 + \left(y-y'\right)^2 + \left(x-x'\right)^2}{4\alpha\left(t-\tau\right)}\right] dy'dx'd\tau \\ &= \alpha\int_{\tau=0}^{t} f\left(\tau\right)\frac{z}{2\sqrt{\pi}\left[\alpha\left(t-\tau\right)\right]^{3/2}}\exp\left[\frac{-z^2}{4\alpha\left(t-\tau\right)}\right] d\tau \end{aligned} \tag{3.14}$$

Assuming the surface temperature conforming to the rule of sine function,

$f\left(\tau\right)=A\cdot\sin(\omega t+\varepsilon)$, this boundary solution can be solved by Laplace method (H.S. CARSLAW):

$$\begin{aligned}\theta_{b,c}(z,t) &= A\cdot\exp(-z\sqrt{\frac{\omega}{2\alpha}})\cdot\sin(\omega t+\varepsilon-z\sqrt{\frac{\omega}{2\alpha}}) \\ &+\frac{2\alpha A}{\pi}\int_0^{\infty}\frac{\omega\cos(\varepsilon)-\alpha\mu^2\sin(\varepsilon)}{\omega^2+\alpha^2\mu^4}\exp(-\alpha\mu^2 t)\sin(\mu z)\mu d\mu\end{aligned} \tag{3.15}$$

The boundary solution independents with *x* and *y*, and only related to the depth of the observation point. In Eq.(3.15), the second term caused by the uniform initial temperature dies away as time increases, leaving the steady fluctuation of the period $2\pi/\omega$.

3.3 Numerical and Experimental Validation

Both numerical and experimental methods were used to validate the new horizontal ring-coil model. The experimental method is reliable but hard to monitor the temperature response of every point in the heat transfer medium. Besides, collecting long-term operation data always takes several years. Thus, to save the time cost, a numerical model is established.

3.3.1 On-site experiment

The test rig was established based on a solar-hybrid GCHP system on the campus of Shandong Jianzhu University, China in 2012. The system mainly consists of a water-refrigerant heat pump unit, GHEs, solar collectors of 12 m^2, a thermal storage tank with 800 liters and a data collection system. There are two typical GHE systems, i.e. vertical GHEs with 12 boreholes and a vertical spiral HGHE. For the spiral heat exchanger, the dimensions of the spiral radius and the spiral pitch are the same as 0.4m. The horizontal heat exchanger is buried in a 12m-long trench with the depth of 2.0m. The buried tubes are high-density polyethylene pipe with an outer diameter of 32mm. The experiment was carried out on 8th Jun 2015.

The performance of the spiral HGHEs was monitored by a data collection system. As shown in Figure 3-5, three temperature sensors (Pt100) were installed at the pipes wall to measure the temperatures at the inlet, the middle point and the outlet of the heat exchanger. Additionally, in the ground soil, a temperature sensor was installed 1m below the ground surface at the central of the trench. All the Pt100 sensors have an accuracy of ±0.1℃. The water flow rate was measured by a flow meter, whose flow range is within 0.2-2 m^3/h, and the flow meter has been calibrated by the manufacturer to ±0.5% of full scale.

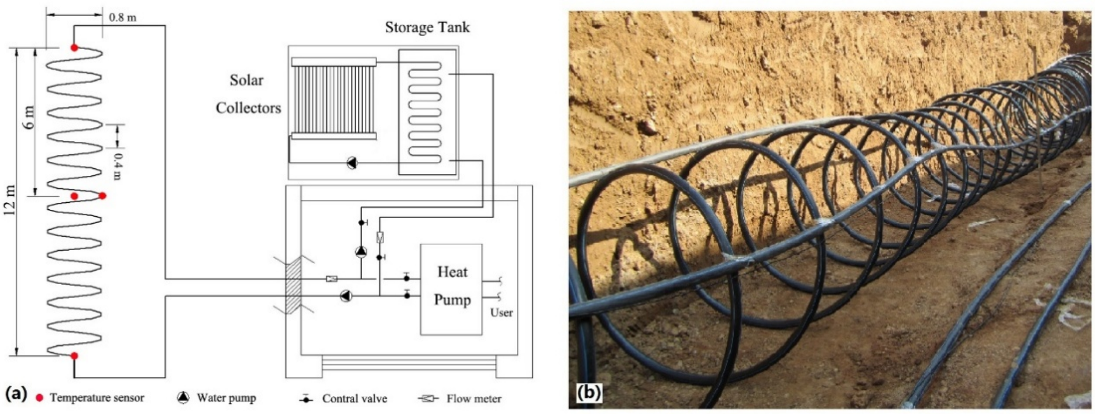

Figure 3-5 (a) Schematic representation of the experiment and (b) a photo of the on-site spiral heat exchanger

3.3.2 3-D simulation model

As the numerical model is hard to fully model the transient heat transfer process of the HGHEs, simplifying assumptions are necessary before establishing the numerical model. Similar to the simplification in the analytical model, the ground is regarded as a homogeneous medium, and its thermal properties are independent of temperature. Table 3.1 shows the main parameters used in the simulation model. Additionally, for numerical simulation, a large finite domain was established to represent the semi-infinite ground. The dimensions of this finite domain should be sufficient to ensure that the heat exchanger has no thermal influence on the domain boundary within the concerned time.

Table 3.1 Physical properties used in the numerical model for model validation

Parameters	Unit	Soil	Water
Density, ρ	Kg m^{-3}	3125	998
Heat capacity, c	J kg^{-1} K^{-1}	800	4182
Thermal conductivity, k	W m^{-1} K^{-1}	2.5	0.6069

As shown in Figure 3-6 (a), the calculation domain for this simulation was regarded as a parallelepiped of 32m (length) × 15m (width) × 9m (depth). The spiral heat exchanger simulated here is a circular pipe with 25.3-m-long. The spiral radius and pitch of this spiral heat exchanger are assumed to be 0.4m. In order to validate the boundary solution, the temperature of the ground surface is expressed as a sinusoidal function:

$$\theta_b = 15 \cdot \sin\left(\frac{2\pi}{365 \times 24 \times 3600} t + 0.47\pi\right) \tag{3.16}$$

Except for the boundary of the ground surface, all the other boundary conditions are thermally insulated. The heat transfer process between the circulating water and the surrounding soil is simplified as a heat conduction process with a line source discharging heat along the spiral heat exchanger.

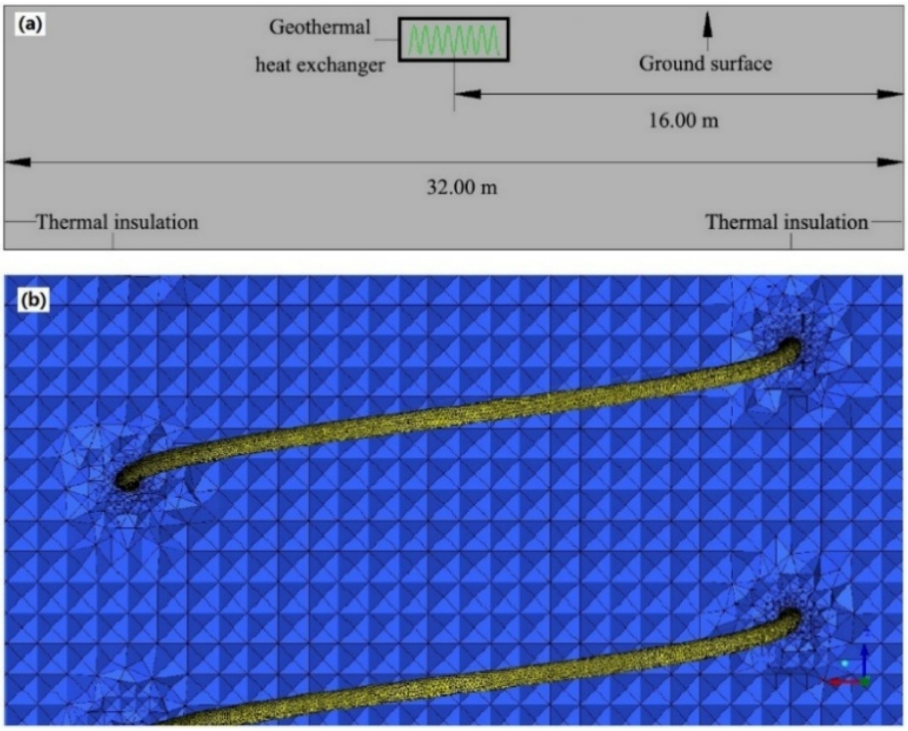

Figure 3-6 (a) Schematic representation of the simulation and (b) magnification of the mesh adjacent to the heat exchanger

This heat transfer problem is solved with the commercial code, ANSYS CFX. It uses a unique hybrid finite-element/finite-volume approach to discretizing Navier-Stokes equations. As a finite volume method, it satisfies strict global conservation by enforcing local conservation over control volumes that are constructed around each mesh vertex or node.

ICEM is used to generate the 3D mesh. The dense mesh is applied near the heat exchange wall and the relatively loose mesh is used to the ground domain. 16,685,436 tetrahedral meshes are created in this simulation model. It has been checked that the numerical calculation results are independent with the grid-size, as shown in Figure 3-7.

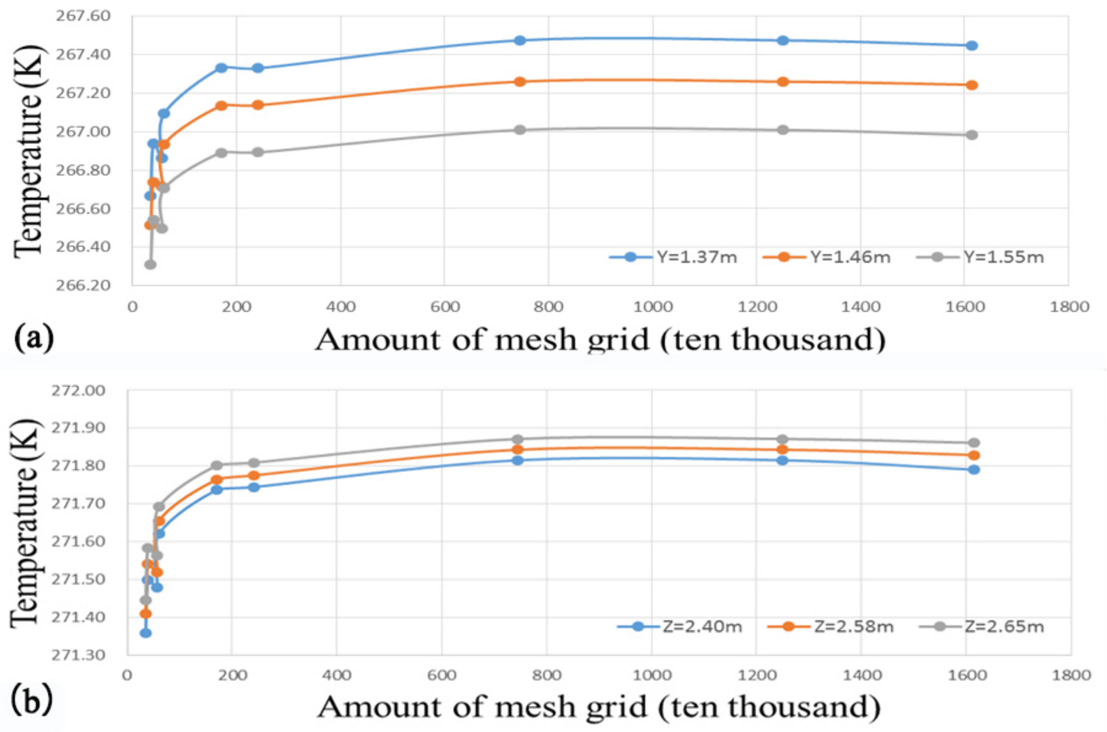

Figure 3-7 Grid independence analysis of horizontal heat exchanger.

3.4 Comparisons and Discussion

3.4.1 Comparisons of the new ring-coils source model and on-site experiment

The tested heat transfer rates of the horizontal ring-coils heat exchanger are given in Figure 3-8. As shown in this figure, the heat injection curve dropped to zero several times during the operation time. The first two times were caused by the manual intervention, and the others were controlled by the system which should be the consequence of cooling demand decreasing. However, it should point out that the injection rate, calculated by the water flux and the temperature difference between inlet and outlet of the heat exchanger, cannot accurately represent the real heat transfer process. For example, when the circulation pump was shut down, the water flux became zero, so the measured injection rate became zero. But, in the reality, the high heat capacity of water makes the heat exchanger continuously release heat into the ground after the circulation pump shut down until the temperature of the water was the same as the one of surrounding ground. The measured heat injection rate fluctuated greatly with the operation time, which requires a lot of discrete points to simulate it fully. Thus, to save the calculation time, a series of average heat pulses by taking an average in every ten minutes, was applied in the predicted calculation.

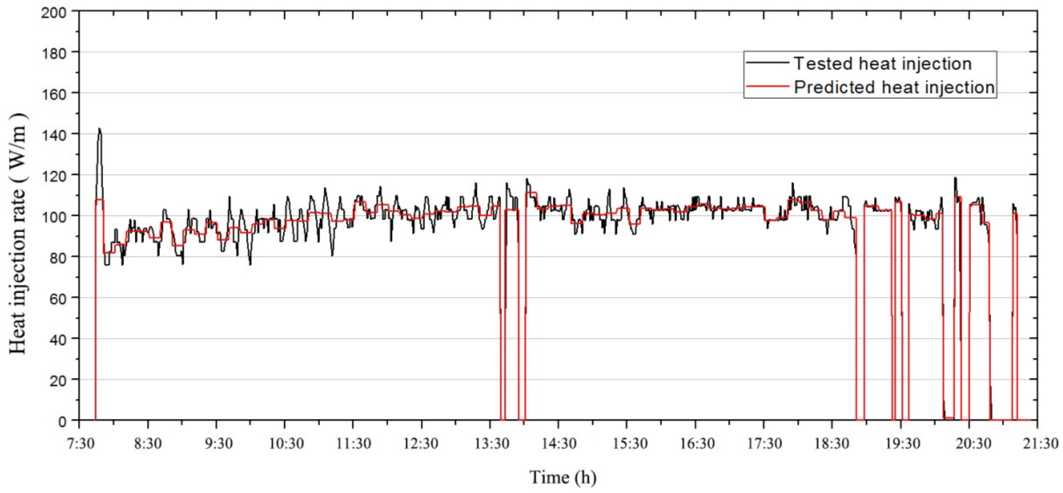

Figure 3-8 Illustration of the heat injection rate during the cooling operation

Figure 3-9 illustrates the comparisons between the predicted and measured pipe wall temperatures at the middle monitoring point. It can be seen from this figure, besides a large relative error at the beginning, the general variation trends of the experimental and analytical models agree well during the operating time. The relative error is defined in Eq.(3.17) to better analyse the difference between these two methods.

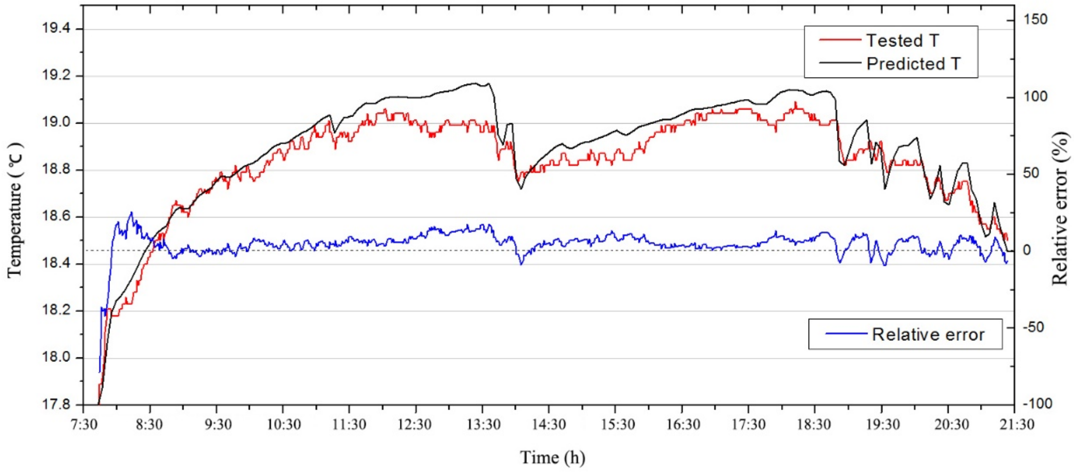

Figure 3-9 Soil temperature determined by experiment test and analytical calculation

$$\text{Relative error} = \frac{\text{Analytical value - Experimental value}}{\text{Experimental value - Initial value}} \tag{3.17}$$

It can be seen that, from Figure 3-9, the maximum relative error is less than 25% after the initiative period, which may be acceptable for the practical engineering. The temperature rise calculated from these two methods shows a small difference at the beginning of the test case, from 7:30 a.m. to 11:30 a.m. After that, an obvious difference occurs in the time period between 11:30 a.m. and 13:30 p.m. The analytical results increase continuously while the measured temperature decreases slightly during this operation time. Generally, under a uniform thermal excitation of the heat source, the temperature should keep growing until the heat transfer process becomes stable. The heat transfer process usually takes a long-time to approach the stable stage, so, obviously, the temperature of the pipe wall should increase during this short operation time, as presented by analytical results. According to the meteorological records, there was a shower rain in the night before the field test. Thus, a possible interpretation of the experimental results is that a part of heat energy was taken away by the rainwater infiltration. The temperature rise may be prevented by the rainwater infiltration. Additionally, compared with the measured data, the analytical value of the temperature rise on the pipe wall fluctuated more sharply when the heat injection rate was unstable. This can be observed between 18:30 p.m. to 21:30 p.m. This is due to the assumption of the line source in the centre of the heat exchanger pipe, which neglects the physical size and specific heat of the circulating water.

3.4.2 Comparisons of the new analytical model and the proposed numerical model

In order to determine the long-term performance of this new ring-coils model, a comparison is conducted between the numerical model and the vertical ring-coils source model. Taking an example of N=8 and maintaining the ground surface temperature at zero, the pipe wall temperatures located at the middle of vertical spiral HGHEs are illustrated in Figure 3-10. These representative temperature rise obtained from the numerical and analytical methods. It can be seen that the analytical results (A-N8) agree perfectly with the numerical results (N-N8). After a rapid growth, the temperature begins to stabilize. Obviously, compared with the shorter horizontal heat exchanger (A-N1), the longer one (A-N32) takes less time to reach the steady-state. But, in this case, when the number of ring-coils is larger than 40, the influence of the pipe length becomes insignificant.

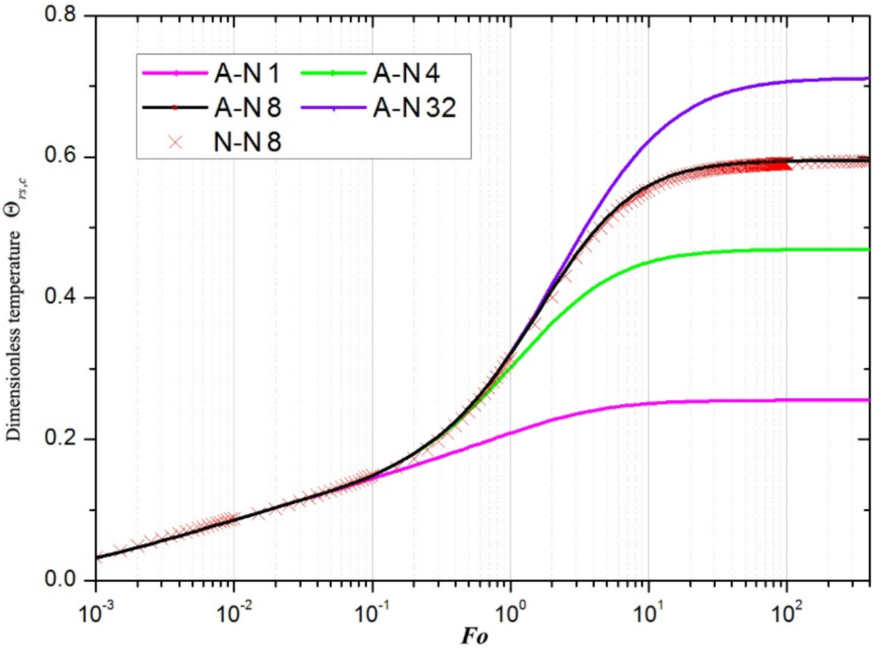

Figure 3-10 Variations of dimensionless temperature responses calculated by analytical and numerical methods with *Fo* with different numbers of coils

The temperature rise under sinusoidal surface temperature (N-Sinusoidal BC) is also calculated and plotted in Figure 3-11. Compared with the results from the case of zero surface temperature, the temperature response is greatly changed by the sinusoidal surface temperature. The temperature becomes steady after a few days for the case of zero surface temperature, but the pipe temperature fluctuates significantly for the case with sinusoidal surface temperature. The analytical solution is matched well with the numerical one, which means that the boundary solution is reliable.

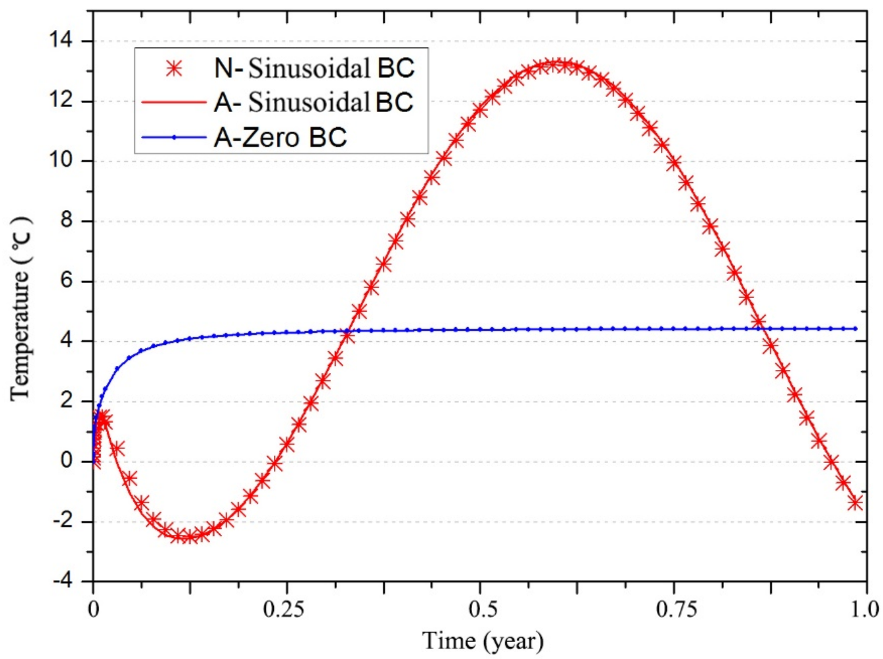

Figure 3-11 Temperature response calculated by analytical and numerical method with sinusoidal surface temperature

For the horizontal heat exchanger with N=8, the temperature responses on the middle pipe wall along the axis direction with different instants are calculated and plotted in Figure 3-12. As shown in this figure, for the case of Fo=1, the analytical and the numerical results agree well with each other. Eight peak values are located at each ring coil. For a long-term operation, the temperature at the centre of the spiral heat exchanger is remarkably higher than those at top and bottom. Additionally, the structure simplification of the spiral heat exchanger becomes obvious when the Fourier number is large. The temperature rise calculated from the analytical model is lower than the simulation results at the top of the heat exchanger but higher at the bottom. Even though the analytical results show little difference with the numerical one in long-term operation, the relative error is quite small.

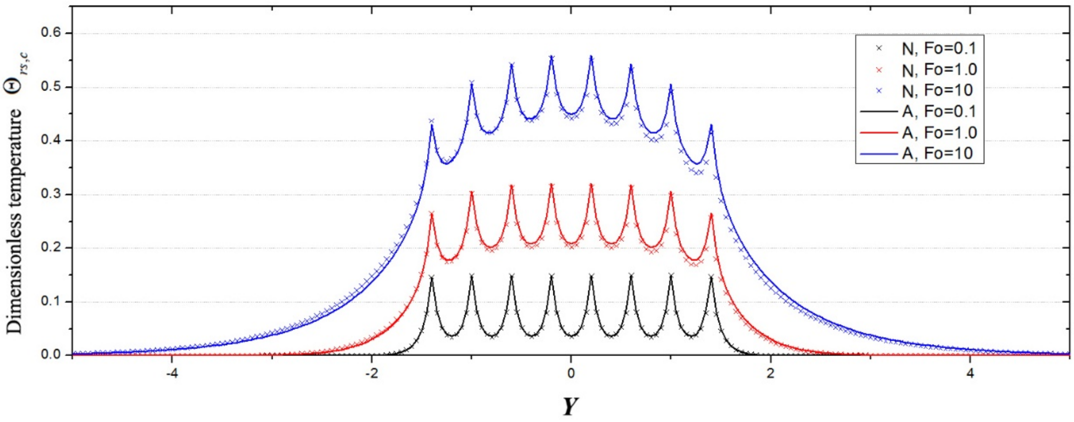

Figure 3-12 Temperature profiles along the axial direction with different *Fo*

3.4.3 Comparisons of the new analytical model with different boundary conditions

Taking a simple heat transfer design case for example, different boundary conditions, constant temperature, and sinusoidal temperature are applied to the ground surface. It assumed that the heat pump operates in the cooling mode in the first three months, and the heat exchanger injects heat energy into the ground soil. The heat flow of the ring-coils source is assumed to be 50W per ring. Then, the system stops working in the next three months. After this recovery period, the heat exchanger extracts the heat from the ground to warm the indoor room. The heat extraction rate is considered as the same as the heat injection rate. After heating operation for three months, the system enters the next recovery period. According to the climatic data recorded in the year of 2014 by a meteorological station located in Jinan, China (latitude 36° 40′ north and longitude 117° 00′ east), a sinusoidal changed temperature was applied to the ground surface.

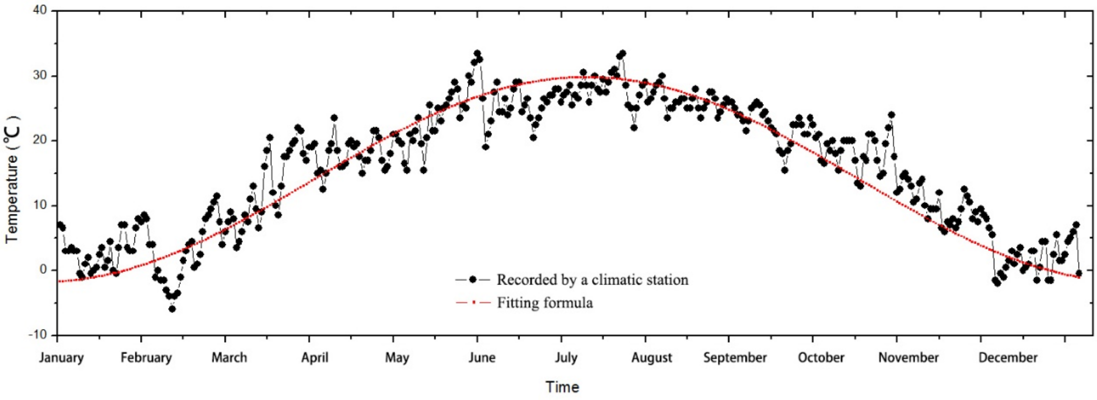

Figure 3-13 Annual climatic data, recorded by the climatic station, used as boundary conditions in the simulations

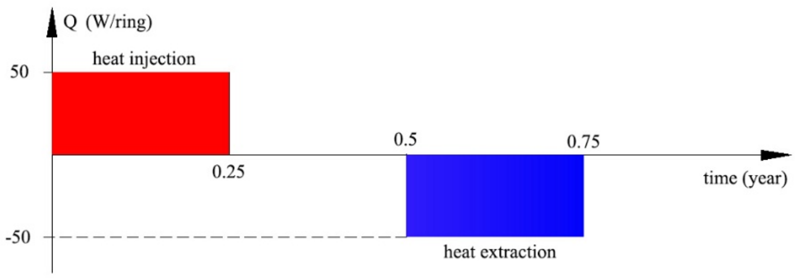

Figure 3-14 Illustration of the heat injection and extraction in one year

As shown in Figure 3-15, five points, at different depths below the ground surface, are selected to monitor the ground temperature variation during the heat injection/extraction of the spiral heat exchanger. These points are along the ground depth and passes through the centre of the fourth ring-coil.

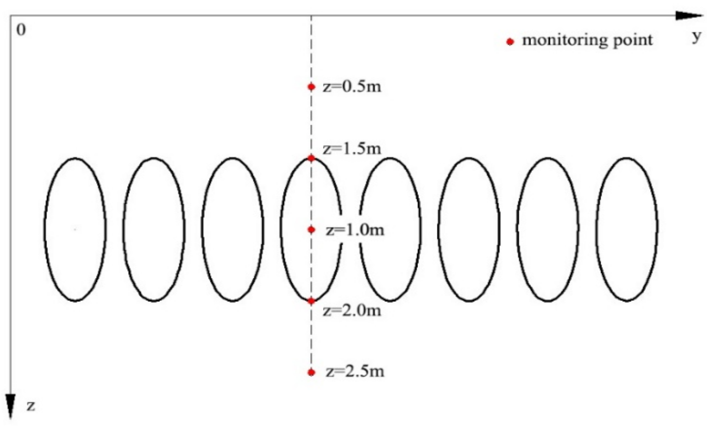

Figure 3-15 Arrangement of monitoring points and the vertical heat exchanger.

Figure 3-16 shows the ground temperature profile under sinusoidal surface temperature but without heat source influence. Clearly, the ground temperature variation shows the feature of periodic changes, and the delayed effects can be easily observed with the depth increase. In addition, the point closer to the ground surface is more susceptible to the periodic temperature.

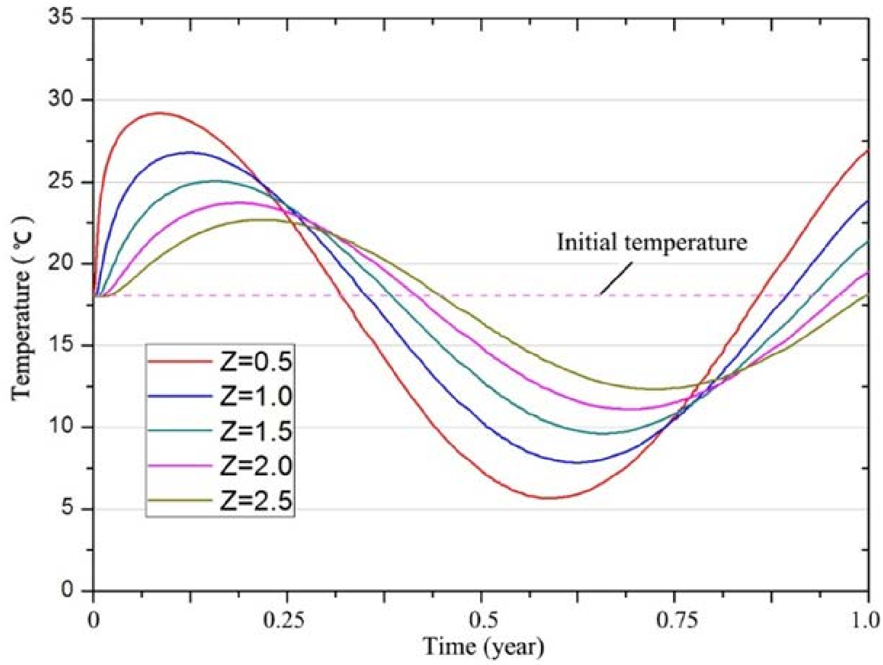

Figure 3-16 Soil temperature variation at different depths under periodically changed ground temperature without heat source influence.

By using the Eq.(3.10), the temperature rises with a constant surface temperature are calculated and plotted in Figure 3-17. As seen from this figure, in the heat injection stage, soil temperature increases rapidly from the initial temperature. Influenced by the boundary of constant temperature, the point near the ground surface easily becomes stable during the operation period. When the cooling operation ends, the ground temperature recovers gradually and the ground temperatures of all the points recover to the initial temperature at the end of the recovery stage. Then, in the following heating season and its recovery period, because the heat transfer energy is same but in different directions, the trend of the temperature curve shows symmetrical distribution along *Y* axis with the value equal to the constant boundary temperature. It indicated that if the surface temperature unchanged during the operation, the heat pump, which not only provides cooling but also generates heating, can operate well in the whole year.

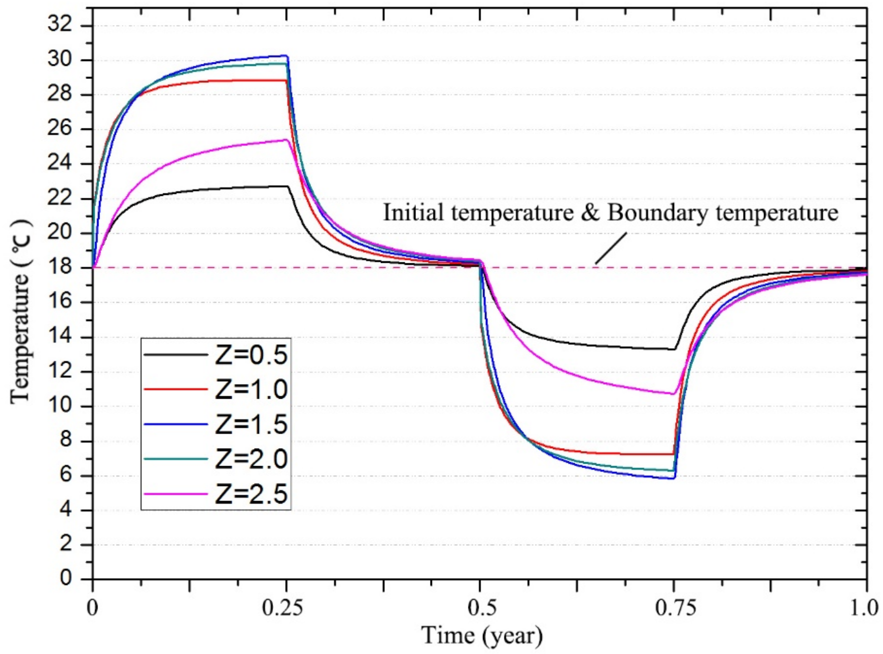

Figure 3-17 Soil temperature variation at different depths under constant ground temperature with heat injection/extraction.

Figure 3-18 illustrates the temperature profile in different monitoring points by considering both the sinusoidal surface temperature and the season changed heat transfer condition. Obviously, the surface temperature greatly affects the temperature response of ground soil. Since the temperature of ground surface is much higher in the first three months, the ground temperature increases faster than those in Figure 3-17.

Additionally, the temperature drops significantly in the heating operation season, and goes below zero in the medium-term in this season. The water cannot be used as circulating fluid in such medium-term season. The original heat transfer design is hard to achieve under such local meteorological conditions, which means that the system may need more heat exchangers to meet the design requirement or the heating demand needs to be reduced to ensure the system can operate normally.

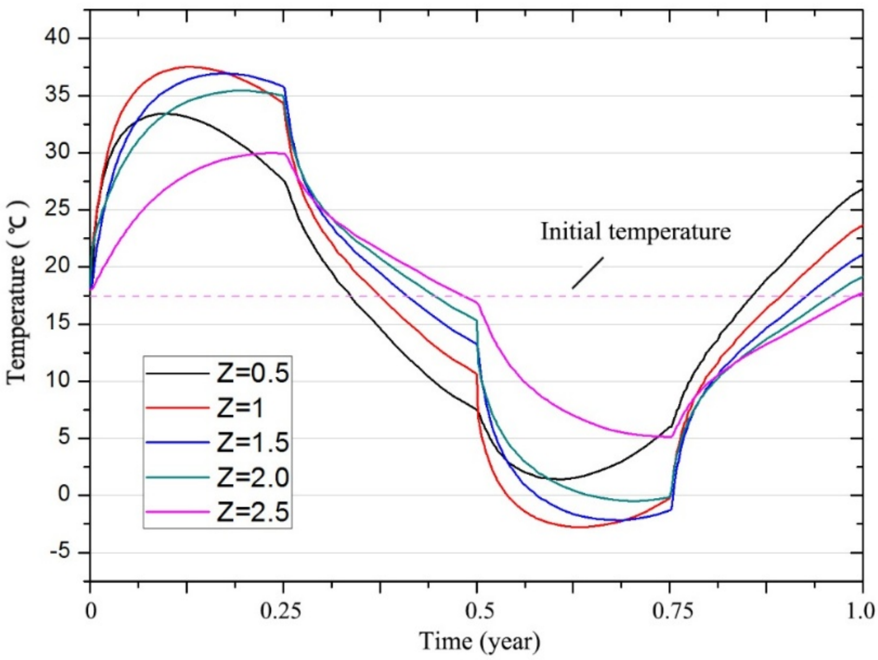

Figure 3-18 Soil temperature variation at different depths under periodically changed ground temperature with heat injection/extraction

Based on these calculation results, it can be seen that the surface temperature has a significant effect on the heat transfer performance of the horizontal heat exchangers and then influences the system efficiency of GCHP. The annual variation of the local ground surface temperature should be fully considered in designing the horizontal spiral heat exchangers.

3.5 Summary

As the configuration features of HGHE with spiral-tubes lead to the invalidation of the traditional analytical mode, the new analytical model, ring source model, becomes an irreplaceable solution in describing the heat transfer process of HGHE with spiral-tubes. In this new model, the ground is regarded as a semi-infinite medium, and a sinusoidal changed boundary condition is applied on the ground surface. A good agreement was shown in the comparisons between the results obtained from the field test and the proposed model, and the new analytical model was further validated by the numerical simulation.

By applying this new model, two different ground surface conditions (constant temperature and sinusoidal surface temperature) were calculated and discussed. The results indicated that the surface temperature can directly influence the heat transfer performance of the horizontal heat exchangers, which should be fully considered in the system design. As the proposed analytical model successfully takes the annual variation of surface temperature into consideration, this new model should be a great aid to the engineers in designing and optimizing the size or arrangement of the horizontal geothermal heat exchangers with vertical spiral coils.

Except the application in horizontal GCHP systems, the spiral-tubes is also applied in pile geothermal heat exchangers. The next chapter will focus on the heat transfer modelling of PGHE with spiral-tubes.

CHAPTER 4

HEAT TRANSFER MODEL DEVELOPMENT FOR PGHE WITH SPIRAL COILS

4.1 Introduction

As discussed in the literature review in chapter 2, the spiral-tubes, in addition to being applied in horizontal GHEs, can also be widely used in pile GHE systems, which is regarded as an optimal solution for vertical GHE system for its less installation costs and less installation area. Although many investigations have been conducted to model the heat transfer process of PGHE, especially for PGHE with spiral-tubes, the previous models were developed by assuming the thermal properties of pile and soil being the same. Thus, large error always exists for the long-term operation estimation. The heat transfer investigation in composite medium is also limited. Therefore, it is necessary to propose a new analytical solution which can fully represent the inhomogeneity of thermal properties and consider the configuration features of PGHE with spiral-tubes.

In this chapter, a new transient analytical model, composite ring source model, has been established for accurately modelling the PGHE with spiral-tubes. Similar to the ring-coil source model, the spiral-tube is simplified as a series of coils capturing/releasing heat energy into a semi-infinite medium. By applying this new model, the temperature response either in pile or soil can be easily and accurately obtained. To verify this new model, the calculated temperature results were compared with those from a 3-D numerical simulation model.

4.2 Development of the New Ring-coils Source Model in Composite Solids

For the PGHE with spiral-tubes, the geometry of a spiral pipe is quite difficult to be described accurately in mathematical terms and hence, similar to the ring-coils source model (P. Cui et al., 2011), the spiral heat exchanger in this new model is simplified as a series of separated ring-coils stretching from depth h_1 to depth h_2.

$$\theta_r = \frac{bq_{ring}}{8\rho c_p \pi^{3/2}} \int_0^{\tau} \frac{1}{\left[\alpha\left(\tau - \tau'\right)\right]^{3/2}} I_0\left[\frac{rr_0}{2\alpha\left(\tau - \tau'\right)}\right] \times \exp\left[-\frac{r^2 + r_0^2}{4\alpha\left(\tau - \tau'\right)}\right] \\ \times \sum_{n=0}^{N-1}\left\{\exp\left[-\frac{\left(z - h_1 - nb - 0.5b\right)^2}{4\alpha\left(\tau - \tau'\right)}\right] - \exp\left[-\frac{\left(z + h_1 + nb + 0.5b\right)^2}{4\alpha\left(\tau - \tau'\right)}\right]\right\} d\tau' \tag{4.1}$$

To investigate the heat transfer around buried coils in composite medium, the Green's function was employed (H. Carslaw et al., 1962). The derivation of the 2-D Green's function solution equation (GFSE), with the auxiliary boundary value problem for Green's function (GF) that corresponds to the PGHE problem, can be simplified as two one-dimensional GFs (Beck, 1984, 1986; Cole et al., 2010). For ring-coil source models in a homogeneous medium, its solution, Eq.(4.1), can be rewritten as the GFSE expression.

$$\begin{aligned} \theta_{ring} &= \frac{\alpha}{k} \int_0^{\infty} \int_0^{\infty} \int_0^{\tau} 2\pi r' G_{rz}\left(r, z, t \middle| r', z', \tau\right) g\left(r', z', \tau\right) d\tau' dr' dz' \\ g\left(r', z', \tau\right) &= \frac{q_{ring}^{i}}{2\pi r_0} \delta\left(\tau - \tau_0\right) \delta\left(r' - r_0\right) \sum_{n=0}^{N-1} \delta\left(z' - nb - 0.5b\right) \end{aligned} \tag{4.2}$$

where N equals the number of ring-coils, N = int [(h_2-h_1)/b] and the GF can be broken down into:

$$G_{rz}\left(r,z,t\middle|r',z',\tau\right)=G_r\left(r,t\middle|r',\tau\right)G_z\left(z,t\middle|z',\tau\right) \tag{4.3}$$

$$G_r\left(r,t\middle|r',\tau\right)=\frac{1}{4\pi\alpha\left(\tau-\tau'\right)}\times I_0\left[\frac{rr'}{2\alpha\left(\tau-\tau'\right)}\right]\times\exp\left[-\frac{r^2+r'^2}{4\alpha\left(\tau-\tau'\right)}\right] \tag{4.4}$$

$$G_z\left(z,t\middle|z',\tau\right)=\frac{1}{\sqrt{4\pi\alpha\left(\tau-\tau'\right)}}\times\left\{\exp\left[-\frac{\left(z-z'\right)^2}{4\alpha\left(\tau-\tau'\right)}\right]-\exp\left[-\frac{\left(z+z'\right)^2}{4\alpha\left(\tau-\tau'\right)}\right]\right\} \tag{4.5}$$

Similarly, this method was applied to derive the GFSE for a composite medium. Firstly, the GFSEs of the composite medium in the ***R*** and ***Z*** directions are established, respectively. Based on these one-dimensional GFSEs, two analytical models are then, established to simulate the heat transfer process of the PGHE with spiral-tube in a composite medium.

4.2.1 Cylindrical-surface (*R*) source in composite media

The temperature response due to an unit instantaneous infinite line source in a composite region has been solved by Jaeger (1944). This instantaneous line source initially releases heat into a composite solid at zero temperature. It assumes that this composite solid consists of two regions: one is the region $0\le r<l_r$, in which the unit instantaneous heat release source is located along the line (r', θ') and the other is the outer region, when $l_r<r$, where the thermal property is different from that of the inner region. The governing equation of this two-dimensional heat conduction problem is expressed in cylindrical coordinates as:

$$\frac{1}{\alpha_1}\frac{\partial T_{r1}}{\partial t}=\frac{\partial^2 T_{r1}}{\partial r^2}+\frac{1}{r}\frac{\partial T_{r1}}{\partial r}+\frac{1}{r^2}\frac{\partial^2 T_{r1}}{\partial \theta^2}+\frac{g(r,\theta,t)}{k_1} \qquad \text{for } 0 \le r < l_r,\ 0 \le \theta < 2\pi,\ 0 < t$$

$$\frac{1}{\alpha_2}\frac{\partial T_{r2}}{\partial t}=\frac{\partial^2 T_{r2}}{\partial r^2}+\frac{1}{r}\frac{\partial T_{r2}}{\partial r}+\frac{1}{r^2}\frac{\partial^2 T_{r2}}{\partial \theta^2} \qquad \text{for } l_r < r < +\infty,\ 0 \le \theta < 2\pi,\ 0 < t$$

$$T \to 0 \qquad \text{for r} \to +\infty, 0 \le \theta < 2\pi,\ 0 < t$$

$$\frac{\partial T}{\partial r} \to 0 \qquad \text{for } r = 0,\ 0 \le \theta < 2\pi,\ 0 < t$$

$$T\Big|_{t=0} = 0 \qquad \text{for } 0 \le r < +\infty,\ 0 \le \theta < 2\pi,\ 0 < t$$

(4.6)

Thus, the temperature response in cylindrical coordinates is obtained by the Laplace transform method. The thermal conductivity, density and specific heat of the region $0 \le r < l_r$ are defined as k_1, ρ_1 and c_1, respectively. Similarly, k_2, ρ_2 and c_2 are the thermal parameters for $l_r < r$. The solutions are given below (Jaeger, 1944):

$$T_{in}(r,r',\theta,\theta',t,\tau)= \frac{1}{2\pi}\sum_{n=-\infty}^{\infty}\cos n\left(\theta-\theta'\right)\int_0^{\infty} e^{-\alpha_1 u^2 (t-\tau)} \frac{J_n(ur)J_n(ur')\left[R_{\phi,n}R_{g,n} - R_{\psi,n}R_{f,n}\right]u}{R_{\phi,n}{}^2 + R_{\psi,n}{}^2} du$$

(4.7)

$$T_{out}(r,r',\theta,\theta',t,\tau)= \frac{1}{\pi^2 l_r}\sum_{n=-\infty}^{\infty}\cos n\left(\theta-\theta'\right)\int_0^{\infty} e^{-\alpha_1 u^2 (t-\tau)} \frac{J_n(ur')\left[R_{\psi,n}J_n(aur) - R_{\phi,n}Y_n(aur)\right]}{R_{\phi,n}{}^2 + R_{\psi,n}{}^2} du$$

(4.8)

where:

$$R_{\phi,n} = aKJ_n(l_r u)J_n'(al_r u) - J_n'(l_r u)J_n(al_r u); \qquad R_{\psi,n} = aKJ_n(l_r u)Y_n'(al_r u) - J_n'(l_r u)Y_n(al_r u)$$

$$R_{f,n} = aKY_n(l_r u)J_n'(al_r u) - Y_n'(l_r u)J_n(al_r u); \qquad R_{g,n} = aKY_n(l_r u)Y_n'(al_r u) - Y_n'(l_r u)Y_n(al_r u)$$

$$a = \sqrt{\alpha_1 / \alpha_2} \ ; \ K = k_2 / k_1$$

The continuous cylindrical surface heat source solution can be obtained by integrating the line source equation from 0 to 2π into the azimuth direction (M. Li & Lai, 2012) over the time from 0 to *t*:

$$\begin{aligned} T_{in}(r,r') &= \frac{q_r \alpha_1}{2\pi k_1} \int_0^t \int_0^{2\pi} T_{in}(r,r',\theta,\theta',t,\tau) \, d\tau d\theta \\ T_{out}(r,r') &= \frac{q_r \alpha_1}{2\pi k_1} \int_0^t \int_0^{2\pi} T_{out}(r,r',\theta,\theta',t,\tau) \, d\tau d\theta \end{aligned} \tag{4.9}$$

Finally, the solution for a continuous infinite cylindrical surface can be written more compactly using the Green's function expression:

$$T_{in}(r,t) = \frac{\alpha_1}{k_1} \int_{\tau=0}^{t} \int_0^{l_r} 2\pi r' G_{r,in}(r,t \,|\, r',\tau) \big|_{\tau=0} \, g\left(r',\tau\right) dr' d\tau$$

$$\text{for } 0 \le r < l_r, \ 0 \le r' < l_r, \ 0 < t \tag{4.10}$$

where the Green's function is defined as:

$$G_{r,in}(r,t \,|\, r',\tau) = \frac{1}{2\pi} \int_0^{\infty} e^{-\alpha_1 u^2 (t-\tau)} \frac{J_0(ur) J_0(ur') \left[R_{\phi,0} R_{g,0} - R_{\psi,0} R_{f,0} \right] u}{R_{\phi,0}{}^2 + R_{\psi,0}{}^2} du \tag{4.11}$$

$$\text{for } 0 \le r < l_r, \ 0 \le r' < l_r, \ 0 < t$$

$$G_{r,\text{out}}(r,t \,|\, r',\tau) = \frac{k_1}{\pi^2 l_r} \int_0^{\infty} e^{-\alpha_1 u^2 (t-\tau)} \frac{J_0(ur') \left[R_{\psi,0} J_0(aur) - R_{\phi,0} Y_0(aur) \right]}{R_{\phi,0}{}^2 + R_{\psi,0}{}^2} du \tag{4.12}$$

$$\text{for } l_r < r < +\infty, \ 0 \le r' < l_r, \ 0 < t$$

4.2.2 Plan-surface source (*Z*) in composite media

Similarly, the unit instantaneous response function for an infinite plan-surface source can also be obtained by the Laplace transfer method assuming the heat source being located at z' in the region of $0 \le z < l_z$ which has conductivity k_1, density ρ_1 and specific heat c_1. The heat source releases heat from zero time into a semi-infinite region with zero initial temperature, as follows:

$$
\begin{aligned}
&\frac{1}{\alpha_1}\frac{\partial T_{z1}}{\partial t} = \frac{\partial^2 T_{z1}}{\partial z^2} + \frac{1}{k_1} g(\mathrm{z},t) && \text{for } 0 \le z < l_z,\ 0 < t \\
&\frac{1}{\alpha_2}\frac{\partial T_{z2}}{\partial t} = \frac{\partial^2 T_{z2}}{\partial z^2} && \text{for } l_z < z < +\infty,\ 0 < t \\
&T = 0 && \text{for } z = 0,\ 0 < t \\
&T \to 0 && \text{for } \mathrm{z} \to +\infty,\ 0 < t \\
&T\big|_{t=0} = 0 && \text{for } 0 \le z < +\infty,\ 0 < t
\end{aligned}
\tag{4.13}
$$

The detailed derivation process is given in Appendix A, and this composite solution can be expressed as:

$$
\begin{aligned}
T_{in}(z,z',t,\tau) = &\frac{1}{\pi}\int_0^\infty e^{-\alpha_1 u^2 t}\cos(uz - uz')du \\
&+\frac{1}{\pi}\int_0^\infty e^{-\alpha_1 u^2 t}\left[\frac{Z_a Z_\psi - Z_b Z_\phi}{Z_\phi{}^2 + Z_\psi{}^2} + (Ka-1)\frac{Z_c Z_\psi + Z_d Z_\phi}{Z_\phi{}^2 + Z_\psi{}^2}\right]du \\
&\qquad \textit{for } 0 \le z < l_z,\ 0 < z' < l_z,\ 0 < t
\end{aligned}
\tag{4.14}
$$

$$
\begin{aligned}
T_{out}(z,z',t,\tau) = &\frac{2}{\pi}\int_0^\infty e^{-\alpha_1 u^2 t}\left\{\frac{\left[Z_e Z_\psi - Z_f Z_\phi\right]}{\left[Z_\phi{}^2 + Z_\psi{}^2\right]}\right\}du \\
&\qquad \textit{for } 0 \le z < l_z,\ 0 < z' < l_z,\ 0 < t
\end{aligned}
\tag{4.15}
$$

where:

$$
\begin{aligned}
Z_a = &\sin(uz)\cos\left(ul_z - uz'\right)\sin\left(aul_z\right) - Ka\sin(uz)\sin\left(ul_z - uz'\right)\cos\left(aul_z\right) \\
&-\cos(uz)\cos\left(ul_z - uz'\right)\cos\left(aul_z\right) - Ka\cos(uz)\sin\left(ul_z - uz'\right)\sin\left(aul_z\right)
\end{aligned};
$$

$$\begin{aligned}Z_b =& \sin(uz)\cos\left(ul_z - uz'\right)\cos\left(aul_z\right) + Ka\sin(uz)\sin\left(ul_z - uz'\right)\sin\left(aul_z\right)\\ &+\cos(uz)\cos\left(ul_z - uz'\right)\sin\left(aul_z\right) - Ka\cos(uz)\sin\left(ul_z - uz'\right)\cos\left(aul_z\right)\end{aligned};$$

$$Z_c = \sin\left(uz\right)\cos\left(ul_z + aul_z\right)\sin\left(uz'\right) - \cos\left(uz\right)\sin\left(ul_z + aul_z\right)\sin\left(uz'\right);$$

$$Z_d = \cos\left(uz\right)\cos\left(ul_z + aul_z\right)\sin\left(uz'\right) + \sin\left(uz\right)\sin\left(ul_z + aul_z\right)\sin\left(uz'\right);$$

$$Z_e = \sin\left(uz'\right)\sin\left(auz\right); \; Z_f = \sin\left(uz'\right)\cos\left(auz\right);$$

$$Z_\phi = \sin\left(aul_z\right)\cos\left(ul_z\right) - Ka\sin\left(ul_z\right)\cos\left(aul_z\right);$$

$$Z_\psi = \cos\left(ul_z\right)\cos\left(aul_z\right) + Ka\sin\left(ul_z\right)\sin\left(aul_z\right);$$

$$a = \sqrt{\frac{\alpha_1}{\alpha_2}}; \; K = \frac{k_2}{k_1}$$

The solution for a continue plan source in the composite materials can then, be rewritten using Green's function expression:

$$T_{in}(z,t) = \frac{\alpha_1}{k_1}\int_{\tau=0}^{t}\int_0^{l_z} G_{z,in}(z,t\left|z',\tau\right)\Big|_{\tau=0}\, g\left(z',\tau\right)dz'd\tau \tag{4.16}$$

$$T_{out}(z,t) = \frac{\alpha_1}{k_1}\int_{\tau=0}^{t}\int_0^{l_z} G_{r,\mathrm{out}}(z,t\left|z',\tau\right)\Big|_{\tau=0}\, g\left(z',\tau\right)dz'd\tau \tag{4.17}$$

where:

$$\begin{aligned}G_{z,in}(z,t\left|z',\tau\right) =& \frac{1}{\pi}\int_0^\infty e^{-\alpha_1 u^2 t}\cos(uz - uz')du\\ &+\frac{1}{\pi}\int_0^\infty e^{-\alpha_1 u^2 t}\left[\frac{Z_a Z_\psi - Z_b Z_\phi}{Z_\phi{}^2 + Z_\psi{}^2} + \left(Ka - 1\right)\frac{Z_c Z_\psi + Z_d Z_\phi}{Z_\phi{}^2 + Z_\psi{}^2}\right]du\end{aligned} \tag{4.18}$$

$$G_{r,\mathrm{out}}(z,t\left|z',\tau\right) = \frac{2}{\pi}\int_0^\infty e^{-\alpha_1 u^2 t}\left\{\frac{\left[Z_e Z_\psi - Z_f Z_\phi\right]}{\left[Z_\phi{}^2 + Z_\psi{}^2\right]}\right\}du \tag{4.19}$$

4.3 Application to the PGHE with Spiral Coils

Based on the Green's function solutions given above, a new ring-coils composite analytical model was established successfully which considered both the discontinuity of the heat source and the difference of thermal properties between the pile and soil. In this section, a numerical model is established to compare and validate the results given by the analytical model. The application of these ring-coil composite models is based on the following assumptions:

5) The medium has a uniform initial temperature, T_0;

6) The ground is considered to be a semi-infinite medium and the temperature of the ground surface is assumed to be unchanged with a fixed value of T_0;

7) No groundwater advection exists around the pile foundation;

8) The ring-coils heat source with its radius of r_0 releases heat energy since the initial time, $t = 0$.

4.3.1 Solution of ring-coils source model in a composite medium

The new composite ring source model simplifies the spiral pipe as a series of separated ring coils, but with composite medium. To consider the effect of different thermal properties in two dimensions, the new GF is established by combining the composite medium GFs in the R and Z directions while maintaining the former assumptions. This solution represents the heat transfer process of a series of separated ring-coils in a special region consisting of four sub-regions, as shown in Figure 4-1 (b).

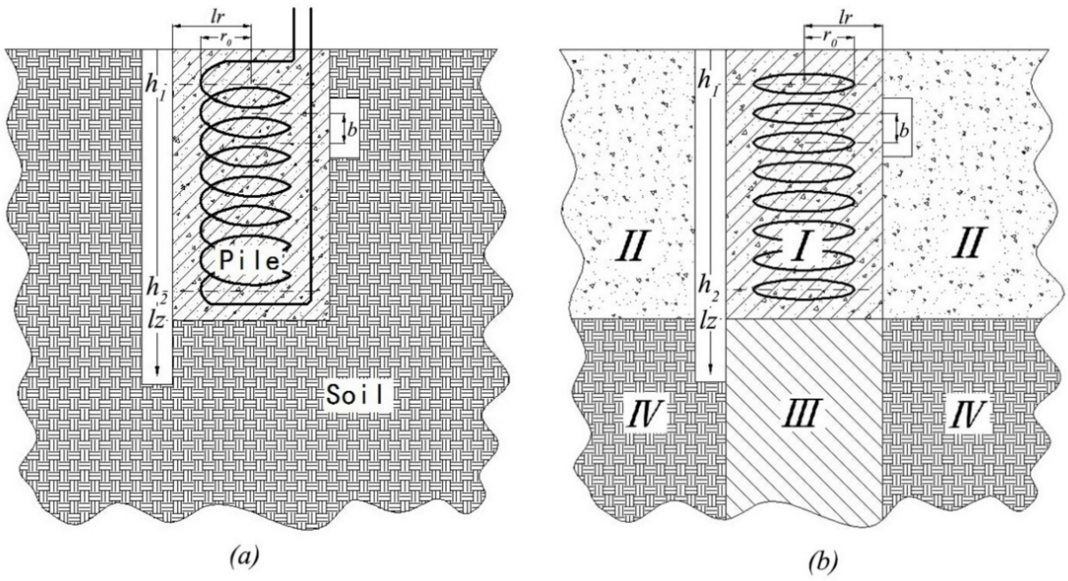

Figure 4-1 Schematic diagram of (a) the PGHE with spiral-tube and (b) the composite ring-coil source model

One sub-region is the foundation pile that has the conductivity k_1, density ρ_1 and specific heat c_1 in region I. The others are three assumed soil regions. Region II has the same thermal properties (k_1, ρ_1, c_1) of the pile in the Z direction, but different peroperties in the R direction (k_2, ρ_2, c_2). The thermal properties of region III are the same as those of the pile in the R direction but differ in the Z direction. Region IV has the soil conductivity of k_2, the density of ρ_2 and specific heat of, c_2 in both R and Z directions. The radius and depth of the pile are assumed to be l_r and l_z, respectively. The item *b* is the pitch of every two adjacent coils along the depth direction of pile. This finite analytical solution can then, be rewritten in cylindrical coordinates:

$$\theta_{crz,i} = \frac{\alpha_1}{k_1}\int_0^\infty \int_0^\infty \int_0^\tau 2\pi r' G_{crz,i}\left(r,z,t\middle|r',z',\tau\right) g\left(r',z',\tau\right) d\tau' dr' dz' \qquad i = \mathrm{I},\ \mathrm{II},\ \mathrm{III}\ \text{and}\ \mathrm{IV}$$

$$g\left(r',z',\tau\right) = \frac{q_l}{2\pi r_0}\delta\left(\tau-\tau_0\right)\delta\left(r'-r_0\right)\sum_{n=0}^{m-1}\delta\left(z'-nb-h_1\right) \tag{4.20}$$

where:

$$G_{crz,\mathrm{I}}\left(r,z,t\middle|r',z',\tau\right) = G_{cr,in}\left(r,t\middle|r',\tau\right)G_{z,in}\left(\mathrm{z},t\middle|z',\tau\right)$$

$$G_{crz,\mathrm{II}}\left(r,z,t\middle|r',z',\tau\right) = G_{cr,out}\left(r,t\middle|r',\tau\right)G_{z,in}\left(\mathrm{z},t\middle|z',\tau\right)$$

$$G_{crz,\mathrm{III}}\left(r,z,t\middle|r',z',\tau\right) = G_{cr,in}\left(r,t\middle|r',\tau\right)G_{z,out}\left(\mathrm{z},t\middle|z',\tau\right)$$

$$G_{crz,\mathrm{IV}}\left(r,z,t\middle|r',z',\tau\right) = G_{cr,out}\left(r,t\middle|r',\tau\right)G_{z,out}\left(\mathrm{z},t\middle|z',\tau\right)$$

$$G_{cr,in}\left(r,t\middle|r',\tau\right) = \frac{1}{2\pi}\int_0^\infty e^{-\alpha_1 u^2 (t-\tau)}\frac{J_0(ur)J_0(ur')\left[R_{\phi,0}R_{g,0}-R_{\psi,0}R_{f,0}\right]u}{R_{\phi,0}{}^2+R_{\psi,0}{}^2}du$$

$$G_{cr,out}\left(r,t\middle|r',\tau\right) = \frac{k_1}{\pi^2 l_r}\int_0^\infty e^{-\alpha_1 u^2 (t-\tau)}\frac{J_0(ur')\left[R_{\psi,0}J_0(aur)-R_{\phi,0}Y_0(aur)\right]}{R_{\phi,0}{}^2+R_{\psi,0}{}^2}du$$

$$G_{z,in}(z,t|z',\tau) = \frac{1}{\pi}\int_0^\infty e^{-\alpha_1 u^2 t}\cos(uz-uz')du + \frac{1}{\pi}\int_0^\infty e^{-\alpha_1 u^2 t}\left[\frac{Z_aZ_\psi - Z_bZ_\phi}{Z_\phi{}^2+Z_\psi{}^2}+\left(Ka-1\right)\frac{Z_cZ_\psi+Z_dZ_\phi}{Z_\phi{}^2+Z_\psi{}^2}\right]du$$

$$G_{r,\mathrm{out}}(z,t|z',\tau)=\frac{2}{\pi}\int_0^\infty e^{-\alpha_1 u^2 t}\left\{\frac{\left[Z_eZ_\psi - Z_fZ_\phi\right]}{\left[Z_\phi{}^2+Z_\psi{}^2\right]}\right\}du$$

4.3.2 Numerical model of PGHE with spiral coils

To validate the new analytical model, a 3-D numerical model was established. This is commonly believed to be a reliable approach to the modelling of complex heat transfer problems with arbitrary geometries in a composite medium. The PGHE with spiral-tube was simulated by a spiral surface heat source, with its radius and screw pitch taken as 1.0m. The radius and depth of the foundation pile were assumed to be 1.5m and 9.0m, respectively. The soil region in the analytical model was assumed semi-infinite, but this is difficult to simulate numerically. The soil, therefore, is simulated by a finite domain, and this soil domain is made sufficiently large to ensure the heat energy released by the heat exchanger cannot reach the soil's outer boundaries. The depth of the soil is assumed to be 20m and the radius of this domain is 10m which is ten times as the radius of the pile. The pile and soil were simulated as solid domains and the heat transfer processes by the partial differential equation (PDE) for heat conduction. After completion of the geometrical process, ANSYS ICEM was used to create the 3-D mesh. A small mesh size was selected in the pile region where the temperature changes dramatically and in a rough mesh in the soil region, as shown in Figure 4-2. The numbers of elements in pile and soil are 3,976,842 and 664,651, respectively. It has been checked that the numerical calculation results are independent with the grid-size, as shown in Figure 4-3. A zero temperature condition was applied to the top surface of the model, and the boundary conditions of the simulation model were set to be the same as for the analytical model. By changing the thermal properties, a series of cases were then computed, and these heat transfer problems were solved using the commercial code ANSYS CFX.

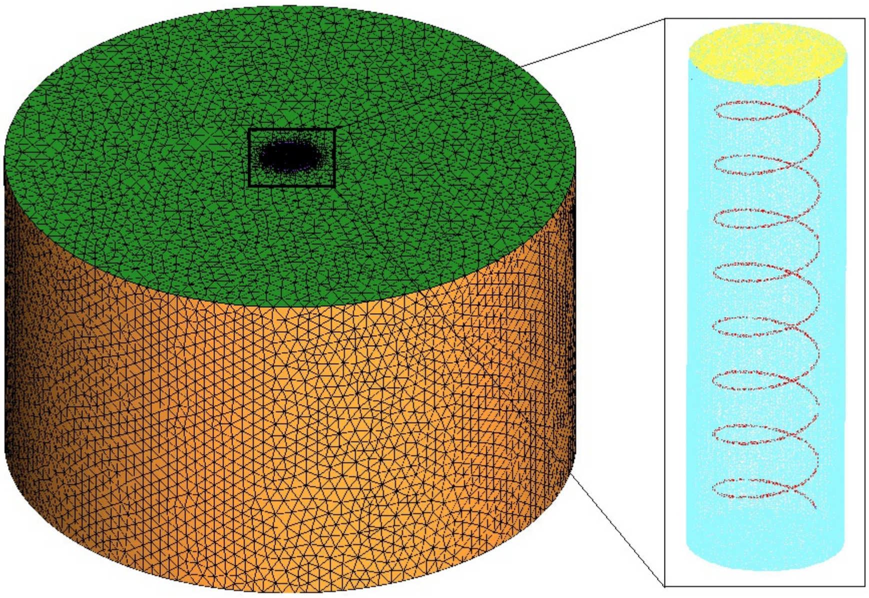

Figure 4-2 3-D meshed model of the PGHE with spiral coils

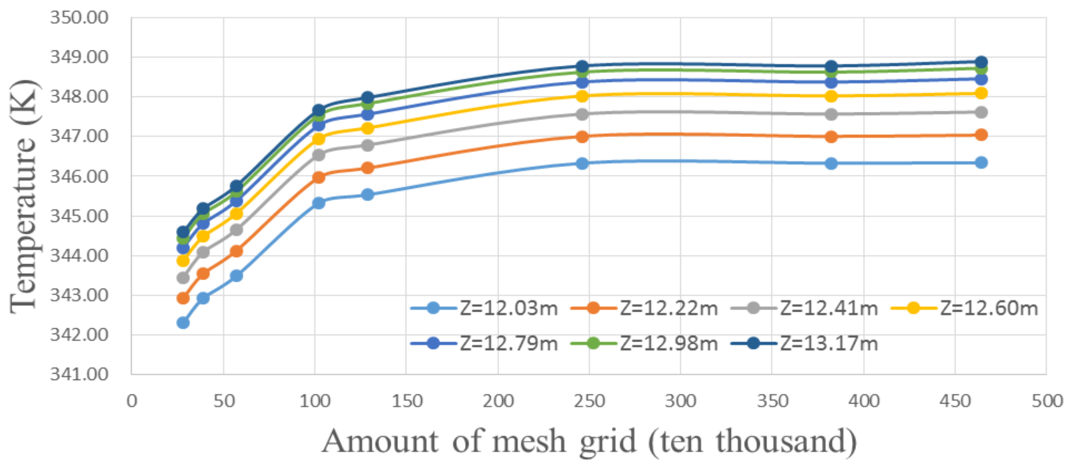

Figure 4-3 Grid independence analysis of pile heat exchanger

4.4 Comparison and Discussion

4.4.1 Analysis of the basic GF for the composite ring-coil source model

Before analyzing the composite ring-coil source model, the basic GFs for a composite medium are compared with the homogeneous GF solution by setting the thermal property factors K and a equal to one. Assuming a single ring-coil heat source located at (r_0, z_0), the temperature response was calculated and summarized in

Table 4.1. As shown in this table, when the calculation domain is a homogeneous medium, the composite medium solutions almost perfectly match the results of the homogenous solution. Taking an example of GF with $r / r_0 = 1$ and $l_r / r_0 = 1.5$, the effect of thermal property difference on GF is then calculated by changing the thermal property factors K and a. To understand the influence of the material difference on thermal diffusivity on GF, K is kept as a constant, $K = k_2 / k_1$, and, a changes from 1.0 to 3.0, $a = \sqrt{\alpha_1 / \alpha_2}$. A similar strategy is used to study the influence of the thermal conductivity by fixing a equal to 1 and increasing K from 0.5 to 2.0. The same settings were employed in the case of GF in the Z direction with $z / z_0 = 1$ and $l_z / z_0 = 1.5$. In this study, the dimensionless time, $Fo = \frac{\alpha t}{r_0^2}$, was introduced, and the temperature responses of the GFs at different times (***Fo***) are computed, as shown in Figure 4-4.

Table 4.1 Comparison of the cylindrical-surface GF and plan-surface GF with K=1 and α =1.

Fo	GF-R Homogenous	GF-R Composite	GF-Z Homogenous	GF-Z Composite
0.001	0.000440	0.000440	0.002766	0.002766
0.005	0.003984	0.003932	0.024844	0.024819
0.010	0.006629	0.006567	0.041374	0.041344
0.050	0.017907	0.017825	0.111120	0.111099
0.100	0.026421	0.026317	0.163377	0.163337
0.500	0.065277	0.065165	0.375419	0.375377
1.000	0.096072	0.095955	0.498904	0.498860
5.000	0.199796	0.199583	0.740742	0.740698
10.00	0.251535	0.251271	0.809472	0.809428
50.00	0.378934	0.378654	0.905446	0.905402
100.0	0.434091	0.433785	0.928644	0.928601

The composite GFs of ***R*** (infinite cylinder source) and ***Z*** (infinite plane source) show different trends with different Fourier numbers. As the GF-***R*** ignores the effect of ground surface temperature, the temperature response unrealistically keeps enlarging over time. For the GF-***Z*** case, however, the temperature growth rate slows down when the Fourier number is greater than 10, and becomes stable over a long period. Another outstanding characteristic of these composite GFs is that they can be used to analyze the influences of the thermal property differences on the heat transfer process, as summarized in Figure 4-4. As shown in Figure 4-4 (a), the temperature grows slowly when the thermal diffusivity ratio is high. A similar characteristic can be seen in Figure 4-4 (b). When the thermal conductivity ratio is higher, however, the temperature rise is slower. This temperature response delay effect becomes significant and notable when Fo is greater than 0.2, indicating that the effect of the material difference can only be ignored for short-term calculations or estimations. In addition, the GF of ***Z*** data also shows that high ratios of thermal conductivity and thermal diffusivity delay the achievement of the stability of the heat transfer process.

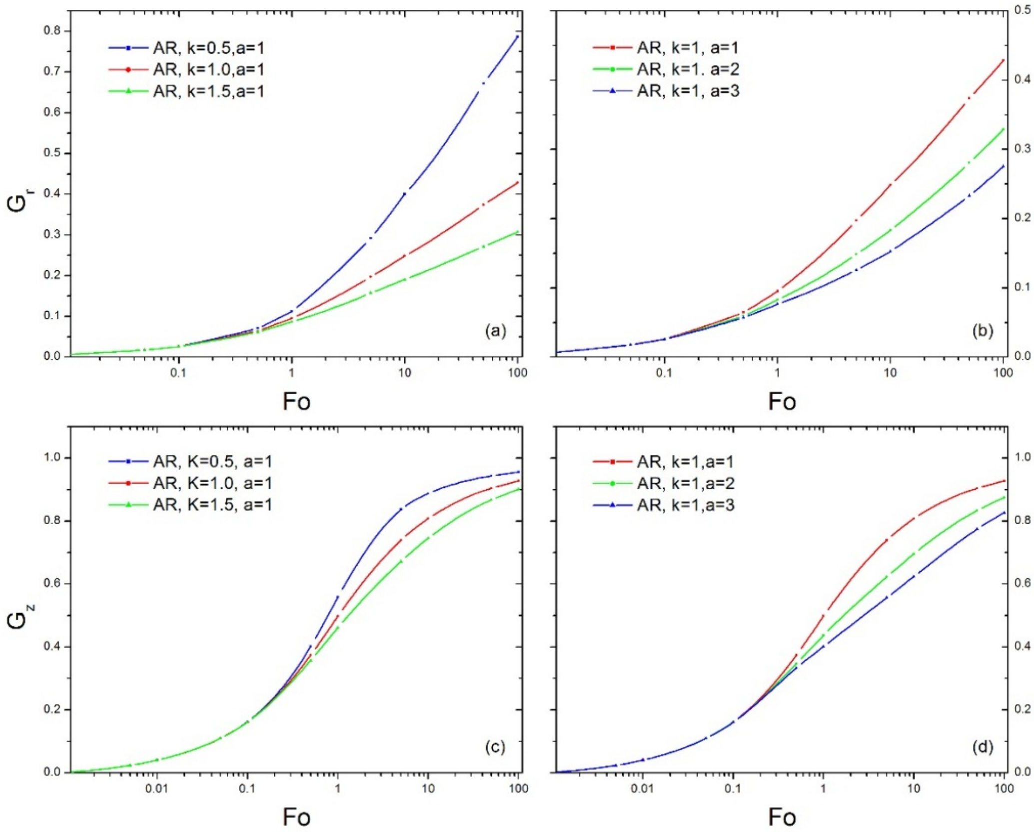

Figure 4-4 (a) GF of R with different thermal conductivity ratios; (b) GF of R with different thermal diffusivity ratios; (c) GF of Z with different thermal conductivity ratios; (d) GF of Z with different thermal diffusivity ratios

Compared with the homogeneous situation, the temperature rise takes longer to become zero when the material property difference is large. This phenomenon is much more obvious for the single ring-coil GF in a composite medium.

To analyze the ring-coils model step by step, a single ring-coil solution is introduced established directly from the basic G functions (GF-***R*** and GF-***Z***). In the next step, the solution for the composite ring-coil source model can then, be considered as the linear superposition of a number of single ring-coil GFs. The single ring-coil source is assumed to be located at $z^{'} = z_0$ with its axis coinciding with the z-axis and with a radius of r_0. This two-dimensional heat conduction problem can be formulated by replacing $g\left(r^{'}, z^{'}, \tau\right)$, in Eq. (4.20), by $\frac{q_l}{2\pi r_0}\delta\left(\tau-\tau_0\right)\delta\left(r^{'}-r_0\right)\delta\left(z^{'}-z_0\right)$. The temperature response of the point (r, z) can be calculated using Eq. (4.21).

$$\theta_{crz,i} = \frac{\alpha_1}{k_1}\int_0^{\infty}\int_0^{\infty}\int_0^{\tau} 2\pi r^{'} G_{crz,i}\left(r, z, t \middle| r^{'}, z^{'}, \tau\right) g\left(r^{'}, z^{'}, \tau\right) d\tau^{'} dr^{'} dz^{'} \qquad i = \mathrm{I}, \mathrm{II}, \mathrm{III} \text{ and } \mathrm{IV}$$
$$g\left(r^{'}, z^{'}, \tau\right) = \frac{q_l}{2\pi r_0}\delta\left(\tau-\tau_0\right)\delta\left(r^{'}-r_0\right)\delta\left(z^{'}-z_0\right) \tag{4.21}$$

Taking a single ring-coil source model as an example with $z_0 = 1$, $l_r / r_0 = 1.5$ and $l_z / z_0 = 1.5$, the temperature response at the point ($z = z_0$, $r = r_0$) for different thermal properties are described in Figure 4-5. Similar to the GF-Z, the temperature of the composite medium shows a good agreement with the homogeneous results during the short initial time, but remarkable discrepancy when ***Fo*** > 0.2.

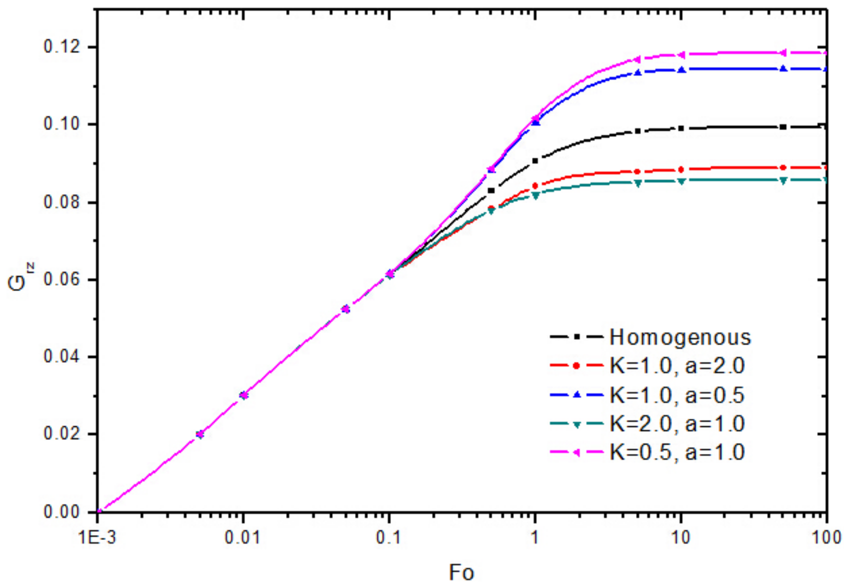

Figure 4-5 Comparison of the GFs of a single ring-coil for different heat-transfer conditions

4.4.2 Analysis of the composite ring-coils model

As no available analytical solution can accurately describe the PGHE with spiral-tube heat transfer process, the numerical simulation method was introduced to compare and validate the novel composite ring-coils source model. The temperature responses in different heat transfer mediums were calculated by both the analytical and numerical methods to investigate their impact on a PGHE with spiral-tube of thermal property differences between the pile and soil. To better compare analytical results (AR) and simulation results (SR), a dimensionless temperature variable, $\Theta = k_1\theta / q_r$, was introduced. Taking eight heat exchanger loops in a pile foundation as an example, the temperature distributions, for Fo=5.0, given by the simulation model are summarized in Figure 4-6.

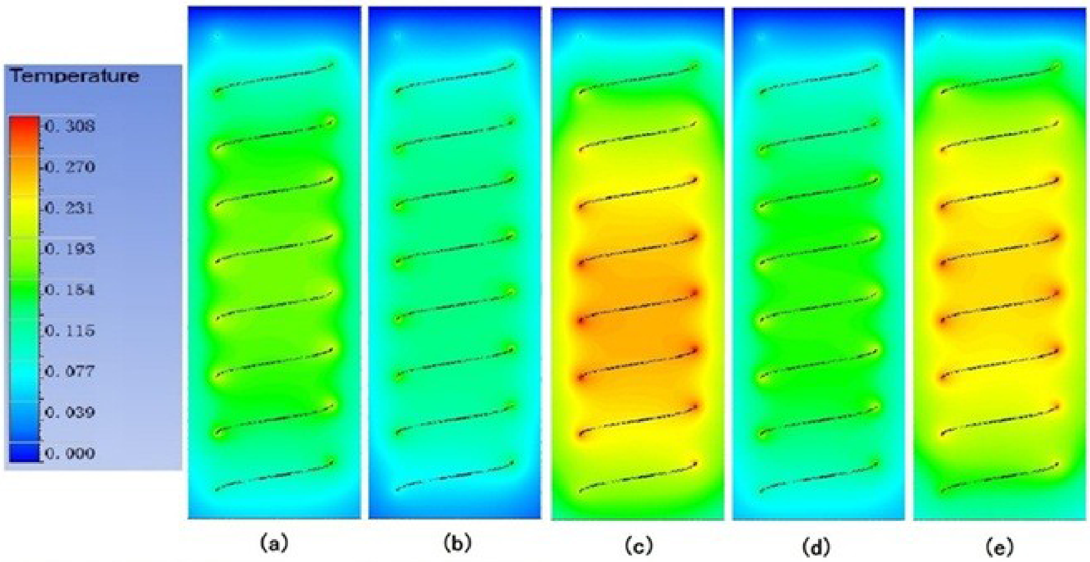

Figure 4-6 The dimensionless temperature distribution for a pile with different heat-transfer conditions when *Fo* = 5.0, obtained by a numerical method. (a) Homogenous; (b) K=2.0, α=1.0; (c) K=0.5, α=1.0; (d) K=1.0, α=2.0 and (e) K=1.0, α=0.5.

Unlike the homogeneous case, when the thermal conductivity ratio is small, the soil traps more heat energy in the pile foundation, and a high-temperature domain is created at its centre. A similar phenomenon, shown in Figure 4-6 (e), is observed when the thermal diffusivity is 0.5, but its effects are less pronounced than the thermal conductivity effects.

The temperature responses ($r = r_0 = 1$) given by the analytical model, calculated using Eq. (4.21), together with the numerical results, are demonstrated in Figure 4-7 and Figure 4-8 for the Fourier number of 10. As shown in these figures, the temperature fluctuates greatly along the z direction and becomes zero with the increase of depth. This feature distinguishes this new model from the infinite composite cylindrical model.

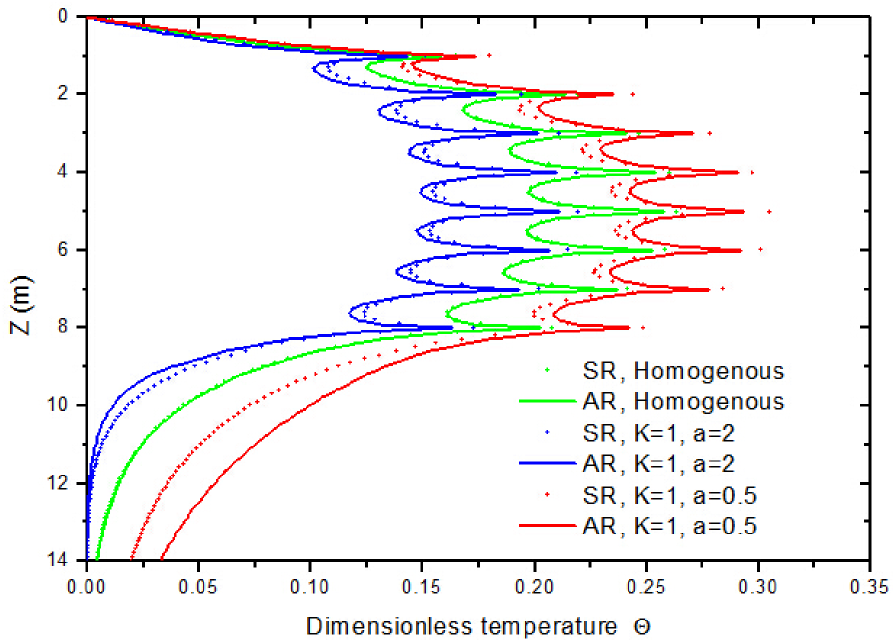

Figure 4-7 Dimensionless temperature response of numerical and analytical results with *Fo* = 10 and r=1 for different ratios of thermal diffusivity.

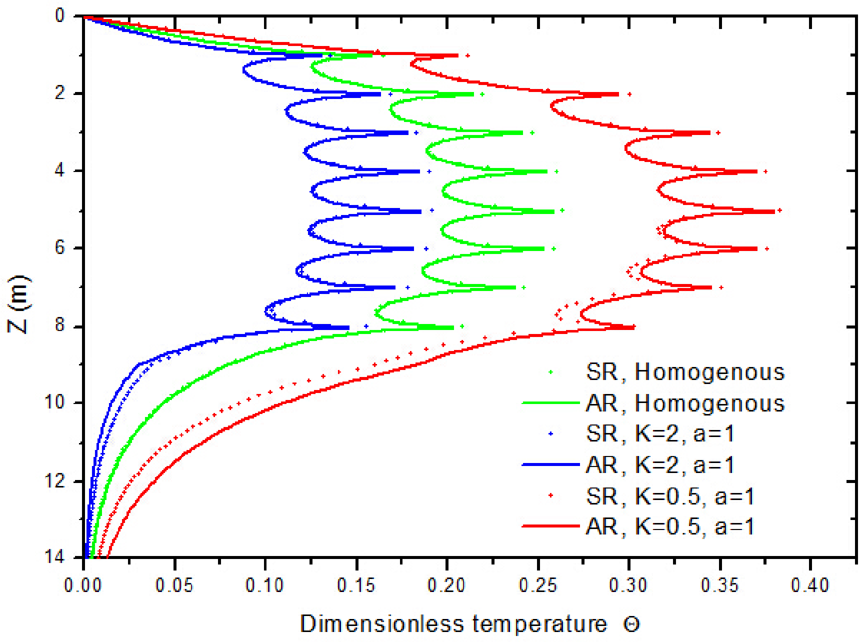

Figure 4-8 Dimensionless temperature responses of numerical and analytical results with *Fo* = 10 and r=1 for different ratios of thermal conductivity.

The analytical solutions agree well with the numerical solutions, especially in the region close to the pile foundation itself. But, a relatively large calculated error can be observed in the soil region. This phenomenon may be caused by the simplification of the soil thermal properties. In the analytical modeling process, the soil is considered as a compound medium, and this is different to the real case. This difference is not obvious when Fo is small but increases with the growth of Fo. For the case of Fo=10, which represents about 6000 hours of PGHE with spiral-tube operation, the results are still acceptable. The figures also indicate that this new model can effectively represent the effects of the thermal difference between pile and soil. The temperature response decreases with the increasing heat capacity and heat conductivity of the soil. This phenomenon, however, is more sensitive to the thermal conductivity than thermal capacity. In addition, an obvious inflection point can be found at the interface between pile and soil. When the thermal conductivity of pile is twice as the one of soil, the dimensionless temperature at the middle of the pile is 0.3832 which is almost twice as the temperature response of the homogeneous case, as shown in Fig.8. An inflection point can be observed at z of 9.0m also exists at the location r/r_0=1.5 in Figure 4-9. It should be the consequence of energy conservation. The heat flux flowing in and out of the interface must be the same, so the temperature gradients differ for different thermal conductivities of soil and pile.

The temperature responses at the middle of the spiral heat exchanger along with its radius are plotted and shown in Figure 4-9 and Figure 4-10. Obviously, in any temperature line, there is a peak value where $r = r_0$, and the temperature decreases with the distance from the peak point. The impact of heat transfer medium properties on the PGHE with spiral-tube can also be clearly observed in these figures. When the heat release rate is the same, the higher the ratio of thermal conductivities or thermal diffusivities, the lower the temperature response.

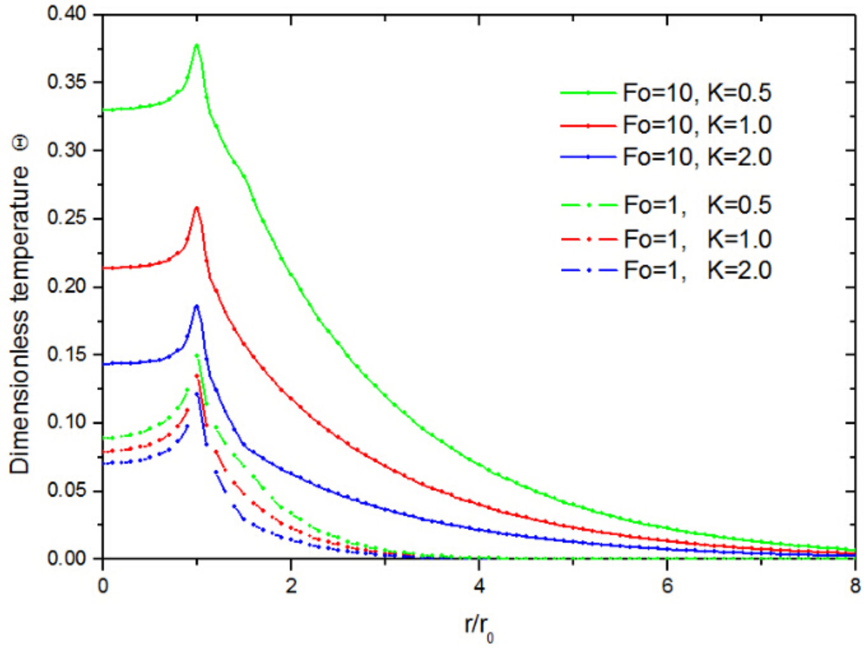

Figure 4-9 Dimensionless analytical temperature response with z=6 for different ratios of thermal conductivity.

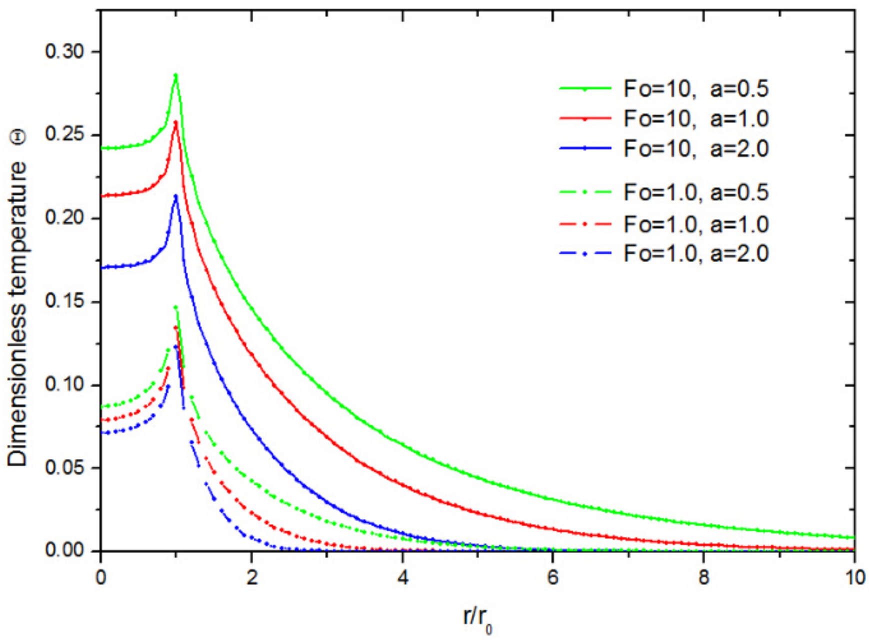

Figure 4-10 Dimensionless analytical temperature response with z=6 for different ratios of thermal diffusivity.

4.5 Summary

In this chapter, based on the Green's function theory and Jaeger's instantaneous line-source model, a new model, a composite ring-coil source analytical model, has been established which can effectively represent the heat transfer process of a pile geothermal heat exchanger with spiral coils set within a surrounding composite media. Several important conclusions are given as follows:

1) This chapter has developed a new analytical solution using the Laplace method. This new model successfully represents the different thermal properties of the pile and the surrounding soil in the case of the pile geothermal heat exchanger containing spiral coils. It has proven to be a new tool for energy pile system design and evaluation.

2) The finite size and discontinuities associated with pile geothermal heat exchangers with spiral coils are considered, by modelling the composite medium. The influence of ground temperature and the limited length of the pile are fully examined in this new model.

3) Comparisons between the homogeneous medium model and composite medium model prove that the thermal property differences between pile material and the soil have a significant influence on the heat transfer processes occurring in the operation of pile geothermal heat exchangers.

As mentioned in the assumptions, this new model does not consider the influence of groundwater advection. But, in some cases, the pile foundation is built upon the area with rich water resources. As the pile is usually more than ten meters in depth, it sometimes goes across the soil vadose zone. Accordingly, the heat transfer performance of PGHE will be affected when the groundwater flow exists. Therefore, the influence of groundwater advection of PGHE with spiral-tubes are investigated and discussed in next chapter.

CHAPTER 5

NUMERICAL AND ANALYTICAL ANALYSIS OF GROUNDWATER INFLUENCE ON PILE GHE WITH SPIRAL-TUBES

5.1 Introduction

If groundwater advection exists in the installation area of GHEs, water flow will transport heat released by GHEs from upstream to downstream. This effect of borehole GHEs has been widely discussed (Sutton et al., 2003; Diao et al., 2004; Molina-Giraldo et al., 2011; Zhang et al., 2012), but few studies have focused on PGHEs, especially for PGHE with spiral-tube.

Compared with borehole GHEs, PGHEs are larger in radial dimension and the pipe structure of PGHE is more complicated. The heat transfer process under groundwater flow of PGHEs with spiral-tubes is quite different from that of a borehole GHE. Based on the moving spiral coil source model (Zhang et al., 2014), the effect of groundwater on PGHEs in long-term operation was investigated by Go et al. (2014). Comparison results between the moving infinite line source model and moving spiral coil source model suggested there is no great difference in long-term operation. However, these studies failed to evaluate the heat transfer performance of PGHEs in short-term operation and have not provided a method to predict the temperature response of pipe wall, which plays a key role in GCHP design.

Hence, the objective of this section is to develop an improved analytical model which can better estimate the heat transfer process of PGHE with spiral-tubes under the groundwater advection, pecially the temperature response at the pipe wall. Besides, a 3-D simulation model is established to investigate the effect of groundwater flow on PGHE with spiral-tube in the short-term operation. The numerical model is validated by ring-coils source model in which no groundwater flow is considered. The influences of the hydraulic gradient are simulated and discussed according to the simulation results.

5.2 Numerical Model

The numerical model presented here is managed to simulate the heat transfer process of PGHE with spiral-tube under groundwater advection. This heat transfer process is a combined effect of various heat transfer mechanisms, such as conduction, convection and radiation. But, the heat radiation mainly exists in soil and is found to be less than 1% of the total heat transfer within 0 ~ 40 ℃ (Rees et al., 2000). Thus, in this study, only conduction and convection effects are taken into consideration. For this purpose, ANSYS code has been selected to simulate this 3-D heat transfer process (Ansys, 2009).

5.2.1 Governing equation and boundary condition

The heat transfer processes mainly include the heat convection process between circulating fluid and pipe wall, the heat conduction in pipe and concrete pile, and convection and conduction in the soil. The heat convection process is complicated and influenced by a number of factors, such as fluid temperature, fluid velocity and surface properties of pipe wall. Additionally, the inlet water temperature can be obtained easily when the pipe wall temperature is known (Y. Man et al., 2011). Thus, the heat transfer in circulating fluid is not required to be simulated, and the heat convection process is simplified by a heat flux boundary condition on the pipe wall. The heat transfer in pile is simulated by a pure solid heat conduction process and no heat transfer is induced by convection. For the soil, it is regarded as a homogeneous porous medium with water flowing through. Besides, it is assumed that there is no occurring phase change heat transfer both in pile and soil.

The heat transfer simulation in a porous medium is unsteady and is not in thermal equilibrium. A dual method, in which the solid zone is spatially coincident with the porous fluid zone and heat transfer only exists in soil and fluid interface, is adopted. The governing equations in solid and fluid are expressed in Eq. (5.1) and Eq. (5.2), respectively.

$$\frac{\partial}{\partial t}\left[(1-g)r_s E_s\right] = \nabla \times \left[(1-g)k_s \nabla T_s\right] + S_f^h + h_{fs}A_{fs}(T_s - T_f) \tag{5.1}$$

$$\begin{aligned}&\frac{\partial}{\partial t}\left(\gamma\rho_f E_f\right) + \nabla\cdot\left[\vec{v}\left(\rho_f E_f + p\right)\right] \\ &\quad = \nabla\cdot\left[\gamma k_f \nabla T - \left(\sum_i h_i J_i\right) + \left(\overline{\overline{\tau}}\cdot\vec{v}\right)\right] + S_f^h + h_{fs}A_{fs}(T_f - T_s)\end{aligned} \tag{5.2}$$

Where E_f and E_s are the total fluid energy and total solid medium energy, respectively, ρ_f is the fluid density, γ is the porosity of the medium, k_f is the fluid phase thermal conductivity, k_s is the solid medium thermal conductivity, h_{fs} is the heat transfer coefficient for the fluid/solid interface, A_{fs} is the interfacial area density and S_f^h is the fluid enthalpy source term.

Groundwater flow is determined by soil properties and hydraulic characteristics. The properties of underground water flow are usually described as mean parameters or comprehensive parameters. Porosity and bulk density are usually adopted to describe the degree of soil density. Effective porosity, a characteristic parameter in groundwater advection analysis, describes the fraction of void space in the material and is an important influencing factor on hydraulic conductivity (Freeze & Cherry, 1979). Based on the components of soil, the soil can be classified into cohesive soil, sand soil, gravel, crushed stone soil and so on. Due to the diversity of settlement mechanism and geological process, even though the soil is classified into the same category, the internal structures are also different. But, in general, the ground water flows slowly in soil and can be considered to be laminar. This laminar flow can be modelled by an addition of a momentum source term, including a viscous loss term and an inertial loss term:

$$S_i = -\left(\sum_{j=1}^{3} D_{ij} \mu v_j + \frac{1}{2} \sum_{j=1}^{3} C_{ij} \rho |v| v_j \right) \tag{5.3}$$

where S_i is the source term for the *i* th coordinate direction in momentum equation, $|V|$ is the magnitude of the velocity and *D* and *C* are prescribed matrices. Due to a further assumption that the soil is a homogeneous domain, Eq. (5.3) can be further simplified into Eq. (5.4)：

$$S_i = -\left(\frac{\mu}{\alpha_p} v_i + \frac{1}{2} C_2 \rho |v| v_i \right) \tag{5.4}$$

where α_p is the permeability and C_2 is the inertial resistance factor. The permeability and the inertial resistance factor, which mainly depend on material's skeleton structure, are the main control parameters for porous media. A semi-empirical correlation equation, called the Ergun equation (Ergun, 1952), was adopted to determine these key parameters of the surrounding ground. This equation is obtained by an experiment on the packed bed, but can be applied to a wide range of Reynolds numbers and for many types of porous medium:

$$\frac{|\Delta p|}{L}=\frac{150\mu}{D_p^2}\frac{(1-\varepsilon)^2}{\varepsilon^3}v+\frac{1.75\rho}{D_p}\frac{(1-\varepsilon)}{\varepsilon^3}v^2 \tag{5.5}$$

where μ is the viscosity, D_p is the mean particle diameter and ε is the void fraction. Compared with the Eq. (5.5), the permeability and inertial loss coefficient in each component direction can be identified by Eq. (5.6):

$$\alpha_p=\frac{D_p^2}{150}\frac{\varepsilon^3}{(1-\varepsilon)^2}\ ;\ C^2=\frac{3.5}{D_p}\frac{(1-\varepsilon)}{\varepsilon^3} \tag{5.6}$$

In this study, turbulence in the porous media is ignored by assuming that the groundwater flow is laminar flow and there is no turbulence generation or dissipation rates.

5.2.2 Numerical implementation

As mentioned above, the heat transfer process of PGHE is unsteady and nonlinear. It is hard to find a precise analytical solution. Thus, the numerical method, which has been demonstrated successes in providing a relatively accurate simulation solution, is adopted for the calculations of temperature response of PGHE. In this study, the numerical model is solved by a commercial Computational Fluid Dynamics (CFD) program, ANSYS CFX. The sketch of this 3-D simulation model is shown in Figure 5-1. As a large steep temperature gradient may occur near the pipe well, a fine mesh is generated in this area. Total meshes of the pile and soil domain are 3,255,962 and 977,936, respectively. The radius and depth of the pile model are 0.75m and 5.5m, respectively. Spiral radius and screw spacing of the PGHE are both assumed to be 0.5m. The soil domain is simulated as a rectangular solid with the dimension of 20m×20m×12.25m. The initial temperature of pile and soil domain is assumed to be uniform. In this study, the operation process of PGHE in cooling mode is simulated by applying a constant heat flux on the inner face of the heat exchange pipe. It is assumed that groundwater flows along the X direction from negative direction to positive direction. The boundary surface at the negative and positive directions of the soil domain is regarded as upstream and the downstream, respectively. Different hydraulic gradient conditions have been considered by providing various hydrostatic pressure on the upstream and downstream of the soil domain. The basic information of this numerical model is summarized in Table 5.1.

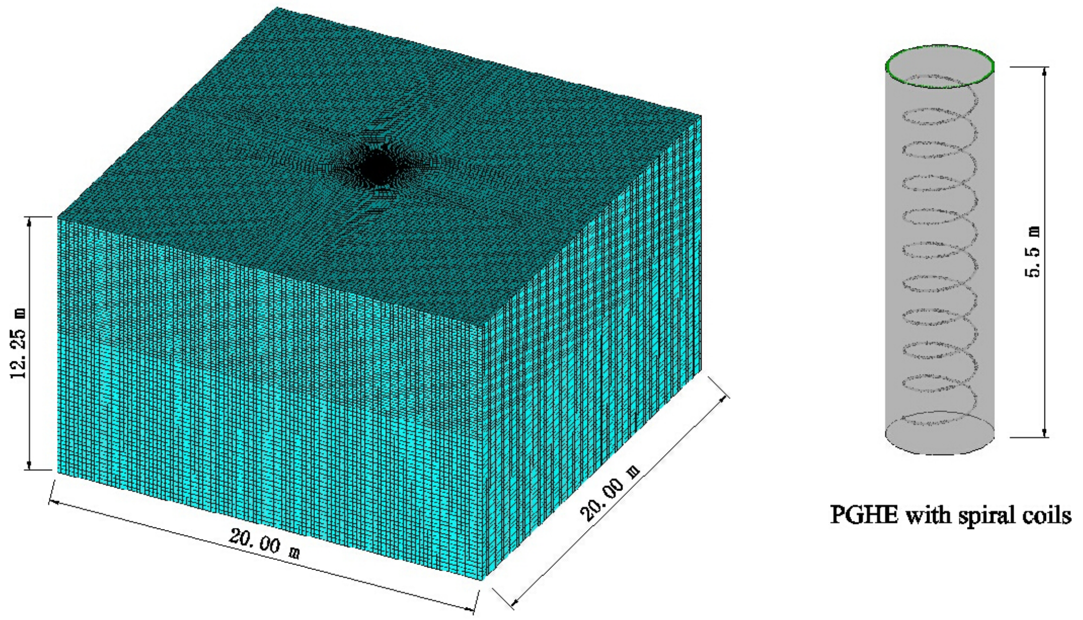

Figure 5-1 3-D view of mesh and the detailed structure of PGHE with spiral-tube

Table 5.1 Boundary conditions used in the numerical model

Item	Boundary Type	Values	Unit
Upper surface of soil (+Z)	Constance Temperature	25	℃
Down surface of soil (-Z)	Adiabatic	-	-
Front surface of soil (-Y)	Adiabatic	-	-
Back surface of soil (+Y)	Adiabatic	-	-
Left surface of soil (-X)	Groundwater Inlet-Constant Velocity	2.55/3.83/5.10/7.65 /10.20/12.75/15.30 /17.85/20.4/22.95/25.5	*10-4 m2 s-1
Right surface of soil (+X)	Groundwater Outlet-Constant Pressure	0	Pa
Spiral pipe surface	Constant Heat Flux	200	W/m2

5.3 Improved Analytical Model

For PGHE with spiral-tube, finite ring-coils source model (P. Cui et al., 2011) has been proved to be an accurately and effectively analytical model. Compared with other classic analytical model, such as “hollow” cylindrical source model, this model takes discontinuity of heat source and pitch effect into consideration. However, this ring-coils source model regards the ground as a pure solid and only conduction occurs in the heat transfer process. This model may bring an inaccurate result when PGHE system operates in the groundwater flow condition.

5.3.1 The original moving ring-coils source model

Based on the ring-coils source model and moving heat source method, an analytical model has been established to simulate the heat transfer process under groundwater flow (Zhang et al., 2014). As the difficulties in modelling the soil particle-size distribution and calculating the velocity fluctuations of groundwater, the ground is assumed to be a homogeneous porous medium. The analysis of the groundwater flow effect on the heat transfer for PGHE with spiral-tube is also based on the following assumptions (P. Cui et al., 2011; Y. Man et al., 2011):

1) The ground is regarded as a homogeneous saturated porous medium, and its thermal properties do not change with the time and temperature;
2) The ground region is assumed to be a semi-infinite medium, and every ring-coils has a constant pitch, b;
3) Whole region (pile and ground) has a uniform initial temperature, T_0; the excessive temperature, θ, is defined as $\theta = T - T_0$
4) The heat emission rate per unit of pile length is constant, q_{ring}.

By assuming the groundwater flow direction being along with the X-axis forward direction, the heat conduction and convection between the groundwater flow and pile in porous medium should comply with the basic heat-conduct differential equation (Eskilson, 1987):

$$\frac{\partial\theta}{\partial\tau}+\frac{\rho_f c_f u}{\rho c}\frac{\partial\theta}{\partial x}=\frac{k}{\rho c}\left(\frac{\partial^2\theta}{\partial x^2}+\frac{\partial^2\theta}{\partial y^2}+\frac{\partial^2\theta}{\partial z^2}\right) \tag{5.7}$$

where ρc and $\rho_f c_f$ are volume-specific heat capacity of porous medium and water respectively, k is the coefficient of heat conductivity and u is the groundwater flow velocity.

The Green's function theory has been adopted to solve the heat transfer equation. Based on its governing equation and boundary conditions, Eq. (5.7) can be rewritten in cylindrical co-ordinates:

$$\begin{aligned}
&\frac{\partial\theta}{\partial\tau}+U\frac{\partial\theta}{\partial(r\cos\varphi)}=\alpha\left(\frac{\partial^2\theta}{\partial r^2}+\frac{1}{r}\frac{\partial\theta}{\partial r}+\frac{\partial^2\theta}{\partial z^2}\right)+\frac{q\delta(r-r_0,z-z^{'})}{2\pi r_0\rho c}, && for\ 0<r<\infty,\ -\infty<z<\infty,\ \tau>\tau^{'}\\
&\frac{\partial\theta}{\partial r}=0, && for\ r=0,\ -\infty<z<\infty,\ \tau>\tau^{'}\\
&\theta=0, && for\ 0<r<\infty,\ -\infty<z<\infty,\ \tau>\tau^{'}\\
&\theta=0, && for\ r\to\infty,\ -\infty<z<\infty,\ \tau>\tau^{'}\\
&\theta=0, && for\ 0<r<\infty,\ z\to\pm\infty,\ \tau>\tau^{'}
\end{aligned} \tag{5.8}$$

Then, the temperature response of a single ring coil under groundwater flow with location (r, z) and time variable can be expressed,

$$\theta_{r,z}=\frac{q}{2\pi\rho c}\int_0^{\tau}d\tau^{'}\int_0^{2\pi}Gd\varphi^{'} \tag{5.9}$$

where G is the Green's function in the cylindrical co-ordinates:

$$G = \frac{1}{8\left[\pi\alpha(\tau-\tau^{'})\right]^{3/2}} \times \exp\left\{-\frac{\left[r\cos\varphi - r_0\cos\varphi^{'} - U(\tau-\tau^{'})\right]^2 + \left(r\sin\varphi - r_0\sin\varphi^{'}\right)^2 + \left(z-z^{'}\right)^2}{4\alpha(\tau-\tau^{'})}\right\} \tag{5.10}$$

Then, using the simplification method in ring-coils source model, the spiral heat exchanger is regarded as a series of ring coils. These ring coils are assumed to be along the Z direction and each ring coil has constant spacing, *b*. The distance between the first ring coil and the last ring coil is defined as $(h_1 + \frac{b}{2})$ and $(h_2 + \frac{b}{2})$, respectively. By applying the moving heat source method on the ring-coil source model by image method, a moving ring-soils source model (Zhang et al., 2014) can be obtained. This model was named as original analytical model (OAM) to distinguish with the improved one.

$$\theta = \frac{qb}{16\pi^{5/2}}\sum_{n=0}^{m-1}\int_0^{2\pi} d\varphi^{'}\int_0^{\tau}\exp\left[-\frac{\left[x - r_0\cos\varphi^{'} - L\left(\tau-\tau^{'}\right)\right]^2 + \left(y - r_0\sin\varphi^{'}\right)^2}{4\alpha\left(\tau-\tau^{'}\right)}\right]\cdot \left\{\exp\left[-\frac{\left(z-h_1-nb-0.5b\right)^2}{4\alpha\left(\tau-\tau^{'}\right)}\right] - \exp\left[-\frac{\left(z+h_1+nb+0.5b\right)^2}{4\alpha\left(\tau-\tau^{'}\right)}\right]\right\}\frac{d\tau^{'}}{\sqrt{\alpha}\left(\tau-\tau^{'}\right)^{3/2}} \tag{5.11}$$

5.3.2 The improved moving ring-coils model

However, the effect of groundwater flow on PGHE with spiral-tube will be overestimated by using the OAM, because the pile is assumed to be a porous medium with the groundwater flowing directly into the pile in the modelling process. According to the simulation results, it is found that this simplification can be acceptable only when the groundwater flow is extremely small. Besides, the OAM failed to consider the relative sizes between pile and heat exchange pipe. Obviously, even when the groundwater flow velocity is the same, the installation forms of PGHE can also affect its heat transfer process. When the pipe is settled near the pile wall, the heat transfer process is more sensitive to groundwater. On the contrary, the temperature response of PGHE is not seriously affected by groundwater flow when the pile radius is much larger than the helical radius of pipe. In order to improve the reliability and practicability of the OAM, a series of numerical simulation has been conducted. Based on the simulation solution, a new modified parameter, i.e., effective groundwater flow velocity (L_{eff}), was proposed for moving ring-coils model. It is defined to replace the original expression (L) of groundwater flow velocity and its expression is shown in Eq. (5.13).

$$L = \frac{u\rho_w c_w r_0}{\alpha \cdot \rho c} \tag{5.12}$$

$$L_{eff} = 0.168\frac{\rho_w c_w}{\rho c}\frac{u r_0}{\alpha}\left(\frac{r_0}{R_p}\right)^{1.6} \tag{5.13}$$

where α is the mean thermal diffusivity of pile and soil, r_0 is the helical radius of heat exchange pipe and R_p is the radius of the pile.

To better express the heat transfer equation, relevant dimensionless variables are introduced: $Fo = \alpha\tau / r_0^2$, $\Theta = k\theta / q$, $R = r / r_0$, $X = x / r_0$, $Y = y / r_0$, $Z = z / r_0$, $B = b / r_0$, $H_1 = h_1 / r_0$, $H_2 = h_2 / r_0$, $H = H_2 - H_1$. Then, the improved analytical model (IAM) has been established:

$$\Theta = \frac{B}{16\pi^{5/2}} \sum_{n=0}^{m-1} \int_0^{2\pi} d\varphi' \int_0^{Fo} \exp\left[-\frac{\left[X - \cos\varphi' - L_{eff}\left(Fo - Fo'\right)\right]^2 + \left(Y - \sin\varphi'\right)^2}{4\left(Fo - Fo'\right)} \right] \cdot$$
$$\left\{ \exp\left[-\frac{\left(Z - H_1 - nB - 0.5B\right)^2}{4\alpha\left(Fo - Fo'\right)} \right] - \exp\left[-\frac{\left(Z + H_1 + nB + 0.5B\right)^2}{4\left(Fo - Fo'\right)} \right] \right\} \frac{dFo'}{4\left(Fo - Fo'\right)^{3/2}} \tag{5.14}$$

5.4 Comparison and Findings

5.4.1 Numerical model validation with ring-coils source model

To validate the numerical model, the numerical results are compared to the analytical model solutions. Because no analytical solution, which can effectively describe the heat transfer process, has been established, the pure conduction model of ring-coils, established by Cui et.al. (2011), is applied to validate the numerical model. In this pure conduction model, the calculation domain of pile and soil is treated as a fully homogeneous medium. Thus, it is assumed that the pile and soil have the same thermal properties in the validation stage. The borehole midpoint temperature is respectively calculated by the numerical and analytical methods over a period of operation time from 20h to 2160h, which equals to the Fourier number between 0.11 and 12.25. The thermal properties of the borehole used for the calculations are summarized in Table 5.2.

Table 5.2 Physical properties used in the numerical model for model validation

Parameters	Values	Unit
Pile & Soil density, ρ	2645	Kg m-3
Pile & Soil heat capacity, c	960	J kg-1 K-1
Pile & Soil thermal diffusivity, α	3.93e-7	m2 s-1

Figure 5-2 illustrates the calculation results of dimensionless temperature response obtained from the numerical and analytical methods. At the operation time of 2160h, the dimensionless temperature is 0.2797 for the numerical model and the analytical solution is 0.2806. The relative error is adopted to better compare these two models in detail, and the expression is shown in Eq. (5.15).

$$\text{Relative error} = \frac{T_{analytical} - T_{numerical}}{T_{numerical} - T_{initial}} \times 100\% \tag{5.15}$$

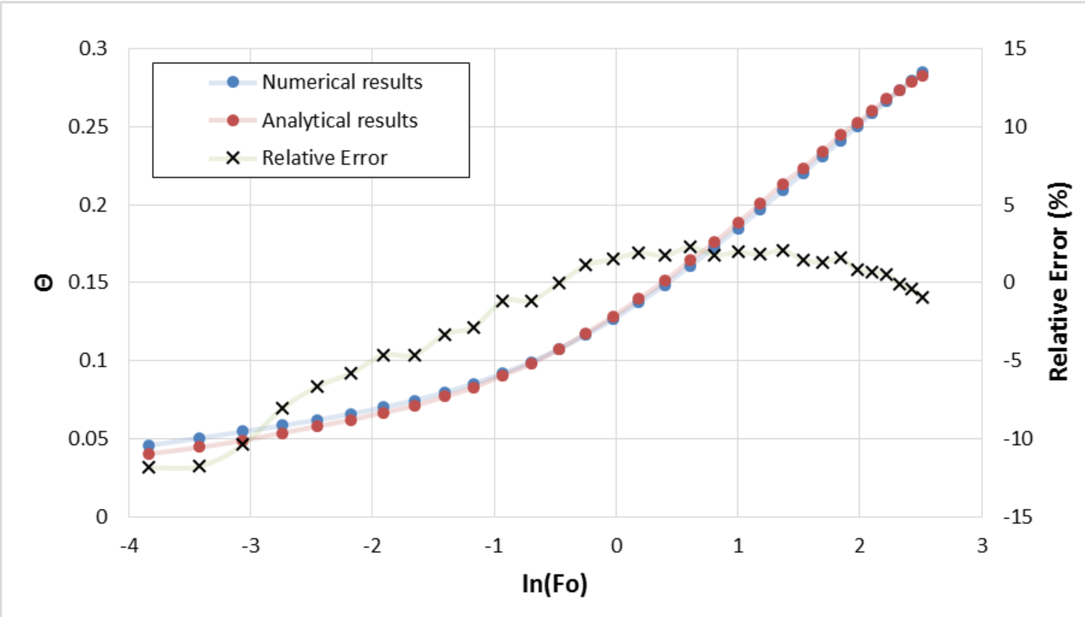

Figure 5-2 Comparison of temperature between the numerical and analytical results and relative errors

It can be seen that the numerical solution agrees well with the analytical solution within the operation period, as shown in Figure 5-2. The relative error is within an acceptable range and becomes smaller with the increasing Fourier number. This comparison results also indicate that the ring-coils source model has a good accuracy even when the operation time is small. At 0.25 (***Fo***), equal to 45h in this study, the relative error is about -3.3%, which means the ring-coils source model can be used to describe an alternative operation for PGHE with spiral-tube.

5.4.2 Comparison between the validated numerical model and original moving ring-coils model

Temperature responses respectively obtained from the OAM and from the numerical model with different hydraulic gradients are plotted in Figure 5-3 and Figure 5-4. To better understand the groundwater affects, two points on the pipe surface are selected as reference points. One is located in the middle of the pipe wall on the upstream face and the other one is at the same depth but on the downstream face. As shown in Figure 5-3, both analytical and numerical results indicate that the groundwater flow has a significant influence on the heat transfer process of PGHE with a stronger effect on the upstream face. This effect will reduce when the hydraulic gradient becomes smaller, and the heat transfer process becomes a pure conduction process when the hydraulic gradient is equal to zero.

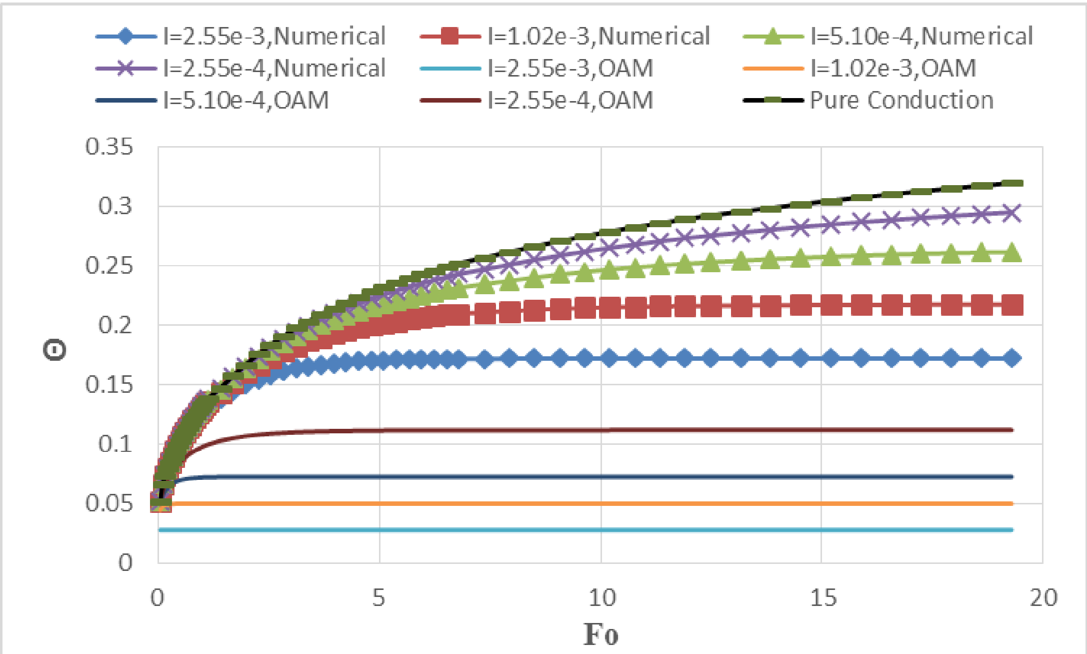

Figure 5-3 Temperature response at the middle point of upstream face with different *Fo* (X=1, Y=0, Z=6.5, B=1)

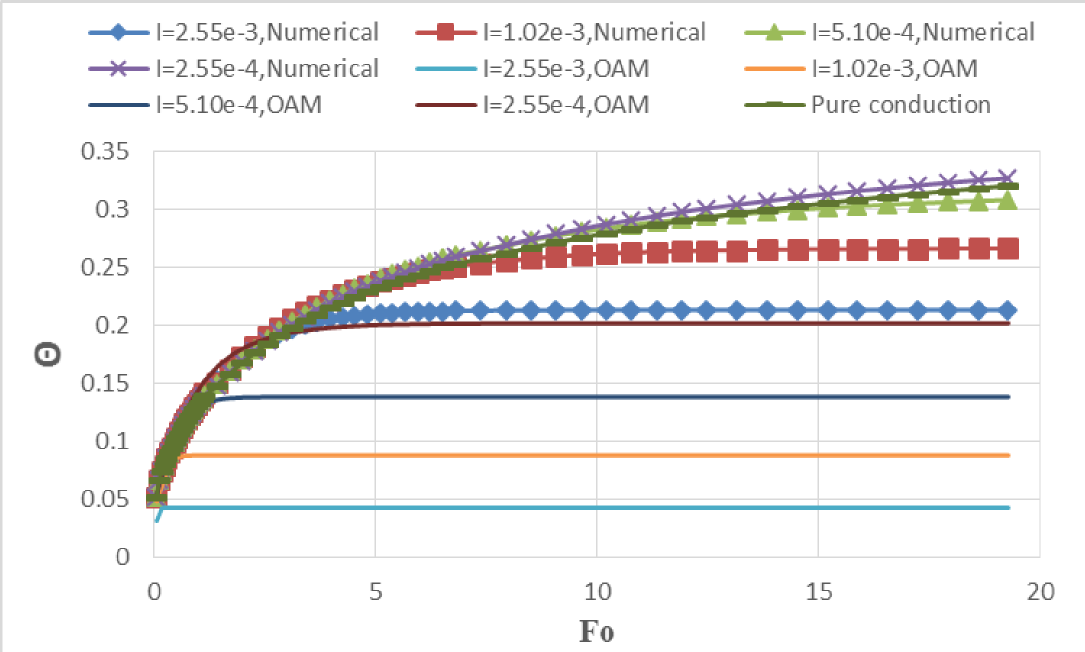

Figure 5-4 Temperature response at the middle point of downstream face with different *Fo* (X=-1, Y=0, Z=6.5, B=1)

Comparing the results obtained from OAM and from the numerical model, plotted in Figure 5-3 and Figure 5-4, it can be seen clearly that the temperature response curve from the analytical model is far from the numerical solution and this situation is more obvious when hydraulic gradient is high. For the case of I=2.55e^{-4}, $\boldsymbol{Fo}$=19.2 on upstream face, the dimensionless temperature is 0.295 which is almost triple of the analytical results. When the hydraulic gradient increases to I=2.55e^{-3}, only a small temperature rise can be detected by the analytical method. This phenomenon is caused by the modelling simplification by assuming that the pile is also a porous medium and the groundwater flow can pass through the gap between ring-coils. Based on this simplification, the conduction process in a concrete pile is replaced by a convection process in porous medium. Thus, a large calculation error can be found in high hydraulic gradient cases. But, both the analytical and numerical solutions suggest that groundwater flow is helpful to control the temperature rise and can improve the heat transfer performance of PGHE system.

5.4.3 Comparisons between the validated numerical and improved analytical models

The temperature response as a function of operation time in cooling mode with different hydraulic gradients is plotted in Figure 5-5 to Figure 5-7. In view of the comparisons between the analytical and the numerical solutions, an error analysis parameter is defined as:

$$E = \frac{\left|T_{analytical} - T_{numerical}\right|}{T_{numerical}} \times 100\% \tag{5.16}$$

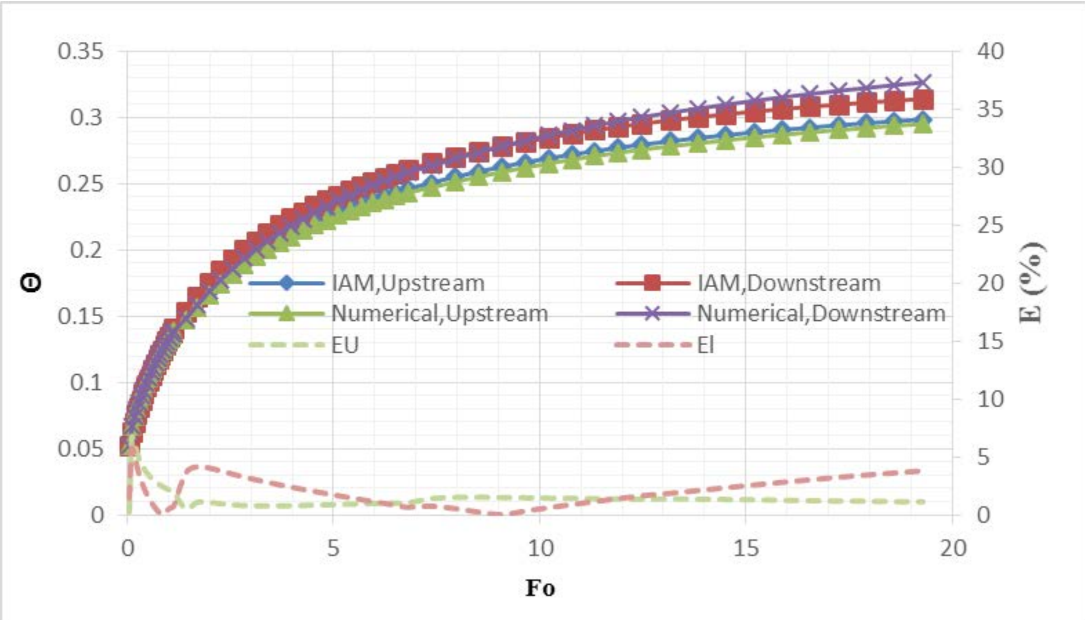

Figure 5-5 Comparisons of temperature responses from improved analytical model and numerical model of *I=2.55e-4*

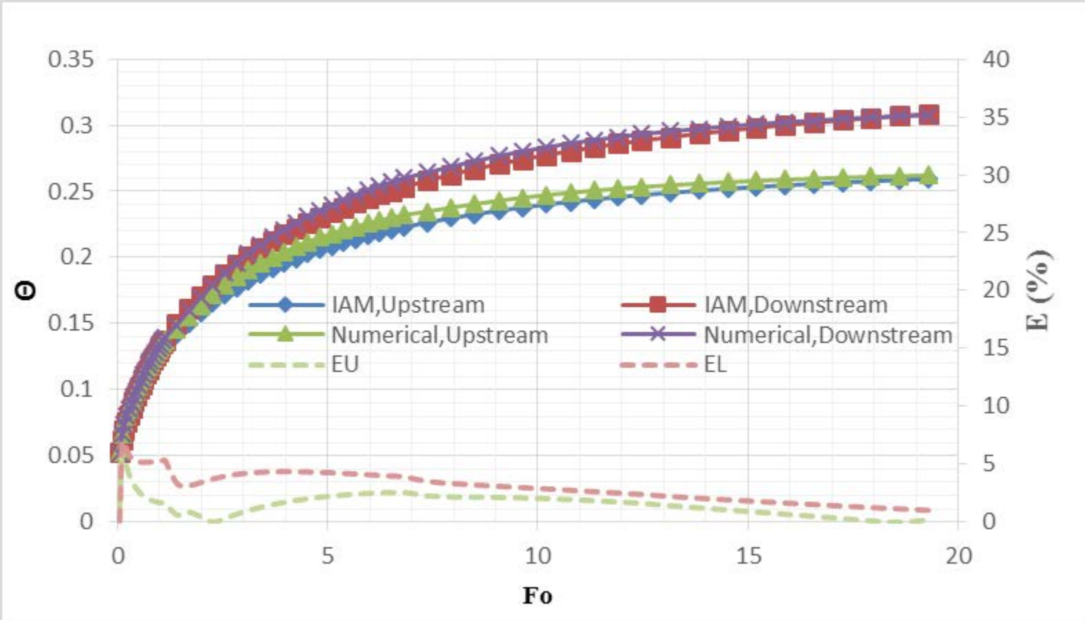

Figure 5-6 Comparisons of temperature responses from improved analytical model and numerical model of *I=5.10e-4*

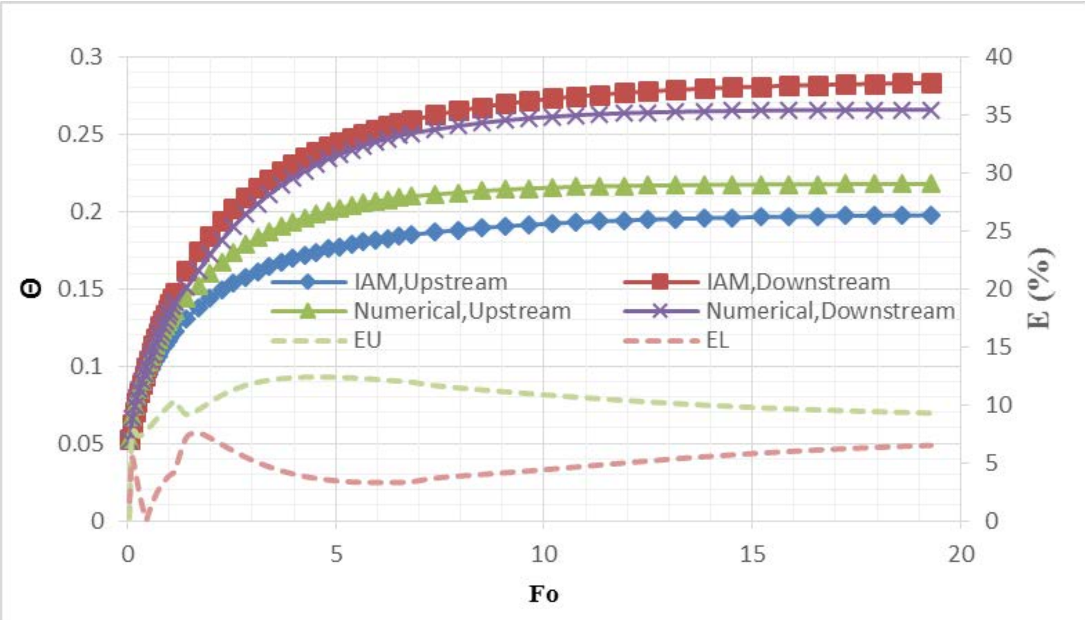

Figure 5-7 Comparisons of temperature responses from improved analytical model and numerical model of *I=1.02e-3*

Figure 5-5 shows the comparison of dimensionless temperature from the IAM and the numerical model with the hydraulic gradient of I=2.55e^{-4} which equals to 0.16 in effective groundwater flow velocity expression. A good agreement can be seen both on upstream and downstream sides. During the whole operation time, the relative calculation error is less than 5%. The temperature profiles with the hydraulic gradients of I=5.10e^{-4} and I=1.02e^{-3} are illustrated in Figure 5-6 and Figure 5-7, respectively. Comparing with the results from the OAM, the computational accuracy has been improved significantly. Similar to the data in Figure 5-5, the relative error in Figure 5-6 fluctuates slightly and keeps within specified bounds. The maximum error appears in the early stages of the test and becomes smaller at the end of the operation. As shown in Figure 5-7, a higher relative error has been found in the high hydraulic gradient, but it is still acceptable with an average error of 10%.

Figure 5-8 shows the temperature distribution at the upstream side under different groundwater flow conditions along the pile depth with R=1 and ***Fo***=19.2. Because of the discontinuity of heat source along the sampling line, the temperature fluctuates regularly along the depth. Due to the finite length of the pile, temperature response is high in the middle of the pile and becomes smaller at the end of the pile. Basically, numerical solution and analytical one are in good agreement with each other.

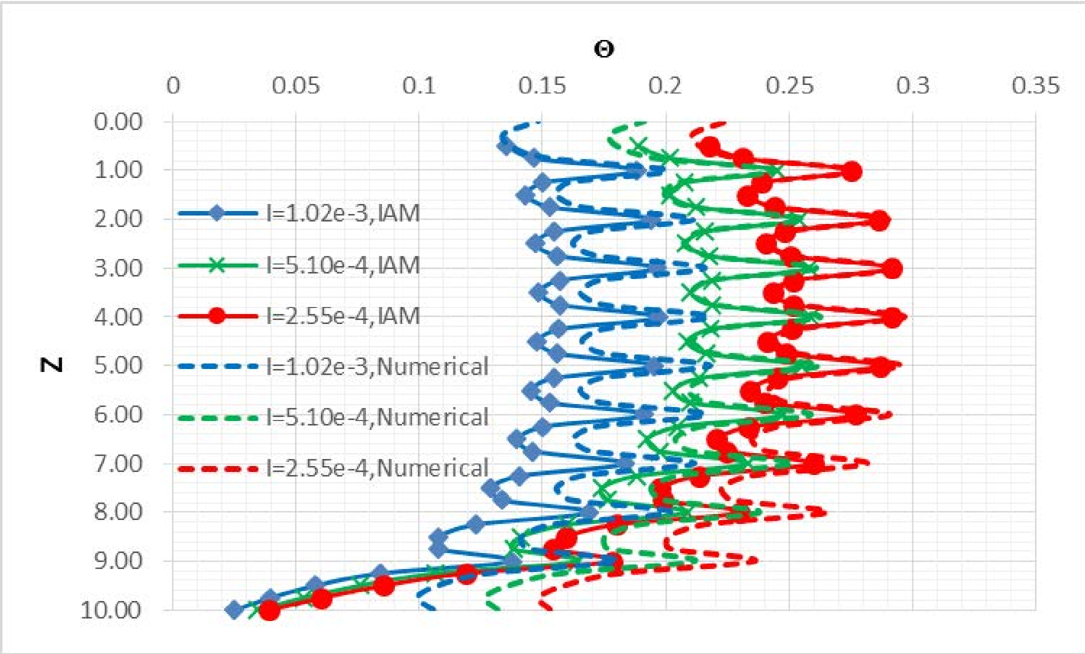

Figure 5-8 Temperature profiles along the pile depth from improved analytical model and numerical model with different hydraulic gradient (*Fo=20*)

Based on the computation data and charts, it is obvious that the IAM can better describe the temperature response of PGHE under groundwater flow compared with OAM. But, it should be pointed out that this improved model has its suitable application range. This improved model can be only used to estimate the temperature rise in pile and its accuracy decreases with the increase of the distance between heat exchange pipe and test point. Besides, the groundwater velocity should be less than 1e^{-5}m/s. Otherwise there might be a trend of divergence in the high hydraulic gradient. Generally, this velocity range can meet most application requirements (Chiasson et al., 2000), because the groundwater flow around the foundation pile should be as small as possible for safety considerations.

5.4.4 Findings

From the above numerical and analytical solution, it illustrates that the groundwater flow can effectively control the temperature rise of the heat exchange pipe. When ***Fo*** equals to 18.0, the dimensionless temperature response from numerical solution of I=2.55e^{-3} is 0.172, which is about half of the temperature calculated from the pure conduction model. The simulation results, as shown in Figure 5-3, also indicate that the groundwater flow has an accelerating effect on the heat transfer process of PGHE and this effect becomes more obvious with higher groundwater flow velocity. For the case of I=5.10e^{-4}, the heat transfer process becomes a steady state after Fourier number reaches 14.5. But, in the case of I=2.55e^{-3} and I=1.02e^{-3}, the Fourier number of steady state is much smaller, which equals to 7.1 and 4.0, respectively. The groundwater flow can effectively carry away the heat generated by energy pile and remove it to downstream.

Similar results can also be found at the downstream face, as shown in Figure 5-4. But, the temperature response of the downstream face is always higher than that of the upstream face under the same water flow condition, which can be seen clearly in Figure 5-9. The temperature profiles are calculated by simulation model at the same time but with different hydraulic gradients. Figure 5-9 (a) is under the smaller hydraulic gradient of I=2.55e^{-4}, and the hydraulic gradient of Figure 5-9 (d) is I=2.55e^{-3}. The effect of groundwater flow on PGHE with spiral-tube can be better understood by introducing a comparison parameter. Assuming a same temperature response on the pipe surface in both non-groundwater and groundwater condition, the average heat exchange ratio can be calculated as follow:

$$\frac{\overline{q_s}}{q_c} = \frac{\int_0^t \frac{k_s}{k_c} \frac{\Theta_c(t)}{\Theta_s(t)} \frac{\theta_s(t)}{\theta_c(t)} dt}{t} = \frac{\int_0^t \frac{\Theta_c(t)}{\Theta_s(t)} dt}{t} \tag{5.17}$$

where Θ_c is the dimensionless temperature of non-groundwater condition and Θ_s is the dimensionless temperature of groundwater condition.

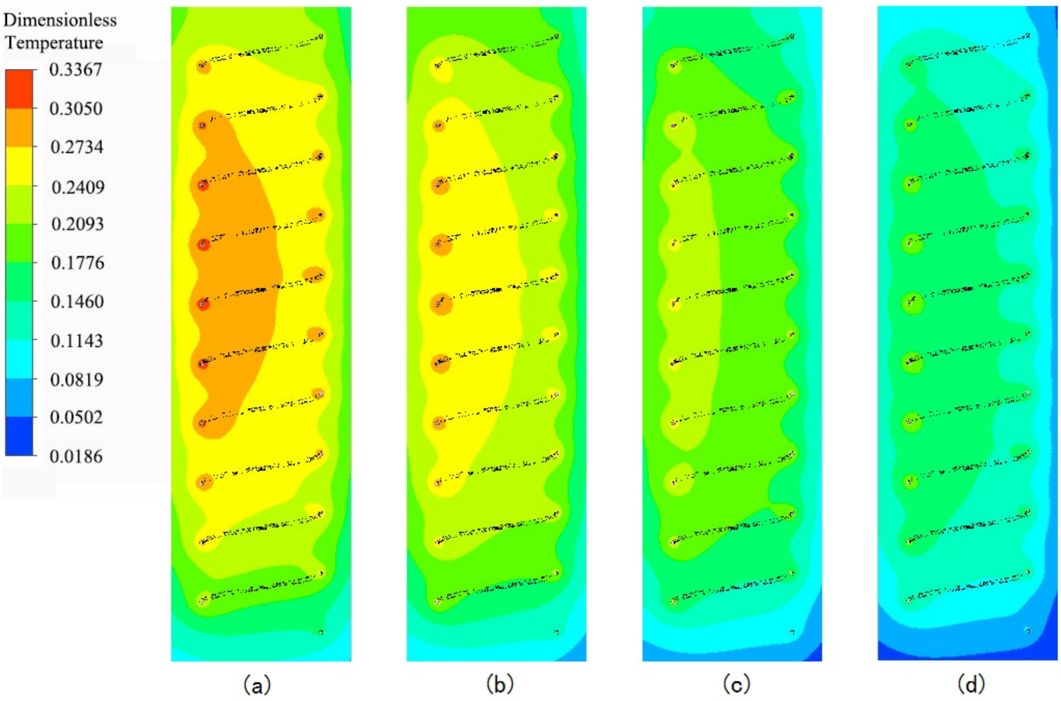

Figure 5-9 Temperature profile (a) of I=2.55e^{-4}, (b) of I=5.10e^{-4}, (c) of I=1.02e^{-3} and (d) of I=2.55e^{-3} with *Fo*=19.5

As shown in Figure 5-10, the average heat exchange ratio increases with the hydraulic gradient increase. For the case of the hydraulic gradient of I=2.55e^{-3} which equals to the groundwater flow mean velocity of 6.98e^{-6} m/s, the amount of heat exchange is 26.72% higher than that of the non-groundwater situation.

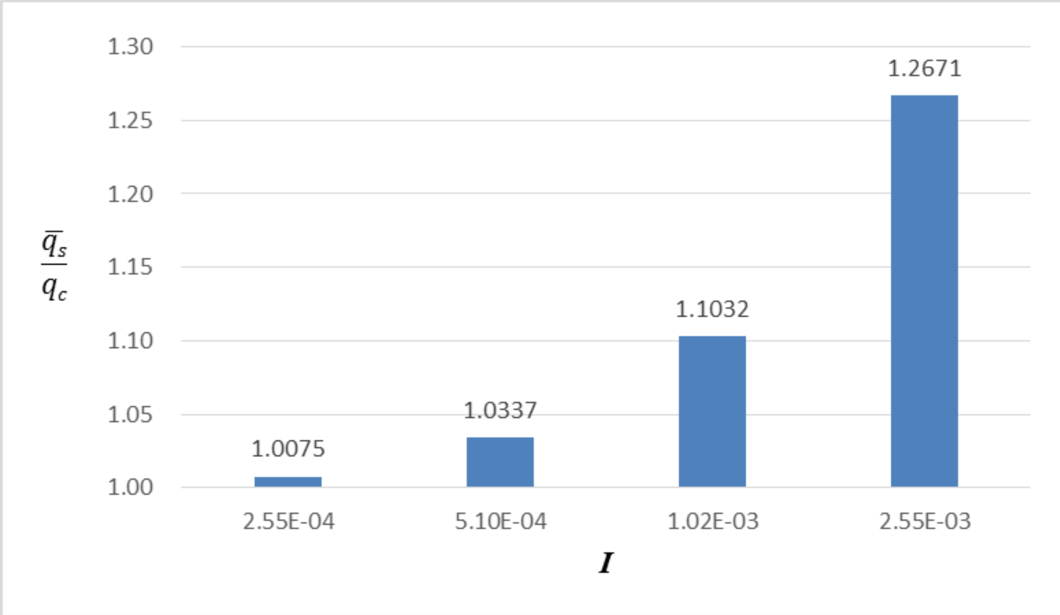

Figure 5-10 The average heat exchange ratio with different hydraulic gradient

5.5 Summary

In this chapter, the effect of groundwater flow on PGHE with spiral-tube was examined by using a simulation method. To model the groundwater advection, the heat transfer process in soil is regarded as a conduction and convection process in a porous medium. A good agreement is shown between the numerical model and ring-coils source model after few hours of operation. The results show that the groundwater flow can effectively control the temperature rise of the PGHE and make the heat exchange process enter the steady state more quickly. Accordingly, the heat transfer performance is improved by the groundwater advection, and its effects will be enhanced when the groundwater flow increases.

Based on the moving ring-coils model and simulation model, an improved analytical model has been established to better describe the heat transfer process of PGHE with spiral-tube under groundwater flow by introducing a key parameter of effective dimensionless velocity. Compared with the original moving ring-coils model, the accuracy of the approved analytical model has been improved significantly. But, it should be noticed that this improved model also has its application limitations. When the groundwater flow velocity is larger than $1e^{-5}$m/s, an obvious deviation can be detected. Besides, because this improved model is based on a serious numerical simulation solution, which serves as a baseline, its accuracy generally decreases with the increase of the distance between estimate point and heat exchange source along the radius direction. This could be a great help for PGHE design when groundwater advection exists.

Referring to the discussion in Chapter 2, the PGHE not only serves as a geothermal heat exchanger, but also provides supporting force for the super-structure. Thus, its thermo-mechanical performance has aroused great research concern. In the next chapter, focusing on the interface behaviour, the thermal load induced effect is investigated and discussed.

CHAPTER 6

INTERFACE BEHAVIOUR EXPERIMENT OF CONCRETE AND SOIL UNDER DIFFERENT THERMAL LOAD

6.1 Introduction

As the analysis in Chapter 2, it is of great importance to experimentally investigate the element behaviour of the interface between soil and structure under different thermal load. The interface behaviour is a key factor in the design and analysis of the ultimate bearing capacity of the pile foundation and can directly affect the mechanical response of pile. Thus, the influence of thermal load on the interface behaviour should be investigated firstly before any theoretical or numerical analysis for PGHE with spiral-tube.

The soil-structure interface is defined as a thin zone of soil which can be subjected to different boundary conditions with respect to the surrounding soil. Its thickness is generally considered to be 5 to 10 times the average particles diameter (Boulon & Foray, 1986). According to the previous studies, the interface behaviour is mainly influenced by the normal stress, the soil density, the volumetric response, the moisture content of the soil (matric suction) and structure roughness.

Although there are some researches in the field of soil-structure interface behaviour, the effect of temperature on the soil-concrete interface is only partially considered. Therefore, the main goal of this experiment is to investigate the mechanical response of the soil-concrete interface behaviour under heating/cooling conditions. Firstly, a summary of the state of knowledge relating to the interface behaviour test is presented. Then, based on the traditional direct shear apparatus, a modified direct shear apparatus with temperature control is introduced. Special attention is paid to the description of the components assembling the new shear apparatus. A detailed experiment program is described as follows. Quartz sand and red clay are selected as investigating objects in this study. Both two kinds of interface behaviours (sand-concrete and clay-concrete) are tested under different thermal loads (heating or cooling). Finally, all the results of the experiments are presented and discussed. A rough analysis is given to explain the phenomenon existing in the interface behaviour test, and the limitations in this test are also presented at the end of this chapter.

6.1.1 Effect of normal stress and soil density

The shear force, τ_f, in the interface behaviour test generally increases linearly with the normal stress, $\sigma_n^{'}$. The higher normal stress, the higher shear force. If considering the adhesive force, when the normal stress is equal to zero, the shear force can be expressed as follows:

$$\tau_f = c^{'} + \sigma_n^{'} \tan\left(\varphi_f\right) \tag{6.1}$$

where δ is the fiction angle at soil-structure interface. For the sandy soil, the shear force pushes the particle rolling up from the lower. Thus, the tight sandy soil always shows dilatancy under the shear test. The clay interface behaviours are generally contractive, but show dilation if the soil sample experience very high consolidated force.

6.1.2 Effect of structure roughness

The structure roughness is also an important parameter in interface behaviour experiment. It is commonly defined as the normalized roughness R_n by Uesugi and Kishida (1986):

$$R_n = \frac{R_{\max}}{D_{50}} \tag{6.2}$$

where R_{max} is the maximum vertical distance between the highest and the lowest point of the structure surface and D_{50} is the soil mean grain size, shown in Figure 6-1. Alice et al. (2015) studied the effect of the surface on the soil-concrete interface in a direct shear device. They tested three values of roughness (R_n equal to 0.001, 0.06 and 0.1) in the sand-concrete experiment and two values (R_n equal to 0.001 and 0.06) in the clay-concrete experiment. Borana et al. (2015) studied the influence of roughness on soil-steel interface behaviour. Three interface specimens are designated (R_n equal to 0.041, 5 and 10) in the experiment. Their results showed that the resistance between soil and structure is higher in the case of rough interface and lower in smooth case, but always lower than the resistance of soil-soil.

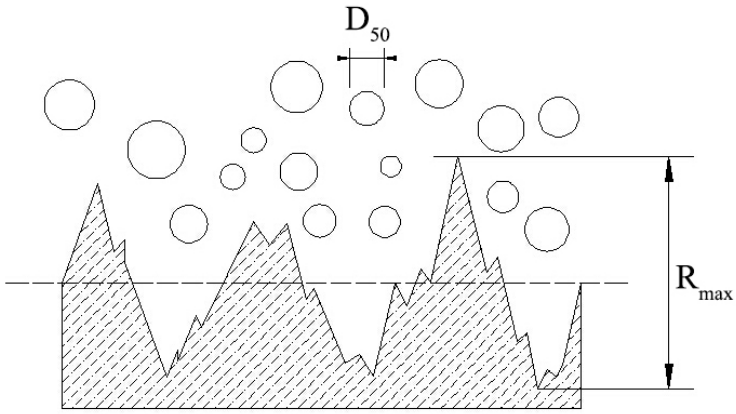

Figure 6-1 Representation of the soil-structure interface roughness

6.2 New experimental apparatus and test materials

6.2.1 The original direct shear device

The original version was a direct shear apparatus with suction control (DSA-S), which was installed in 2008. The DSA-S consists of an air pressure chamber, two high air entry porous disks (HAEPD), diffused air volume indicator (DAVI), pressure/volume controller and measuring device. The shear displacement is controlled by an electro-motor, which can provide a minimum shear rate of 0.001mm/min. The horizontal and vertical displacements are monitored by two linear voltage displacement transformers (LVDT). The shear box is designed with an accommodation area of $10\text{cm}\times10\text{cm}$ and height of 40mm. The box consists of two parts: the upper box and the lower box. The upper one is designed to accommodate soil samples and the concrete is placed in the lower one. These two boxes are separated during shearing.

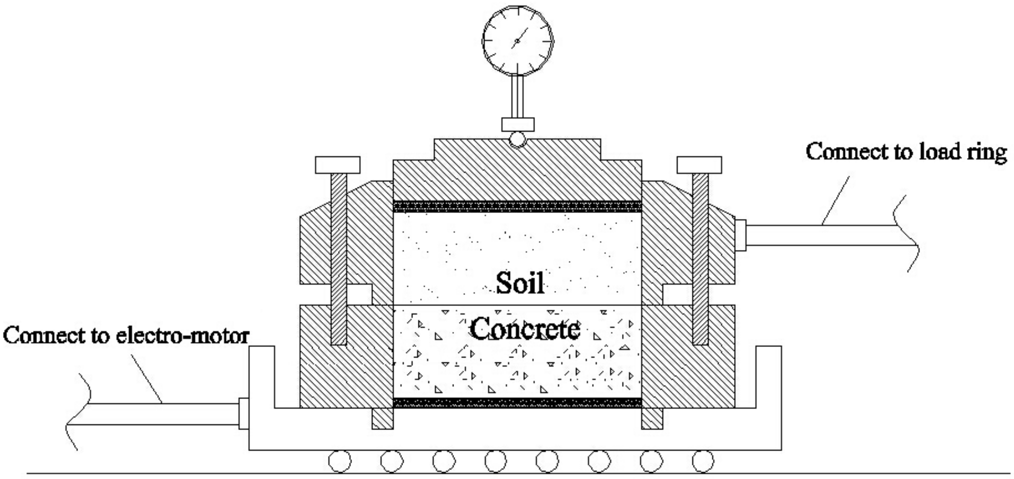

Figure 6-2 Schematic diagram of traditional modified direct shear apparatus.

The axis parallel translation technique is applied in the original DSA-S. HAEPD is embedded in the steel plate and installed over the water chamber. The HAEPD has a constant air entering pressure and can be easily replaced based on the target suction values. By controlling the air and water pressure, the DSA-S can obtain a target suction of the soil sample, but with a limited control ability.

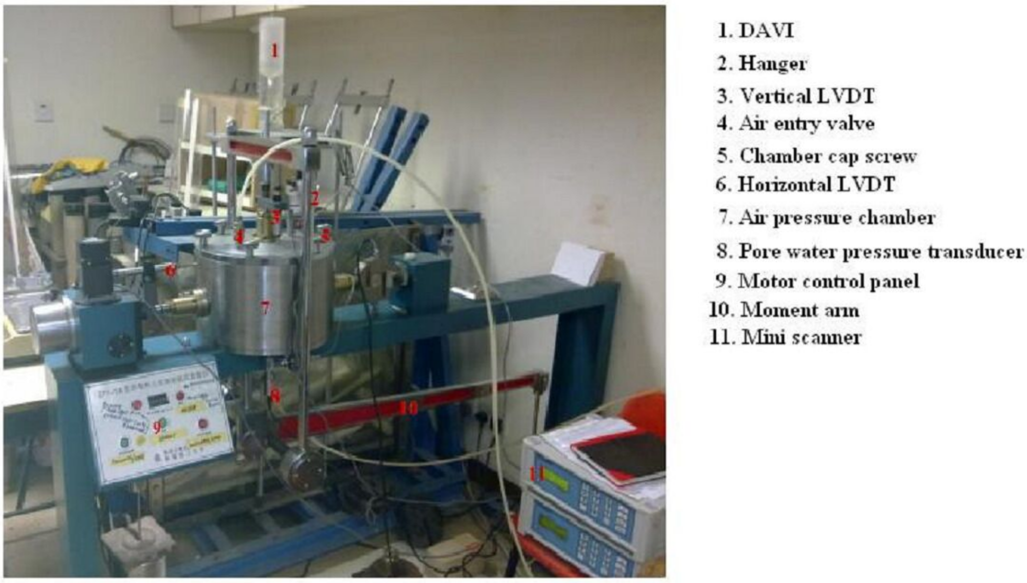

Figure 6-3 A photograph of the original direct shear apparatus used in the previous study (Borana, 2013)

6.2.2 New experimental apparatus

Based on the state of art, there is no available direct shearing device which can control the temperature during the shearing process. Thus, to control the temperature, a new direct shearing apparatus with temperature control (DSA-T) was designed, developed and employed. The new apparatus consists of an air pressure chamber, an air circulation pump, a heating/cooling system, a solution system and measuring/monitoring system, as shown in Figure 6-4.

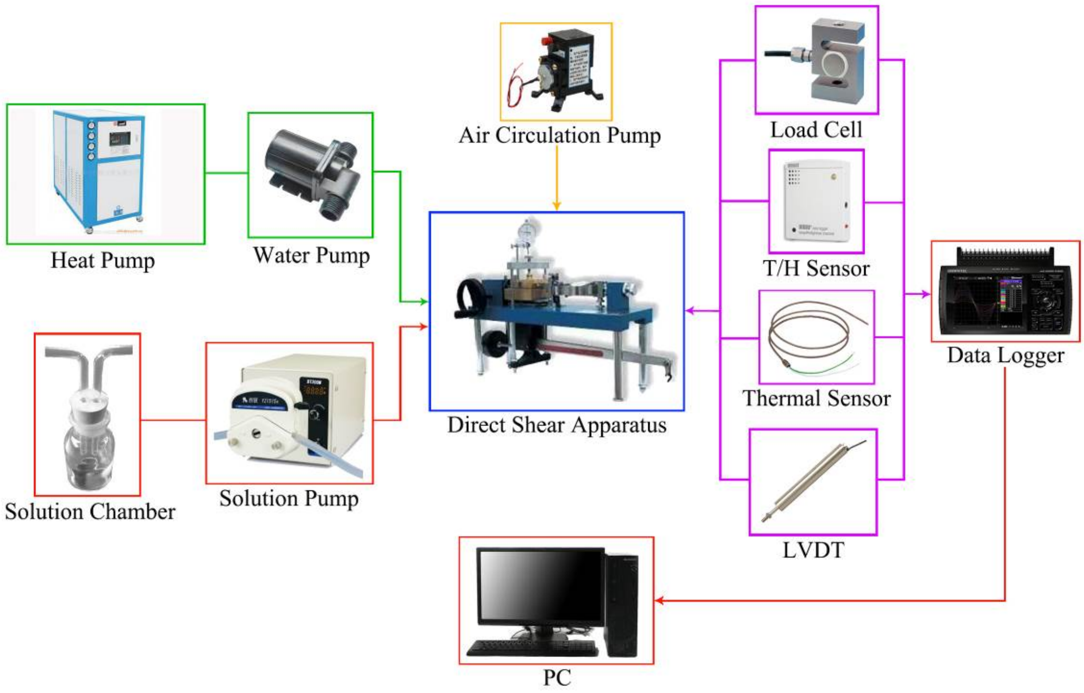

Figure 6-4 The schematic diagram of the testing and data acquisition system of the MDS test bed

The design of the DSA-T is based on a shear apparatus design by Borana (2013). The original apparatus is a suction controlled direct shear device. An airtight chamber is isolated the shear box from the atmospheric condition in order to using the axis-translation technology to control the suction of soil. Two load cells are installed to measure the force in vertical and horizontal direction. The vertical and horizontal displacement are measured by the two linear voltage displacement transformers (LVDT).

Comparing with the original device, one of the major differences of the DSA-T in this study is the temperature control system that can simulate the heating and cooling process of energy pile. Another one is the suction control method. A solution circulation system is applied to control the humidity level in the air chamber, so that the suction will be maintained during the shearing process. To enhance the heat and mass transfer in air chamber, an air circulation pump is installed and has a maximum flow rate of 1 L/min. Thermal and humidity sensors are applied to monitor the heat and mass transfer in the shear box. The data logger reads all the measurements and communicates to the computer during the whole experiment.

Table 6.1 Main parts list

No.	Item	Number	No.	Item	Number
M01	Main Chamber	1	M07	Air Circulation Pump	1
M02	Direct Shear Apparatus	1	M08	Load Cell	1
M03	Water Tank	1	M09	T/H Sensor	2
M04	Water Pump	1	M10	Thermal Sensor	5
M05	Solution Chamber	1	M11	LVDT	2
M06	Solution Pump	1	M12	Data Logger	1

6.2.3 Air chamber

For the soil-concrete test, the air chamber was required to accommodate the shear box, solution control box, and heat/cooling box. Based on this concept, the shear box can be divided into two parts, the upper box and the lower box plate, shown in Figure 6-5. During the shearing experiment, the upper box cannot move as it is and connected to the load cell. The moving part is the lower box plate which is fixed to the solution box and water box through four screws. The upper box has a square section of 100×100 mm^2 and height of 30mm, designed for soil samples. The concrete sample is accommodated into the lower box plate with the same section area of the upper box, but the height of 20mm. An air/solution chamber under the lower box was used to generate a designed humidity air for suction control.

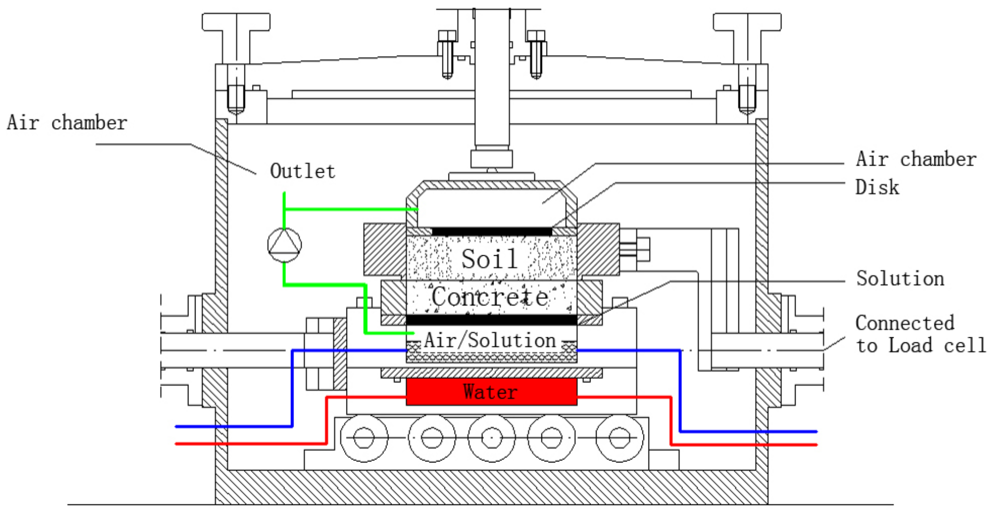

Figure 6-5 Schematic diagram of direct shear apparatus with temperature control for soil-concrete interface test.

To enhance the airflow exchange, a small circulation pump was installed in the air chamber. The upper box and the lower one were linked by the circulation pump. Two air vent holes are located on the upper box cover, shown in Figure 6-6 (b), to ensure the air humidity uniform between upper box and air chamber. For the purpose of heating/cooling the air chamber, a water tank was fixed at the bottom of the air/solution box. Two water pipes come out from the water box and are connected to a water tank through two holes made on the air chamber. Figure 6-6 gives the photographic view of all the parts in the air chamber used for soil-concrete interface behaviour experiment. All the parts are made of stainless steel.

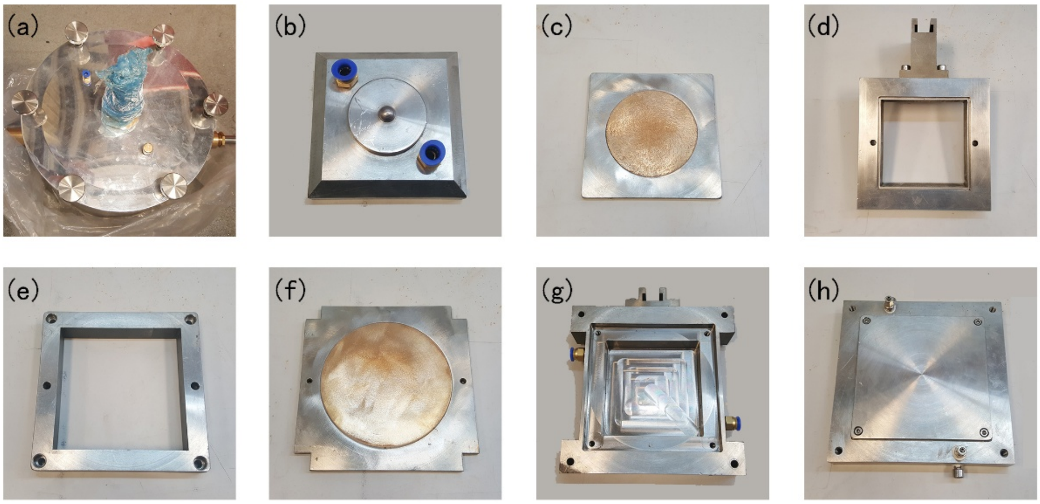

Figure 6-6 Development of the shear box for soil-concrete interface test:
(a) air chamber, (b) upper box cover, (c) upper porous, (d) upper box, (e) lower box plate, (f) lower porous, (g) solution box and (h) water box.

Table 6.2 Item list of Main Chamber

No.	Item	Quantity	No.	Item	Quantity
C01	Up chamber	1	C07	Bottom box	1
C02	Chamber body	1	C08	Bottom porous	1
C03	Top box cover	1	C09	Air box	1
C04	Up porous stone	1	C10	Water box	1
C05	Top box body	1	C11	Set bolt	4
C06	Link box	1	C12	Holding bolt	6

6.2.4 Temperature control and monitoring system

The heating/cooling system used in DSA-T is composed of (1) a water tank, (2) a water circulation pump, (3) a water box and (4) two thermocouples. The water tank with a volume of 50 L has a good accuracy (±1℃) and can automatically maintain a required temperature. This tank is protected by an insulation cover so that it can easily heat the water up to 95 ℃. A water chilling unit is used to provide the chilled water when simulating the cooling condition during the shearing test. The water tank is connected to the air chamber by two high-temperature resistance pipes, and a variable frequency pump is installed to circulate the hot/cooling water between the tank and the air chamber. To monitor the temperature changing during the shearing test, two thermocouples are installed in the air chamber. One is located on the side between the upper box and the lower box to monitor the temperature of soil-concrete interface and the other one is placed on the inner side of the air chamber to measure the air temperature inside the chamber. All the sensors used in this experiment are calibrated.

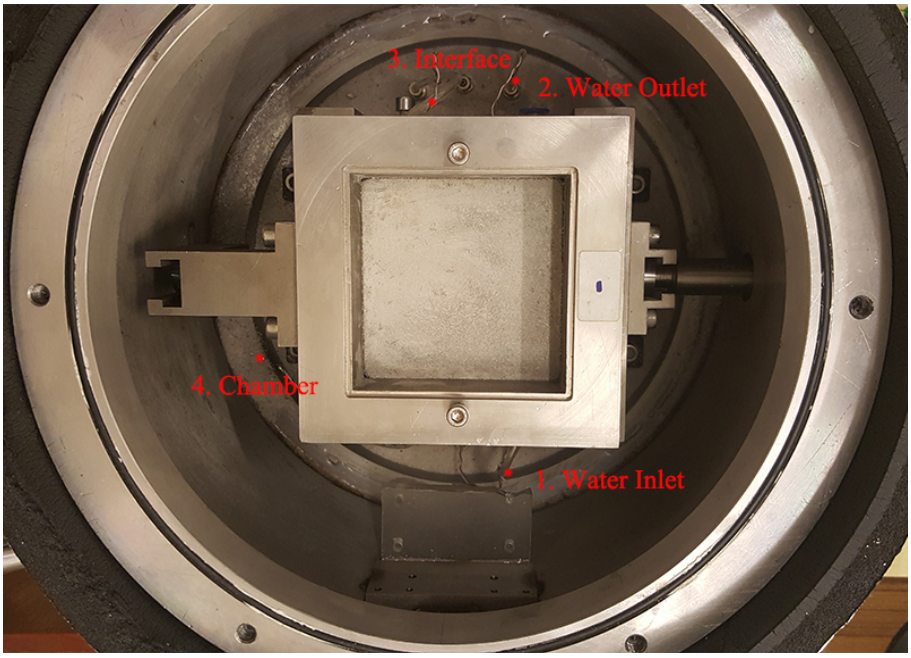

Figure 6-7 Schematic diagram of the temperature monitoring sensors

6.3 Experiment program

6.3.1 Tested materials

Concrete is selected as the structure material in this soil-structure interface behaviour experiment. For the soil material, two typical soil materials are selected. One is quartz sand, and the other one is clay. The detail information of the experiment materials is summarized as follows.

- **Quartz sand**

The quartz sand, extracted from a China quarry, was selected for the interface experiment of the sand-concrete. The grain size of the test sand ranges between 0.008 and 1.0 mm. The grain size distribution is presented in Figure 6-8.

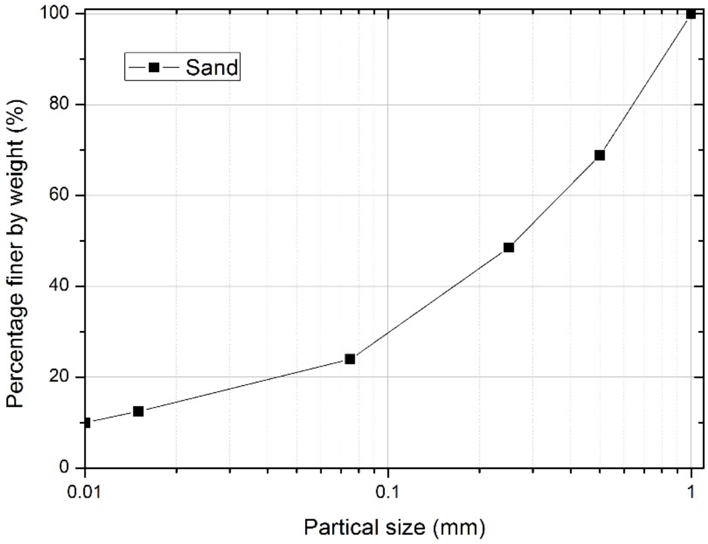

Figure 6-8 Particle size distribution of quartz sand

The main properties of the sand are summarized in Table 6.3. D_{50} is the median diameter of the sand particle size distribution, and D_{10} is the value of the particle diameter at 10% in the cumulative distribution. All test samples of the sand were prepared by dry sample, at 105 ℃ for over 24 hours.

Table 6.3 Main properties of the quartz sand

10% Sand diameter	D10 [mm]	0.015
50% Sand diameter	D50 [mm]	0.285
Grain density	ρs [g/cm3]	2.59

- **Clay**

The red clay soil, which is widely distributing in the east of China and used as a backfill material locally, was used in this study. The original soils used in this test were collected from a clay quarry at Hebei province, China. It can be seen in Figure 6-9, that the clay has a fine fraction, as shown in the grain size distribution curve.

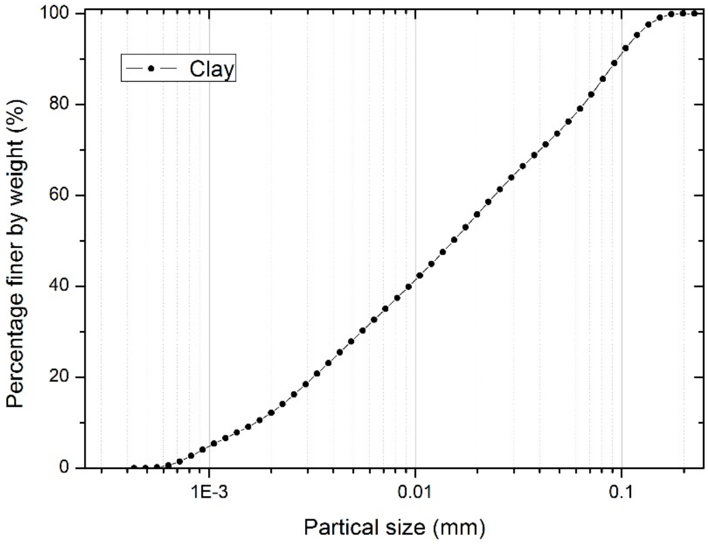

Figure 6-9 Particle size distribution of clay

This material is composed of Fe_2O_3 (15.2%), Al_2O_3 (30.03%), SiO_2 (46.85%), K_2O (3.16%), MgO (2.09%). The main properties (liquid limit, plastic limit, plasticity index, grain density, maximum dry density, etc.) are summarized in Table 6.4. The soil material was dried in oven at 105 ℃ over 24 hours, and conserved tightly sealed. Before the shearing test, the specimens were mixed with distilled water to a target water content of 23%, and filled into the shear box.

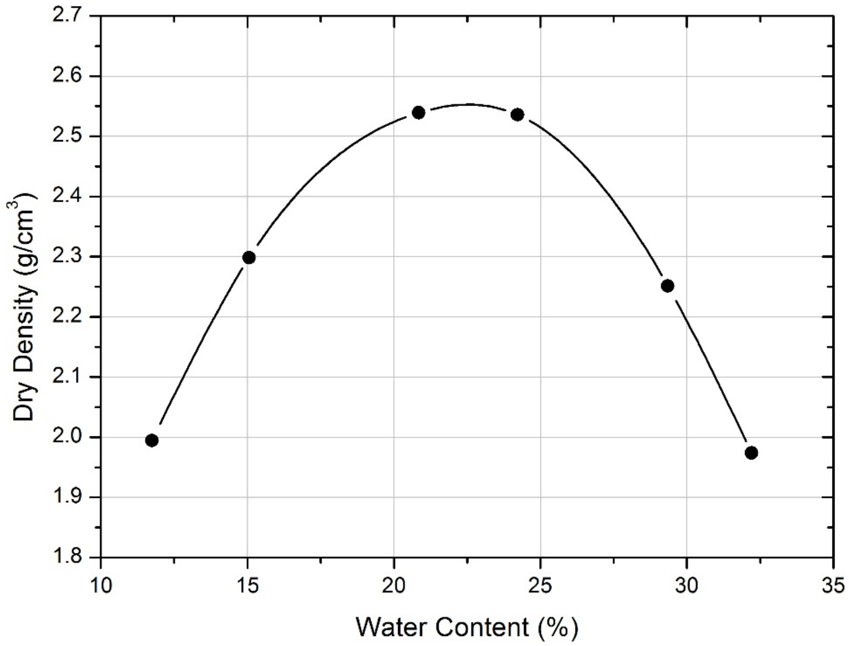

Figure 6-10 The relationship curve of ρ and w

Table 6.4 Main properties of the clay

Liquid limit	WL [%]	22.6
Plastic limit	WP [%]	49.5
Plasticity index	IP [%]	26.9
95% Clay diameter	D95 [mm]	0.12
Max. dry density	ρm [g]	2.54

- **Concrete**

The concrete was prepared in the laboratory mixing cement, water and aggregates, based on the JGJ 55-2011. The target density of concrete is assumed to be around 2100 kg/m^3, thus the volume of aggregates is 250g and the cement is 125g mixed with 250g water. The normal river sand is used as the aggregate with particles diameter equal or smaller than 1mm.

Table 6.5 Concrete mixing proportion

Cement mass	Mc [g]	250
Water mass	Mw [g]	125
Aggregate mass	Mi [g]	250
Water/cement ratio	w/c [-]	0.5

A smooth concrete surface is created for the shear test of san-concrete. For the interface test of clay-concrete, the surface roughness is assumed to be 0.25. Thus, to obtain the target concrete roughness, the sand with an average target size was sprinkled on a layer of glue spread on a support plane and the concrete was poured on it. In this way, once the concrete has hardened and is removed, the sand remains glued to the support plane and the lower surface of the concrete sample is characterized by a roughness which depends on the sand grain size. The normalized roughness employed for this study is presented in the following. Finally, a slide of the concrete sample is cut and a specimen of the correct dimension for the shear box is cut in it. For the smooth surface specimen, the surface was treated on purpose employing a grinding machine.

6.3.2 Experiment arrangement

The experimental campaign can be divided into three parts: 1) preliminary test on soil sample, 2) interface test on sand-concrete and 3) interface test on clay-concrete. For the first part, both the clayey and sandy soil are sheared under room temperature (24℃) to test the selected soil under standard direct shear condition and to determine their normal soil mechanics properties. Three normal stress, 50kPa, 100kPa and 150kPa, are considered as the effective normal stress both for preliminary test and interface test.

Details are shown in Table 6.6. For the second part, interface test on sand-concrete, all the sand samples were sheared under dry conditions and a smooth concrete surface was applied during the test. All the prepared samples firstly experienced a consolidation process, and then a target thermal load was applied to the test chamber until the end of each shear test. After 24 hours, it is assumed that the test sample achieves the thermal equilibrium (Figure 6-11). Then, the sample was sheared under certain normal stress. For the interface test on clay-concrete, the loading path is basically the same with the sand-concrete test, but with a little difference in some aspects. All the clay soil samples are run under full saturated vapour pressure conditions, and a rough concrete surface was applied during the test. Both for these two interface behaviour tests of sand-concrete and clay-concrete, three different temperature conditions, 8℃, 24 ℃ and 60℃ are investigated.

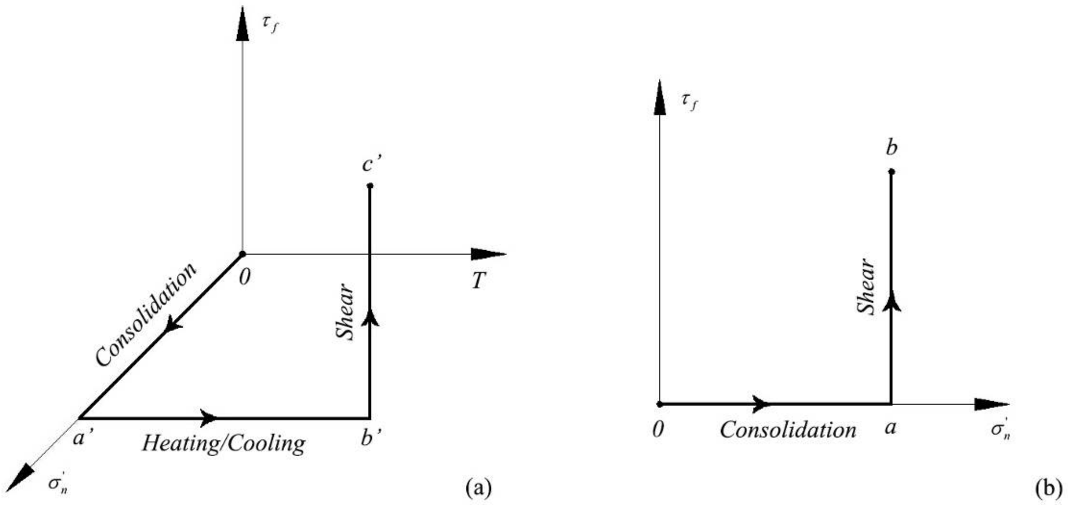

Figure 6-11 Loading path during the interface test of soil-concrete at (a) heating/cooling condition and at (b) normal temperature

As the sandy interface test mostly happens under drained conditions, the shearing velocity does not play an important role in the case of sand-structure interface experiment. Thus, referring to the ASTM Standard (2012), the decision was taken to assume a shear rate of 0.25mm/min. For the case of clayey soil, referring to the previous interface research studies of clay (Borana, 2013; Di Donna et al., 2015), the shear rate applied for clay-concrete interface experiment is determined as 0.006mm/min.

Table 6.6 Preliminary test of soil samples

Test number	Test name	Material	Normal effective stress[kPa]	Hydraulic condensation
101	SS_TN_50a	Sand	50	Dry
102	SS_TN_100	Sand	100	Dry
103	SS_TN_150	Sand	150	Dry
104	SS_TN_50b	Sand	50	Dry

Table 6.7 Sand-concrete interface test

Test number	Test name	R	T [℃]	Normal effective stress [kPa]	Hydraulic condensation
301	SC_TN_S_50	Smooth	24	50	Dry
302	SC_TN_S_100	Smooth	24	100	Dry
303	SC_TN_S_150	Smooth	24	150	Dry
304	SC_TH_S_50	Smooth	60	50	Dry
305	SC_TH_S_100	Smooth	60	100	Dry
306	SC_TH_S_150	Smooth	60	150	Dry
307	SC_TC_S_50	Smooth	10	50	Dry
308	SC_TC_S_100	Smooth	10	100	Dry
309	SC_TC_S_150	Smooth	10	150	Dry

Table 6.8 Clay-concrete interface test

Test number	Test name	R	T [℃]	Normal effective stress [kPa]
401	CLC_TN_S_50	Rough	24	50
402	CLC_TN_S_100	Rough	24	100
403	CLC_TN_S_150	Rough	24	150
404	CLC_TH_S_50	Rough	60	50
405	CLC_TH_S_100	Rough	60	100
406	CLC_TH_S_150	Rough	60	150
407	CLC_TC_S_50	Rough	10	50
408	CLC_TC_S_100	Rough	10	100
409	CLC_TC_S_150	Rough	10	150

6.3.3 Test specimen preparation

In this experiment, all the clay specimen either for preliminary soil-soil test or for the soil-concrete test were prepared as follow steps: pre-treatment of the intact sample, mixing with water, and compacting the specimen.

- Pre-treatment of the intact sample

The intact was cut into several pieces and dried in an oven for 24 hours at 105 ℃. The drying intact samples were broken into small particles by using a rubber plate. Then, the particles were sieved by a 1 mm sieve and the particles larger than 1 mm sieve were removed. The soil particles passing through this sieve were collected and continued to be dried for over two days under the temperature of 105 ℃.

- Mixing with water

The dry soil particles were mixed with the distilled water in a mixing bowl. In this study, the target water content is 23%, when the sample achieves compaction.

- Compacting specimens

The wet soil sample was compacted inside a square mould, with a dimension of 100×100 mm^2. The inner side of the mould was brushed with a little of lubricating oil. Then, the prepared wet soil sample was put into the mould layer by layer. For the preliminary test, a 40 mm thick specimen needs to be prepared. The specimen was compacted into the mould by four layers, and each layer has the thickness of 10mm. The required mass of every player needs to be controlled with the accuracy within 0.05g. For the soil-concrete test, a 20mm specimen was required, which was fabricated by three layers. After the compacting process, the soil specimen should achieve a target dry density of 2.53 g/cm^3.

6.4 Results

The experiment results obtained from the interface behaviour test are summarized and discussed separately for both sand and clay soil. With the aims of further calibrating the device, the preliminary tests firstly run. Then, the interface behaviour test was conducted and presented as follows.

6.4.1 Preliminary test

Figure 6-12 and Figure 6-13 show the shear stress and vertical displacement variation with the change of horizontal displacement. All the sand-sand specimens are sheared under room temperature conditions (24℃) with a constant shear rate of 0.25mm/min. As shown in Figure 6-13, under each normal stress, the shear force keeps increasing within the initial horizontal displacement, and then maintains at a constant value. The maximum shear force with the relationship of normal stress is summarized in Figure 6-13 (b). A clearly linear relationship can be obtained with a friction angle of 31.06°.

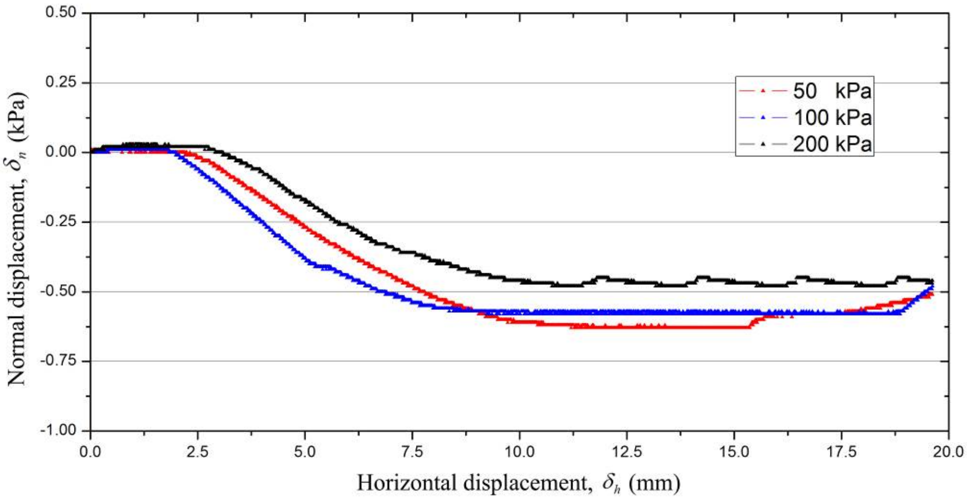

Figure 6-12 Variation of normalized vertical displacement versus horizontal displacement under different normal stress during the sand-sand shear test

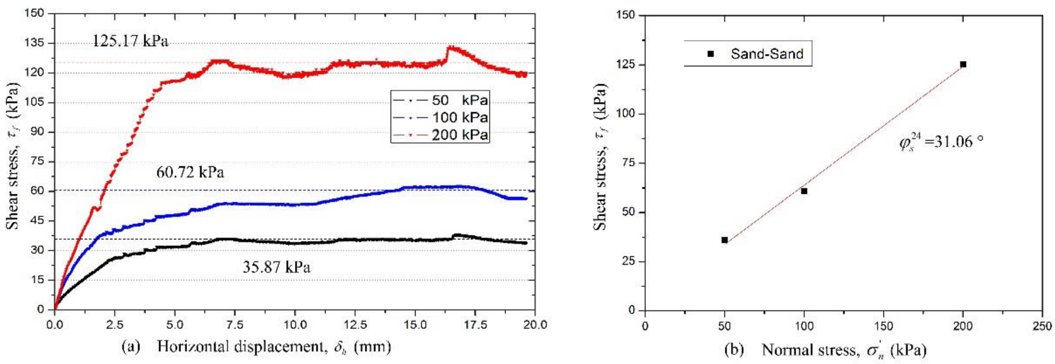

Figure 6-13 Quartz sand response during the shear test

6.4.2 Sand-concrete behaviour

Three series of tests were conducted for the sand-concrete interface behaviour investigations. All the sand-concrete tests were run at fully dry conditions. The first series of tests were sheared under room temperature (24℃) with a strain rate of

0.25mm/min. Three target normal stresses (50kPa, 100kPa and 150kPa) were considered in this series. As shown in Figure 6-14, the sand-concrete interface shows a continuous dilation response (suppose the negative normal displacement is dilation) after a small compression phase. The degree of dilation induced by shear movement shows an increase with the shear stress and decrease with the increase of the normal stress.

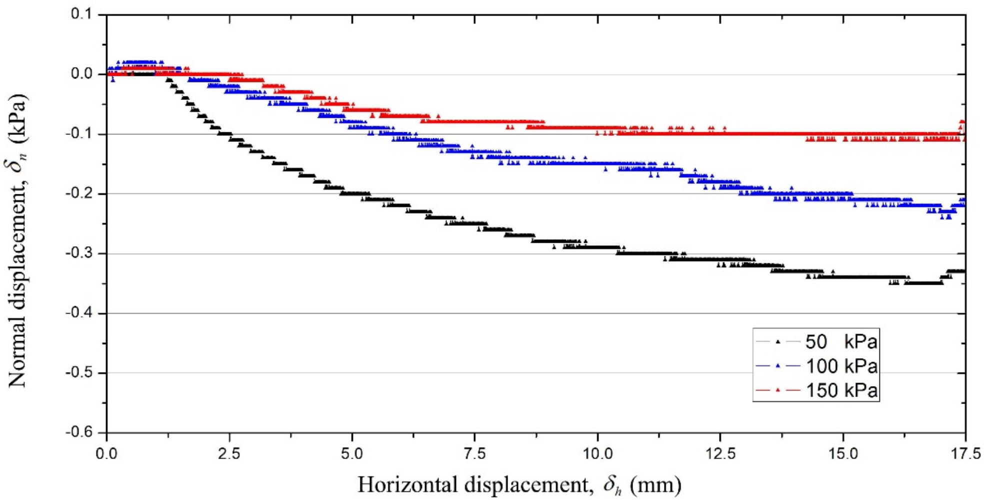

Figure 6-14 Variation of normalized vertical displacement versus horizontal displacement under different normal stresses at room temperature condition (24°C) during sand-concrete interface test.

Figure 6-15 presents the relationship between shear stress and horizontal displacement under different normal stress loads. It is clearly pointed out that the maximum shear stress increase with the increase of normal stress. Additionally, compared with the stress curve under high normal stress condition (150kPa), the interface is noted to become stable with less time.

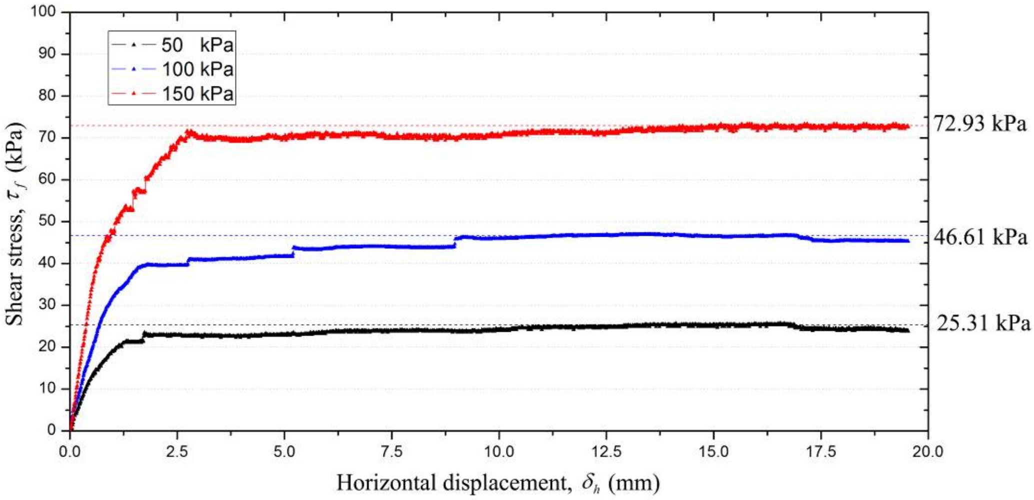

Figure 6-15 Variation of shear stress versus horizontal displacement under different normal stresses at room temperature condition (24˚C) during sand-concrete interface test

To achieve the main purpose of investigating the influence of temperature on the interface behaviour, two series of interface tests were run under heating and cooling conditions. Only dry conditions are considered in the sand-concrete tests. Each series consists of three tests under different normal stress. For the series under the heating condition, every test was run at a constant temperature of 60℃. The experiment data are summarized in Figure 6-16 and Figure 6-17. As shown in these figures, even if the temperature undergoes to be 60℃, the thermal load does not much affect the sand-concrete interface behaviour.

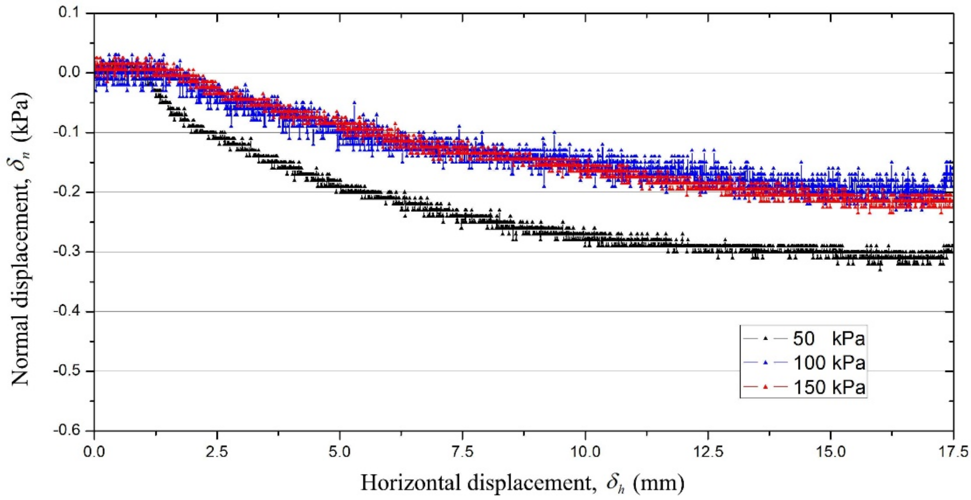

Figure 6-16 Variation of normalized vertical displacement versus horizontal displacement under different normal stresses at heating condition (60˚C) during sand-concrete interface test.

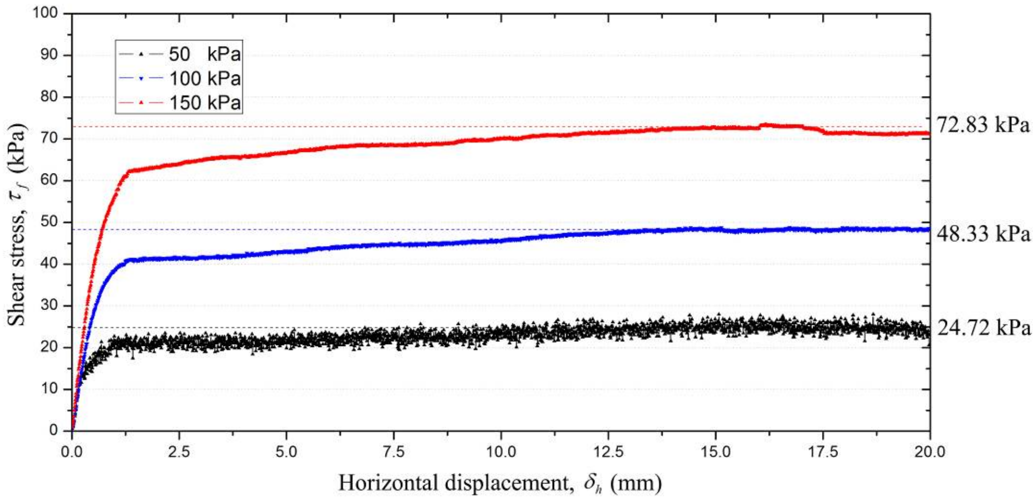

Figure 6-17 Variation of shear stress versus horizontal displacement under different normal stresses at heating condition (60˚C) during sand-concrete interface test.

For the series of the cooling condition, three tests were run under different normal stress loads and the test environment is maintained at 10℃. The main results are plotted in Figure 6-18 and Figure 6-19. The shear stress profile is much similar to that of the normal condition, which indicates that the interface has little influence by the low temperature.

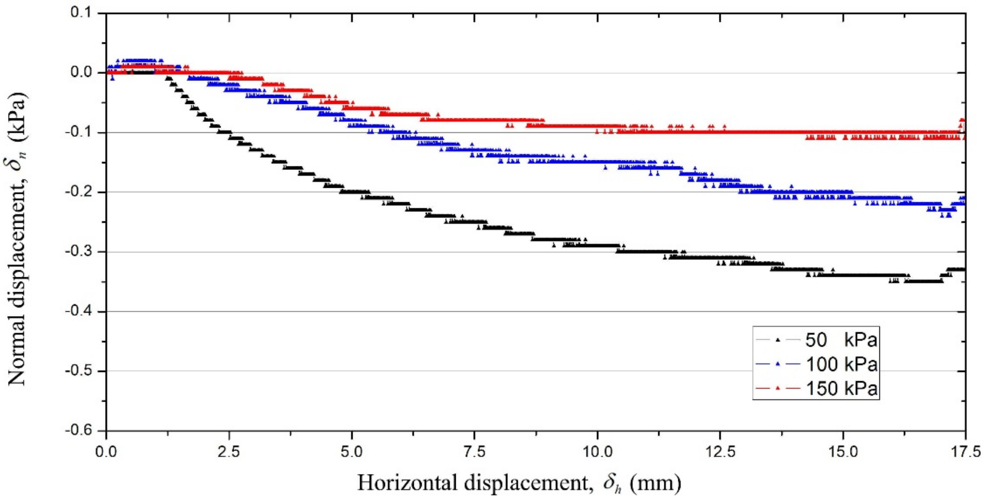

Figure 6-18 Variation of normalized vertical displacement versus horizontal displacement under different normal stresses at cooling condition (10˚C) during sand-concrete interface test.

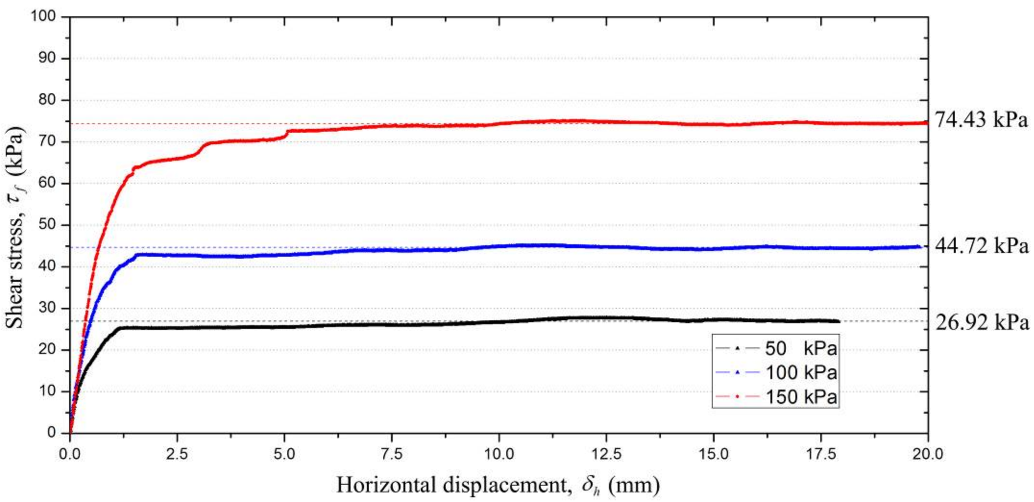

Figure 6-19 Variation of shear stress versus horizontal displacement under different normal stresses at cooling condition (10˚C) during sand-concrete interface test.

All the sand-concrete interface test results are summarized in Figure 6-20. It is clearly shown that the interface response either at high or low temperature conditions does not have the obvious difference to that at normal temperature condition. The friction angle (φ) of sand-concrete is found to be 25.51 on average.

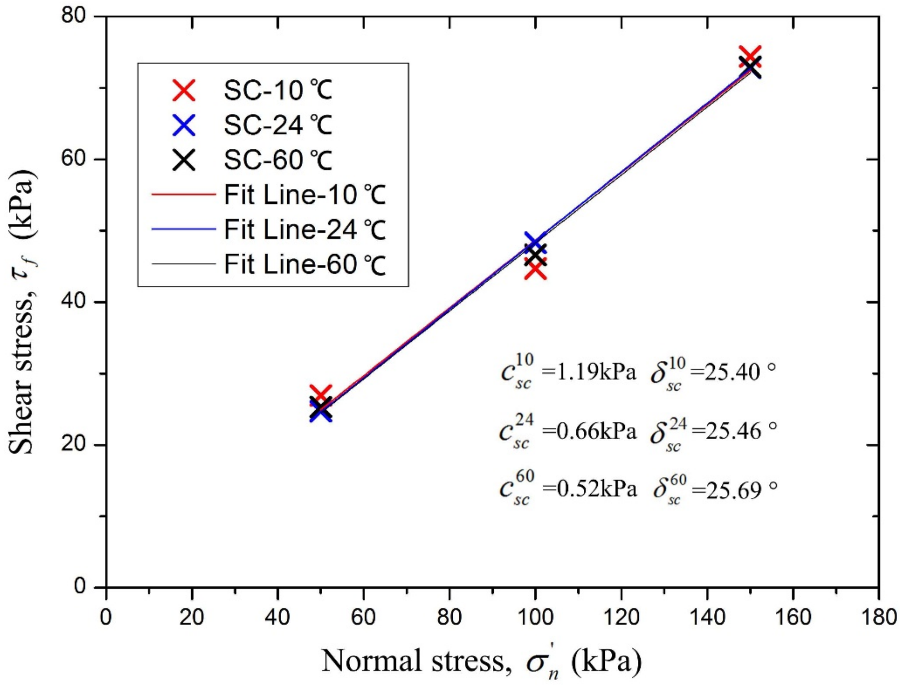

Figure 6-20 Relationships between shear strength and net normal stress under different thermal load during sand-concrete interface test

The test results were rearranged according to the normal stress load, and plotted in Figure 6-21. At a certain normal stress, the shear stress response of interface is always lower than that of the sand-sand test. This phenomenon indicates that the surface roughness of interface is lower than that of the sand, as a consequence, the shear failure occurs at the interface, but not in the sand. Additionally, at a certain normal stress, comparing the stress curves among 10℃, 24℃ and 60℃, it is further confirmed that no thermal induced effect can be clearly observed on the interface behaviour between sand-concrete in fully dry conditions.

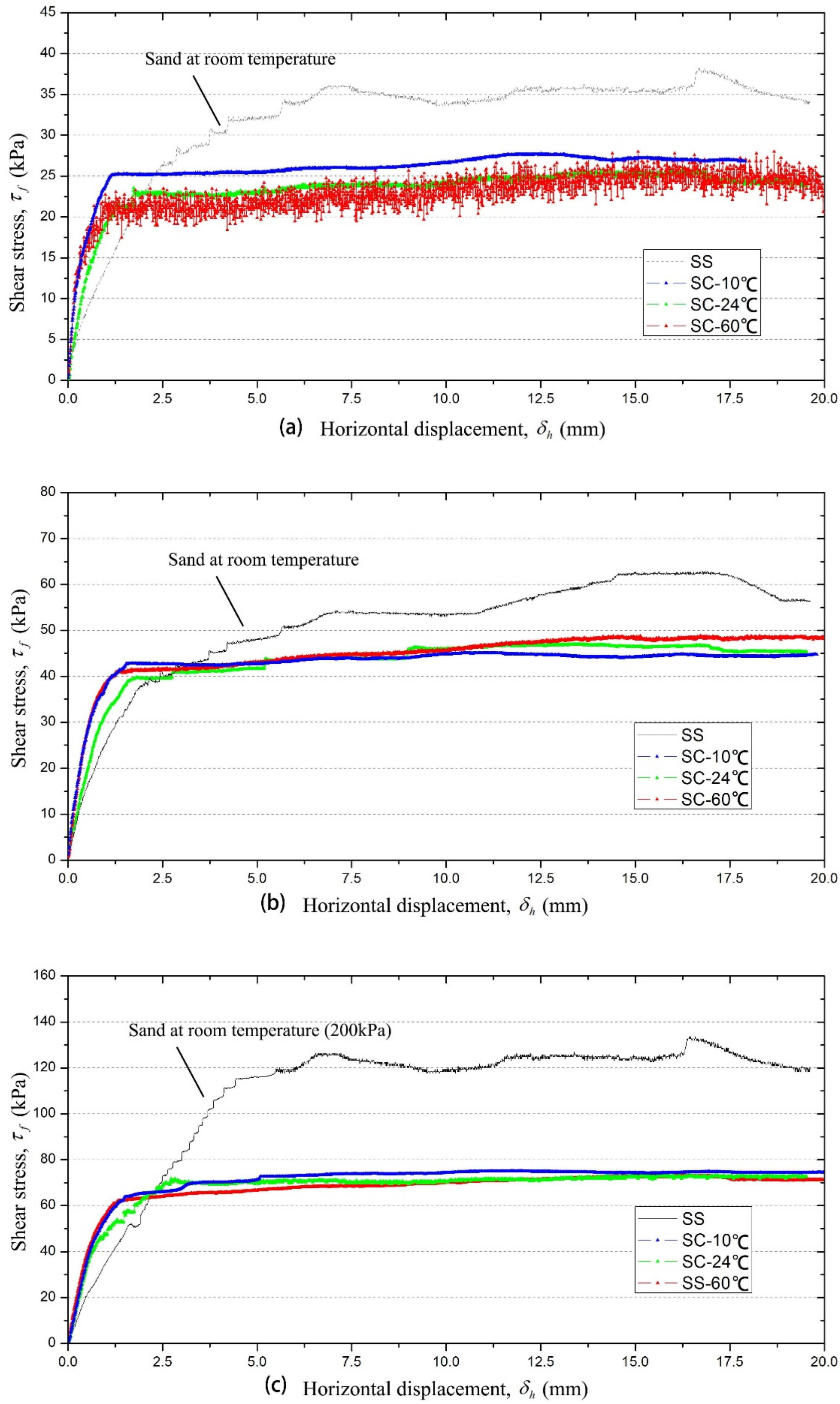

Figure 6-21 Variation of shear stress versus horizontal displacement under different thermal load at (a) 50kPa (b)100kPa and (c)150kPa normal stress during sand-concrete interface test.

6.4.3 Clay-concrete behaviour

Similar to the interface test of sand-concrete, three series of tests were conducted under three different thermal loads. In the first series, three tests were run under room temperature condition, and a target normal stress (50/100/150kPa) was applied on each interface test. The shear rate is assumed to be 0.006mm/min. Figure 6-22 and Figure 6-23 show the interface response of clay-concrete during the shearing test. A slight dilation response can be detected at lower normal stress, but it is not obvious at the higher one. The shear stress increases linearly with the growth of normal stress.

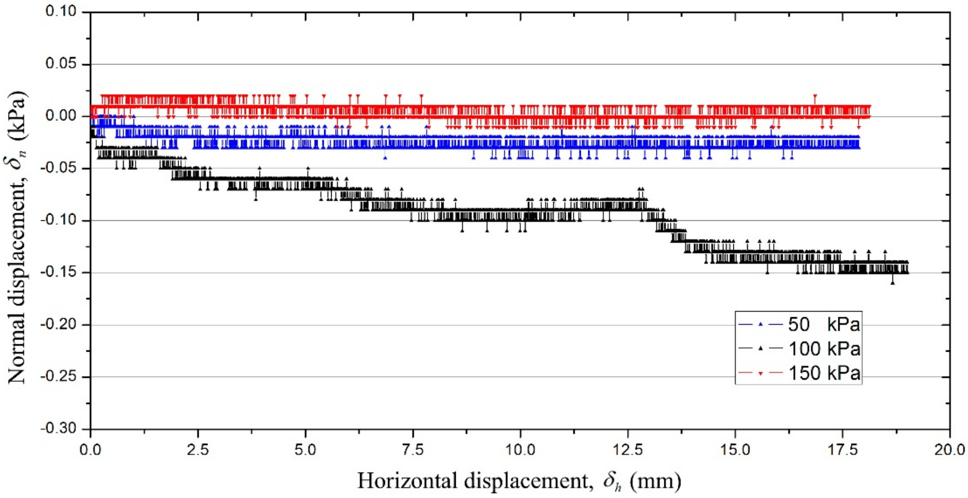

Figure 6-22 Variation of normalized vertical displacement versus horizontal displacement under different normal stresses at room temperature condition (24°C) during clay-concrete interface test.

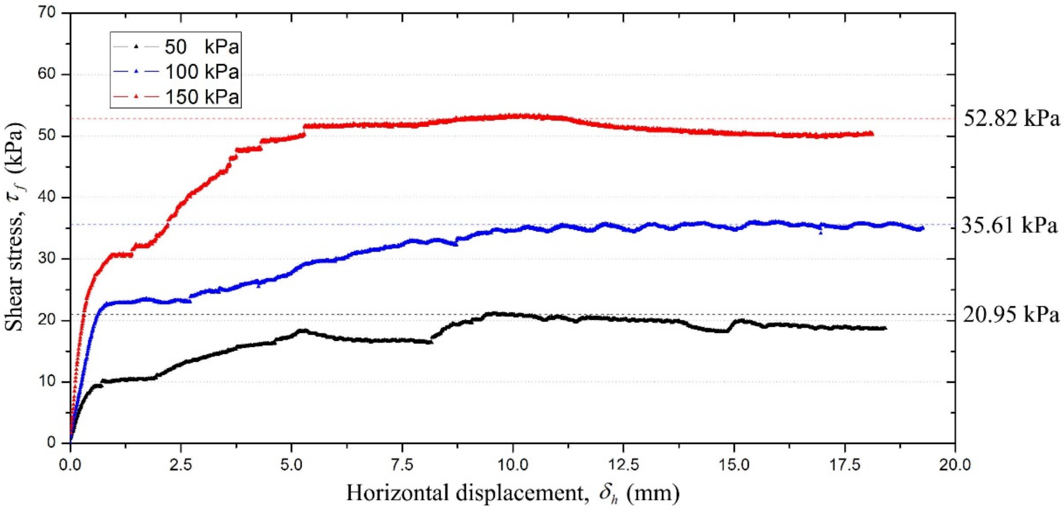

Figure 6-23 Variation of shear stress versus horizontal displacement under different normal stresses at heating condition (24°C) during clay-concrete interface test.

The second series of test run under the heating condition. The main results are summarized in Figure 6-24 and Figure 6-25. It can be seen clearly that all the clay specimens experience a compression process during the shearing process, which should be the consequence of the loss of moisture. The high temperature increases the saturated vapour pressure of water, and much more moisture drained away. The data from Table 6.9 further proof this explanation. The water content ratio drops from 28.24% in the case of normal temperature to 18.45% in the case of high temperature. Additionally, Figure 6-25 also shows that the shear stress is increased by the high temperature compared with the case of normal temperature condition.

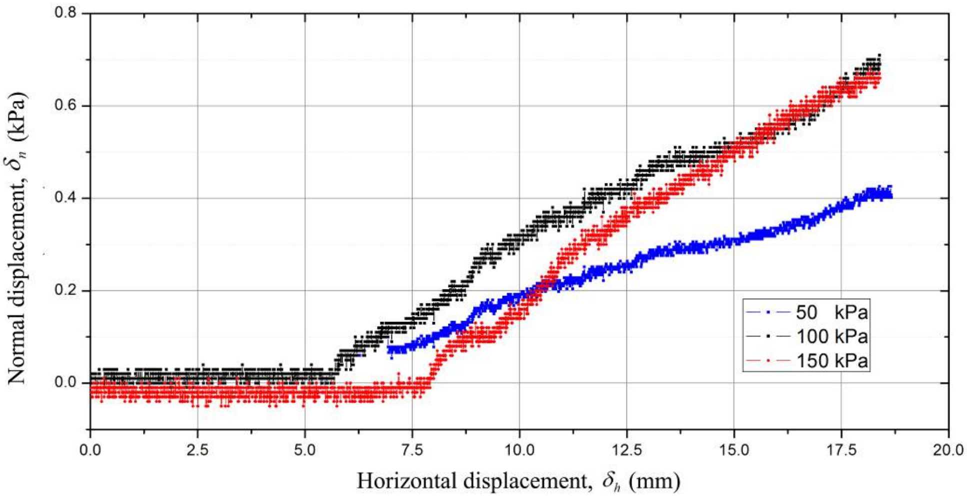

Figure 6-24 Variation of normalized vertical displacement versus horizontal displacement under different normal stresses at heating condition (60˚C) during clay-concrete interface test.

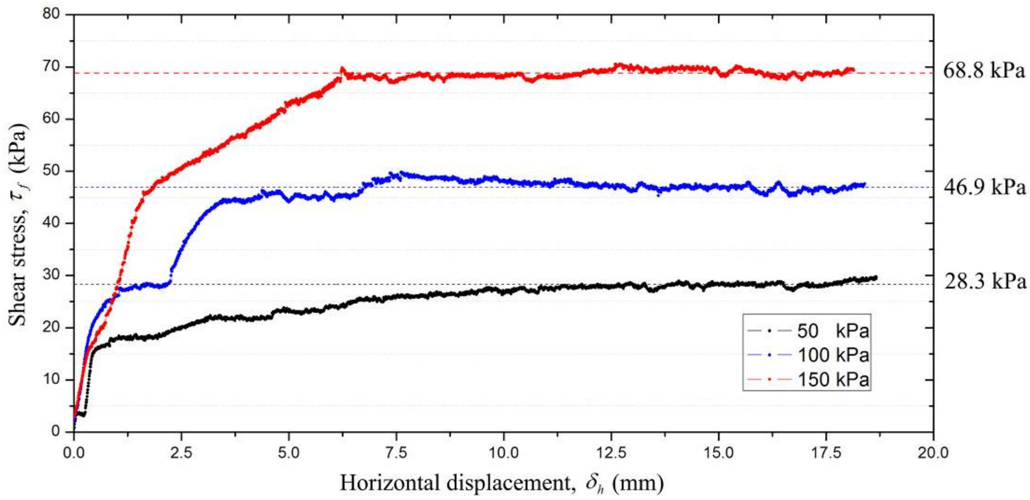

Figure 6-25 Variation of shear stress versus horizontal displacement under different normal stresses at heating condition (60˚C) during clay-concrete interface test.

The final three specimens were run under low temperature (10℃) conditions. The test results are plotted in Figure 6-26 and Figure 6-27. As shown in Figure 6-26, the volume change at low temperature is not obvious, and only a small dilation was detected under small normal stress condition. Compared with the case at normal temperature, the shear stress of the interface decreases slightly.

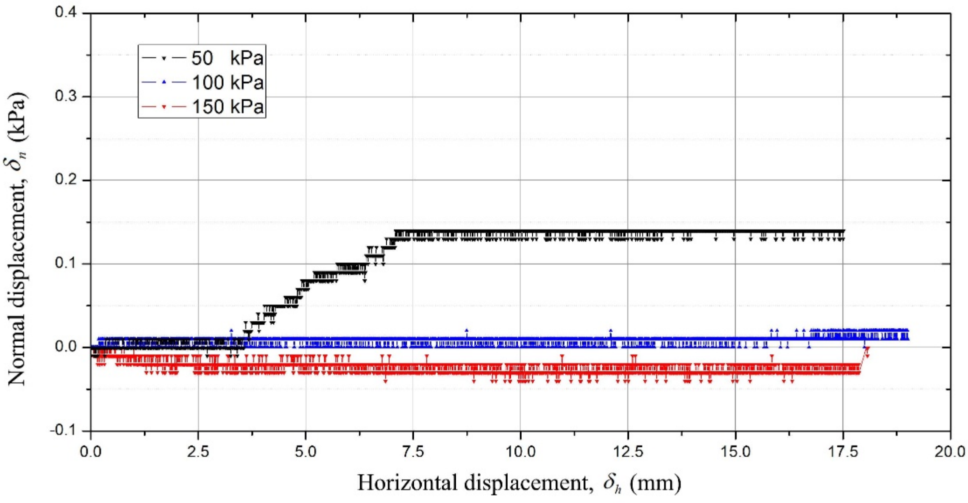

Figure 6-26 Variation of normalized vertical displacement versus horizontal displacement under different normal stresses at cooling condition (10℃) during clay-concrete interface test.

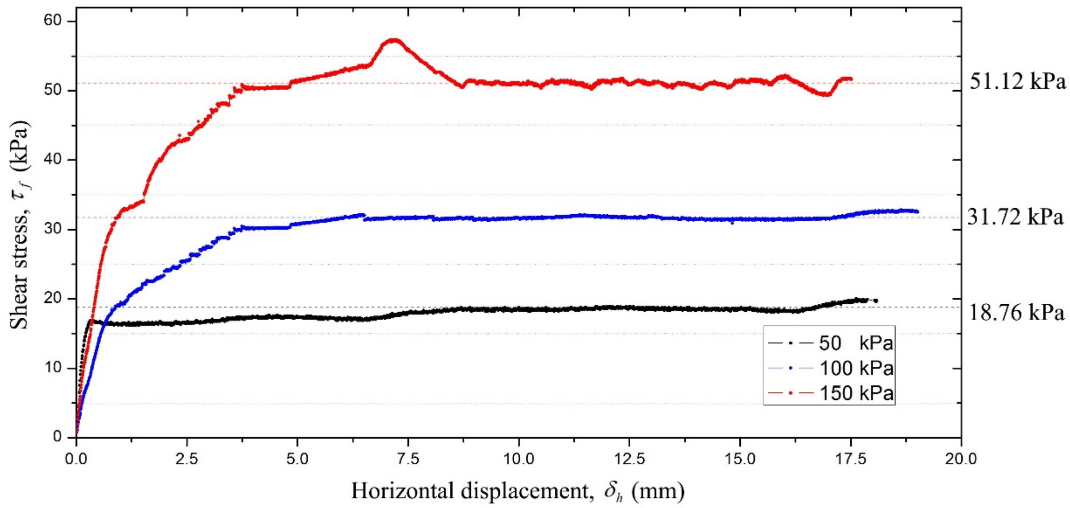

Figure 6-27 Variation of shear stress versus horizontal displacement under different normal stresses at cooling condition (10℃) during clay-concrete interface test.

Table 6.9 Water content of clay specimens

Normal Pressure (kPa)	Shear stress (kPa)		
	24℃	60℃	10℃
50	28.18	18.96	31.86
100	28.24	18.45	31.33
150	28.64	18.32	32.12

All the test results of the interface behaviour are rearranged and summarized in

Figure 6-28. The failure criterion was assumed to be the stress value that the shear force decreased/remained to a constant load. It is clear that, under a given temperature environment, the shear strength envelopes of shear stress has a linear relationship with the normal stress. Additionally, the temperature has an obvious influence on the interface response of clay-concrete. As shown in this figure, the interface friction angle, δ, and adhesion strength, c, increases with the increase of temperature.

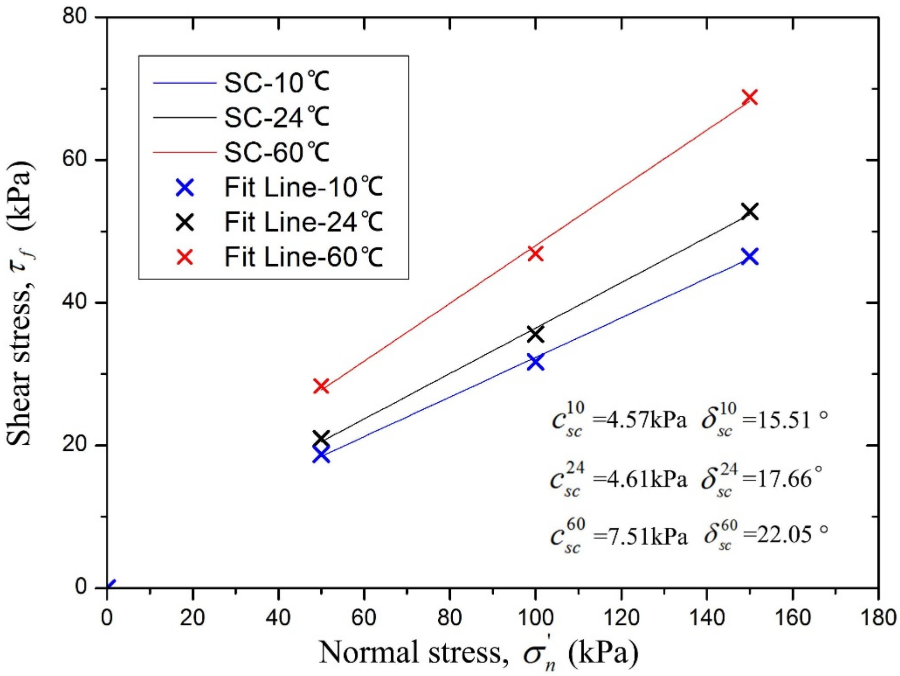

Figure 6-28 Relationships between shear strength and net normal stress under different thermal load during clay-concrete interface test

6.5 Summary

In this chapter, a new direct shear apparatus which could control and monitor the test temperature was introduced, including the design concept and implement method. Based on this new apparatus, two groups of interface tests were conducted, and the related results are summarized and discussed in this chapter. Several important observations noted from the experiments are listed in the following:

1) At a given normal stress, the shear stress curve of sand-concrete interface always lower than that of the sand-sand shear test, which confirms that the shear failure occurs at the interface, but not in the sand.

2) Within the proposed temperature range, no thermal induced effect can be noticed on the interface behaviour between sand-concrete in fully dry condition.

3) For the clay-concrete, an obvious loss of moisture in clay specimens was detected at high temperature (60℃). The water content ratio drops from 28.24% (24℃) to 18.45%. On the contrary, an increase of moisture in clay has been founded under low temperature.

4) The properties (friction angle and adhesion strength) of the interface friction are enhanced by the high temperature. Compared with the case of normal temperature, the adhesion strength has an improvement of about 63%, and the friction angle increased by 24% at high temperature. Conversely, the friction properties decrease with the as the temperature dropped.

CHAPTER 7

NUMERICAL SIMULATION OF THE THERO-MECHANICAL PERFORMANCE OF PGHE WITH SPIRAL-TUBES

7.1 Introduction

The temperature within the concrete pile and soil always varies during the heating or cooling season. This temperature change can induce additional thermal deformation and stress in the pile (Knellwolf et al., 2011; Batini et al., 2015) and physical property changes of soil. Because of this geothermal characteristics, the application of pile GHE faces an innovative challenge for geotechnical design.

This challenge has aroused great concerns in the recent years. Although different research studies were conducted to examine this thermo-mechanical behaviour of pile GHEs through on-site experiments (Laloui et al., 2006; P. J. Bourne-Webb et al., 2009; Sutman et al., 2015), small-scale lab experiments (Goode III, 2013; Sutman et al., 2015) and numerical simulations (Laloui & Nuth, 2005; Rotta Loria et al., 2015; Di Donna et al., 2016), the thermo-mechanical behaviour of PGHE is not fully understood.

There should be two extreme cases of the thermo-mechanical response of PGHE. One is the pile body is totally free to move. As a result, no stress is generated, and the deformation of the pile should be equal to the product of the thermal expansion coefficient and the change of temperature. The other one is the pile is perfectly restrained. The pile body cannot be moved, and the change of temperature induces a uniform thermal stress profile. However, these two conditions are not in nature.

The real situation always happens between these two extreme conditions. The temperature change forces the pile to expand/contract. At the same time, a thermal load induced stress is generated. If there is no mechanical load at the top of the pile, the restrained force only comes from the surrounding soil. Within the maximum shaft friction, the thermal stress will increase with the increase of heating/cooling rate. For the case of the heating condition, the pile suffers from a compressive stress, and for the case of cooling, a tensile stress will be generated, as shown in Figure 7-1. Then, the realistic stress distribution should be the combination of mechanical load and the thermal load induced stress, as shown in Figure 7-2.

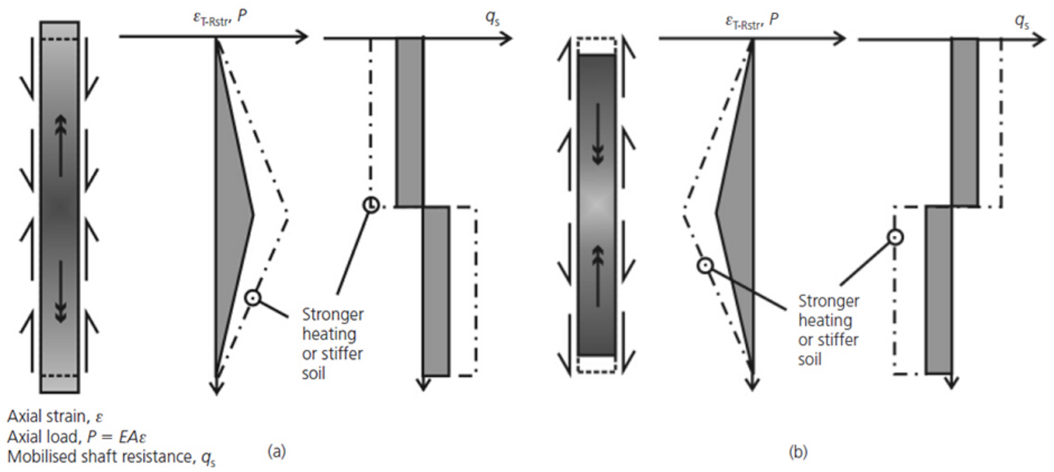

Figure 7-1 Effect of soil restraint during thermal loading: (a) pile heated and (b) pile cooled (Peter J. Bourne-Webb et al., 2013)

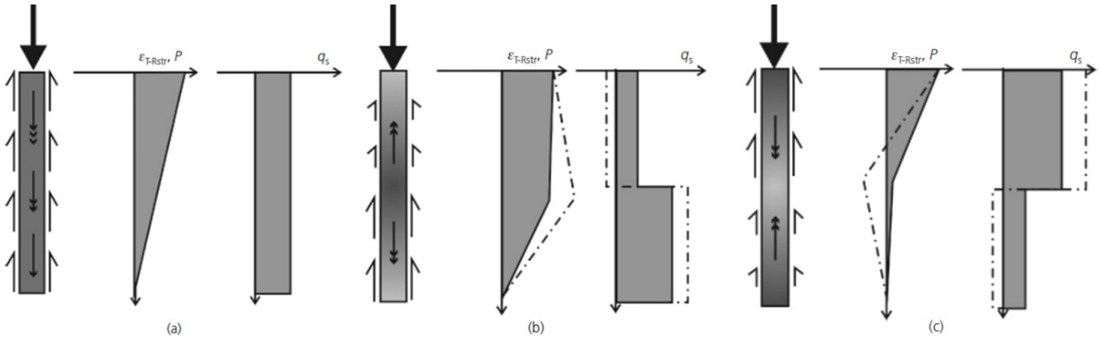

Figure 7-2 Combined mechanical and thermal load effects. Note dash-dotted lines represent the effect of stronger heating/resistance: (a) load only; (b) combined load and heating; (c) combined load and cooling (Peter J. Bourne-Webb et al., 2013)

Previous studies are mainly focused on the axial strain and stress which induced by the heat transfer process of PGHE. But, to the best of knowledge, there is no research study to consider the influence of temperature change on the interface behaviour between pile and soil, especially for the PGHE with spiral-tubes. As presented in Chapter 6, the friction of pile is dependent not only on the confining pressure but also on the friction angle of pile and soil. The results from our lab experiments clearly show that the temperature change has a great influence on the friction angle. Additionally, the expansion/ constriction induced by temperature change can also affect the confining pressure of pile. As a consequence, these two factors can directly influence the ultimate bearing capacity of PGHE. Therefore, based on the results of the modified direct shear test, a finite element simulation has been established to further understand the thermo-mechnical behaviour between the pile and soil under different thermal conditions.

7.2 Finite Element model

The thermo-mechanical performance of PGHE with spiral-tubes was analysed using the commercial finite element analysis software, ABAQUS 6.13. The simulations were carried for a single energy pile with a diameter of 1.2m and a depth of 15m. It is assumed that a spiral-tube was buried in the pile with a loop diameter of 1.0 m and a spiral pitch of 0.4 m. The depth of the soil domain was set to be the double of the pile depth, and its radius was considered to be 15 times of the pile radius. The large enough soil domain is to ensure that the boundary condition of the soil has less influence for the heat transfer and mechanical performance of PGHE within the simulation period. Two typical heat transfer conditions (heating and cooling) was taken into consideration to simulate the working status of PGHE in winter and summer. As the influence of thermo-mechanical behaviour of PGHE is not obvious in short time operation, it would be preferable to carry out a long-term simulation, i.e., 30 days, which would be a better way to understand the thermal and mechanical performances of PGHE.

The model and the mesh generation were built on the ABAQUS CAE. The sensitivity to the grid resolution of this numerical model has been considered and validated. In this analysis, the spiral tube is simplified as a series of separated ring-coils, and the whole calculation domain is axial symmetry. Thus, this three-dimensional problem can be simplified as an axial symmetry model. Three kinds of physical mechanisms were taken into consideration: 1) the heat transfer process from the geothermal heat exchanger to concrete pile and soil, 2) the mechanical behaviour between pile and soil, and 3) the additional thermal stress induced by heat transfer.

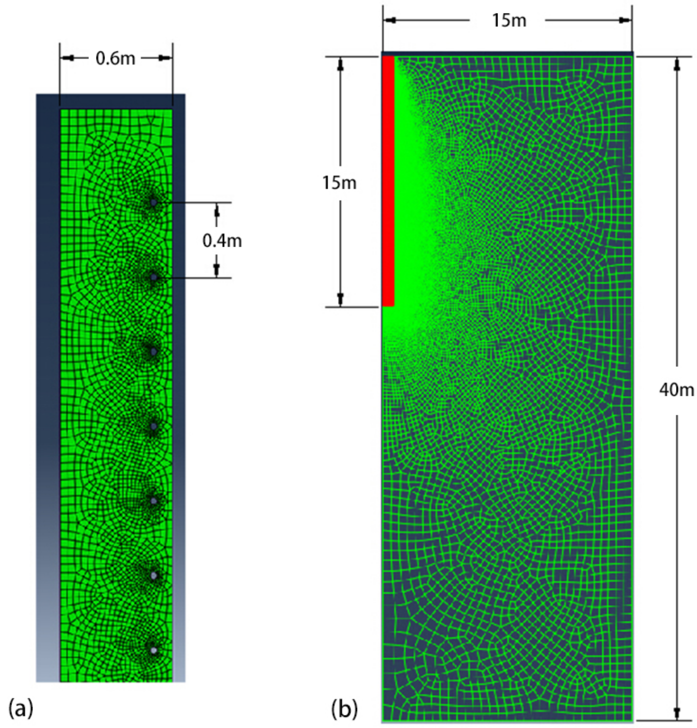

Figure 7-3 The details of geometry and mesh generated as PGHE with spiral tubes

7.2.1 Governing equation

In this study, the thermal performance in terms of heat transfer rate was calculated based on a three-dimensional transient heat transfer model, which was subjected to the heat transfer equation:

$$\rho C_p \frac{\partial T}{\partial t} + \nabla\left(k \nabla T\right) = H \tag{7.1}$$

where T is the temperature (K), t is the time, k is the thermal conductivity (W/mK) and H is the heat generation or extraction rate (W/m^3).

As the stress in this study is dependent on the temperature distribution within the calculation domain, the mechanical and thermal equations are required to be solved simultaneously. Therefore, a fully coupled thermal-displacement analysis is needed. In ABAQUS (Documentation, 2010), the temperature is integrated using a backward difference scheme, and the thermal-stress coupled issue is solved by Newton's method. By applying the exact implementation of Newton's method, the coupled issue can be expressed by a non-symmetric Jacobian matrix:

$$\begin{bmatrix} K_{uu} & K_{u\theta} \\ K_{\theta u} & K_{\theta\theta} \end{bmatrix} \begin{Bmatrix} \Delta u \\ \Delta \theta \end{Bmatrix} = \begin{Bmatrix} R_u \\ R_\theta \end{Bmatrix} \tag{7.2}$$

where Δu and $\Delta \theta$ are the respective corrections to the variation of displacement and temperature, K are the submatrices of the fully coupled Jacobian matrix, and R_u and R_θ are the mechanical and thermal residual vectors, respectively.

The classical friction model of Coulomb is used to simulate the contact behaviour of pile and soil in this study. It assumes that no relative motion occurs if the equivalent frictional stress (τ_{eq}) is less that the critical stress, which goes proportionally with the contact pressure: $\tau_f = \mu P$, where the μ is the friction coefficient and P is the contact pressure. If the equivalent frictional stress is at or above the critical stress, slip can occur, and the direction of the slip is same with the frictional stress, $\tau_i / \tau_{eq} = \gamma_i / \gamma_{eq}$.

7.2.2 Boundary conditions and material properties

As the radius of soil domain is more than ten times than that of the pile, the far-field boundary of soil was treated as adiabatic surfaces and blocked the displacement in the radial direction. The bottom boundary of soil domain was given a constant temperature of 20 ℃, which was equal to the initial temperature of the whole calculation domain. A fixed mechanical boundary condition was applied at the soil bottom to ensure that the vertical and horizontal displacements at this position is zero. The boundary condition at the top surface of soil and pile was assumed to be a constant temperature of 20 ℃. As the main focus is the thermo-mechanical performance of pile and soil, the fluid dynamic within the spiral heat exchanger was not be simulated in this study, which was simplified as a heat flux boundary condition applied on the pipe surface.

Both the pile and soil were assumed to be a purely elastic material, and the plastic deformation of soil is not considered. The metrical properties of soil are based on the results from the interface behaviour tests, proposed in the last chapter, and the main properties for this numerical study are summarised in Table 7.1.

Table 7.1 Summary of concrete and soil properties for the simulation cases

Material			Concrete	Soil
Item	Symbol	Unit		
Conductivity	K	W/(m*K)	1.628	1.82
Density	rho	kg/m3	2500	2500
Specific Heat	Cp	J/(kg*K)	837	880
Young Modulus	E	Pa	2.8E10	5.2E6
Poisson's Ratio	nu	1	0.25	0.35
Coefficient of Thermal Expansion	alpha	1/K	1.2E-5	1.75E-5
Internal Friction Angle	φ	°	-	15.51/17.66/22.05
Cohesion	C	kPa	-	4.57/4.61/7.51

Under each heat transfer condition (heating or cooling), two mechanical load behaviours were conducted: one is that no load force was applied on the pile top and the stress was only induced by gravity and temperature variation; the other one is that the pile is under an axis displacement, and both the mechanical and thermal loads were applied on the pile. The displacement rate of pile top was assumed to be 5 mm/day.

7.3 Results

The results of the numerical simulations for the PGHE with spiral-tubes were presented for both heating and cooling conditions. The thermal performances of the PGHE were presented firstly, and then the thermo-mechanical performances were shown and discussed according to the effect of axis load force.

7.3.1 Thermal response

Figure 7-4 shows the temperature profiles of PGHE in the case of injecting and extracting heat from the surrounding soil after 30' days operation. The deformation induced by the temperature change is also shown in this picture. To better observe the thermal deformation, an amplification factor of 1000 was adopted to enlarge the thermal influence on pile structure. For the case of heat injection (Figure 7-4 a), it could be seen clearly that the temperature rise can cause thermal expansion of pile, and this deformation increases with the temperature. On the contrary, a shrinking deformation can be observed with the temperature decrease.

The detailed temperature distributions along the axis and side walls of pile are plotted in Figure 7-5. Under the heating condition, the heat energy accumulates in the centre of the pile, and, therefore the temperature response along the axis is always stronger than that along the pile wall. A similar phenomenon can also be seen in the case of the cooling condition. The temperature curves at the pile axis are uniform and lower than that at the pile wall. After 30' days heat transfer process, and the temperature of the pile wall reaches at 5 ℃ in the case of cooling and 60 ℃ in the case of heating.

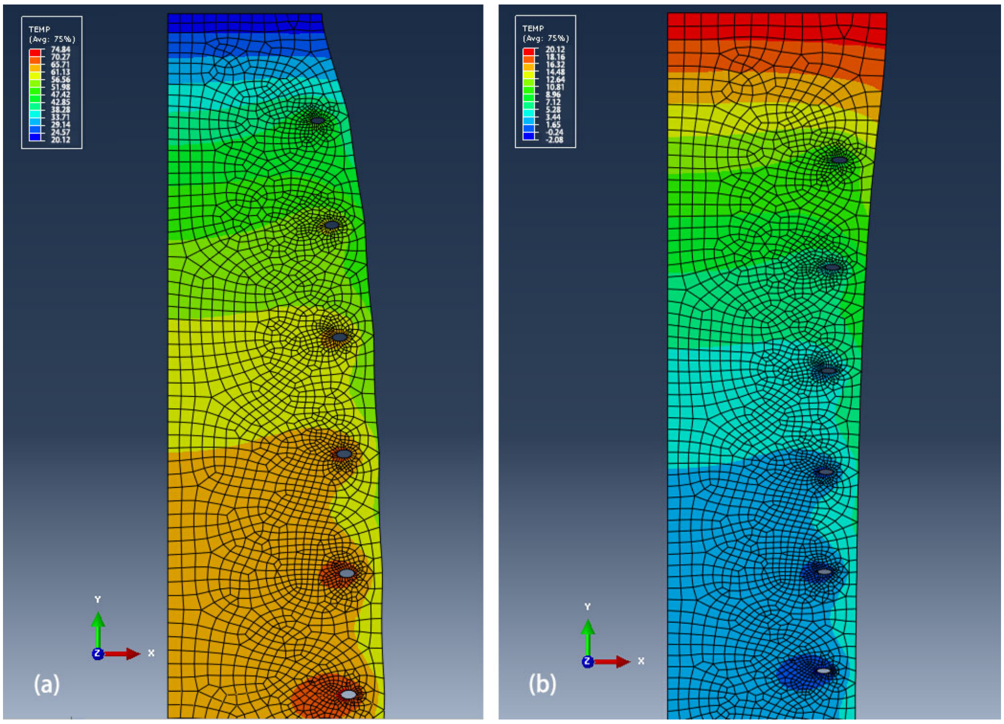

Figure 7-4 Temperature and deformation (with an amplification factor of 1000) profiles of PGHE at (a) heating and (b) cooling at 30 days

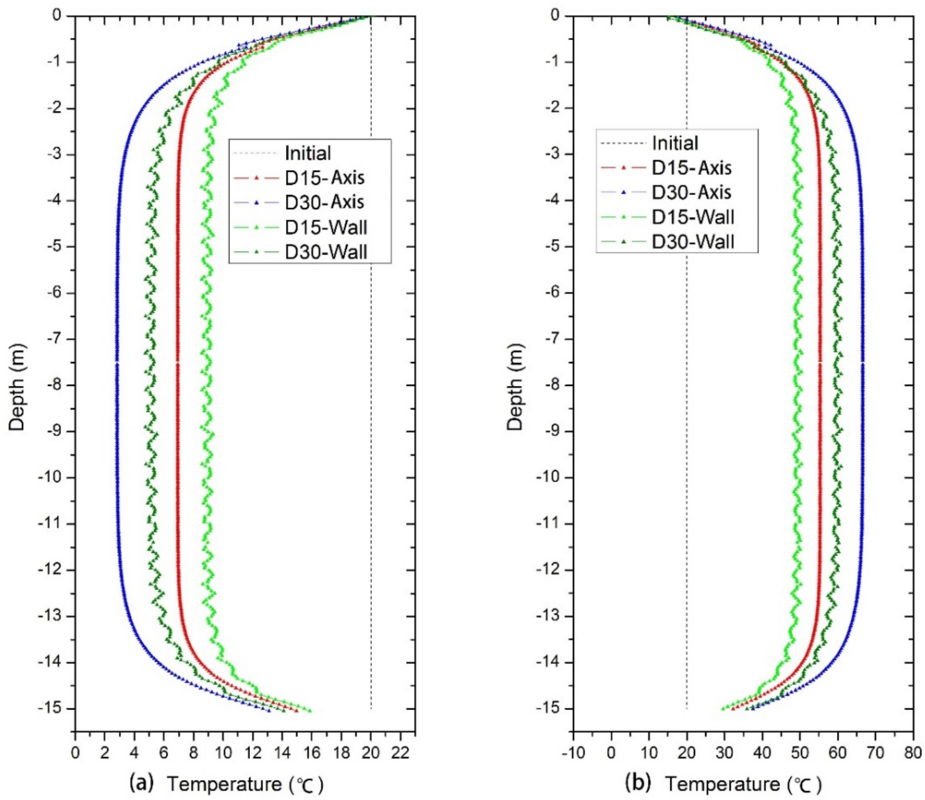

Figure 7-5 Temperature distribution along the pile axis and the pile wall at (a) cooling and (b) heating

7.3.2 Thermo-mechanical response with no axial force

By assuming the pile top is free to move, a simple thermo-mechanical simulation was firstly carried out. If there is no additional mechanical force applied on the pile top, the stress within the pile foundation should only comes from the gravity. Therefore, the initial stress increases linearly with the pile depth, and the frictional shear force should be closed to zero, as shown in Figure 7-6.

When the spiral heat exchanger injects heat energy into the concrete pile, the thermal stress was excited and pushed the pile to expand from the null point to the top and bottom. In this case, the null point was located at the depth of 8.5 m. A positive shear stress (assuming the direction from the pile bottom to the top is positive) is mobilised under this null point, and a negative one occurs above this point. An inflection point can be observed near the top of the pile, which should be the consequence of the decrease of the normal contact force. An additional thermal stress was mobilised simultaneously. As shown in the stress distribution curves, this thermal load induced stress along the axis is obvious but less than 5% of the concrete ultimate compressive strength. The maximum compressive stress is equal to 5.75Mpa, which was detected in the area near the spiral heat exchanger pipe.

For the case under the cooling condition, a similar phenomenon was shown in Figure 7-6 (a), but the friction direction is opposite to the case of the heating condition. The temperature change induced a contraction behaviour of the pile, and the friction was mobilised to restrict this behaviour. The stress distribution curves along the pile axis show that the pile suffered an additional pressure stress with the temperature increase and tensile stress with the temperature decrease. But, it should be pointed out that the tensile stress only occurs near the pile top, and the tensile stress fades away with an increase in depth,. The maximum tensile stress detected near the spiral heat exchanger is 0.4 Mpa, which has almost reached 50% of the ultimate tensile strength of normal concrete pile.

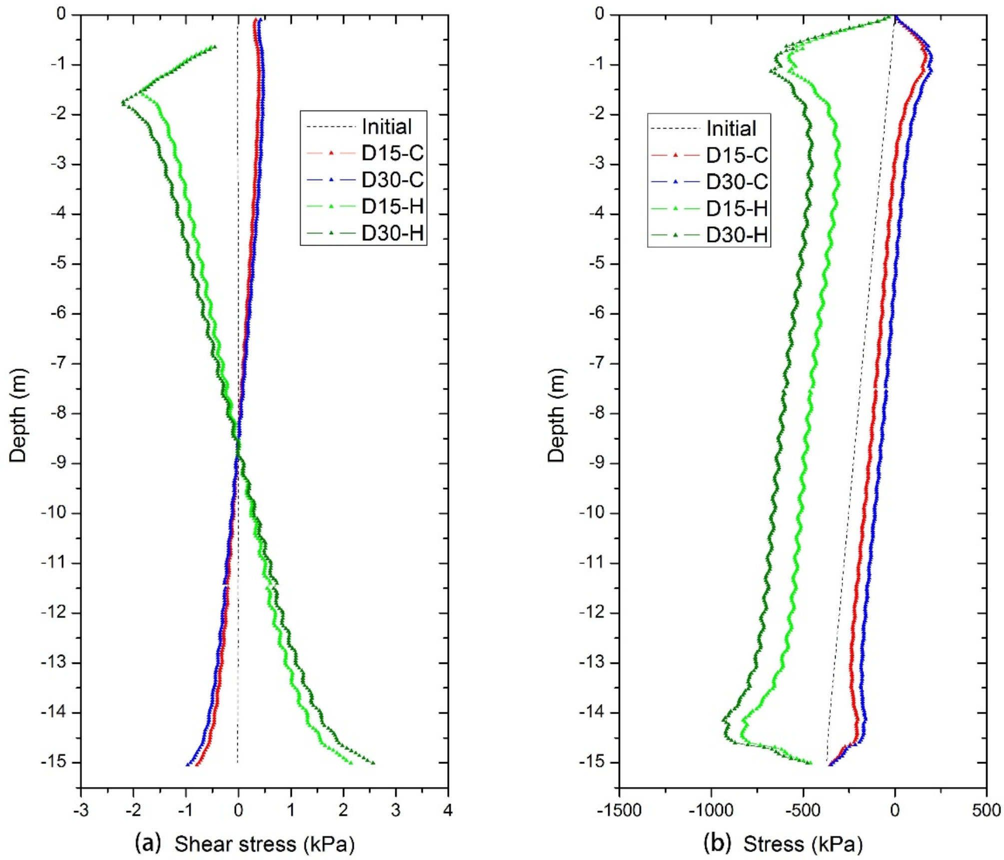

Figure 7-6 Distribution of (a) shear stress and (b) axis vertical stress at cooling and heating conditions with no axial force

7.3.3 Thermo-mechanical response under axis load

Taking the axial load force into consideration, the results from the simulations were summarised from Figure 7-7 to Figure 7-10. As shown in Figure 7-7, to realise a constant vertical displacement, the requied load force was influenced greatly by the temperature distribution of PGHE. Compared with the case of no heat disturbance, the total required load force is increased from 5496kN to 6573kN in the case of heating condition, with an increasing ratio of 19.6% (23.93kN/℃). On the contrary, the carrying capacity decreased with the temperature, and a decrease ratio of 9.15% (25.83 kN/℃) was detected in the case of the cooling condition.

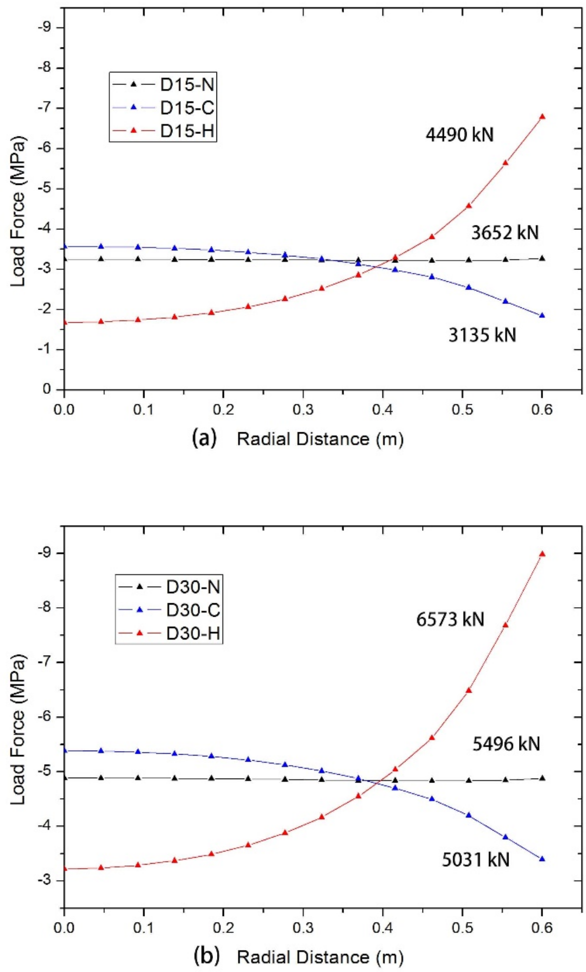

Figure 7-7 Load force distributions at the pile surface at (a) day-15 and (b) day-30.

Figure 7-8 shows that the stress distribution along the pile axis under different thermal loads. Clearly, the temperature rise can induce a stress increase in the pile foundation. It could be noted that the stress curve of heating increase greatly near the pile top. This is due to the ununiformed distribution of the load force. The load force at the centre of pile surface is always lower than that of the around area. The maximum pressure stress is found to be 6.25 MPa at the depth of 1.12m, and at the same position, the pressure stress in the case of no thermal disturbance is only 4.96 MPa. A 0.5 MPa decrease was shown in the case of the cooling condition.

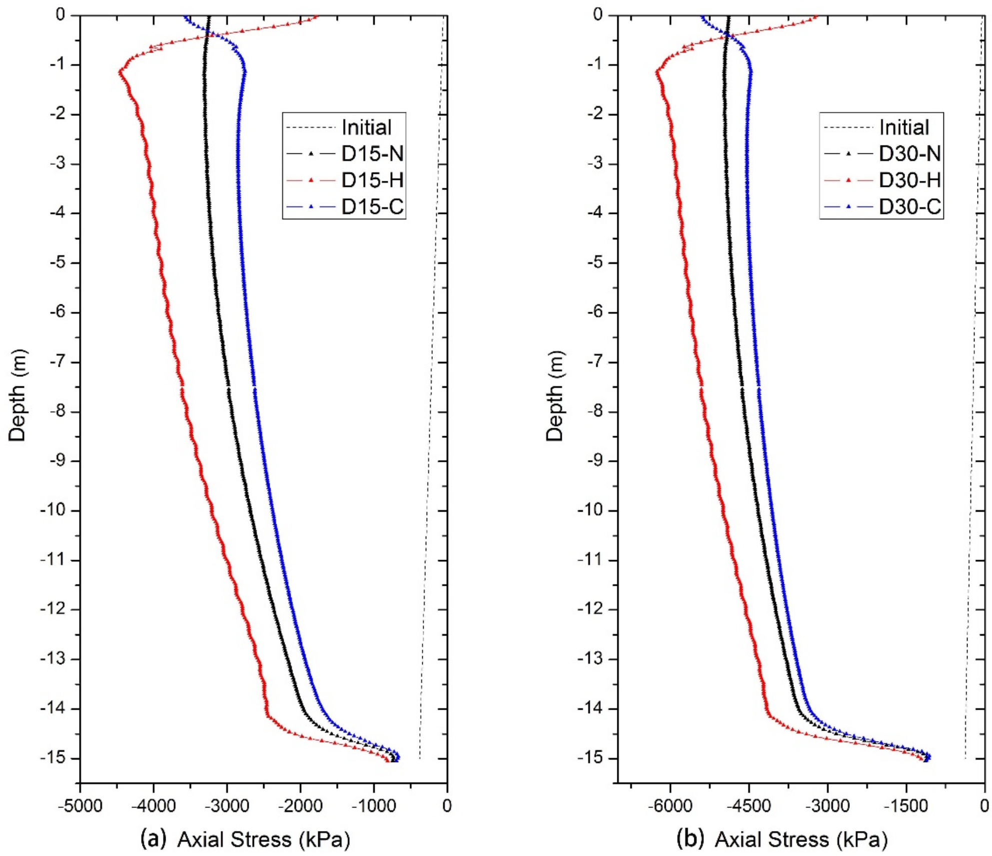

Figure 7-8 Axis vertical stress at cooling and heating condition at (a) day-15 and day-30 with a constant vertical deformation boundary

The simulation results also show that, in the case of heating, the temperature rise near the heat exchanger pipe is greater than that in the pile axis, and thus a convergence stress area occurs at this position with a compressive stress of 9.35MPa, as shown in Figure 7-9. It is more than threefold to stress at the pile centre.

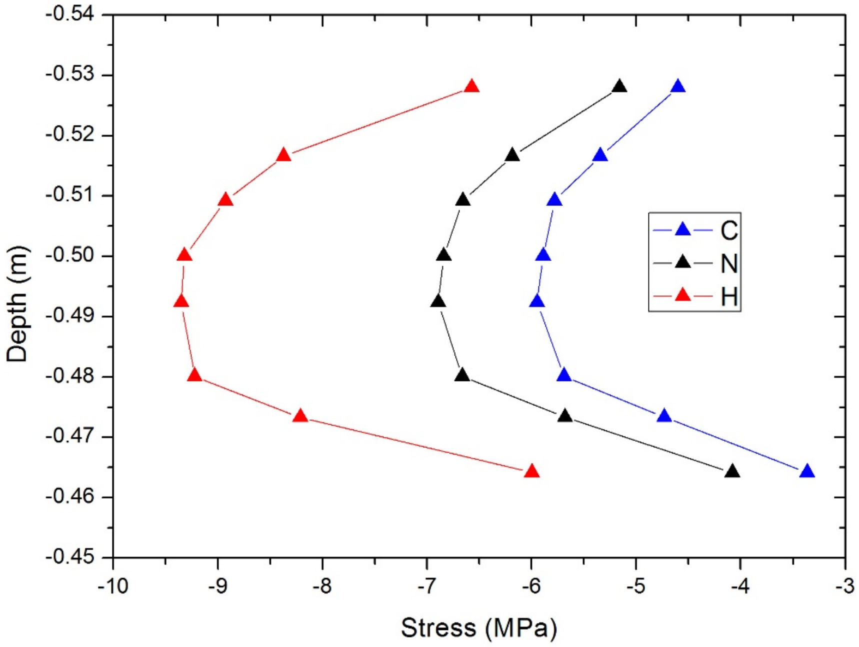

Figure 7-9 Convergence stress distribution near the spiral heat exchanger

The shear stress along the pile wall at different heat transfer conditions are plotted in Figure 7-10. The shear stress along the pile is almost with linear distribution. It is because the compressive deformation of the pile is relatively small, and the slip between pile and soil is uniform. As seen in Figure 7-10, the shear stress can be enhanced by the temperature rise, and weakened by the heat absorbing process. The temperature does not only increase the friction angle for the interface between soil and pile, but the expansion deformation is also increased by the normal pressure on the interface. These two behaviours are combined to generate an enhanced ratio of 48% on the first third of the pile, when the PGHE operation in the heating mode. This enhancement effect is more remarkable at the top of the pile, and decreases with the pile depth. A similar phenomenon can also be observed in the case of cooling simulation. The average enhancing ratio at the 15' days and 30' days of heating operation are equal to 33.39% and 34.40 %, respectively. On the contrary, the temperature decrease caused a weakening effect on the shear stress, with an average weaken ratio of 15.37%.

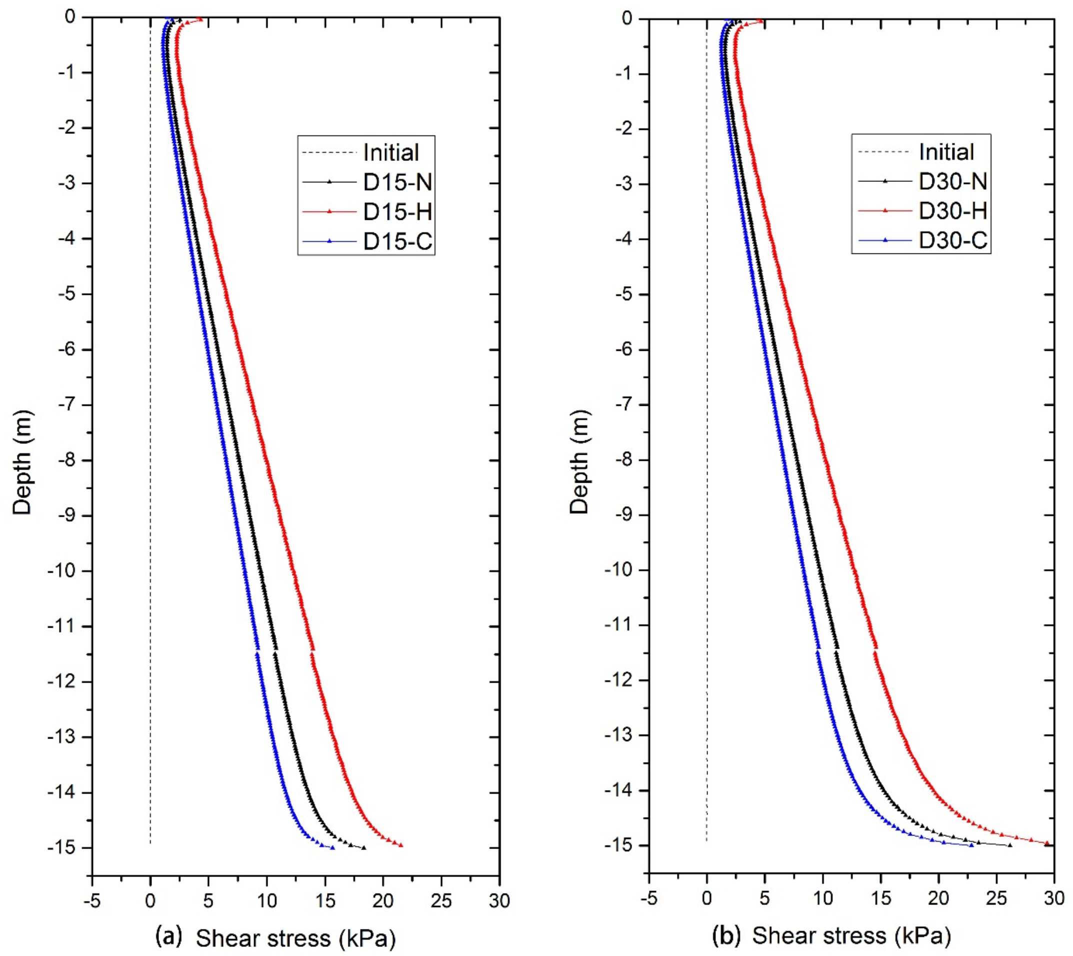

Figure 7-10 Shear stress at cooling and heating condition at (a) day-15 and day-30 with a constant vertical deformation boundary

7.4 Summary

This chapter presents a finite element model to analyse the thermo-mechanical behaviour of PGHE with spiral-tubes. Two typical heat transfer conditions were examined in this simulation study. In the simulation model, the required experiment parameters, such as friction angle between the pile and soil, and thermal properties, were referring to the data in Chapter 6. In this context, the main conclusions are:

1) The thermal load induced stress not only depends on the temperature variation but also corresponds to the mechanical load applied at the pile top. The tensile stress only occurs with a limited value at the cooling condition, when there is no mechanical load. If considering the load force effect, no tensile stress was detected either in heating or cooling conditions.

2) Under high thermal and mechanical load conditions, the local compressive stress can reach to 9.35MPa near the heat exchanger pipe at the heating condition, which is more than threefold to stress at the pile axis.

3) The temperature rise increases the friction angle of the interface between soil and pile, and the expansion deformation also increases the normal pressure on the interface. The average enhancing ratio when GHE operated for 15 days and 30 days under heating condition are equal to 33.39% and 34.40 %, respectively.

4) The cooling process led to the decrease of friction angle and normal contact pressure at the interface between soil and pile, and as a consequence, the shear force decreases with the temperature drop. Compared with no thermal disturbance, the ultimate friction resistance of pile is weakened by 15.37%.

In summary, heat exchange process of GHE has a great effect on the skin friction behaviour of the pile. A 34.4% increase of bearing capacity is observed in the case of heating simulation and a 15.37% capacity decrease has been found in the case of cooling simulation. This variation of bearing capacity should be fully taken into consideration in the design and calculation of energy pile, especially for the friction pile. A safety factor of thermal effect should be added or considered in the design stage to ensure the pile can safely operate in the worst-case. For the case of cooling condition, a safety factor of 1.20 could be chosen for the bearing capacity design. Additionally, the thermal load induced stress at the pile axis has a limited impact on the concrete strength, but the stress-concentrated area around the spiral heat exchanger tube should be paid more attention on the pile design of structural mechanics. Under such a great stress variation, the pile may suffer from the concrete fatigue for the long-term heating/cooling operation. Thus, it is of importance to conduct fatigue analysis in the future works.

CHAPTER 8 CONCLUSIONS AND RECOMMENDATIONS FOR THE FUTURE WORK

For ground-coupled hear pump system, the applications of spiral-tubes as a geothermal heat exchanger horizontally or vertically have been attracting increasing attentions. This thesis aims to investigate the thermal and thermo-mechanical behaviours related to the spiral-tubes by 1) developing the analytical heat transfer model for Horizontal Geothermal Heat Exchanger with spiral-tubes, 2) developing the analytical heat transfer model for Pile Geothermal Heat Exchanger with spiral-tubes, 3) investigating the heat transfer performance of Pile Geothermal Heat Exchanger with spiral-tubes under groundwater advection by a simulation model, and 4) investigating the thermo-mechanical performance of Pile Geothermal Heat Exchanger with spiral-tubes by experimental and numerical method. In this chapter, the main results are summarized as below.

8.1 Analytical model for HGHE with spiral-tubes

A new analytical model, ring source model, in a semi-infinite has been established to describe the transient heat transfer process of Horizontal GHE with spiral-tubes:

- The ground is regarded as a semi-infinite medium, and a sinusoidal changed boundary condition is applied on the ground surface. A good agreement was shown in the comparisons between the results obtained from the field test and the proposed model, and the new analytical model was further validated by the numerical simulation.

- Two different ground surface conditions (constant temperature and sinusoidal surface temperature) were calculated and discussed. The results indicated that the surface temperature can directly influence the heat transfer performance of the horizontal heat exchangers, which should be fully considered in the system design.

- As the proposed analytical model successfully takes the annual variation of surface temperature into consideration, this new model should be a great aid to the engineers in designing and optimizing the arrangement of the horizontal geothermal heat exchangers with vertical spiral coils.

8.2 Analytical model for Pile GHE with spiral-tubes

The spiral configuration of GHE is also applied in pile geothermal heat exchangers. A new transient analytical model, composite ring source model, has been established for accurately modelling the PGHE with spiral-tubes.

- A new analytical solution was developed based on the Green's function theory. This new model successfully and firstly examines the difference of thermal properties between the pile and the surrounding soil. Meanwhile, the finite size and discontinuities associated with pile geothermal heat exchangers with spiral coils are also considered. It has been proven to be a new tool for the design and evaluation of energy pile system.

- Comparisons between the homogeneous medium model and composite medium model prove that the thermal property differences between the concrete and soil have a significant influence on the heat transfer processes in the long-term operation of PGHE with spiral tubes.

8.3 Numerical analysis on PGHE with spiral-tubes under groundwater advection

As the pile is usually more than ten meters in depth, it sometimes goes across the soil vadose zone. Accordingly, the heat transfer performance of PGHE will be affected when the groundwater advection exists. Therefore, the influence of groundwater advection of PGHE with spiral-tube is investigated and discussed.

Based on the moving ring-coils model and simulation model, an improved analytical model has been established to better describe the heat transfer process of PGHE with spiral coils under groundwater advection by introducing a key parameter of effective dimensionless velocity. Compared with the original moving ring-coils model, the accuracy of the approved analytical model has been improved significantly. But, it should be noticed that this improved model also has its application limitations. When the groundwater flow velocity is larger than $1e^{-5}$m/s, an obvious deviation can be detected. Besides, because this improved model is based on a serious numerical simulation solution, which serves as a baseline, its accuracy generally decreases with the increase of the distance between estimate point and heat exchange source along the radius direction. In general, this could be a great help for PGHE design when groundwater advection exists.

8.4 Thermo-mechanical analysis on PGHE with spiral tubes

The temperature within the concrete pile and soil always varies during the heating or cooling season. This temperature change can induce additional thermal deformation and stress in the pile and physical property changes of soil. Because of this geothermal characteristic, the application of pile GHE faces an innovative challenge for geotechnical design. The interface behaviour was investigated by a new direct shear apparatus with temperature control. Based on the experiment results, a finite element model is established to investigate the thermo-mechanical behaviour of PGHE with spiral-tubes.

- For the fully dry sand, no thermal load induced effect can be noticed on the interface behaviour between sand and concrete. For the clay-concrete, an obvious loss of moisture in clay specimens was detected at high temperature (60℃). The water content ratio drops from 28.24% (24℃) to 18.45%. On the contrary, an increase of moisture in clay has been founded under low temperature (℃).

- The friction parameters (friction angle and adhesion strength) of the soil-concrete interface are enhanced by the high temperature. Compared with the case of normal temperature, the adhesion strength has an improvement of about 63%, and the friction angle increased by 24% at the heating condition. Conversely, the friction properties decrease slightly with the temperature reduction.

- The thermal load induced stress not only depends on the temperature variation but also corresponds to the mechanical load applied at the pile top. The tensile stress only occurs with a limited value at the cooling conditions, when there is no mechanical load. If considering the load force effect, no tensile stress was detected either in heating or cooling conditions. Under high thermal and mechanical load conditions, the local compressive stress can reach to 9.35MPa near the heat exchanger pipe at the heating conditions, which is more than threefold to the stress at the pile centre.

- The temperature rise can increase the friction angle of the interface between soil and pile, and the thermal deformation can also increase the normal pressure at the interface. For the case of heating conditions, the average enhancing ratio is equal to 33.39% (15 days) and 34.40 % (30 days), respectively. The cooling process could cause a decrease of friction angle and normal contact pressure at the interface, and as a consequence, the shear resistance decreases with the temperature reduction. Compared with the one without thermal disturbance, the ultimate friction resistance of pile is weakened by 15.37%.

In summary, heat exchange process of GHE has a great effect on the skin friction behaviour of the pile. A 34.4% increase of bearing capacity is observed in the case of heating simulation and a 15.37% capacity decrease has been found in the case of cooling simulation. Additionally, the thermal load induced stress at the pile axis has a limited impact on the concrete strength, but the stress-concentrated area around the spiral heat exchanger tube should be paid more attention on the pile design of structural mechanics. Under such a great stress variation, the pile may suffer from the concrete fatigue for long-term heating/cooling operation. Thus, it is of importance to conduct fatigue analysis in the future works.

8.5 Recommendations for future work

The spiral-tubes were applied widely as the geothermal heat exchanger in ground-coupled heat pump system, especially for energy pile. There is some insufficiency on this topic in this study due to time and facility limitation, so it is worthwhile and necessary to conduct further researches.

During the interface shear experiments, it was observed that the thermal loads have remarkable influence on the interface behaviour between clay and concrete, but its exact mechanism of this influence is still unclear. The moisture content change during the clay consolidation and shearing process should be the main influencing factor on the experiment results. However, due to the limitations of the experimental rig, this transit mass transfer process is not able to be monitored during the experimental process. Thus, the quantitative analysis is hard to carry out. Additionally, the interface behaviour also depends largely on the types of soil materials. A grand scope of different type soils needs to be investigated to fully understand the thermal load induced influence on the interface behaviour between the soil and concrete.

Furthermore, the stress near the heat exchanger is concentrated and changed greatly based on the numerical results. Under such a great stress variation, the pile may suffer the concrete fatigue for long-term operation. Thus, it is of importance to conduct fatigue analysis in the future works.

Finally, although a thermo-mechanical simulation model has been established for investigating the thermal influence on pile stress and friction resistance, it is limited to apply for a design tool for reality works, since the interaction effect between PGHEs is not considered in this study. Thus, the study of the thermo-mechanical performance of a group of PGHEs is expected forward.

APPENDIX A

The temperature response of an instantaneous plan temperature source at zero time in an infinite medium can be expressed by:

$$H = \frac{1}{2\sqrt{\pi\alpha_1 t}}\exp\left[-\frac{\left(z-z'\right)^2}{4\alpha_1 t}\right] \tag{A,1}$$

The solution for the temperature response, T_1, in the region of $0 \le z < l_z$ may be expressed as:

$$T_1 = H + W \tag{A,2}$$

In which the function W has to satisfy the equation of conduction of heat in this region and tends to zero as $z \to \infty$. The boundary condition at $z = l_z$ should satisfy the flowing equation:

$$\begin{cases} T_1 = T_2 \\ k_1 \dfrac{\partial T_1}{\partial z} = k_2 \dfrac{\partial T_2}{\partial z} \end{cases} \tag{A,3}$$

Using the Laplace transform method to translate H, W and T_2 into $\overline{H}, \overline{W}$ and $\overline{T_2}$. These equations have to satisfy:

$$\frac{\partial^2 \overline{W}}{\partial z^2} - q_1{}^2 \overline{W} = 0 \qquad \text{for } 0 \le z < l_z \tag{A,4}$$

$$\frac{\partial^2 \overline{T_2}}{\partial z^2} - q_2{}^2 \overline{T_2} = 0 \qquad \text{for } 0 \le z < l_z \tag{A,5}$$

where: $q_1 = \sqrt{\lambda / \alpha_1}$ and $q_2 = \sqrt{\lambda / \alpha_2}$. the boundary condition at $z = l_z$ is then, transformed as:

$$\begin{cases} \overline{H} + \overline{W} = \overline{T_2} \\ k_1 \dfrac{\partial \overline{H}}{\partial z} + k_1 \dfrac{\partial \overline{W}}{\partial z} = k_2 \dfrac{\partial \overline{T_2}}{\partial z} \end{cases} \tag{A,6}$$

Based on these equations and conditions, the solution can be obtained as the Laplace image:

$$\overline{T_1} = \frac{1}{2\alpha_1 q_1} \exp\left[-\left(q_1 z - q_1 z'\right)\right]$$
$$- \frac{\exp(-q_1 z)}{2\alpha_1 q_1} \frac{\left(k_1 q_1 + k_2 q_2\right)\exp\left[q_1 l_z - q_1 z' - q_2 l_z\right] + (k_1 q_1 - k_2 q_2)\exp\left[-q_1 l_z + q_1 z' - q_2 l_z\right]}{\left(k_1 q_1 + k_2 q_2\right)\exp\left(q_1 l_z - q_2 l_z\right) + \left(k_1 q_1 - k_2 q_2\right)\exp\left(-q_1 l_z - q_2 l_z\right)}$$
$$+ \frac{\exp(q_1 z)}{2\alpha_1 q_1} \frac{(k_1 q_1 - k_2 q_2)\exp\left[-q_1 l_z + q_1 z' - q_2 l_z\right] - (k_1 q_1 - k_2 q_2)\exp\left[-q_1 l_z - q_1 z' - q_2 l_z\right]}{\left(k_1 q_1 + k_2 q_2\right)\exp\left(q_1 l_z - q_2 l_z\right) + \left(k_1 q_1 - k_2 q_2\right)\exp\left(-q_1 l_z - q_2 l_z\right)}$$

(A,7)

$$\overline{T_2} = \frac{k_1 \exp(-q_2 z)}{\alpha_1} \frac{\exp\left[q_1 z'\right] - \exp\left[-q_1 z'\right]}{\left(k_1 q_1 + k_2 q_2\right)\exp\left(q_1 l_z - q_2 l_z\right) + \left(k_1 q_1 - k_2 q_2\right)\exp\left(-q_1 l_z - q_2 l_z\right)}$$

(A,8)

The true values of T are obtained from those of $\overline{T}$ by the inverse Laplace transfer theorem for $\overline{T_1}$ and $\overline{T_2}$:

$$T_p(t) = \frac{1}{2\pi i} \int_{r-i\infty}^{r+i\infty} e^{\lambda t} \overline{T_p}(\lambda) d\lambda \qquad p = 1, 2 \tag{A,9}$$

The integration line is shown in Figure A. The infinite integration of AB can be replaced by B-C-D-E-F-A and according to extended Jordan's lemma, it is easy to find that the line integrals in ED, BC and FA are zero. The origin integration can then, be rewritten as:

$$\frac{1}{2\pi i} \int_A^B e^{\lambda t} \overline{T_p}(\lambda) d\lambda = \frac{-1}{2\pi i} \left\{ \int_C^D e^{\lambda t} \overline{T_p}(\lambda) d\lambda + \int_E^F e^{\lambda t} \overline{T_p}(\lambda) d\lambda \right\} \tag{A,10}$$

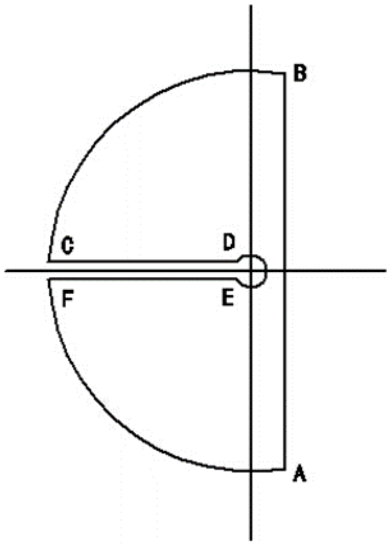

Figure A The integration line

Finally, the results are:

$$T_{in}(z,z',t,\tau)=\frac{1}{\pi}\int_0^{\infty}e^{-\alpha_1u^2t}\cos(uz-uz')du$$
$$+\frac{1}{\pi}\int_0^{\infty}e^{-\alpha_1u^2t}\left[\frac{Z_aZ_\psi-Z_bZ_\phi}{Z_\phi{}^2+Z_\psi{}^2}+\left(Ka-1\right)\frac{Z_cZ_\psi+Z_dZ_\phi}{Z_\phi{}^2+Z_\psi{}^2}\right]du$$
$$for\ \ 0\le z<l_z,\ 0<z'<l_z,\ 0<t$$

(A,11)

$$T_{out}(z,z',t,\tau)=\frac{2}{\pi}\int_0^{\infty}e^{-\alpha_1u^2t}\left\{\frac{\left[Z_eZ_\psi-Z_fZ_\phi\right]}{\left[Z_\phi{}^2+Z_\psi{}^2\right]}\right\}du \qquad for\ \ l_z<z<\infty,\ 0<z'<l_z,\ 0<t$$

(A,12)

where:

$$Z_a=\sin(uz)\cos\left(ul_z-uz'\right)\sin\left(aul_z\right)-Ka\sin(uz)\sin\left(ul_z-uz'\right)\cos\left(aul_z\right)$$
$$-\cos(uz)\cos\left(ul_z-uz'\right)\cos\left(aul_z\right)-Ka\cos(uz)\sin\left(ul_z-uz'\right)\sin\left(aul_z\right)$$

$$Z_b = \sin(uz)\cos\left(ul_z - uz'\right)\cos\left(aul_z\right) + Ka\sin(uz)\sin\left(ul_z - uz'\right)\sin\left(aul_z\right)$$
$$+\cos(uz)\cos\left(ul_z - uz'\right)\sin\left(aul_z\right) - Ka\cos(uz)\sin\left(ul_z - uz'\right)\cos\left(aul_z\right)$$

$$Z_c = \sin\left(uz\right)\cos\left(ul_z + aul_z\right)\sin\left(uz'\right) - \cos\left(uz\right)\sin\left(ul_z + aul_z\right)\sin\left(uz'\right)$$

$$Z_d = \cos\left(uz\right)\cos\left(ul_z + aul_z\right)\sin\left(uz'\right) + \sin\left(uz\right)\sin\left(ul_z + aul_z\right)\sin\left(uz'\right)$$

$$Z_e = \sin\left(uz'\right)\sin\left(auz\right)$$

$$Z_f = \sin\left(uz'\right)\cos\left(auz\right)$$

$$Z_\phi = \sin\left(aul_z\right)\cos\left(ul_z\right) - Ka\sin\left(ul_z\right)\cos\left(aul_z\right)$$

$$Z_\psi = \cos\left(ul_z\right)\cos\left(aul_z\right) + Ka\sin\left(ul_z\right)\sin\left(aul_z\right)$$

$$a = \sqrt{\frac{\alpha_1}{\alpha_2}} \; ; \quad K = \frac{k_2}{k_1}$$

REFERENCES

Alonso, E. E., Gens, A., & Hight, D. (1987). *Special problem soils. General report.* Paper presented at the Proceedings of the 9th European conference on soil mechanics and foundation engineering, Dublin.

Alonso, E. E., Gens, A., & Josa, A. (1990). A constitutive model for partially saturated soils. *Géotechnique, 40*(3), 405-430.

Ansys, C. (2009). ANSYS CFX-solver theory guide. *ANSYS CFX Release, 11*, 69-118.

Armaleh, S., & Desai, C. (1987). Load-deformation response of axially loaded piles. *Journal of geotechnical engineering, 113*(12), 1483-1500.

ASHRAE, H. (2011). Applications, Geothermal Energy, Chapter 34. *ASHRAE Handbook HVAC Applications IP Edition*, 34.31-34.30.

Bøhm, B. (2000). On transient heat losses from buried district heating pipes. *International journal of energy research, 24*(15), 1311-1334.

Ball, D., Fischer, R., & Hodgett, D. (1983). Design methods for ground-source heat pumps. *ASHRAE transactions, 89*, 416-440.

Barbier, E. (2002). Geothermal energy technology and current status: an overview. *Renewable and Sustainable Energy Reviews, 6*(1), 3-65.

Batini, N., Rotta Loria, A. F., Conti, P., Testi, D., Grassi, W., & Laloui, L. (2015). Energy and geotechnical behaviour of energy piles for different design solutions.

Applied Thermal Engineering, 86, 199-213. doi: 10.1016/j.applthermaleng. 2015.04.050

Beck, J. V. (1984). Green's function solution for transient heat conduction problems. *International Journal of Heat and Mass Transfer, 27*(8), 1235-1244.

Beck, J. V. (1986). Green's functions and numbering system for transient heat conduction. *AIAA journal, 24*(2), 327-333.

Bernier, M. A. (2001). SYMPOSIUM PAPERS-AT-01-8 Pumping Design and Performance Modeling of Geothermal Heat Pump Systems-Ground-Coupled Heat Pump System Simulation. *ASHRAE Transactions-American Society of Heating Refrigerating Airconditioning Engin, 107*(1), 605-616.

Bishop, A. W. (1960). *The principles of effective stress*: Norges Geotekniske Institutt.

Bloomquist, R. G. (1999). Geothermal heat pumps: four plus decades of experience. *GHC Bulletin, 20*(4), 13-18.

Borana, L. (2013). *Study on The Interface Behavior between Unsaturated Soil and Steel Surface.* (PhD), The Hong Kong Polytechnic University.

Borana, L., Yin, J.-H., Singh, D., & Shukla, S. (2013). A Modified Suction Controlled Direct Shear Device for Testing Unsaturated Soil and Steel Plate Interface. *Marine Georesources & Geotechnology*(just-accepted).

Borana, L., Yin, J.-H., Singh, D., & Shukla, S. (2015). A Modified Suction-Controlled

Direct Shear Device for Testing Unsaturated Soil and Steel Plate Interface. *Marine Georesources & Geotechnology, 33*(4), 289-298.

Bose, J. E., & Smith, M. D. (1992). Performance of new ground heat exchanger configurations for heat pumps. *Solar Engineering, 1*.

Boulon, M., & Foray, P. (1986). *Physical and numerical simulation of lateral shaft friction along offshore piles in sand.* Paper presented at the Proc. 3rd International Conference on Numerical methods in offshore piling, Nantes, France.

Bourne-Webb, P. J., Amatya, B., Soga, K., Amis, T., Davidson, C., & Payne, P. (2009). Energy pile test at Lambeth College, London: geotechnical and thermodynamic aspects of pile response to heat cycles. *Géotechnique, 59*(3), 237-248. doi: DOI 10.1680/geot.2009.59.3.237

Bourne-Webb, P. J., Soga, K., & Amatya, B. (2013). A framework for understanding energy pile behaviour. *Proceedings of the ICE - Geotechnical Engineering, 166*(2), 170-177. doi: 10.1680/geng.10.00098

Carslaw, H., Jaeger, J. C., & Feshbach, H. (1962). Conduction of heat in solids. *Physics Today, 15*, 74.

CARSLAW, H. S. Conduction of heat in solids.

Chen, W.-F., & McCarron, W. O. (1991). Bearing capacity of shallow foundations *Foundation Engineering Handbook* (pp. 144-165): Springer.

Chiasson, A. D., Rees, S. J., & Spitler, J. D. (2000). A preliminary assessment of the effects of groundwater flow on closed-loop ground source heat pump systems: Oklahoma State Univ., Stillwater, OK (US).

Chiu, C., & Ng, C. (2003). A state-dependent elasto-plastic model for saturated and unsaturated soils. *Géotechnique, 53*(9), 809-829.

Chung, M., Jung, P.-S., & Rangel, R. H. (1999). Semi-analytical solution for heat transfer from a buried pipe with convection on the exposed surface. *International Journal of Heat and Mass Transfer, 42*(20), 3771-3786.

Cole, K. D., Beck, J. V., Haji-Sheikh, A., & Litkouhi, B. (2010). *Heat Conduction Using Green's Functions*: Taylor & Francis.

Congedo, P. M., Colangelo, G., & Starace, G. (2012). CFD simulations of horizontal ground heat exchangers: A comparison among different configurations. *Applied Thermal Engineering, 33-34*, 24-32. doi: 10.1016/j.applthermaleng.2011.09.005

Coyle, H. M., & Reese, L. C. (1900). Load transfer for axially loaded piles in clay. *Journal of Soil Mechanics & Foundations Div, 92*(SM2, Proc Paper 4702).

Coyle, H. M., & Reese, L. C. (1966). *Load transfer for axially loaded piles in clayJ of SMFE Div.* Paper presented at the ASCE.

Cui, P., Li, X., Man, Y., & Fang, Z. (2011). Heat transfer analysis of pile geothermal heat exchangers with spiral coils. *Applied Energy, 88*(11), 4113-4119. doi:

10.1016/j.apenergy.2011.03.045

Cui, P., Wang, D., Yang, J., & Diao, N. (2013). *Numerical simulation and experimental verification of horizontal ground heat exchangers*. Paper presented at the 12th International Conference on Sustainable Energy technologies Hong Kong.

Cui, Y., & Delage, P. (1996). Yielding and plastic behaviour of an unsaturated compacted silt. *Géotechnique, 46*(2), 291-311.

Davisson, M. (1993). Negative skin friction in piles and design decisions.

De Vries, D. (1958). Simultaneous transfer of heat and moisture in porous media. *Transactions, American Geophysical Union, 39*, 909-916.

Deerman, J. (1990). Simulation of vertical U-tube ground-coupled heat pump systems using the cylindrical heat source solution. *ASHRAE Transaction: Research, 3472*, 287-295.

Demir, H., Koyun, A., & Temir, G. (2009). Heat transfer of horizontal parallel pipe ground heat exchanger and experimental verification. *Applied Thermal Engineering, 29*(2-3), 224-233. doi: 10.1016/j.applthermaleng.2008.02.027

Di Donna, A., Ferrari, A., & Laloui, L. (2015). Experimental investigations of the soil-concrete interface: physical mechanisms, cyclic mobilisation and behaviour at different temperatures. *Canadian Geotechnical Journal*(ja).

Di Donna, A., Rotta Loria, A. F., & Laloui, L. (2016). Numerical study of the response of a group of energy piles under different combinations of thermo-mechanical loads. *Computers and Geotechnics, 72,* 126-142. doi: 10.1016/j.compgeo.2015.11.010

Diao, N., Li, Q., & Fang, Z. (2004). Heat transfer in ground heat exchangers with groundwater advection. *International Journal of Thermal Sciences, 43*(12), 1203-1211.

Documentation, A. (2010). ABAQUS Analysis User's Manual. *Materials. Other plasticity models. Concrete.*

Doherty, P., Al-Huthaili, S., Riffat, S., & Abodahab, N. (2004). Ground source heat pump—description and preliminary results of the Eco House system. *Applied Thermal Engineering, 24*(17), 2627-2641.

Edlefsen, N. E., & Anderson, A. (1943). Thermodynamics of soil moisture.

Ergun, S. (1952). Fluid flow through packed columns. *Chem. Eng. Prog., 48,* 89-94.

Esen, H., Inalli, M., & Esen, M. (2007). Numerical and experimental analysis of a horizontal ground-coupled heat pump system. *Building and Environment*, *42*(3), 1126-1134. doi: 10.1016/j.buildenv.2005.11.027

Eskilson, P. (1987). *Thermal analysis of heat extraction boreholes*: Lund University.

Ewen, J., & Thomas, H. (1989). Heating unsaturated medium sand. *Géotechnique, 39*(3), 455-470.

Fang, Z., Diao, N., & Cui, P. (2002). Discontinuous operation of geothermal heat exchangers. *Tsinghua Science and Technology, 7*(2), 194-197.

Fellenius, B. H. (1980). The analysis of results from routine pile load tests. *Ground Engineering*, *13*(6), 19-31.

Fleming, K., Weltman, A., Randolph, M., & Elson, K. (2008). *Piling engineering*: CRC press.

Frank, R. (1982). Estimation par les paramètres pressiométriques de l'enfoncement sous charge axiale de pieux forés dans des sols fins. *BULL LIAISON LAB PONTS CHAUSS*(119).

Frank, R., Kalteziotis, N., Bustamante, M., Christoulas, S., & Zervogiannis, H. (1991). Evaluation of performance of two piles using pressuremeter method. *Journal of geotechnical engineering*, *117*(5), 695-713.

Fredlund, D. G., & Rahardjo, H. (1993). *Soil mechanics for unsaturated soils*: John Wiley & Sons.

Freeze, R. A., & Cherry, J. A. (1979). Groundwater, 1979. *Printice-Hall, New Jersey*.

Go, G.-H., Lee, S.-R., Yoon, S., & Kang, H.-b. (2014). Design of spiral coil PHC energy pile considering effective borehole thermal resistance and groundwater advection effects. *Applied Energy, 125*, 165-178. doi: 10.1016/j.apenergy.2014.03.059

Goode III, J. C. (2013). Centrifuge modeling of the thermo-mechanical response of energy foundations.

Hellström, G. (1991). *Ground heat storage: Thermal analyses of duct storage systems*: Lund University.

Hermansson, Å., Charlier, R., Collin, F., Erlingsson, S., Laloui, L., & Sršen Sr, M. (2009). Heat transfer in soils *Water in Road Structures* (pp. 69-79): Springer.

Hossain, M. A. (2010). *Experimental study on the interface behavior between unsaturated completely decomposed granite soil and cement grout.* The Hong Kong Polytechnic University.

Hossain, M. A., & Yin, J.-H. (2009). Behavior of a compacted completely decomposed granite soil from suction controlled direct shear tests. *Journal of Geotechnical and Geoenvironmental Engineering, 136*(1), 189-198.

Hossain, M. A., & Yin, J.-H. (2010). Shear strength and dilative characteristics of an unsaturated compacted completely decomposed granite soil. *Canadian Geotechnical Journal, 47*(10), 1112-1126.

Ingersioll, L., Zobel, O. J., & Ingersoll, A. C. (1954). Heat Conduction: With Engineering Geological And Other Applications.

Ingersoll, L., Adler, F., Plass, H., & Ingersoll, A. (1950). Theory of earth heat exchangers for the heat pump. *ASHVE Trans, 56*, 167-188.

Ingersoll, L., & Plass, H. (1948). Theory of the ground pipe heat source for the heat pump. *ASHVE transactions, 47*(7), 339-348.

Ingersoll, L., Zabel, O. J., & Ingersoll, A. C. (1954). Heat conduction with engineering, geological, and other applications.

Jaeger, J. G. (1944). Some problems involving line sources in conduction of heat. doi: 10.1080/14786444408521476

Jiang, Y., & Wu, X. (2014). Annual report on China building energy efficiency. *China Architecture &Building Press, Beijing (2010)(in Chinese).*

Jun, Z. (2007). *Design and Application of Ground Source Heat Pump System*: China building industry press.

Kanno, T., Kato, K., & Yamagata, J. (1996). Moisture movement under a temperature gradient in highly compacted bentonite. *Engineering geology, 41*(1), 287-300.

Kavanaugh, S. P. (1985). Simulation and experimental verification of vertical ground-coupled heat pump systems: Oklahoma State Univ., Stillwater (USA).

Knellwolf, C., Peron, H., & Laloui, L. (2011). Geotechnical analysis of heat exchanger piles. *Journal of Geotechnical and Geoenvironmental Engineering, 137*(10), 890-902.

Laloui, L., & Nuth, M. (2005). Numerical modelling of the behaviour of a heat exchanger pile. *Revue Européenne de Génie Civil, 9*(5-6), 827-839. doi: 10.1080/17747120.2005.9692787

Laloui, L., Nuth, M., & Vulliet, L. (2006). Experimental and numerical investigations of the behaviour of a heat exchanger pile. *International Journal for Numerical and Analytical Methods in Geomechanics, 30*(8), 763-781.

Lamborn, M. J. (1986). *A micromechanical approach to modeling partly saturated soils.* Texas A&M University.

Li, H., Nagano, K., & Lai, Y. (2012a). Heat transfer of a horizontal spiral heat exchanger under groundwater advection. *International Journal of Heat and Mass Transfer, 55*(23-24), 6819-6831. doi: 10.1016/j.ijheatmasstransfer.2012.06.089

Li, H., Nagano, K., & Lai, Y. (2012b). A new model and solutions for a spiral heat exchanger and its experimental validation. *International Journal of Heat and Mass Transfer, 55*(15-16), 4404-4414. doi: 10.1016/j.ijheatmasstransfer.2012.03.084

Li, M., & Lai, A. C. K. (2012). New temperature response functions (G functions) for pile and borehole ground heat exchangers based on composite-medium line-source theory. *Energy, 38*(1), 255-263. doi: 10.1016/j.energy.2011.12.004

Ling, F., & Zhang, T. (2004). A numerical model for surface energy balance and thermal regime of the active layer and permafrost containing unfrozen water. *Cold Regions Science and Technology, 38*(1), 1-15.

Lund, J., Sanner, B., Rybach, L., Curtis, R., & Hellström, G. (2004). Geothermal (ground-source) heat pumps–a world overview. *GHC Bulletin, 25*(3), 1-10.

Man, Y., Yang, H., Diao, N., Liu, J., & Fang, Z. (2010). A new model and analytical solutions for borehole and pile ground heat exchangers. *International Journal of Heat and Mass Transfer, 53*(13-14), 2593-2601. doi: 10.1016/j.ijheatmasstransfer.2010.03.001

Man, Y., Yang, H. X., Diao, N. R., Cui, P., Lu, L., & Fang, Z. H. (2011). Development of spiral heat source model for novel pile ground heat exchangers. *Hvac&R Research, 17*(6), 1075-1088. doi: Doi 10.1080/10789669.2011.610281

Mei, V. C. (1991). Heat transfer of buried pipe for heat pump application. *Journal of solar energy engineering, 113*(1), 51-55.

Meyerhof, G. G. (1983). Scale effects of ultimate pile capacity. *Journal of geotechnical engineering, 109*(6), 797-806.

Mihalakakou, G. (2002). On estimating soil surface temperature profiles. *Energy and Buildings, 34*(3), 251-259.

Molina-Giraldo, N., Blum, P., Zhu, K., Bayer, P., & Fang, Z. (2011). A moving finite line source model to simulate borehole heat exchangers with groundwater advection. *International Journal of Thermal Sciences, 50*(12), 2506-2513.

Nakano, M., & Miyazaki, T. (1979). THE DIFFUSION AND NONEQUILIBRIUM THERMODYNAMIC EQUATIONS OF WATER VAPOR IN SOILS UNDER TEMPERATURE GRADIENTS. *Soil Science*, *128*(3), 184-188.

Negiz, A., Hastaoglu, M. A., & Heidemann, R. A. (1995). Three-dimensional transient heat transfer from a buried pipe: solidification of a stationary fluid. *Numerical Heat Transfer, Part A: Applications, 28*(2), 175-193.

Ng, C., & Menzies, B. (2007). *Advanced unsaturated soil mechanics and engineering*: CRC Press.

Ng, C., & Zhou, R. (2005). *Effects of soil suction on dilatancy of an unsaturated soil.* Paper presented at the Proceedings of the 16th International Conference on Soil Mechanics and Geotechnical Engineering, Vols 1-5: GEOTECHNOLOGY IN HARMONY WITH THE GLOBAL ENVIRONMENT.

Oloo, S., & Fredlund, D. (1996). A method for determination of φ b for statically compacted soils. *Canadian Geotechnical Journal, 33*(2), 272-280.

Philip, J., & De Vries, D. (1957). Moisture movement in porous materials under temperature gradients. *Transactions, American Geophysical Union, 38*, 222-232.

Randolph, M. F., & Wroth, C. P. (1978). Analysis of deformation of vertically loaded piles. *Journal of the Geotechnical Engineering Division, 104*(12), 1465-1488.

Rees, S., Adjali, M., Zhou, Z., Davies, M., & Thomas, H. (2000). Ground heat transfer effects on the thermal performance of earth-contact structures. *Renewable and Sustainable Energy Reviews, 4*(3), 213-265.

Reese, L., & O'Neill, M. (1989). *New design method for drilled shafts from common* *soil and rock tests.* Paper presented at the Foundation Engineering: Current principles and practices.

Rotta Loria, A. F., Gunawan, A., Shi, C., Laloui, L., & Ng, C. W. W. (2015). Numerical modelling of energy piles in saturated sand subjected to thermo-mechanical loads. *Geomechanics for Energy and the Environment, 1,* 1-15. doi: 10.1016/j.gete.2015.03.002

Sanaye, S., & Niroomand, B. (2010). Horizontal ground coupled heat pump: Thermal-economic modeling and optimization. *Energy conversion and management, 51*(12), 2600-2612.

Sarbu, I., & Sebarchievici, C. (2014). General review of ground-source heat pump systems for heating and cooling of buildings. *Energy and Buildings, 70,* 441-454. doi: 10.1016/j.enbuild.2013.11.068

Schofield, R. (1935). The pF of the water in soil. *Trans. 3rd Int. Congr. Soil Sci, 2,* 37-48.

Seed, H. B., & Reese, L. C. (1900). The action of soft clay along friction piles. *American Society of Civil Engineers Transactions*.

Seed, H. B., & Reese, L. C. (1957). The Action of Clay Along Friction Piles. *J Geoteh Engng, 504,* 92.

Self, S. J., Reddy, B. V., & Rosen, M. A. (2013). Geothermal heat pump systems: status review and comparison with other heating options. *Applied Energy, 101*, 341-348.

Sivakumar, V. (1993). *A critical state framework for unsaturated soil.* University of Sheffield.

Sophocleous, M. (1979). Analysis of water and heat flow in unsaturated‐saturated porous media. *Water Resources Research*, *15*(5), 1195-1206.

Standard, A. (2012). D3080/D3080M-11 Standard test method for direct shear test of soils under consolidated drained conditions. *West Conshohocken, PA: ASTM International*.

Stas, C. V., & Kulhawy, F. H. (1984). *Critical evaluation of design methods for foundations under axial uplift and compression loading*: Electric Power Research Institute.

Sutman, M., Olgun, C. G., & Brettmann, T. (2015). *Full-scale field testing of energy piles.* Paper presented at the IFCEE 2015.

Sutton, M. G., Nutter, D. W., & Couvillion, R. J. (2003). A ground resistance for vertical bore heat exchangers with groundwater flow. *Journal of Energy Resources Technology-Transactions of the Asme, 125*(3), 183-189. doi: Doi 10.1151/1.1591203

Uesugi, M., & Kishida, H. (1986). Frictional resistance at yield between dry sand and mild steel. *Soils and Foundations, 26*(4), 139-149.

Vanapalli, S., Fredlund, D., Pufahl, D., & Clifton, A. (1996). Model for the prediction of shear strength with respect to soil suction. *Canadian Geotechnical Journal, 33*(3), 379-392.

Wheeler, S., & Sivakumar, V. (1995). An elasto-plastic critical state framework for unsaturated soil. *Géotechnique, 45*(1), 35-53.

Wu, Y., Gan, G., Verhoef, A., Vidale, P. L., & Gonzalez, R. G. (2010). Experimental measurement and numerical simulation of horizontal-coupled slinky ground source heat exchangers. *Applied Thermal Engineering, 30*(16), 2574-2583.

Xiong, Z., & Lee, E. S. (2013). Development of a Horizontal Slinky Ground Heat Exchanger Model. *ASHRAE transactions, 119*, 1G.

Xue, Z. Y., Jiang. (2005). Study on the air conditioning energy guide line in commercial. *HV&AV, 35*(1), 37-41.

Zhai, X. Q., Qu, M., Yu, X., Yang, Y., & Wang, R. Z. (2011). A review for the applications and integrated approaches of ground-coupled heat pump systems. *Renewable and Sustainable Energy Reviews, 15*(6), 3133-3140. doi: 10.1016/j.rser.2011.04.024

Zhang, W., Yang, H., Lu, L., Cui, P., & Fang, Z. (2014). The research on ring-coil heat transfer models of pile foundation ground heat exchangers in the case of groundwater seepage. *Energy and Buildings, 71*, 115-128. doi: 10.1016/j.enbuild.2013.12.016

Zhang, W., Yang, H., Lu, L., & Fang, Z. (2012). Investigation on heat transfer around buried coils of pile foundation heat exchangers for ground-coupled heat pump applications. *International Journal of Heat and Mass Transfer, 55*(21-22), 6023-6031. doi: 10.1016/j.ijheatmasstransfer.2012.06.013

Zhang, W., Yang, H., Lu, L., & Fang, Z. (2013). The analysis on solid cylindrical heat source model of foundation pile ground heat exchangers with groundwater flow. *Energy, 55*, 417-425. doi: 10.1016/j.energy.2013.03.092